Measuring Single Charged Pion Production in Muon Neutrino Interactions on Argon with MicroBooNE

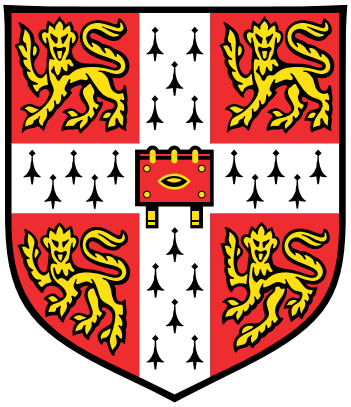

Jan Philip Detje

Cavendish Laboratory
University of Cambridge
Sidney Sussex College
October 2025

This thesis is submitted for the degree of
Doctor of Philosophy

Declaration

This thesis is the result of my own work and includes nothing which is the outcome of work done in collaboration except as declared in the preface and specified in the text. It is not substantially the same as any work that has already been submitted, or is being concurrently submitted, for any degree, diploma or other qualification at the University of Cambridge or any other University or similar institution except as declared in the preface and specified in the text. It does not exceed the prescribed word limit for the relevant Degree Committee.

Jan Philip Detje

Abstract

Neutrinos are the most abundant massive particles known, but they interact only rarely with matter. Next-generation experiments such as DUNE aim to measure charge-parity violation in the lepton sector through flavour oscillations of neutrinos propagating over long distances before interacting with a liquid argon target. Accurate determination of the neutrino energy, crucial for oscillation studies, requires a good understanding of neutrino–nucleus interactions. At the neutrino energies planned for DUNE, resonance production with pion emission will be the dominant interaction mode. This thesis presents new flux-integrated charged-current muon neutrino cross-section measurements on argon for final states containing exactly one charged pion and no other hadrons beyond nucleons. The analysis uses data from the liquid argon time-projection chamber experiment MicroBooNE, situated in the Booster Neutrino Beam at Fermilab, corresponding to 1.11×10^{21} protons-on-target. Total and single-differential cross sections are reported within a restricted phase space of muon momenta above 150 MeV, pion momenta above 100 MeV, and muon–pion opening angles below 2.65 rad. Differential results are given with respect to the muon and pion momenta, their scattering angles relative to the beam, and their opening angle. The total cross section is measured to be $\sigma = (3.75 \pm 0.07\ (\text{stat.}) \pm 0.80\ (\text{syst.})) \times 10^{-38}\,\text{cm}^2$ per argon nucleus at a mean neutrino beam energy of ~ 0.8 GeV. Comparisons with multiple neutrino–nucleus generators highlight areas for model improvement, particularly at very forward muon angles and at low pion momentum. Together, these high-statistics measurements provide essential input for constraining systematic uncertainties and improving interaction models for future experiments.

Acknowledgements

I would like to thank Melissa Uchida for welcoming me into her group, first as a master's student and then as a PhD student. Thank you also to Andy Smith and Steve Green for helping me get started. To the past and present PhD students of the Cambridge Neutrino Group, with whom I shared the dark closet that was our Rutherford office, Stefano, Andy, Alex, Karolina, Jing, Natsumi, and Magnus, thank you for making the PhD journey enjoyable. I would also like to thank the postdocs of the group, Steve Dennis and Leigh Whitehead, for making the group a better place to work. Special thanks also go to Leigh for helping navigate a period of change in the group and for serving as a de facto second supervisor. I am grateful to Oleg Brandt for officially taking over as supervisor of this PhD despite his commitments to his own group. The support from both of you made finishing this work possible. Thank you to all the members of the MicroBooNE collaboration for their consistently helpful attitude and the spirit of collaboration that made working in such a large international experiment enjoyable. Working with so many people across the Atlantic has been a remarkable experience. I am particularly grateful to Kirsty Duffy and Patrick Green from the Oxford Neutrino Group, whose guidance and time investment were crucial to much of this work. I also gratefully acknowledge the generous support of the German Academic Scholarship Foundation, without which this research would not have been possible. Finally, I want to express my deepest gratitude to my parents and my girlfriend, who have been unwavering sources of support and encouragement throughout my academic journey.

Table of contents

Abbreviations

ΛCDM Lambda Cold Dark Matter. 22

1p1h One-particle-one-hole. 43, 73

2p2h Two-particle-two-hole. 43, 128

ADC Analog-to-digital converter. 62, 63, 82

AGKY Andreopoulos-Gallagher-Kehayias-Yang. 75

AGS Alternating Gradient Synchrotron. 14

ArgoNeuT Argon Neutrino Teststand. 88, 152, 167

ASIC Application-specific integrated circuit. 61, 65

BAO Baryon acoustic oscillations. 22

BDT Boosted decision tree. 2, 88, 91, 93–95, 100–104, 112, 116, 135, 143, 167

BEST Baksan Experiment on Sterile Transitions. 29

BNB Booster Neutrino Beam. 2, 45, 46, 48, 49, 64, 65, 68, 69, 85, 132, 146, 167

BS Berger-Sehgal. 75

BSM Beyond the Standard Model. 24, 30

BUU Boltzmann-Uehling-Uhlenbeck. 73, 74, 77

BY Bodek-Yang. 75

C Charge. 1, 13, 19

CC Charged current. 2, 11, 12, 15, 34, 36–38, 41, 70, 73, 74, 81, 84, 88, 89, 91, 92, 102, 106, 115, 120, 128, 136, 137, 161, 167

CC1$\pi^{\pm}$ Muon neutrino charged-current single charged-pion production. 84, 85, 89, 136, 152, 160

CCQE Charged-current quasi-elastic. 32, 33, 37, 128

CDHS CERN-Dortmund-Heidelberg-Saclay. 28

CKM Cabibbo-Kobayashi-Maskawa. 12, 13, 15, 20

CL Confidence level. 21, 22

CMB Cosmic microwave background. 22

CORSIKA Cosmic Ray Simulations for KASCADE. 58, 130

CP Charge-parity. 1, 13, 15, 19–21, 26, 30, 84, 168

CPT Charge-parity-time. 13

CRT Cosmic ray tagger. 55, 56, 64, 65, 67

CV Central value. 123, 124, 126–129, 131, 132, 141, 143, 146, 148

CVC Conserved vector current. 36

DAQ Data acquisition. 62–65

DESI Dark Energy Spectroscopic Instrument. 22

DIS Deep inelastic scattering. 41–43, 73, 75

DONUT Direct Observation of the Tau Neutrino. 14

DUNE Deep Underground Neutrino Experiment. 1–3, 30, 70, 84, 168, 169

EM Electromagnetic. 35, 36, 42, 90

FEB Front end board. 64

FEM Front end module. 62, 64

Fermilab Fermi National Accelerator Laboratory. 1, 2, 21, 28, 45, 48, 49, 62, 64, 68, 84, 88, 168

FPGA Field-programmable gate array. 62, 63

FSI Final-state interactions. 75, 77, 84, 85, 140, 148, 162, 168

GALLEX Gallium Experiment. 29

GiBUU Giessen Boltzmann-Uehling-Uhlenbeck. 70, 73–76, 157, 160–162, 164, 166

HARP Hadron Production Experiment. 68, 127

INC Intranuclear cascade. 75

J-PARC Japan Proton Accelerator Research Complex. 21

JUNO Jiangmen Underground Neutrino Observatory. 30

KLM-BS Kuzmin-Lyubushkin-Naumov Berger-Sehgal. 74

KNO Koba-Nielsen-Olesen. 75

LAr Liquid argon. 50, 131

LArIAT Liquid Argon In A Testbeam. 169

LArSoft Liquid Argon Software. 68, 78

LArTPC Liquid argon time projection chamber. 1, 2, 49, 68, 77, 81, 169

LEE Low energy excess. 83

LFG Local Fermi gas. 72, 73

LINAC Linear accelerator. 45

LSND Liquid Scintillator Neutrino Detector. 28

MAID Mainz Unitary Isobar Model. 74

MC Monte Carlo. 64, 68, 70, 76, 78, 79, 82, 90, 91, 96, 100, 110, 115, 125, 127, 129, 132, 133, 146

MCS Multiple Coulomb scattering. 58, 77, 88, 114, 115

MEC Meson-exchange current. 43, 70, 72, 74

MicroBooNE Micro Booster Neutrino Experiment. 2, 3, 28, 45, 48–50, 55–57, 59–61, 65, 66, 68–70, 77, 78, 80–85, 88–92, 96, 100, 114, 124, 126–129, 132, 133, 136, 137, 143, 146, 148, 150, 152, 157, 161, 164, 167–169

MINERvA Main Injector Experiment for ν-A. 89, 161

MiniBooNE Mini Booster Neutrino Experiment. 28, 68, 69, 126, 161

MINOS Main Injector Neutrino Oscillation Search. 28, 161

MIP Minimum ionising particle. 50, 54, 96, 135

MSW Mikheyev-Smirnov-Wolfenstein. 16

NC Neutral current. 11, 12, 28, 33, 35–38, 41, 84, 92, 128

NEOS Neutrino Experiment for Oscillation at Short Baseline. 29

NuMI Neutrinos at the Main Injector. 21, 45, 48, 49, 64, 67, 88, 167, 168

NuWro Wrocław Neutrino Generator. 70, 73–75, 77, 79, 128, 146, 148, 160–162, 164, 166

P Parity. 1, 13

PCAC Partially conserved axial current. 36, 75

PDF Parton distribution function. 42

PID Particle identification. 57

PMNS Pontecorvo-Maki-Nakagawa-Sakata. 15, 19, 20, 26, 28

PMT Photomultiplier tube. 59–64, 66, 67, 77–80, 131

POT Protons on target. 65, 88, 90, 143, 146

ppm Parts per million. 50

ppt Parts per trillion. 50

PROSPECT Precision Reactor Oscillation and Spectrum Experiment. 29

QCD Quantum Chromodynamics. 6, 7

QE Quasi-elastic. 32, 33, 37, 44, 70–75, 140, 168

RENO Reactor Experiment for Neutrino Oscillation. 29

RES Resonance production. 37, 38, 75

RF Radio frequency. 45

RFG Relativistic Fermi gas. 72

ROI Region of interest. 80

RPA Random phase approximation. 73, 128

RS Rein-Sehgal. 74, 128

SAGE Soviet-American Gallium Experiment. 29

SAM Serial Access to Metadata. 62

SBN Short-Baseline Neutrino. 2, 49, 84

SBND Short-Baseline Near Detector. 70, 168

SCE Space charge effect. 56–59

SciBooNE SciBar Booster Neutrino Experiment. 68

SiPM Silicon photomultiplier. 64

SIS Shallow inelastic scattering. 42, 75

SM Standard Model. 4–6, 8, 10, 12–14, 20, 23, 24, 27, 28

SNO Sudbury Neutrino Observatory. 15

STEREO Short-distance Neutrino Oscillations with a Reactor. 29

SVD Singular value decomposition. 143, 145, 146, 155, 157, 191–193

SVM Support vector machine. 81, 97

T Time. 13

T2K Tokai to Kamioka. 21, 30, 89, 127

TMVA Toolkit for Multivariate Data Analysis. 100

TPB Tetraphenyl butadiene. 60, 62

TPC Time projection chamber. 49, 50, 57, 58, 64, 65, 67, 79, 80, 82, 84, 86, 93, 102

TRISTAN Tritium Sterile Anti-Neutrino Experiment. 30

VEV Vacuum expectation value. 10

VUV Vacuum ultraviolet. 59, 60, 131

Chapter 1

Introduction

1.1 Overview

The observed asymmetry between matter and antimatter in the universe presents a fundamental puzzle in modern physics. Any process capable of generating such an imbalance must violate the combined charge (C) and parity (P) symmetries, a phenomenon known as charge-parity (CP) violation. While this symmetry breaking has been observed among quarks, the degree of CP violation is insufficient to explain the universe's current state. CP violation among leptons, however, remains a viable explanation for the matter-antimatter asymmetry. Neutrinos, which belong to the lepton family, are the lightest and most abundant known matter particles. As they travel, neutrinos and their antiparticles oscillate between different flavours. Measurable differences in the oscillation probabilities between neutrinos and antineutrinos, once the effects of propagation through matter are taken into account, would provide clear signatures of CP violation. Next-generation neutrino oscillation experiments, scheduled to begin operating in the coming decade, aim to measure this effect. Among these is the Deep Underground Neutrino Experiment (DUNE) at the Fermi National Accelerator Laboratory (Fermilab), which will employ a liquid argon time projection chamber (LArTPC) detector.

The study of neutrino oscillations requires precise knowledge of the energies of interacting neutrinos. Since neutrino beams have a broad energy spectrum, neutrino energies must be estimated from the visible particles produced during interactions. Energy lost through undetectable particles, such as neutrons, must be accounted for using interaction simulations. These simulations face significant challenges. They must model complex neutrino-nucleus interactions, including initial nucleon states and various interaction modes. They must also capture subsequent intra-nuclear processes

that can lead to particle absorption and production. The accuracy of cross-section simulations directly impacts energy reconstruction quality and represents one of the major sources of uncertainty in oscillation experiments.

At the beam energies planned for DUNE, $\sim 1 - 5\,\text{GeV}$, the production of baryon resonances will be the dominant interaction channel. These resonances decay predominantly into a pion and a nucleon. The Micro Booster Neutrino Experiment (MicroBooNE), an existing LArTPC experiment at Fermilab that operated from 2015 to 2021 as part of the Short-Baseline Neutrino (SBN) programme, can provide valuable insights into these interactions. With its 85-tonne active volume and exposure to the Booster Neutrino Beam (BNB) in the ~ 1 GeV neutrino energy range, MicroBooNE has collected a large data set of neutrino-argon interactions. The detector's high-resolution imaging and precise calorimetric measurements make it ideally suited for measuring a wide variety of final states.

This thesis presents measurements of muon neutrino charged-current single charged pion cross sections on argon using MicroBooNE data. These measurements are essential for understanding resonant interactions and for constraining systematic uncertainties that would otherwise limit the sensitivity of oscillation analyses. Both the total cross section and single differential cross sections with respect to muon and pion kinematic variables are measured. By comparing these measurements with current neutrino interaction generator models, this work provides constraints on the underlying physics of neutrino-argon interactions needed for future neutrino oscillation experiments.

1.2 Contributions

MicroBooNE is a collaborative research endeavour with shared tools and datasets. Its physics results are the cumulative effort of nearly two decades of work to bring the experiment to the point it is today. Within this collaborative framework, the author has made contributions to MicroBooNE's expanding cross-section programme by being the sole analyser for the experiment's cross-section measurement for muon neutrino interactions producing final-state charged pions. The analysis starting in Chapter 7 is my own work, building upon a foundation established by Alesha Devitt, Andrew Smith, and Kirsty Duffy in charged pion identification in MicroBooNE. Specifically, it employs a charged pion identification method using boosted decision trees (BDTs) developed by A. Smith and K. Duffy, while also relying on a charged current (CC) muon neutrino preselection developed by Wouter Van De Pontseele. The research presented here was conducted with guidance and support from Kirsty Duffy and Patrick Green. Input also

came in the form of the multi-stage MicroBooNE collaboration review of the analysis for publication, most significantly via the review by an editorial board made up of Wes Ketchum, Andy Furmanski, and Steven Dytman. The analysis further makes use of a set of cross-section tools developed primarily by Steven Gardiner, which are used to propagate uncertainties and unfold the data. In addition, the author has worked as part of the Cambridge Neutrino Group on hardware testing and assembly for the DUNE far detector anode plane, and as part of the MicroBooNE production team on processing data and producing simulated samples.

Chapter 2

Neutrinos in the Standard Model

Neutrinos are the most abundant massive particles currently known, but their very low interaction rate also makes them some of the least well understood. This chapter starts with a general overview of the Standard Model (SM) that is at the heart of particle physics before focussing more narrowly on neutrinos and how they do and do not fit within it.

2.1 Introduction to the Standard Model

The SM is a locally gauge-invariant quantum field theory that describes particles as excitations of fields and forces between the particles as mediated by gauge bosons [1]. The accomplishment of the SM is that it brings the three fundamental forces, electromagnetic, weak nuclear, and strong nuclear, into one coherent framework. It is missing gravity, which only becomes significant at macroscopic scales. With few exceptions, the SM is capable of describing all experimental data today. While it has been very successful in describing particle interactions, it is in no way a complete theory, and there are still open questions even with the known particles of the model.

The SM describes a set of particles shown in Figure 2.1. These are categorised as either fermions or bosons. Fermions can be identified by their spin quantum number being an odd multiple of 1/2, using natural units here and throughout this work with the reduced Planck constant and speed of light $\hbar = c = 1$. Fermions obey the Pauli exclusion principle, resulting in identical particles never occupying the same quantum state. The fermions are further categorised into three generations. Quarks are fermions that interact via the strong force, whereas leptons do not interact via the strong force. Neutrinos are leptons that carry no electric charge and thus interact only via the weak force.

Bosons have integer spin and consist of gauge bosons and a single scalar boson, the Higgs boson. Gauge bosons act as the force carriers in the SM, with photons mediating the electromagnetic force, $W^{\pm}$ and Z carrying the weak force, and gluons being responsible for the strong force.

All listed particles with electric charge also have distinct antiparticles. Of the bosons, only the W^+ and W^- form a distinct particle-antiparticle pair. All other bosons are their own antiparticles. Among the fermions, the antiparticle of the negatively charged electron, for instance, is the positively charged positron.

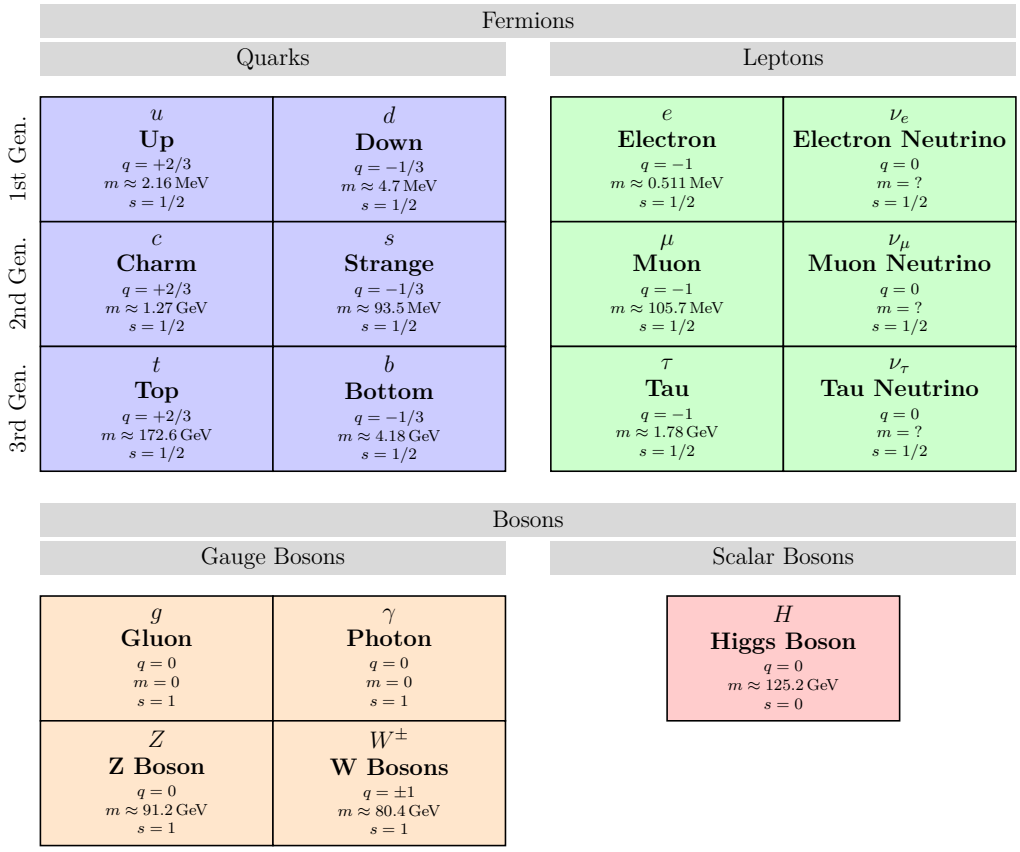

Fig. 2.1 Particles in the Standard Model with their electric charge q, mass m and spin s with values from Ref. [1].

Much of particle physics is concerned with uncovering and understanding fundamental symmetries in nature. Mathematician Emmy Noether showed in the first quarter of the twentieth century that continuous symmetries in the action of a system free from non-conservative forces, such as friction, result in conservation laws [2]. A classical example is an object moving in a central rotationally-symmetric potential, giving rise to angular momentum conservation.

The SM can be described by the symmetry group

$$SU(3)_C \times SU(2)_L \times U(1)_Y, \tag{2.1}$$

which is a group of transformations that leave the physics unchanged. Mathematically, a group here is a set of elements following the group axioms [3]. In particular, the three groups considered above are sets of unitary matrices, for which $U^\dagger U = 1$ with $U^\dagger = (U^*)^T$ denotes the conjugate transpose, with the matrix dimension given in brackets. The S stands for special and denotes groups in which the matrices also have determinant one. These are Lie groups, as they describe continuous symmetries.

2.2 Strong Force and Hadrons

The gauge symmetry of Quantum Chromodynamics (QCD) is $SU(3)_C$, which governs the strong force responsible for binding quarks into hadrons. The generators of $SU(3)_C$ are the eight Gell-Mann matrices λ^a $(a = 1, \ldots, 8)$, which form the basis of its Lie algebra. Quarks carry a property called colour charge, which can take three values: red, green, and blue, along with their corresponding anticolours for antiquarks. The strong force is responsible for confining quarks into bound states known as hadrons. Bound states consisting of one or more quark-antiquark pairs are called mesons, with examples including pions, while bound states with odd numbers of quarks are baryons, such as protons and neutrons. However, bound states beyond three quarks decay very quickly, with the longest lifetimes being of the order $\mathcal{O}(10^{-21})$ seconds [4, 5]. Table 2.1 lists the quark compositions of the lightest mesons and baryons.

Type	**Particle**	**Quark Composition**
Meson	Charged Pion (π^+)	$u\bar{d}$
	Charged Pion (π^-)	$d\bar{u}$
	Neutral Pion (π^0)	$\frac{1}{\sqrt{2}}\left(u\bar{u} - d\bar{d}\right)$
Baryon	Proton (p)	uud
	Neutron (n)	udd

Table 2.1 Quark composition of the lightest baryon and meson states.

Gluons mediate the strong force and carry both a colour and an anticolour charge. They alter the colour of quarks during interactions, as illustrated in Figure 2.2. In addition to binding quarks together, the strong force also binds protons and neutrons in

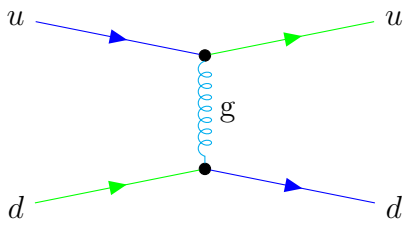

Fig. 2.2 Feynman diagram with quarks changing colour charge via gluon interaction. The gluon carries either blue-antigreen or antiblue-green colour charges depending on the time ordering of the interaction.

the nucleus, overcoming the repulsive electromagnetic force between positively charged protons. This residual strong force is not mediated directly through gluons and instead results from the exchange of virtual mesons, such as π^0, as shown in Figure 2.3.

A fundamental property of QCD is colour confinement, which states that quarks and gluons cannot exist freely outside colour-neutral hadronic states. Colour neutrality is achieved when a colour and its corresponding anticolour are paired, for instance, a red up quark and an antired antidown quark in a π^+. Baryons achieve colour neutrality by having all three (anti-)colours present, resulting in a neutral white state in the colour analogy.

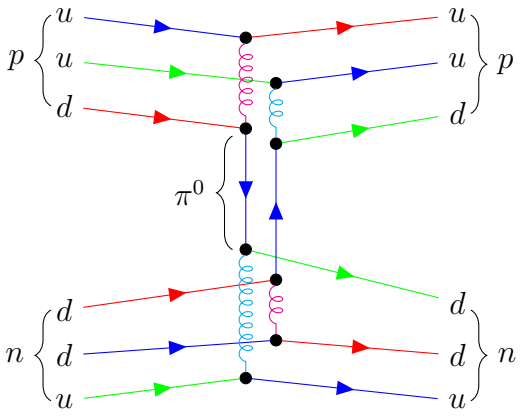

Fig. 2.3 Residual strong force interaction between a proton and a neutron via a virtual meson such as a π^0.

Short-lived excited states of hadrons are called resonances and play an important role in cross-section physics as intermediary particles. For instance, $\Delta^+(uud)$ is a more massive hadron with the same quark flavour composition as the proton.

2.3 Electroweak Force

One of the key accomplishments of the SM is its prediction and the subsequent discovery of the heavy $W^{\pm}$ and Z gauge bosons through electroweak unification, which shows that the weak and electromagnetic forces are different manifestations of a single electroweak force. The gauge group $SU(2)_L \times U(1)_Y$ describes this unified electroweak force. The $SU(2)_L$ group couples only to left-chiral particles, a distinction central to the SM treatment of weak interactions. Chirality is a fundamental property of fermions that can be more easily understood through its connection to helicity. Helicity is the projection of a particle's spin onto its momentum direction. The helicity of a particle can be aligned with its momentum (right-handed) or anti-aligned (left-handed), as illustrated in Figure 2.4.

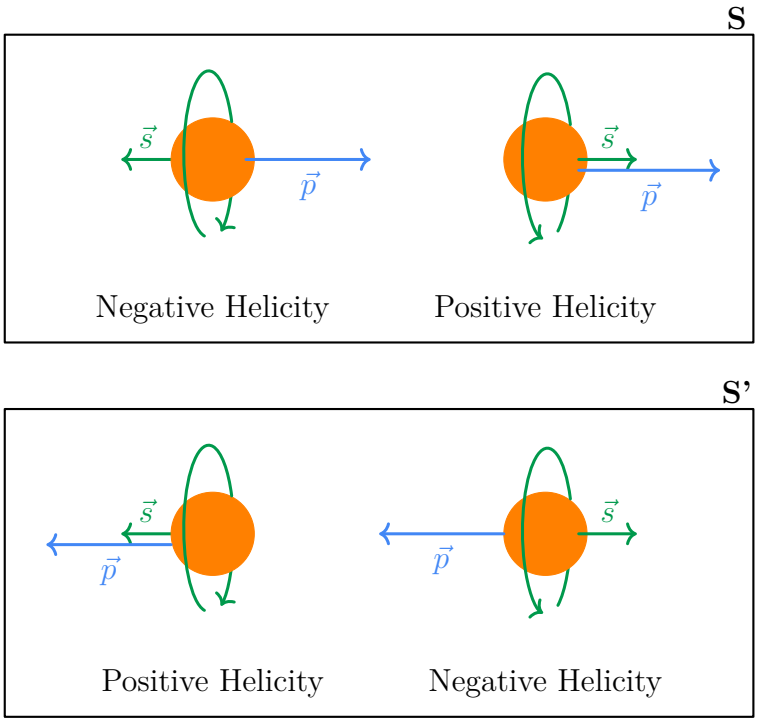

Fig. 2.4 Illustration of helicity before (S) and after (S') Lorentz boosting into a reference frame faster than the particle. The momentum vector flips direction, but spin stays the same. This results in helicity not being invariant under Lorentz transformation for particles travelling slower than the speed of light (massive particles).

For massive particles travelling slower than the speed of light, one can always boost into a reference frame moving faster than the particle itself, causing its momentum vector to flip while its spin remains unchanged. Consequently, the helicity of the

particle changes sign. This demonstrates that helicity is not Lorentz invariant and can differ for observers in different inertial reference frames.

Chirality, on the other hand, is an intrinsic Lorentz-invariant property of fermions. It is determined by the action of the projection operators:

$$\psi_L = \hat{P}_L \, \psi = \tfrac{1}{2}(1 - \gamma^5) \, \psi, \tag{2.2}$$

$$\psi_R = \hat{P}_R \, \psi = \tfrac{1}{2}(1 + \gamma^5) \, \psi, \tag{2.3}$$

where $\psi = \begin{pmatrix} \psi_L \\ \psi_R \end{pmatrix}$ is a Dirac spinor made up of two two-component Weyl spinors in the chiral representation. The Dirac spinor is a four-component object that describes relativistic spin-1/2 particles. It emerges as the solution to the Dirac equation, which generalises the Schrödinger equation to be consistent with special relativity. The matrix $\gamma_5 = i\gamma^0\gamma^1\gamma^2\gamma^3$ is defined in the context of the Dirac equation as the product of the Dirac matrices γ^{0-3} and separates the spinor into left-chiral ψ_L and right-chiral ψ_R components. For massless particles travelling at the speed of light, chirality and helicity are equivalent.

$SU(2)_L$ has three associated gauge fields, W_1, W_2, and W_3, which mediate interactions based on the weak isospin I_3 quantum number. Meanwhile, $U(1)_Y$ conserves the weak hypercharge Y and has one associated gauge field, B. Together, these fields form four gauge bosons: W_1, W_2, W_3 carrying weak isospin, and B carrying weak hypercharge. At very high energies, such as those prevalent shortly after the Big Bang, the symmetry described by $SU(2)_L \times U(1)_Y$ remains intact. At the lower energies we see today, this symmetry is broken, leading to the differentiation between the weak force and electromagnetism. Symmetry breaking in this context is spontaneous, occurring when a symmetric system transitions into a state that is individually non-symmetric. A popular macroscopic analogy is a sphere of liquid in zero gravity. Although the sphere has perfect rotational symmetry, freezing into a crystalline lattice introduces discrete axes, hiding the symmetry [3].

In the electroweak sector, spontaneous symmetry breaking is achieved through the Higgs mechanism. This involves the Higgs field, expressed as a pair of complex scalars:

$$\phi = \begin{pmatrix} \phi^1 \\ \phi^2 \end{pmatrix} \tag{2.4}$$

with a potential given by

$$V(\phi) = \mu^2\phi^\dagger\phi + \lambda\left(\phi^\dagger\phi\right)^2 \quad \text{where } \mu^2 < 0,\ \lambda > 0, \tag{2.5}$$

with μ being the mass parameter of the Higgs field and λ being the self-coupling constant. The negative value of μ^2 results in a 'Sombrero' potential, as illustrated in Figure 2.5. The minimum of this potential is not a single point, but a circle, allowing the system to settle into one of infinitely many ground states. The Higgs doublet can be expressed as:

$$\phi = \frac{1}{\sqrt{2}}\begin{pmatrix} 0 \\ v + h \end{pmatrix}, \tag{2.6}$$

where h describes excitations of the field around a non-zero vacuum expectation value (VEV):

$$v = \sqrt{-\mu^2/\lambda} \approx 246.22 \text{ GeV [1]} \tag{2.7}$$

after settling into its degenerate ground state. This non-zero VEV spontaneously breaks the $SU(2)_L \times U(1)_Y$ symmetry, giving rise to an unbroken $U(1)_{EM}$ symmetry of electromagnetism. The quantum numbers of $SU(2)_L \times U(1)_Y$ are related to the electric charge Q via the Gell-Mann–Nishijima formula [6, 7]:

$$Q = I_3 + \frac{1}{2}Y. \tag{2.8}$$

After symmetry breaking, I_3 and Y are no longer individually conserved, but their combination as electric charge still is under $U(1)_{EM}$.

Another result of the symmetry breaking is the mixing of the unbroken $SU(2)_L \times U(1)_Y$ bosons into the bosons we observe:

$$\gamma = \cos(\theta_W)B + \sin(\theta_W)W_3, \tag{2.9}$$

$$Z = \cos(\theta_W)W_3 - \sin(\theta_W)B, \tag{2.10}$$

$$W^+ = \frac{1}{\sqrt{2}}(W_1 - iW_2), \tag{2.11}$$

$$W^- = \frac{1}{\sqrt{2}}(W_1 + iW_2), \tag{2.12}$$

where $\theta_W \approx 29°$ is the Weinberg angle [8], a free parameter of the SM.

Goldstone's theorem states that the spontaneous breaking of continuous symmetries inevitably leads to massless scalar particles [9]. As a complex doublet, the Higgs field has four degrees of freedom. After symmetry breaking, it retains an unbroken

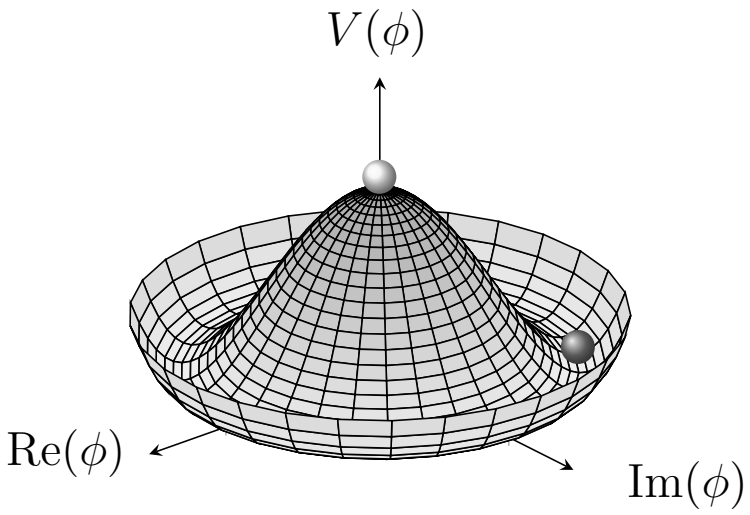

Fig. 2.5 Illustration of the Higgs potential with a metastable state (marked by the top sphere) and a ring of ground states (one of them occupied by the bottom right sphere). The latter spontaneously breaks the electroweak symmetry.

$U(1)_{\mathrm{EM}}$ symmetry. This results in three new Goldstone bosons, which are absorbed into the existing weak force bosons ('gauged away'), giving them an additional degree of freedom that acts as a mass term in the equations of motion. This is known as the Higgs mechanism. The photon is associated with the unbroken $U(1)_{\mathrm{EM}}$ part of the original symmetry and does not acquire a mass term in this way. The fourth remaining degree of freedom of the Higgs field gives rise to the massive Higgs boson described by h in Equation (2.6). Fermion interactions with the Higgs field via Yukawa couplings also result in mass terms for these particles and are described in detail in Section 2.4.4.

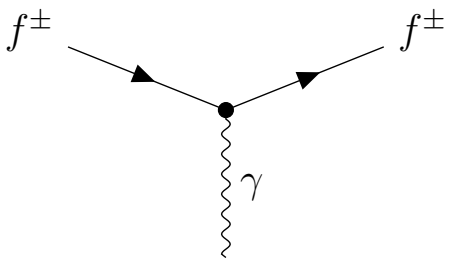

Fig. 2.6 Allowed Feynman diagram vertex for fermions coupling to a photon with $f^{\pm}$ being any charged fermion.

The photon as the mediator of the electromagnetic force couples to all particles with electric charge, with the allowed fermion interactions shown in Figure 2.6. Weak interactions via $W^{\pm}$ are called CC, while interactions via Z are called neutral current (NC). The $W^{\pm}$ bosons consist purely of the components of W_1 and W_2 and thus

only couple to particles with non-zero weak isospin. Table 2.2 shows that this limits interactions to only left-chiral fermions. The Z couples to left-chiral particles just like the $W^{\pm}$, but it also couples to particles with non-zero weak hypercharge. Table 2.2 shows that weak hypercharge is zero for right-chiral neutrinos. As a result, only left-chiral neutrinos couple to Z. In this way, the SM is set up to explain why weak interactions with right-chiral neutrinos are not observed. This still leaves space for the existence of right-chiral neutrinos that do not interact via any of the SM forces. These hypothetical non-interacting particles are called sterile neutrinos.

	Left-chiral		**Right-chiral**	
Fermions	$\mathbf{I_3}$	**Y**	$\mathbf{I_3}$	**Y**
Up-type Quarks (u, c, t)	$+\frac{1}{2}$	$+\frac{1}{3}$	0	$+\frac{4}{3}$
Down-type Quarks (d, s, b)	$-\frac{1}{2}$	$+\frac{1}{3}$	0	$-\frac{2}{3}$
Charged Leptons (e, μ, τ)	$-\frac{1}{2}$	-1	0	-2
Neutrinos $(\nu_e, \nu_\mu, \nu_\tau)$	$+\frac{1}{2}$	-1	0	0*

Table 2.2 Weak isospin I_3 and weak hypercharge Y for left- and right-chiral fermions in the SM [1]. There is currently no evidence for the existence of right-chiral neutrinos.

Allowed NC and CC interactions are shown in Figure 2.7 in the form of Feynman diagram vertices. Of interest here is that $W^{\pm}$ also facilitates flavour changes across the quark generations. The strength of this coupling is proportional to the magnitudes of the elements in the Cabibbo-Kobayashi-Maskawa (CKM) matrix [1]:

$$\mathrm{Mag}(V_{\mathrm{CKM}}) = \begin{pmatrix} |V_{ud}| & |V_{us}| & |V_{ub}| \\ |V_{cd}| & |V_{cs}| & |V_{cb}| \\ |V_{td}| & |V_{ts}| & |V_{tb}| \end{pmatrix} \approx \begin{pmatrix} 0.97 & 0.23 & 0.0037 \\ 0.22 & 0.97 & 0.042 \\ 0.0086 & 0.041 & 1.00 \end{pmatrix}, \tag{2.13}$$

which shows that mixing across generations is suppressed. The unitary CKM matrix can be expressed as just four free parameters consisting of three mixing angles and one complex phase factor [1]:

$$\begin{aligned} \sin(\theta_{12}) &= 0.22501 \pm 0.00068, \\ \sin(\theta_{13}) &= 0.003732^{+0.000090}_{-0.000085}, \\ \sin(\theta_{23}) &= 0.04183^{+0.00079}_{-0.00069}, \\ \delta_{\mathrm{CP}} &= 1.147 \pm 0.026 \text{ rad}. \end{aligned} \tag{2.14}$$

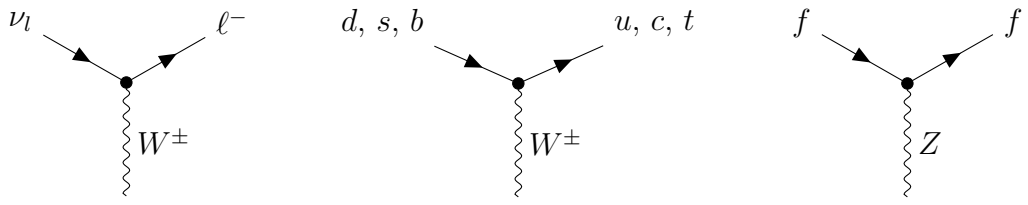

(a) (b) (c)

Fig. 2.7 Feynman diagram vertices showing allowed CC and NC interactions: (a) CC neutrino interaction producing a lepton ℓ, (b) CC interaction involving quarks, and (c) NC interaction for all fermions f. The incoming and outgoing flavours need to be identical in (a) and (c).

The CKM matrix is then parameterised as:

$$V_{\mathrm{CKM}} = \begin{pmatrix} c_{12}c_{13} & s_{12}c_{13} & s_{13}e^{-i\delta_{\mathrm{CP}}} \\ -s_{12}c_{23} - c_{12}s_{23}s_{13}e^{i\delta_{\mathrm{CP}}} & c_{12}c_{23} - s_{12}s_{23}s_{13}e^{i\delta_{\mathrm{CP}}} & s_{23}c_{13} \\ s_{12}s_{23} - c_{12}c_{23}s_{13}e^{i\delta_{\mathrm{CP}}} & -c_{12}s_{23} - s_{12}c_{23}s_{13}e^{i\delta_{\mathrm{CP}}} & c_{23}c_{13} \end{pmatrix}, \quad (2.15)$$

where $s_{ij} = \sin(\theta_{ij})$, $c_{ij} = \cos(\theta_{ij})$. The phase factor δ_{CP} plays a special role here, as it determines whether quarks and antiquarks mix differently.

Apart from continuous symmetries, a system can also have discrete symmetries. For the SM, charge (C), parity (P), and time (T) symmetries are relevant. Charge reversal flips the sign of all quantum numbers, such as the electric charge. Parity is an inversion of all spatial coordinates. Finally, time reversal inverts the flow of time. The charge-parity-time (CPT) theorem states that processes are unchanged after the inversion of all three together [10]. However, the conservation of subsets of these three operations is still an ongoing topic of research. A wealth of experimental evidence, starting with observations from β decay in 1957 [11] and kaon decay in 1964 [12], have clearly established that both P and CP symmetries are violated in the weak sector for quarks. However, the degree of CP violation is fairly small. Currently, there is no evidence for CP violation in electromagnetic or strong interactions.

2.4 Neutrinos

Historically, neutrinos have been the particles whose weak mixing properties have led to the most confusion. The existence of neutrinos was first indirectly inferred from observations of β decay. In 1914, James Chadwick published measurements showing

the continuous energy spectrum of electrons emitted during β decay, as shown in Figure 2.8 [13].

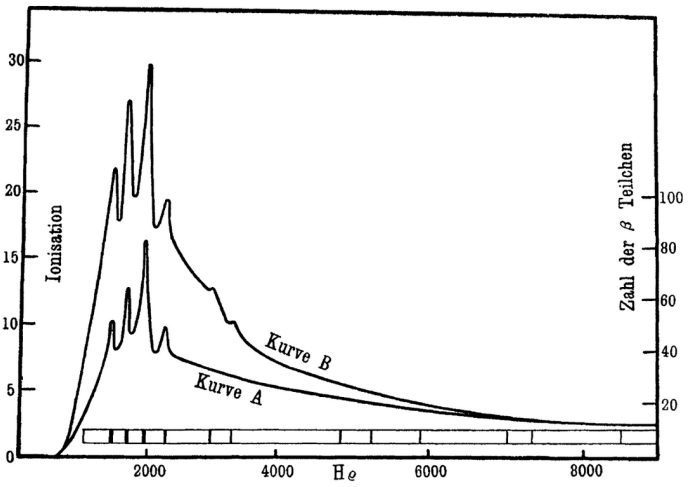

Fig. 2.8 Chadwick's 1914 publication shows particle counts (A) and ionisation (B) of β decay electrons bent in a magnetic field as a function of magnetic rigidity. Magnetic rigidity is the product of the magnetic field strength H and the spectrometer's bending radius ϱ. It is a measure of the ability of particles to resist deflection by a magnetic field, and it is proportional to their momentum [13, 14].

This continuous energy distribution presented a conundrum, as it implied violations of energy, momentum, and spin conservation if only the decaying nucleus and an emitted electron are involved in the process. To resolve this, Wolfgang Pauli postulated in 1930 the existence of a new, neutral, and very light particle that would carry away the missing energy and momentum [14]. Enrico Fermi later named this hypothetical particle the 'neutrino' and incorporated it into his theory of β decay.

Experimental confirmation came in the latter half of the 1950s, when Frederick Reines and Clyde Cowan detected the first electron antineutrinos from a nuclear reactor [15]. This proved Pauli's hypothesis to be correct. Only a few years later, in 1962, an experiment using the Alternating Gradient Synchrotron (AGS) at the Brookhaven National Laboratory observed tracks consistent with muons from neutrino interactions, demonstrating the existence of the muon neutrino [16]. The third lepton flavour, the tau neutrino, was observed by the Direct Observation of the Tau Neutrino (DONUT) experiment in 2000 [17]. This completed the current picture of fermions in the SM.

Unlike quarks, neutrinos exclusively interact via the weak force. In such interactions, lepton flavour is treated as a conserved quantity, and neutrinos are named ν_e, ν_μ, ν_τ

after their charged lepton partners in CC interactions:

$$\begin{aligned} W^+ &\to e^+\nu_e, \\ W^+ &\to \mu^+\nu_\mu, \\ W^+ &\to \tau^+\nu_\tau. \end{aligned} \tag{2.16}$$

The number of neutrino generations that interact via the weak force can be determined by measuring the branching ratio of the Z. Experimental results confirm the existence of exactly three flavours [1], but cannot exclude the possibility of additional neutral leptons that are too massive to be produced in Z decays. However, this result does rule out the existence of any additional light neutrino generations that couple to the weak interaction.

2.4.1 Flavour Oscillation

Early neutrino experiments observed fewer electron neutrinos from the sun than theoretical predictions suggested, a discrepancy known as the solar neutrino problem [18]. Similarly, atmospheric measurements showed a deficit of muon neutrinos [19]. These findings pointed to the phenomenon of neutrino oscillation, wherein neutrinos change flavour as they propagate [20]. The Sudbury Neutrino Observatory (SNO) resolved the solar neutrino problem by demonstrating that the total neutrino flux matches predictions when all flavours are considered [21, 22], confirming that lepton flavour is not conserved during neutrino propagation. Oscillations occur because the flavour states detected in interactions are superpositions of the differently propagating mass eigenstates ν_1, ν_2, ν_3.

The relation between mass eigenstates ν_i and flavour eigenstates ν_α is described through the unitary 3x3 Pontecorvo-Maki-Nakagawa-Sakata (PMNS) matrix U:

$$|\nu_\alpha\rangle = \sum_i U^*_{\alpha i} |\nu_i\rangle \text{ with } \alpha = e, \mu, \tau. \tag{2.17}$$

In analogy to the CKM matrix for quarks, the PMNS matrix can be constructed with three mixing angles θ_{12}, θ_{23}, θ_{13}, and a phase for CP violation δ_{CP}:

$$U = \begin{pmatrix} c_{12}c_{13} & s_{12}c_{13} & s_{13}e^{-i\delta_{\mathrm{CP}}} \\ -s_{12}c_{23} - c_{12}s_{23}s_{13}e^{i\delta_{\mathrm{CP}}} & c_{12}c_{23} - s_{12}s_{23}s_{13}e^{i\delta_{\mathrm{CP}}} & s_{23}c_{13} \\ s_{12}s_{23} - c_{12}c_{23}s_{13}e^{i\delta_{\mathrm{CP}}} & -c_{12}s_{23} - s_{12}c_{23}s_{13}e^{i\delta_{\mathrm{CP}}} & c_{23}c_{13} \end{pmatrix}, \tag{2.18}$$

where again $s_{ij} = \sin(\theta_{ij})$, $c_{ij} = \cos(\theta_{ij})$. This four-degrees-of-freedom parameterisation assumes that neutrinos are Dirac particles, like other fermions, but this need not be the case, as discussed later in Section 2.4.4.

The oscillations depend directly on the squared-mass differences $\Delta m^2_{ij} = m^2_i - m^2_j$ between the eigenstates. The masses and their hierarchy, i.e. which of the three eigenstates is the lightest and which is the heaviest, are not known. In theory, there are six possible orderings of the ν_i states. However, the sign of Δm^2_{21}, also called Δm^2_{sol}, is known to be positive from observations of the Mikheyev-Smirnov-Wolfenstein (MSW) effect [23, 24] on the oscillations of electron neutrinos produced in the Sun [25]. Vacuum oscillations depend solely on the absolute value of the mass-squared difference, but the MSW effect, which describes how neutrino oscillations are modified when propagating through matter, is sensitive to its sign. Foundational to this is a definition of the relation between the lepton flavour and the mass eigenstates. By convention, ν_1 is the mass eigenstate with the largest electron flavour component and ν_3 the one with the least, that is, $|U_{e1}| > |U_{e2}| > |U_{e3}|$. Furthermore, the differences between m^2_3 and both m^2_1 and m^2_2 are known to be much larger than Δm^2_{21} [26]. These constraints leave the normal and inverted orderings shown in Figure 2.9 as possibilities. The larger squared-mass splitting, which is Δm^2_{32} for normal ordering or Δm^2_{31} for inverted ordering, is also called Δm^2_{atm}, after the atmospheric neutrino observations that first alluded to it being non-zero.

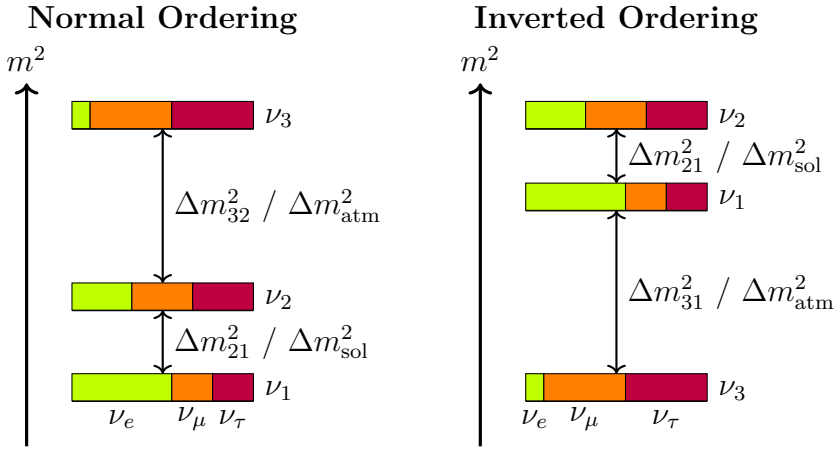

Fig. 2.9 Normal and inverted orderings of the neutrino masses.

Neutrino oscillation experiments look for the appearance or disappearance of flavours. The oscillation probability P for some initial state $|\nu_\alpha\rangle$ of flavour α to some state $|\nu_\alpha(t)\rangle$ at a later time t that is equivalent to a state $|\nu_\beta\rangle$ of flavour β can be computed

as follows:

$$P\left(\nu_\alpha \rightsquigarrow \nu_\beta\right) = \left|\langle \nu_\beta | \nu_\alpha(t) \rangle\right|^2 . \tag{2.19}$$

Describing this in terms of the mass eigenstates using Equation (2.17) gives

$$P\left(\nu_\alpha \rightsquigarrow \nu_\beta\right) = \left| \sum_i \sum_j U^*_{\alpha i} U_{\beta j} \left\langle \nu_j \mid \nu_i(t) \right\rangle \right|^2 . \tag{2.20}$$

The time evolution of the mass eigenstates is governed by the Schrödinger equation

$$i \frac{d}{dt} \left|\nu_i\right\rangle = \hat{H} \left|\nu_i\right\rangle , \tag{2.21}$$

where $\hat{H}$ is the Hamiltonian operator. For propagation in vacuum, $\hat{H} \left|\nu_i\right\rangle = E_i \left|\nu_i\right\rangle$, where

$$E_i = \sqrt{p_i^2 + m_i^2} \tag{2.22}$$

is the energy of the mass eigenstate with three-momentum p_i and mass m_i. In vacuum, a solution to this differential equation is a plane wave of the form [1]

$$\left|\nu_i(t)\right\rangle = e^{-i(E_i t - p_i L)} \left|\nu_i\right\rangle , \tag{2.23}$$

where L is called the baseline and is the distance travelled. Under the assumption that neutrinos are ultrarelativistic due to their small masses, i.e. $(p_i \gg m_i)$, Equation (2.22) can be written as

$$E_i \approx p_i + \frac{m_i^2}{2p_i} \tag{2.24}$$

using a binomial approximation. Assuming that the mass eigenstates are produced with the same momentum[1] and again that the masses are small in relation to the momentum, p_i can be replaced with $E \approx p_i$ for $i \in \{1, 2, 3\}$

$$E_i \approx E + \frac{m_i^2}{2E}, \tag{2.25}$$

where E is the energy of the interacting neutrino. Applying this to Equation (2.23) gives

[1]Under the condition that neutrinos are ultrarelativistic, both fixed energy and fixed momentum assumptions lead to functionally identical neutrino oscillation formulas. More sophisticated treatments do not rely on idealised plane waves with fixed energies or momenta and instead use wave packets with finite spatial and temporal extent, and resulting momentum and energy ranges. This is needed, for instance, for calculations of wave (de-)coherence [27, 28].

$$|\nu_i(t)\rangle = e^{-i\left[\left(E+\frac{m_i^2}{2E}\right)t-EL\right]}|\nu_i\rangle \tag{2.26}$$

$$\approx e^{-i\left[EL+\frac{m_i^2}{2E}L-EL\right]}|\nu_i\rangle \tag{2.27}$$

$$= e^{-i\left(\frac{m_i^2 L}{2E}\right)}|\nu_i\rangle\,, \tag{2.28}$$

where, in natural units, $t \approx L$ is used for the approximately light-speed travelling neutrinos. Putting this into Equation (2.20) and using the orthogonality of the eigenstates $\langle \nu_j \mid \nu_i \rangle = \delta_{ij}$ gives

$$P\left(\nu_\alpha \rightsquigarrow \nu_\beta\right) = \left|\sum_i \sum_j e^{-i\frac{m_i^2 L}{2E}} U_{\alpha i}^* U_{\beta j} \langle \nu_j \mid \nu_i \rangle\right|^2 \tag{2.29}$$

$$= \left|\sum_i \sum_j e^{-i\frac{m_i^2 L}{2E}} U_{\alpha i}^* U_{\beta j} \delta_{ij}\right|^2 \tag{2.30}$$

$$= \left|\sum_i e^{-i\frac{m_i^2 L}{2E}} U_{\alpha i}^* U_{\beta i}\right|^2 . \tag{2.31}$$

Equation (2.31) allows for the calculation of the neutrino transition probabilities from a flavour α to a flavour β using the neutrino energy and distance travelled. However, the neutrino masses are not known because oscillations depend only on the squared-mass differences $\Delta m_{ij}^2 = m_i^2 - m_j^2$. This becomes clear when rewriting the squared-norm term using the complex conjugate rule $|z|^2 = zz^*$:

$$P\left(\nu_\alpha \rightsquigarrow \nu_\beta\right) = \left(\sum_i e^{-i\frac{m_i^2 L}{2E}} U_{\alpha i}^* U_{\beta i}\right) \times \left(\sum_j e^{-i\frac{m_j^2 L}{2E}} U_{\alpha j}^* U_{\beta j}\right)^* \tag{2.32}$$

$$= \sum_i \sum_j e^{-i\frac{\left(m_i^2 - m_j^2\right)L}{2E}} U_{\alpha i}^* U_{\beta i} U_{\alpha j} U_{\beta j}^* \tag{2.33}$$

$$= \sum_i \sum_j e^{-i\frac{\Delta m_{ij}^2 L}{2E}} U_{\alpha i}^* U_{\beta i} U_{\alpha j} U_{\beta j}^* \tag{2.34}$$

$$= \sum_i \sum_j \mathfrak{Re}\left(U_{\alpha i}^* U_{\beta i} U_{\alpha j} U_{\beta j}^*\right) \cos\left(\frac{\Delta m_{ij}^2 L}{2E}\right) \tag{2.35}$$

$$+ \mathfrak{Im}\left(U_{\alpha i}^* U_{\beta i} U_{\alpha j} U_{\beta j}^*\right) \sin\left(\frac{\Delta m_{ij}^2 L}{2E}\right) \tag{2.36}$$

where on the last line $e^{ix} = \cos(x) + i\sin(x)$ was used with $\mathfrak{Im}$ and $\mathfrak{Re}$ being the imaginary and real components of the matrix product.

Neutrinos produced by accelerators via the decay of intermediary mesons are overwhelmingly of muon flavour. This makes the study of electron flavour neutrinos appearing via oscillation from this beam $P(\nu_\mu \rightsquigarrow \nu_e)$ and the general disappearance of muon flavour neutrinos via $1 - P(\nu_\mu \rightsquigarrow \nu_\mu)$ the most common measurements for accelerator experiments.

In summary, knowledge of the squared-mass differences as well as the three mixing angles and the CP violating phase δ_{CP} in the PMNS matrix is needed to calculate the oscillation probabilities for a given ratio of baseline L and neutrino energy E. The current best-fit oscillation parameters are shown in Table 2.3.

Parameter	Normal Ordering	Parameter	Inverted Ordering
$\frac{\Delta m^2_{21}}{10^{-5}\,\mathrm{eV}^2}$	$7.49^{+0.19}_{-0.19}$	$\frac{\Delta m^2_{21}}{10^{-5}\,\mathrm{eV}^2}$	$7.49^{+0.19}_{-0.19}$
$\frac{\Delta m^2_{31}}{10^{-3}\,\mathrm{eV}^2}$	$+2.513^{+0.021}_{-0.019}$	$\frac{\Delta m^2_{32}}{10^{-3}\,\mathrm{eV}^2}$	$-2.484^{+0.020}_{-0.020}$
$\sin^2\theta_{12}$	$0.308^{+0.012}_{-0.011}$	$\sin^2\theta_{12}$	$0.308^{+0.012}_{-0.011}$
$\sin^2\theta_{23}$	$0.470^{+0.017}_{-0.017}$	$\sin^2\theta_{23}$	$0.550^{+0.012}_{-0.015}$
$\sin^2\theta_{13}$	$0.02215^{+0.00056}_{-0.00058}$	$\sin^2\theta_{13}$	$0.02231^{+0.00056}_{-0.00056}$
δ_{CP}	$3.70^{+0.45}_{-0.72}$	δ_{CP}	$4.78^{+0.38}_{-0.44}$

Table 2.3 Oscillation parameters with $\pm 1\ \sigma$ uncertainties from the NuFit 6.0 global fit [26].

2.4.2 CP Violation

As for quarks, CP violation is a possibility for neutrino mixing, which would result in different oscillation behaviour for neutrinos and antineutrinos

$$P(\nu_\alpha \rightsquigarrow \nu_\beta) \neq P(\bar{\nu}_\alpha \rightsquigarrow \bar{\nu}_\beta)\,. \tag{2.37}$$

It is of interest for baryogenesis, which is the study of how the Universe developed its observed asymmetry between matter and antimatter. The Sakharov conditions describe the necessary ingredients for baryogenesis: baryon number violation, C and

CP violation, and a departure from thermal equilibrium [29]. The CP violation among quarks in the SM, when combined with the standard cosmological model, fails to explain the observed baryon asymmetry as the degree of CP violation is too small [30]. There are additional issues insofar that the electroweak phase transition of the early Universe due to the spontaneous symmetry breaking of the SM does not generate a large enough departure from thermal equilibrium [30]. One possible baryogenesis scenario, leptogenesis, involves new heavy neutrinos that would have decayed out of thermal equilibrium, violating lepton number and generating a lepton asymmetry. This would require neutrinos to be their own antiparticles, as discussed in Section 2.4.4.

However, the existence of CP violation in neutrino oscillations is still an open question and depends on the value of δ_{CP} in the PMNS matrix. The degree of CP violation can be quantified as the imaginary part of the PMNS matrix term in Equation (2.36), and is also called the Jarlskog invariant [31]. It is identical for any choice of $\alpha \neq \beta$ and $i \neq j$, up to a sign:

$$J_l = \mathfrak{Im}\left(U^*_{\alpha i} U_{\beta i} U_{\alpha j} U^*_{\beta j}\right), \tag{2.38}$$

where the l subscript emphasises that this describes the degree of violation in the lepton sector. The requirement for different flavours α and β also highlights that to measure CP violation, i.e. the complex matrix product contribution in Equation (2.36), experiments need to look for flavour-changing oscillations like electron neutrino appearance $P\left(\nu_\mu \rightsquigarrow \nu_e\right)$, as disappearance measurements like $1 - P\left(\nu_\mu \rightsquigarrow \nu_\mu\right)$ are not sensitive to complex PMNS contributions:

$$\mathfrak{Im}\left(U^*_{\mu i} U_{\mu i} U_{\mu j} U^*_{\mu j}\right) = \mathfrak{Im}\left(\left|U_{\mu i}\right|^2 \left|U_{\mu j}\right|^2\right) = 0. \tag{2.39}$$

Choosing a positive sign convention then gives

$$\begin{aligned} J_l &= c_{12} s_{12} c_{23} s_{23} c^2_{13} s_{13} \sin\delta_{\mathrm{CP}} \\ &= J_l^{max} \sin\delta_{\mathrm{CP}}, \end{aligned} \tag{2.40}$$

where J_l^{max} is the maximum possible degree of CP violation given the mixing angles. Using the values from Table 2.3, the maximum possible degree of CP violation is

$$J_l^{max} = (3.33 \pm 0.07) \times 10^{-2}. \tag{2.41}$$

Using the values from Equation (2.14) to compare with the identically defined Jarlskog invariant J_q for the CKM matrix, the measured degree of CP-violation among quarks

is

$$J_q = (3.12^{+0.13}_{-0.12}) \times 10^{-5}. \tag{2.42}$$

This shows potential for CP violation among neutrinos to be a more significant effect than it is among quarks as long as $\sin \delta_{\mathrm{CP}}$ is not equal or close to 0.

Two experiments have published measurements of the CP-violating phase δ_{CP}. The Tokai to Kamioka (T2K) experiment [32] utilises the Japan Proton Accelerator Research Complex (J-PARC) to produce a muon (anti-)neutrino beam, which travels 295 km to the 50-kiloton water Cherenkov detector, Super-Kamiokande. The neutrino energy spectrum at the detector peaks at 600 MeV. Similarly, the NOvA experiment [33] in the United States employs the Neutrinos at the Main Injector (NuMI) muon (anti-)neutrino beam produced at Fermilab, directing it 810 km to a 14-kiloton liquid scintillator detector. NOvA's observed energy spectrum peaks at 2 GeV. For inverted ordering, both NOvA and T2K have overlapping confidence regions centred around $\frac{3\pi}{2}$ [34, 35]. For the normal ordering, T2K excludes the CP-conserving phases $\delta_{\mathrm{CP}} = 0, \pi$ at the 90% confidence level (CL), while NOvA excludes a region around $\frac{3\pi}{2}$ in the 2D phase space with $\sin^2 \theta_{23}$, as shown in Figure 2.10. Both T2K and NOvA show a slight preference for normal ordering at their best-fit points, but they are mutually excluded by the other experiment's 90% confidence region.

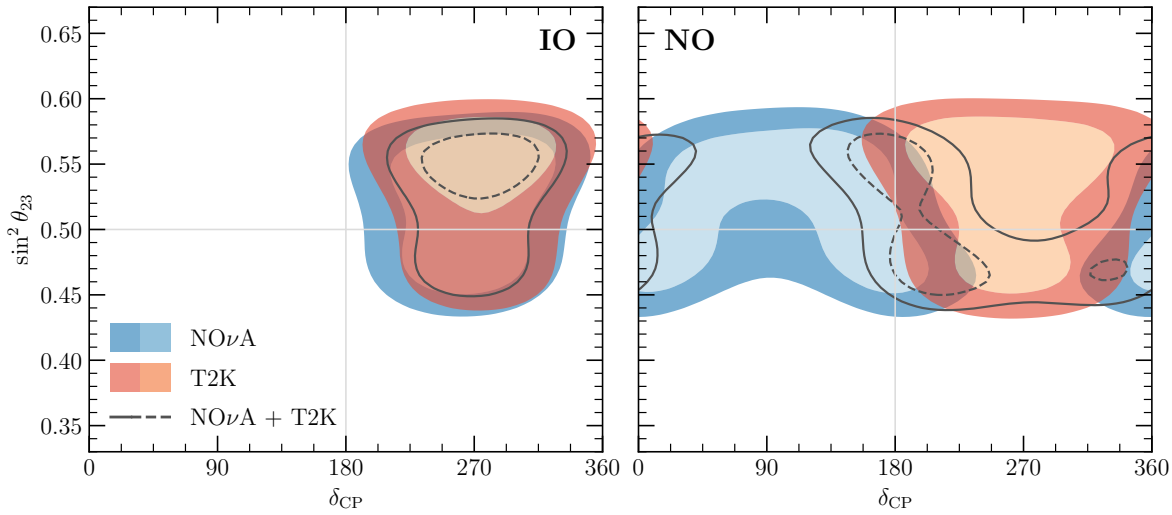

Fig. 2.10 Individual and combined 1 σ and 2 σ included confidence regions of the the $\sin^2 \theta_{23}$ versus δ_{CP} phase space from neutrino oscillation data for NOvA and T2K. The δ_{CP} values are shown in degrees on the x-axis. Inverted ordering is shown in the left panel and normal ordering on the right. The figure is taken from the NuFit 6.0 global fit of neutrino oscillation data [26].

2.4.3 Absolute Masses

Neutrino oscillations imply that neutrino masses are non-degenerate, but oscillation experiments are insensitive to the absolute masses. It is thus not certain that all neutrinos have mass, as the lowest mass eigenstate could be massless. Assuming this, it is possible to compute absolute minima for the sum of the mass eigenstates. These are $\sum_i m_i^{\mathrm{NO}} \approx 0.059\,\mathrm{eV}$ for normal ordering and $\sum_i m_i^{\mathrm{IO}} \approx 0.101\,\mathrm{eV}$ for inverted ordering, based on the NuFit 6.0 squared-mass splittings [26].

Upper constraints on neutrino masses arise from two primary sources. The first is direct mass measurements, which analyse the energy spectrum of electrons from tritium β decay near their endpoint. Massive neutrinos lower the maximum possible electron energy, enabling limits to be placed on the electron antineutrino mass. The most stringent upper limit comes from the KATRIN experiment, with $m_{\nu_e} < 0.45$ eV at 90% CL [36].

The second source is cosmological observations. The Dark Energy Spectroscopic Instrument (DESI) uses the subtle effects of massive neutrinos on cosmic expansion and structure formation to estimate their masses. These effects can be studied through analysis of the cosmic microwave background (CMB) and density fluctuations in visible matter in the form of baryon acoustic oscillations (BAO). This approach provides a much tighter constraint on the combined neutrino masses of

$$\sum m_\nu < 0.072\,\mathrm{eV}\ (95\%\ \mathrm{CL})\ \ [37]. \tag{2.43}$$

This limit is low enough to seemingly disfavour inverted ordering and is very close to the minimum possible for normal ordering. However, several factors make this approach less robust than direct measurements. Cosmological constraints are based on the Lambda Cold Dark Matter (ΛCDM) model of cosmology for a universe with zero spatial curvature, and deviations from this model can significantly weaken the constraints. The choice of data sets also affects the results, as some are in tension with others. Additionally, the Bayesian analysis depends on the chosen priors. For example, incorporating lower limits on neutrino masses from oscillation experiments into the prior increases the derived limits. However, varying some of these factors still tends to give limits lower than current direct measurements [37, 38]. There also remains an arguably higher likelihood of new physics influencing cosmological observations compared to the better-understood processes in β decay. For these reasons, cosmological observations should mainly serve as guidance, but not replace direct measurements.

2.4.4 Dirac vs Majorana

Fermions obtain their masses in the SM via Yukawa couplings of left- and right-handed components to the Higgs field ϕ. As a component of the SM Lagrangian density, this can be written for a fermion field of type f consisting of left- and right-chiral components $\psi = \psi_L + \psi_R$ [39]

$$\begin{aligned}\mathcal{L}^{f}_{\text{Yukawa}} &= -y_f \overline{\psi}\phi\psi \\ &= -y_f(\overline{\psi_L} + \overline{\psi_R})\phi(\psi_L + \psi_R) \\ &= -y_f \overline{\psi_L}\phi\psi_R - y_f \overline{\psi_R}\phi\psi_L \\ &= -y_f \overline{\psi_L}\phi\psi_R + \text{h.c.}\end{aligned} \tag{2.44}$$

where $\overline{\psi} = \psi^\dagger\gamma^0$ is the Dirac adjoint notation, with $\dagger$ being the Hermitian conjugate and γ^0 being the time-like gamma matrix. The Yukawa coupling constant for the fermion f is y_f. The shorthand notation h.c. is used for the Hermitian conjugate of the explicitly written terms.

Choosing the electron with left-handed doublet $\overline{\psi^e_L} = \begin{pmatrix}\overline{\nu_{eL}} \\ \overline{e_L}\end{pmatrix}$ and right-handed singlet $\psi^e_R = e_R$ as an example, and using Equation (2.6) for Equation (2.44) gives

$$\mathcal{L}^{e}_{\text{Yukawa}} = -\underbrace{\frac{y_e v}{\sqrt{2}}\overline{e_L}e_R}_{\text{Mass}} - \underbrace{\frac{y_e}{\sqrt{2}}\overline{e_L}e_R h}_{\text{Fermion-Higgs}} + \text{h.c.} \tag{2.45}$$

where the second term describes interactions between the electron and the Higgs boson, while the first term sets the mass of the electron as

$$m_e = \frac{y_e v}{\sqrt{2}}. \tag{2.46}$$

The left- and right-handed components of a fermion field can be independent, making it a Dirac fermion. This is the case for all charged fermions. However, neutrinos lack the right-handed neutrino field in the SM and were originally expected to be massless. However, neutrino oscillation can only be explained with massive neutrinos. Adding a right-handed neutrino singlet $\psi^{\nu_e}_R = \nu_{eR}$ would make these terms possible with

$$\mathcal{L}^{\nu_e}_{\text{Yukawa}} = -y_{\nu_e}\overline{\psi^e_L}\widetilde{\phi}\psi^{\nu_e}_R + \text{h.c.} \tag{2.47}$$

$$= -m_{\nu_e}\overline{\nu_{eL}}\nu_{eR} - \frac{y_{\nu_e}h}{\sqrt{2}}\overline{\nu_{eL}}\nu_{eR} + \text{h.c.}, \tag{2.48}$$

where the first term is constructed in a gauge-invariant way with the conjugate Higgs field $\widetilde{\phi} = i\sigma_2\phi^* = \frac{1}{\sqrt{2}}\begin{pmatrix} v+h \\ 0 \end{pmatrix}$, defined here using the second Pauli matrix. Focussing only on the mass term and emphasising that this is describing neutrinos that are Dirac fermions with distinct antiparticles gives

$$\mathcal{L}^{\nu_e}_{\text{Dirac}} = -m^{\text{Dirac}}_{\nu_e}\overline{\nu_{eL}}\nu_{eR} + \text{h.c.} \tag{2.49}$$

These new right-handed neutrinos would not interact via the weak force and would also not interact via electromagnetism or the strong force due to their neutral electric and colour charges. This would make them non-interacting particles in the SM and they are commonly referred to as sterile neutrinos.

The other option, only possible for neutrally charged particles, is that the left- and right-handed components are related via a $\hat{C}$-conjugate that transforms particles into antiparticles. This would mean that neutrinos are not Dirac fermions and instead are Majorana fermions that are their own antiparticles, analogous to photons or π^0. For instance, a negatively charged left-handed electron transforms into a positively charged right-handed positron under $\hat{C}$-conjugation. Neutrinos are unique among the fermions as they are neutrally charged, and thus the particle after charge conjugation does not have to differ from the original. The left- and right-handed components then do not need to be independent, making it possible to reduce the degrees of freedom from two chiral components with two antiparticle components after $\hat{C}$-conjugation (^{c}) to two overall [39]

Dirac	**Majorana**
ψ_L	$\psi_L = (\psi_R)^c$
$(\psi_L)^c$	$\psi_R = (\psi_L)^c$.
ψ_R	
$(\psi_R)^c$	

(2.50)

A Lagrangian similar to Equation (2.48) can then be constructed with Majorana mass terms

$$\mathcal{L}^{\nu_e}_{\text{Majorana}} = -\frac{1}{2}m^{\text{Majorana}}_{\nu_e L}\overline{(\nu_{eL})^c}\nu_{eL} - \frac{1}{2}m^{\text{Majorana}}_{\nu_e R}\overline{(\nu_{eR})^c}\nu_{eR} + \text{h.c.} \tag{2.51}$$

These Majorana mass terms would also need to derive from some beyond the Standard Model (BSM) mechanism, different from the one for Dirac fermions [40]. One effect of these Majorana neutrinos would be that lepton number is not conserved. This

would allow for interactions such as neutrinoless double β decay. Double β decay with neutrinos is the well-documented simultaneous transformation of two neutrons into protons under emission of two electrons and two electron antineutrinos as shown in Figure 2.12a. This process is possible for certain isotopes with even numbers of protons and neutrons that cannot decay via regular β decay. The reason for this is that pairing interaction between neutrons as well as protons make the isotope a less energetic state than the odd-odd decay product that β decay would produce. As a result, regular β decay is kinematically forbidden. Figure 2.11 illustrates this for a section of the isobars of mass number $A = 76$, where $^{76}_{32}\mathbf{Ge}$ decays to $^{76}_{34}\mathbf{Se}$ via double β decay. Neutrinoless double β decay is a version of this decay producing no neutrinos. Figure 2.12b shows the difference to regular β decay. It is notable that the neutrino exchange in the Feynman diagram has no direction, as this process does not distinguish between particle and antiparticle and violates lepton number conservation.

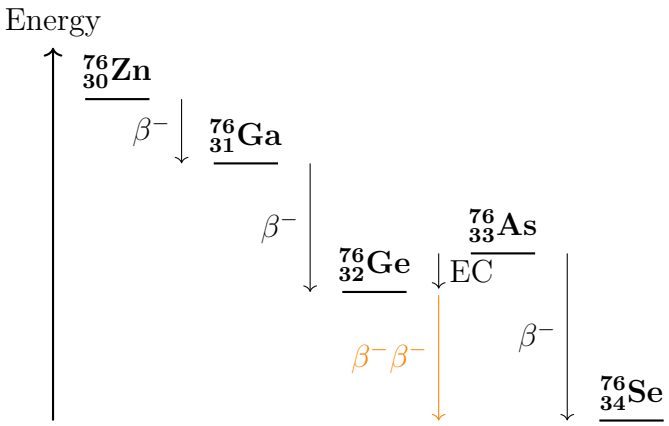

Fig. 2.11 Illustration of some isobars with mass number A=76, showing beta decay β^-, electron capture EC, and double beta decay $\beta^-\beta^-$ between them.

Several experiments have searched for neutrinoless double β decay with no observations yet [41]. There are currently too many unknown parameters to reliably predict half-lives for isotopes from theory. However, experiments have produced lower limits on the half-lives of several neutrinoless double β decay candidate isotopes above 10^{25} yr [42]. For $^{76}_{32}\mathbf{Ge}$, for instance, the GERDA experiment has set a lower limit of $T^{0\nu}_{1/2} > 1.8 \times 10^{26}$ yr [43] on the half-life.

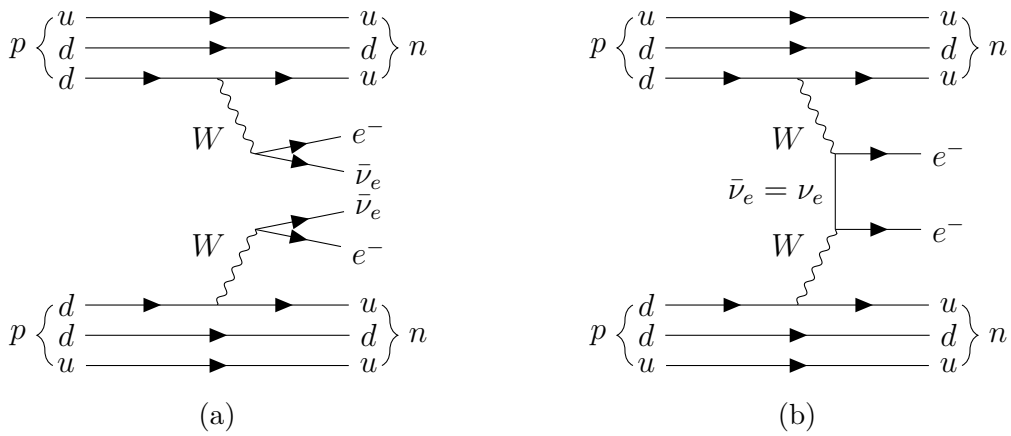

Fig. 2.12 The Feynman diagram for (a) double beta decay ($\beta^-\beta^-$) and (b) hypothetical neutrinoless double beta decay.

Majorana neutrinos would also introduce additional parameters to the PMNS matrix U given in Equation (2.18)

$$U^M = U \cdot \begin{pmatrix} e^{i\alpha_1/2} & 0 & 0 \\ 0 & e^{i\alpha_2/2} & 0 \\ 0 & 0 & 1 \end{pmatrix}, \tag{2.52}$$

where α_1 and α_2 are additional Majorana phases. However, these parameters do not influence the oscillation probabilities. Substituting the modified matrix into the product $U_{\alpha i}U^*_{\beta i}$ in Equation (2.31), and noting that only terms with $\alpha = i = \beta$ can contribute in the additional matrix, leads to the cancellation of the Majorana phases.

2.4.5 The Seesaw Mechanism

To achieve the very small masses of the neutrinos, the Yukawa coupling constants would need to be extremely small for neutrinos compared to other fermions. One popular class of theories that explains the tiny neutrino masses are the so-called seesaw mechanisms. These introduce heavy new particles that in turn result in lower masses for the currently observed neutrinos. The most straightforward, a type-I seesaw theory, introduces a heavy neutral lepton in the form of a right-handed neutrino [44].

A general Lagrangian for the neutrino masses includes a Dirac mass term m_D as well as Majorana mass terms for both the left-chiral components m_L and right-handed components m_R. In the most general case, these are complex matrices. Assuming no CP violation and limiting this example to one generation, the mass terms are real

numbers and the Lagrangian term is [39, 44]:

$$\begin{aligned}\mathcal{L}_{\text{Seesaw}} &= -\frac{1}{2}m_L\overline{(\nu_L)^c}\nu_L - m_D\overline{\nu_L}\nu_R - \frac{1}{2}m_R\overline{(\nu_R)^c}\nu_R + \text{h.c.} \\ &= -\frac{1}{2}\overline{n_L}\mathcal{M}(n_L)^c + h.c.,\end{aligned} \tag{2.53}$$

where

$$n_L = \begin{pmatrix}\nu_L \\ (\nu_R)^c\end{pmatrix} \quad \text{and} \quad (n_L)^c = \begin{pmatrix}(\nu_L)^c \\ \nu_R\end{pmatrix} \tag{2.54}$$

are the neutrino fields in vector form, and the mass matrix is

$$\mathcal{M} = \begin{pmatrix}m_L & m_D \\ m_D & m_R\end{pmatrix}. \tag{2.55}$$

Introducing left-handed Majorana mass terms is not possible without modifying the Higgs field [39]. For a type-I seesaw mechanism, the Higgs mechanism is not altered and instead the left-chiral Majorana term is removed by setting $m_L = 0$. Diagonalising that matrix and extracting the absolute mass eigenvalues gives

$$m_{1,2} = \frac{1}{2}\left|m_R \mp \sqrt{m_R^2 + 4\ m_D^2}\right|. \tag{2.56}$$

For $m_R \gg m_D$, the eigenvalues of the mass matrix approximate to

$$m_{1,2} \simeq \frac{1}{2}\left|m_R \mp \left(m_R + 2\frac{m_D^2}{m_R}\right)\right|, \tag{2.57}$$

which yields

$$m_1 \simeq \frac{m_D^2}{m_R} \ll m_D, \quad m_2 \simeq m_R \gg m_D. \tag{2.58}$$

This leads to a light neutrino mass inversely proportional to the large Majorana scale m_R, and a heavy state with potentially extremely high masses [39]. Theories like this are also attractive because lepton number violating processes would be highly suppressed at accessible energies, making lepton numbers still appear conserved in low-energy interactions.

2.4.6 Sterile Neutrinos

The introduction of right-chiral neutrinos in SM extensions makes the general concept of non-interacting sterile neutrinos interesting. Several anomalies observed in the past decades have hinted at the possibility of other, much lighter, sterile neutrinos with

masses on the order of 1 eV [45]. With the simplest extensions of the SM, $3+1$ models, adding an additional non-interacting neutrino generation and increasing the size of the PMNS matrix to 4×4.

The Liquid Scintillator Neutrino Detector (LSND) experiment at Los Alamos National Lab reported an apparent excess of low-energy electron antineutrinos from a muon antineutrino beam not compatible with parameters of the PMNS matrix starting in the late 1990s [46]. A possible explanation for this was additional oscillations to sterile neutrinos in a larger PMNS matrix. To test this, the Mini Booster Neutrino Experiment (MiniBooNE) was constructed at Fermilab at a similar ratio of baseline and neutrino energy L/E. First published in 2010, it also reported observing an excess, which reached 4.7 σ significance in later publications [47]. However, multiple experiments including the CERN-Dortmund-Heidelberg-Saclay (CDHS) experiment [48], the Main Injector Neutrino Oscillation Search (MINOS) experiment [49], and the IceCube experiment [50] have consistently found no evidence of the expected ν_μ disappearance that would come with increased ν_e appearance.

MicroBooNE is a follow-up experiment to MiniBooNE in the same beam, with the capability to distinguish electron- from photon-induced electromagnetic showers. It has investigated several possible explanations for the discrepancy, including an actual excess of low-energy electron neutrinos producing electrons upon interacting in the detector [51], which would support a sterile neutrino interpretation. It has also investigated the possibility of an excess of background interactions producing photons that could have mimicked electron-flavour neutrinos in MiniBooNE. This includes measurements of the production of NC $\Delta \to N\gamma$ resonances [52], and inclusive single-photon searches that add additional channels such as NC $\pi^0 \to \gamma(\gamma)$, where only one photon is reconstructable [53]. Finally, MicroBooNE has also explored a dark sector explanation, in which a neutrino scattering produces a dark neutrino, ultimately resulting in the production of an electron-positron pair via a new dark gauge boson [54]. The outcome of these searches is that MicroBooNE did not find evidence of an excess of low-energy electron neutrinos. It also did not find clear evidence that the MiniBooNE excess could be explained by mismodelling of a photon-producing background process, disfavouring radiative Δ decay with high confidence. However, there is a 2.2 σ excess observable in the inclusive photon analysis in the low-energy region below 600 MeV, making this a contender for further study. Finally, MicroBooNE ruled out almost all of the phase space for a single dark sector neutrino model. This means that a compelling explanation for the low-energy excesses observed by LSND and MiniBooNE is still missing.

Additional anomalies have arisen from measurements of neutrinos coming from nuclear reactors, where observed neutrino rates for uranium and plutonium isotopes were measured to be several percentage points lower than predictions [55]. This discrepancy was termed the reactor antineutrino anomaly. More recent results, however, reject short-distance oscillations to a sterile neutrino as a possible explanation and point to issues with the historical electron-counting measurements used in calculations of the expected neutrino flux from β decay as the source of the overprediction [56].

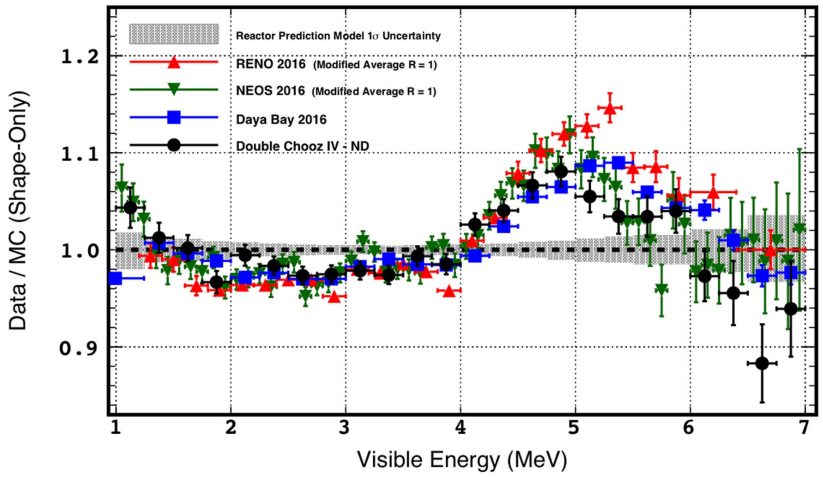

Fig. 2.13 Shape differences between measured and simulated neutrino energy spectra from reactor neutrino experiments. Source: Ref. [57].

The Gallium Experiment (GALLEX) [58], the Soviet-American Gallium Experiment (SAGE) [59] and the Baksan Experiment on Sterile Transitions (BEST) [60] have measured inverse β decay from both solar and nuclear neutrinos on gallium, resulting in the production of germanium $^{71}\mathrm{Ga} + \nu_e \rightarrow e^- + ^{71}\mathrm{Ge}$. The experiments have reported deficits in the range of 13%-24% in the production of germanium. This has been dubbed the Gallium Anomaly. Attempts to find nuclear or chemical explanations have not been successful, and sterile neutrinos remain a possible explanation.

Finally, the '5 MeV' bump is an observed excess of neutrinos with visible energies between 5-6 MeV supported by findings from the reactor neutrino experiments Reactor Experiment for Neutrino Oscillation (RENO) [61], Daya Bay [62], Double Chooz [63], Neutrino Experiment for Oscillation at Short Baseline (NEOS) [64], Neutrino-4 [65], Short-distance Neutrino Oscillations with a Reactor (STEREO) [66] and Precision Reactor Oscillation and Spectrum Experiment (PROSPECT) [67]. Some of these are shown in Figure 2.13. However, issues with flux calculations or the systematic uncertainties of inverse β decay have not yet been ruled out [68].

The phase space for light sterile neutrinos is getting increasingly constrained, and simple $3+1$ models are not as appealing as they were just a decade ago. Phenomenologists are increasingly looking at more complex models involving multiple sterile neutrinos or sterile neutrino decay via new BSM mechanisms [69].

2.5 Experimental Outlook

A wealth of new experiments and results is expected in the next decade that will shine light on many of the open questions in neutrino physics. Below is a brief summary of some of these efforts.

Mass Measurements The KATRIN experiment is continuing to take data and is expecting to eventually reach sensitivities around 0.2-0.3 eV [36] after which it will be used as part of the Tritium Sterile Anti-Neutrino Experiment (TRISTAN) experiment to search for keV-scale sterile neutrinos as dark matter candidates [70]. For cosmological measurements, data from currently conducted surveys of the CMB as well as structures larger than individual galaxies, so called large-scale structures, are expected to enable an increase in sensitivity. Standard deviations on the sum of the neutrino masses could be reduced from $\sigma_{\sum_\nu} = 0.070$ eV to $\sigma_{\sum_\nu} = 0.015$ eV, and potentially as low as $\sigma_{\sum_\nu} = 0.007$ eV with currently proposed experiments [71]. This has the potential to set lower bounds on the combined neutrino mass.

Mass Hierarchy The neutrino mass hierarchy is expected to be resolved in the next few years, likely by combining sensitivities from the medium baseline Jiangmen Underground Neutrino Observatory (JUNO) experiment with the current long baseline experiments NOvA and T2K. The future long baseline experiments DUNE and Hyper-Kamiokande will also be able to resolve this, but their first results are expected later [72].

CP Violating Phase The nature of CP violation in the lepton sector is expected to be first determined at 5 σ by Hyper-Kamiokande in the early to mid-2030s followed by DUNE later in the decade [73].

Majorana Neutrinos Several collaborations are planning scaled-up versions of their neutrinoless double β decay detectors. These include LEGEND-1000, CUPID-1T,

AMoRE-II, nEXO and NEXT-HD that could reach sensitivities to half-lives in the region of 10^{28} years [42].

Sterile Neutrinos Experiments continue to search for signs of sterile neutrinos over a wide range of masses from eV to TeV with a focus on addressing the current anomalies. These programs include short and long baseline experiments, reactor and radioactive source experiments, neutrino telescopes, and collider experiments [74].

Chapter 3

Neutrino Interactions

Neutrino-nucleon interactions can be categorised into several different processes, ranging from coherent interactions with the whole nucleus at the lowest four-momentum transfer squared Q^2, to elastic scattering on individual nucleons, and increasingly inelastic interactions at higher energies. This chapter provides an overview of these interactions, starting with single-nucleon processes and subsequently describing multinucleon interactions. A description of the treatment of these interactions in neutrino interaction simulations, including nuclear effects, will be discussed later in Section 6.1.2.

3.1 Quasi-Elastic Interactions

Quasi-elastic (QE) neutrino-nucleon scattering is the process whereby an incoming neutrino interacts with a single nucleon, producing a charged lepton and ejecting the nucleon from the nucleus intact. The term quasi-elastic refers to the relatively low energy transfer to the struck nucleon compared to inelastic processes, where the nucleon is excited or broken apart. However, it also implies the presence of nuclear binding energy that the ejected nucleon must overcome, distinguishing it from perfectly elastic scattering on a free nucleon.

Experiments with neutrino energies near or below 1 GeV tend to rely heavily on selections of charged-current quasi-elastic (CCQE) appearing events, requiring the presence of a charged lepton and a nucleon in the final state. The focus on CCQE interactions stems from their dominance at these energies and the straightforward neutrino energy reconstruction possible using only the outgoing lepton kinematics in this two-body process. Furthermore, some detector types used in experiments at these energies, such as Cherenkov detectors, are not well suited to capturing more complex hadronic final states.

For CCQE interactions, the reaction takes the form:

$$\nu_\ell + n \to \ell^- + p,$$

with $\ell \in \{e, \mu, \tau\}$. The NC counterpart, where a neutrino remains in the final state, is

$$\nu_\ell + N \to \nu_\ell + N \quad (N = n, p).$$

Additionally, while not a neutrino interaction, charged-lepton scattering on nucleons provides valuable insight into nucleon structure:

$$\ell^- + N \to \ell^- + N \quad (N = n, p).$$

Feynman diagrams for these three processes are shown in Figure 3.1. Antineutrino interactions follow similar forms.

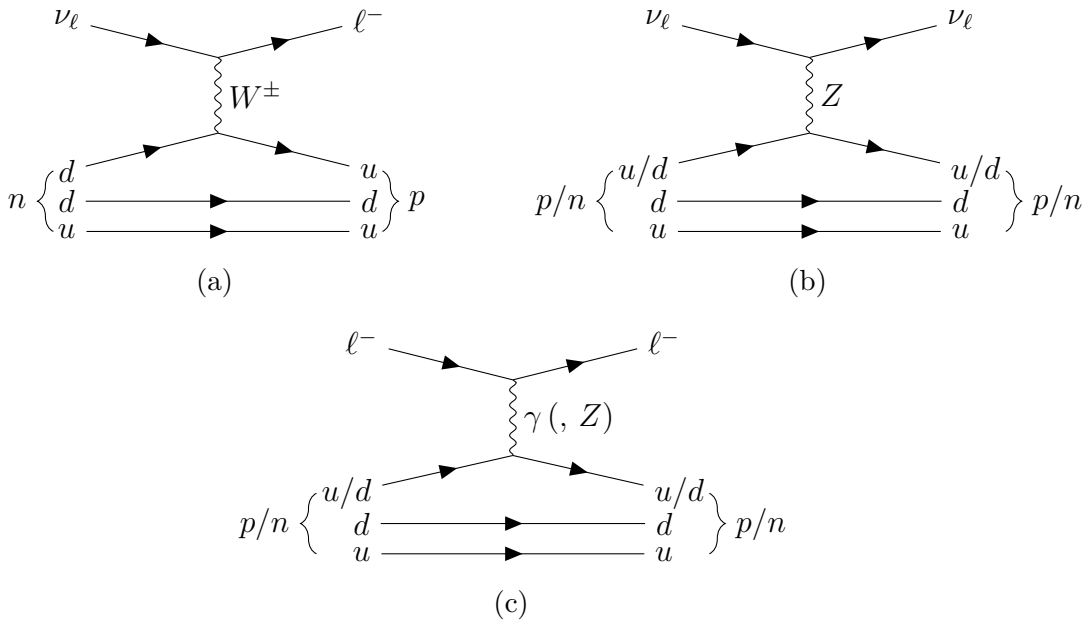

Fig. 3.1 Feynman diagrams for (a) CC, (b) NC, and (c) EM lepton scattering with a nucleon. The weak contributions to (a) become relevant only at momentum transfers approaching the Z-boson mass scale.

The interaction properties are encapsulated in a universal leptonic tensor L and an interaction-dependent hadronic tensor H [75]. The double differential cross section of the two-body QE scattering interaction, here expressed in terms of the solid angle Ω of the outgoing lepton and the energy transfer to the nucleus ω, is proportional to the

contraction of these two tensors [76]:

$$\frac{\mathrm{d}\sigma}{\mathrm{d}\omega\ \mathrm{d}\Omega} \propto L_{\mu\nu} H^{\mu\nu}. \tag{3.1}$$

The leptonic tensor describes the interaction between leptons and the gauge bosons. Leptons are point-like particles with well-known properties and as a result the leptonic tensor component is generally well understood. Hadrons, on the other hand, are not point-like particles and have a complex internal structure of quarks and gluons governed by the strong force. The hadronic tensor is

$$H^{\mu\nu} = \frac{1}{2} \mathrm{Tr}\left[(\not{p} + M_N)\gamma_0 \Gamma^{\mu\dagger} \gamma_0 \left(\not{p}' + M_{N'}\right) \Gamma^{\nu}\right], \tag{3.2}$$

where $\not{p}^{(\prime)} \equiv \gamma^\mu p_\mu^{(\prime)}$ denotes the initial (final) nucleon four-momentum term. The masses of the initial and final nucleons are M_N and $M_{N'}$, which are equal in truly elastic scattering. The hadronic current operator Γ^μ [77] contains vector and axial-vector components

$$\Gamma^\mu = V^\mu - A^\mu. \tag{3.3}$$

Hadrons, such as nucleons, do not interact as point-like particles but as composite systems of quarks and gluons. Their internal structure modifies scattering processes, which are described through form factors. These form factors are Lorentz-invariant functions of Q^2 that encode charge, magnetic, and spin properties of the nucleon. For weak interactions, this can be expressed in terms of four form factors:

$$\Gamma^\mu = \alpha_1^\mu\, F_1(Q^2) + \alpha_2^\mu\, F_2(Q^2) + \alpha_A^\mu\, F_A(Q^2) + \alpha_P^\mu\, F_P(Q^2), \tag{3.4}$$

where α_i^μ are the Lorentz structure terms defined by the Dirac γ-matrices as:

$$\alpha_1^\mu \equiv \gamma^\mu, \qquad \alpha_2^\mu \equiv \frac{i\,\sigma^{\mu\nu} q_\nu}{2M}, \qquad \alpha_A^\mu \equiv \gamma^\mu\gamma^5, \qquad \alpha_P^\mu \equiv \frac{q^\mu \gamma^5}{M}, \tag{3.5}$$

with $M = \frac{1}{2}(M_N + M_{N'})$ being the average mass of the initial and final nucleon. The four-momentum transfer vector q is related to the squared four-momentum transfer via $Q^2 = -q^2$. The antisymmetric tensor $\sigma^{\mu\nu}$ is defined as $\sigma^{\mu\nu} \equiv \frac{i}{2}[\gamma^\mu, \gamma^\nu]$.

For CC neutrino interactions, the vertex is

$$\Gamma^\mu = \Gamma^\mu_{\mathrm{CC}}, \quad \text{and } N = n,\ N' = p, \tag{3.6}$$

and the corresponding form factors are denoted $F^{\mathrm{CC}}_{1,2,A,P}(Q^2)$. NC neutrino interactions are possible with a proton or neutron:

$$\Gamma^{\mu} = \Gamma^{\mu}_{\mathrm{NC,\,N}}, \quad \text{and } N = N' \in \{n, p\}, \tag{3.7}$$

and the form factors are distinguished by nucleon type $F^{\mathrm{NC,\,N}}_{1,2,A,P}(Q^2)$.

In contrast, electromagnetic (EM) charged-lepton scattering proceeds via photon exchange and involves only the vector component of the hadronic current. At low momentum transfer ($Q^2 \ll M_Z^2$), weak contributions are negligible due to the large Z boson mass. The hadronic current for EM interactions is:

$$\Gamma^{\mu}_{\mathrm{EM,\,N}} = \alpha_1^{\mu}\, F_1^{\mathrm{EM,\,N}}(Q^2) + \alpha_2^{\mu}\, F_2^{\mathrm{EM,\,N}}(Q^2). \tag{3.8}$$

The electromagnetic form factors F_1^{EM} and F_2^{EM} can be re-expressed in terms of the Sachs form factors

$$F_1^{\mathrm{EM,\,N}}(Q^2) = \frac{G_E^N(Q^2) + \tau_N G_M^N(Q^2)}{1+\tau_N}, \tag{3.9}$$

$$F_2^{\mathrm{EM,\,N}}(Q^2) = \frac{G_M^N(Q^2) - G_E^N(Q^2)}{1+\tau_N}, \tag{3.10}$$

with $\tau_N = Q^2/(4M_N^2)$. They correspond more directly to measurable quantities: the electric charge and magnetic moment distributions [78]. At zero momentum transfer, these Sachs form factors are normalised to the static charge and magnetic moment of the nucleon:

$$G_E^N(0) = Q_N = \begin{cases} 0 & \text{for } n, \\ 1 & \text{for } p, \end{cases} \tag{3.11}$$

$$G_M^N(0) = \mu_N = \begin{cases} -1.91 & \text{for } n, \\ +2.79 & \text{for } p. \end{cases} \tag{3.12}$$

Scattering off a point-like particle is described by $G_E^N(0)$ and $G_M^N(0)$. However, as Q^2 increases, the form factors decrease, describing the internal structure of the nucleon. Higher Q^2 corresponds to probing shorter distance scales, revealing substructure not apparent at lower energies. The Q^2-dependence of electromagnetic form factors has been measured with high precision in electron scattering experiments on protons and light nuclei [75, 77]. Historically modelled by dipole functions, modern parameterisations of

the Q^2 dependence, such as BBBA05 [79] and BBBA07 [80], better describe a wider range of four-momentum transfers.

The conserved vector current (CVC) hypothesis asserts that the vector component of the weak current is conserved, analogous to conservation of the EM current [81]. Under this assumption, the vector form factors for neutrino scattering can be related to those obtained from charged lepton scattering, as summarised in Table 3.1. The NC form factors include contributions from strange sea quarks. These do not need to be considered for CC interaction, due to their flavour-changing nature that would result in the production of a charm quark, which is kinematically forbidden at low energies. Lattice QCD calculations predict non-zero values of the strange vector form factors $F_i^s(Q^2)$, but current measurements do not yet agree on the sign [82].

Interaction	Vector Form Factors
Electromagnetic	
$\ell^- + n \to \ell^- + n$	$F_i^{\mathrm{EM,\,n}}$
$\ell^- + p \to \ell^- + p$	$F_i^{\mathrm{EM,\,p}}$
Charged Current	
$\nu + n \to \ell^- + p$	$F_i^{\mathrm{CC}} = F_i^{\mathrm{EM,\,p}} - F_i^{\mathrm{EM,\,n}}$
Neutral Current	
$\nu + p \to \nu + p$	$F_i^{\mathrm{NC,\,p}} = \left(\frac{1}{2} - 2\sin^2\theta_W\right) F_i^{\mathrm{EM,\,p}} - \frac{1}{2}F_i^{\mathrm{EM,\,n}} - \frac{1}{2}F_i^s$
$\nu + n \to \nu + n$	$F_i^{\mathrm{NC,\,n}} = \left(\frac{1}{2} - 2\sin^2\theta_W\right) F_i^{\mathrm{EM,\,n}} - \frac{1}{2}F_i^{\mathrm{EM,\,p}} - \frac{1}{2}F_i^s$

Table 3.1 Summary of the relationship between vector form factors for different interactions [76]. For the NC terms, θ_W is the Weinberg angle.

The remaining two non-vector form factors cannot be obtained from charged-lepton scattering. One possible parameterisation of the axial form factor uses a dipole ansatz [77]:

$$F_A(Q^2) = g_A \left(1 + \frac{Q^2}{M_A^2}\right)^{-2}, \tag{3.13}$$

where g_A is the axial coupling constant measured from neutron β decay [83], and the distribution is defined by a single free axial mass parameter M_A, which must be obtained from neutrino scattering or pion electroproduction [84]. The pseudoscalar form factor F_P can be related to F_A via the partially conserved axial current (PCAC) hypothesis for CC interactions, which connects the divergence of the axial current to

the pion field through the Goldberger-Treiman relation [85, 86]

$$F_P(Q^2) = \frac{2M^2 F_A(Q^2)}{M_\pi^2 + Q^2}, \tag{3.14}$$

where M is again the average nucleon mass and M_π is the pion mass. Moreover, the contribution of F_P to the total cross section is suppressed by a factor of m_ℓ^2/M^2, where m_ℓ is the mass of the outgoing lepton. As a result, it is negligible for NC and electron neutrino interactions and only becomes significant for lower energy CC muon or tau neutrino interactions [84].

3.2 Resonance Production

At energies above ~ 1 GeV, neutrino interactions increasingly proceed through nucleon excitation to short-lived higher-mass states in a process called resonance production (RES). The shift away from QE interactions at higher neutrino energies is shown in Figure 3.2. For experiments focused on CCQE interactions, resonant pion production forms a major background. Additionally, NC π^0 production, followed by instant decay to two photons with branching ratio $\mathrm{BR}(\pi^0 \to \gamma\gamma) = 0.99$ [1], can mimic the electromagnetic showers observed from electrons and can interfere with oscillation experiments looking for ν_e-appearance from a ν_μ beam. Similarly, CC $\pi^\pm$ production is a background for ν_μ-disappearance measurements. When the pion is absorbed in the nucleus or not identified correctly, these events are reconstructed as CCQE interactions with incorrect energies. Higher beam energy oscillation experiments, however, do not focus solely on CCQE interactions and need to include more diverse final states as part of the signal, including RES.

The description of RES can be separated into:

1. *Excitation:*
   A baryon resonance R is created

$$\begin{aligned} \nu_\ell + N &\to \ell^- + R \quad \text{(CC)}, \\ \nu_\ell + N &\to \nu_\ell + R \quad \text{(NC)}, \end{aligned}$$

   where N is a nucleon.

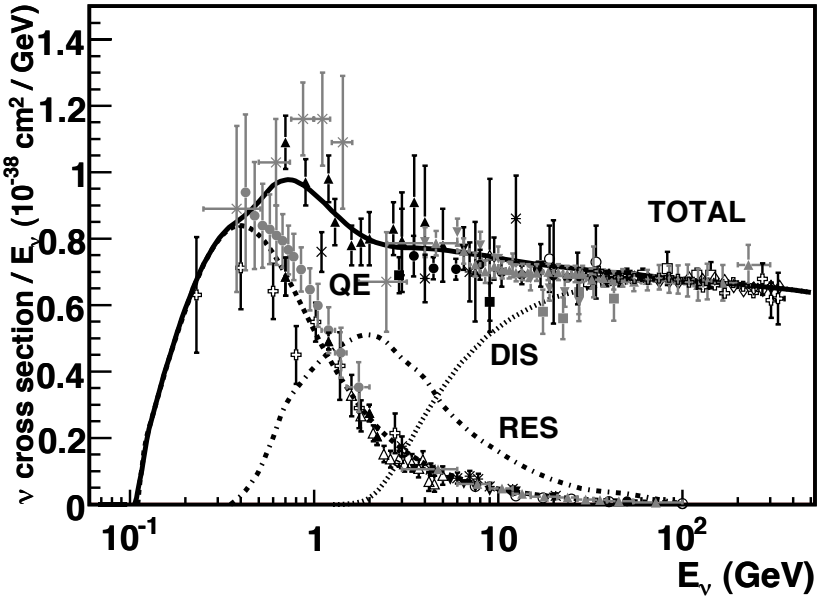

Fig. 3.2 Total neutrino CC cross section per nucleon normalised by neutrino energy. Lines are simulated neutrino-nucleus interaction predictions from the NUANCE generator [87]. The plot shows how, with increasing neutrino energy, interaction modes shift from QE to RES and ultimately to DIS. Source: Ref. [88].

2. *Decay:*
   The resonance decays are dominated by pion production

$$R \;\rightarrow\; N + \pi.$$

   For the lowest-lying excitation, $\Delta(1232)$, 99.4% [1] of the decays are to a nucleon and a single pion

$$\begin{aligned}
&\Delta^{++} \rightarrow p + \pi^{+}\,, \\
&\Delta^{+} \rightarrow p + \pi^{0} \quad \text{or} \quad n + \pi^{+}\,, \\
&\Delta^{0} \rightarrow n + \pi^{0} \quad \text{or} \quad p + \pi^{-}\,, \\
&\left(\Delta^{-} \rightarrow n + \pi^{-}\right)\,,
\end{aligned}$$

   with Δ^{++} only coming from neutrino interactions and Δ^{-} only from antineutrinos. Photon production accounts for most of the remaining Δ resonance decays [1].

Examples of Feynman diagrams for CC and NC RES, followed by decay via strong interaction, are shown in Figure 3.3. The resonance cross-section formula deviates from

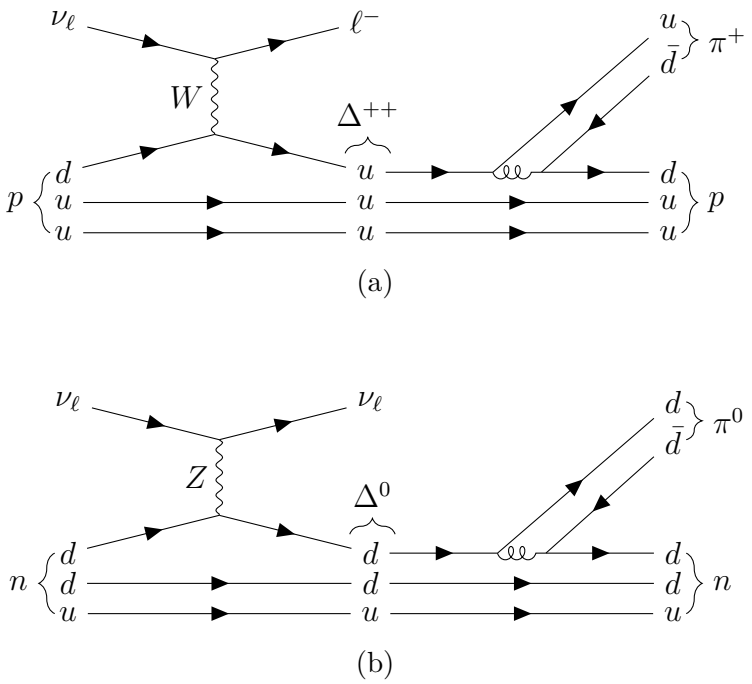

Fig. 3.3 Example Feynman diagrams for (a) CC and (b) NC RES neutrino interactions with a nucleon.

that in Equation (3.1) in two ways. To account for the finite lifetime of the resonance, which gives rise to a distribution of masses around its nominal mass, the resonance cross-section formula now includes a probability function described by a Breit-Wigner distribution [89, 76]

$$\mathcal{A}(p_R^2) = \frac{\sqrt{p_R^2}}{\pi} \cdot \frac{\Gamma(p_R)}{(p_R^2 - M_R^2)^2 + p_R^2\Gamma^2(p_R)}, \tag{3.15}$$

where p_R is the four-momentum of the resonance, M_R is the resonance mass, and Γ is the width of the resonance given the four-momentum. Secondly, the hadronic current needs to account for a more diverse possibility of produced states. Modelling of interactions and form factors depends on the parity, spin, and isospin of the resonance.

The resonances Δ and N^* are both excited states of the nucleons with isospins $I = 3/2$ and $I = 1/2$ respectively. An overview of the lowest-lying resonances is shown in Table 3.2, with their relative importance at GeV-scale neutrino energies shown in Figure 3.4. For transitions to isospin $I = 1/2$ resonances, such as N^*, the vector form factors can be related to electromagnetic form factors analogous to the rules shown in Table 3.1. For transitions to isospin $I = 3/2$ resonances, such as the $\Delta(1232)$, different

relations based on isospin symmetry can be derived [76]. In both cases, the vector form factors can be constrained by electron scattering data.

Name	L	I	J	P	BR($N\pi$)
$\Delta(1232)$	1 (P)	3/2	3/2	+	99.4%
$N(1440)$	1 (P)	1/2	1/2	+	$55-75\%$
$N(1520)$	2 (D)	1/2	3/2	−	$55-65\%$
$N(1535)$	0 (S)	1/2	1/2	−	$32-52\%$

Table 3.2 The four lowest mass baryon resonances. The column L gives the orbital angular momentum, J is total spin, I is isospin, P is parity, and BR($N\pi$) is the branching ratio to single pion-nucleon final states, taken from Ref. [1]. These are also described in spectroscopic notation $L_{(2I)(2J)}$, such that $\Delta(1232)$ is, for instance, $P_{33}(1232)$.

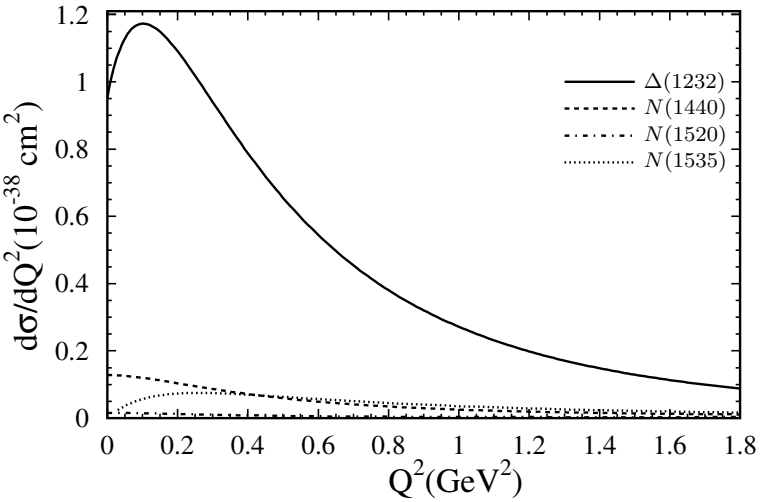

Fig. 3.4 Calculation of neutrino RES cross-sections at $E_\nu = 1.5\,\text{GeV}$ with varying four-momentum transfer, showing the dominance of the $\Delta(1232)$ resonance in the low-GeV region. Adapted from: Ref. [90].

For spin-1/2 resonances, similar connections as before but with a sign dependence on the parity of the resonance can be made between the pseudoscalar and axial form factors [76]

$$F_P\left(Q^2\right) = \frac{\left(M_R \pm M_N\right) M_N}{Q^2 + M_\pi^2} F_A\left(Q^2\right) \tag{3.16}$$

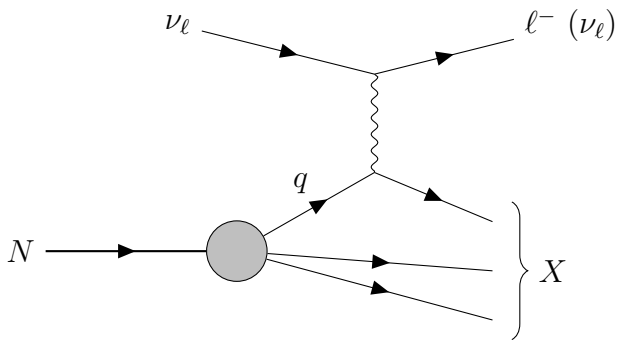

Fig. 3.5 Feynman diagram showing CC (NC) neutrino deep inelastic scattering characterised by hadronisation as the result of significant momentum transfer to a quark. X is the set of possible hadronic final states.

with M_R being the resonance mass and $F_A\,(Q^2)$ again described by a dipole, as in Equation (3.13). For spin-3/2 resonances, the form factor parameterisation differs and derives from the Rarita-Schwinger formalism for spin-3/2 fermions [91]. However, the relationships between the form factors carry over to spin-3/2 resonances, and the axial form factor remains the part that cannot be obtained from charged-lepton scattering [76].

3.3 Deep Inelastic Scattering

At neutrino energies above ~ 2 GeV, scattering transitions from resonance to deep inelastic scattering (DIS), as shown in Figure 3.2. In these interactions, the exchanged boson is energetic enough to resolve individual quarks inside a nucleon. A hadronic shower is produced following significant momentum transfer to a quark in the struck nucleon, as can be seen in the Feynman diagram in Figure 3.5. Both NC and CC interactions are possible

$$\begin{aligned} \nu_\ell + N &\to \ell^- + X \quad \text{(CC)}, \\ \nu_\ell + N &\to \nu_\ell + X \quad \text{(NC)}, \end{aligned}$$

where X is any number of hadrons.

DIS is described in terms of the two kinematic variables y and x. Inelasticity y is the fraction of neutrino energy transferred to the nucleon and, in the lab frame with the nucleon at rest, is given by

$$y \overset{Lab.}{=} \frac{\omega}{E_\nu} \tag{3.17}$$

where $\omega = (E_\nu - E')$ is the energy difference between the incoming neutrino and outgoing neutrino or charged lepton. The Bjorken x gives the fraction of the nucleon's momentum that is carried by the struck quark

$$x \overset{Lab.}{=} \frac{Q^2}{2M_N\omega}. \tag{3.18}$$

Without considering lepton masses or higher-order effects, the inclusive cross section for DIS can be written in terms of these two variables and three structure functions [88]

$$\frac{d^2\sigma}{dxdy} \propto \left(y^2 xF_1(x,Q^2) + \left(1 - y - \frac{M_N xy}{2E_\nu}\right) F_2(x,Q^2) + y\left(1 - \frac{y}{2}\right) xF_3(x,Q^2)\right). \tag{3.19}$$

The last term derives from the existence of axial contributions in weak interactions and is not present in EM scattering. The virtual bosons exchanged in the interaction can have three polarisations: two transverse and one longitudinal. The absorption of transverse states is described by $F_1(x,Q^2)$, while $F_2(x,Q^2)$ describes both transverse and longitudinal contributions. A purely longitudinal structure function can be constructed as [92]

$$F_L(x,Q^2) = \left(1 + x^2\frac{4M_N^2}{Q^2}\right) F_2(x,Q^2) - 2xF_1(x,Q^2). \tag{3.20}$$

Measuring the cross-section ratio of transverse to longitudinally polarised exchange bosons then makes it possible to relate $F_1(x,Q^2)$ and $F_2(x,Q^2)$, reducing the structure functions that need to be measured to two. The remaining structure functions for weak interactions can be expressed as [88]

$$F_2(x,Q^2) = 2x\sum_i \left[q_i(x,Q^2) + \bar{q}_i(x,Q^2)\right], \tag{3.21}$$

$$xF_3(x,Q^2) = 2x\sum_i \left[q_i(x,Q^2) - \bar{q}_i(x,Q^2)\right], \tag{3.22}$$

where $q_i(x,Q^2)$ and $\bar{q}_i(x,Q^2)$ are the parton distribution functions (PDFs) for quarks and antiquarks of flavour i, giving the probability density of finding a parton carrying momentum fraction x at four-momentum transfer Q^2.

Modelling of shallow inelastic scattering (SIS), which is the transition region from resonance to deep inelastic scattering, is an ongoing research effort [93]. With regard to pion production, the low-energy end of deep inelastic scattering produces single pions overlapping with the resonance region. With increasing energy, more complex hadronic final states, including the production of multiple pions, take over.

3.4 Multi-Nucleon Interactions

Aside from the three interactions with single nucleons (partons in the DIS case), there are two more interactions with compound nucleons to discuss.

3.4.1 Coherent Interactions

At low four-momentum transfer $Q^2 < 0.1\,\mathrm{GeV}^2$, coherent interactions with the entire nucleus become relevant [94]. The nucleus remains in the ground state during these interactions, which are dominated by the production of pions

$$\begin{aligned} \nu_\ell + A &\to \ell^- + \pi^+ + A \quad \text{(CC)}, \\ \nu_\ell + A &\to \nu_\ell + \pi^0 + A \quad \text{(NC)}, \end{aligned}$$

as illustrated in Figure 3.6.

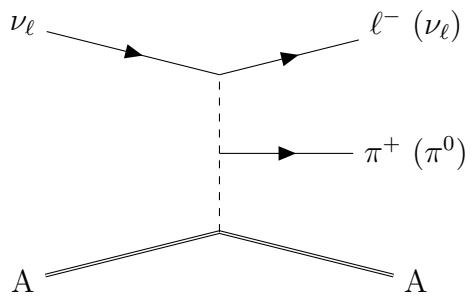

Fig. 3.6 Feynman diagram for a CC (NC) coherent neutrino interaction with a nucleus A producing a pion and leaving the nucleus in the ground state.

Coherent interactions are characterised by leptons and pions exiting at very forward scattering angles, meaning close to the direction of the neutrino beam. Furthermore, the particles produced in these interactions do not undergo further scatterings inside the nucleus, unlike nucleon-level interactions. These interactions constitute a small fraction of events in the GeV neutrino energy range, but still impact the predicted kinematics of pion cross sections and form backgrounds for searches such as ν_e appearance.

3.4.2 Meson Exchange Currents

In addition to quasielastic one-particle-one-hole (1p1h) scattering described in Section 3.1, in which a single nucleon is knocked out of the nucleus, scattering can also occur on correlated nucleon pairs in two-particle-two-hole (2p2h) and higher interactions. These interactions are facilitated by meson-exchange currents (MECs), primarily

through the exchange of pions, and fall in the energy-momentum transfer region between QE and resonance production. They arise via a combination of various interaction diagrams that share the emission of two nucleons [95]. For neutrino interactions, these are

$$\nu_\ell + A \to \ell^- + N_1' + N_2' + (A-2) \text{ with } N_1' = p,\ N_2' \in \{n, p\} \quad \text{(CC)},$$
$$\nu_\ell + A \to \nu_\ell + N_1' + N_2' + (A-2) \text{ with } N_1', N_2' \in \{n, p\} \quad \text{(NC)},$$

where A and $(A-2)$ are the initial and final nuclei. Antineutrino interactions are similar. Neglecting these interactions can skew the neutrino energy reconstruction needed for oscillation experiments, as the presence of undetected neutrons or protons below the detection threshold is not accounted for.

Chapter 4

Neutrino Sources at Fermilab

Neutrino production at Fermilab involves multiple stages, beginning with ion generation and acceleration, stripping of electrons, further acceleration of the resulting protons, and finally collision with a fixed target to produce neutrinos via intermediary particles. This chapter covers both the Booster Neutrino Beam (BNB) and the Neutrinos at the Main Injector (NuMI) beams, with the BNB being the primary beam for MicroBooNE and the focus of the analysis described in this thesis.

4.1 Proton Beam

The Fermilab accelerator complex accelerates hydrogen ions into high-energy proton beams suitable for neutrino production. The structure of the complex is illustrated in Figure 4.1. It starts with hydrogen ions (H^-) that are generated in the pre-accelerator and accelerated to 750 keV. They then pass through a series of radio frequency (RF) cavities and magnetic focusing elements in the linear accelerator (LINAC), which boosts their energy to 400 MeV. The ions are directed to the Booster synchrotron, where a thin foil strips away the electrons, leaving a pure proton beam. The Booster finally accelerates these protons to 8 GeV and sends them either directly to the BNB target hall or to be further accelerated in the Main Injector before being focused on the NuMI target. The Main Injector increases the proton energy to 120 GeV for delivery to the NuMI beamline and other experiments. A storage ring known as the Recycler allows manipulation of the Booster batches through a process called slip-stacking, effectively doubling the beam intensity before transfer to the Main Injector [96].

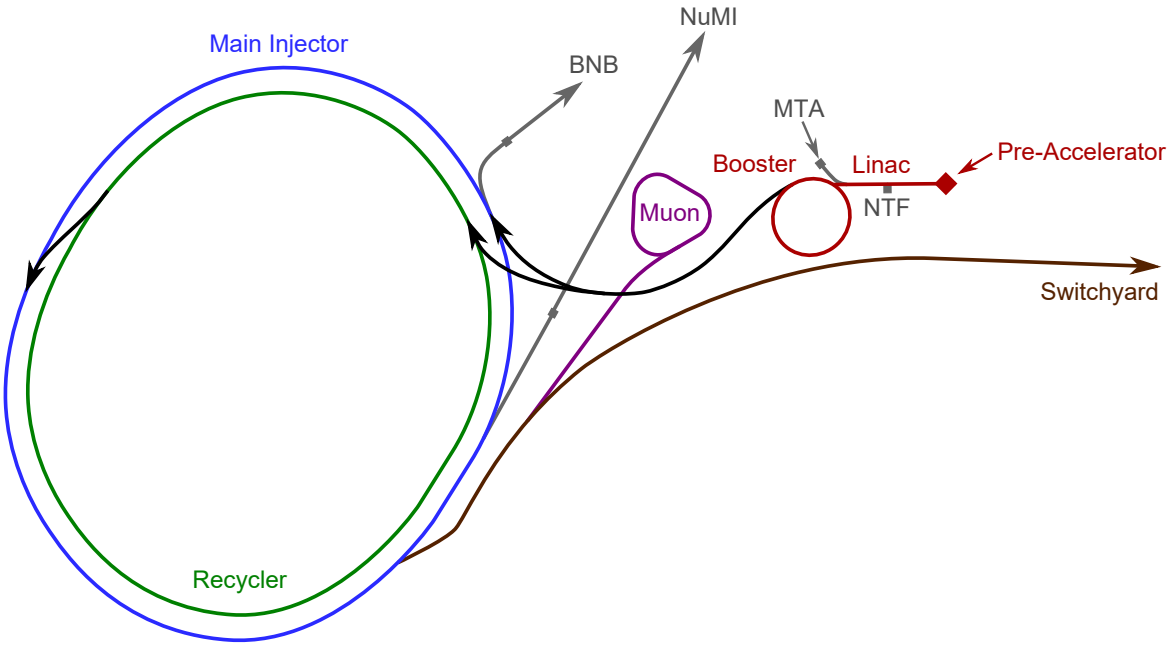

Fig. 4.1 Illustration of the accelerator complex at Fermilab, starting with ions in the Pre-accelerator and ending with accelerated protons delivered to the BNB and NuMI beamlines. Source: Ref. [96].

4.2 BNB Target Hall

The 8 GeV protons from the Booster arrive at the BNB target hall where they collide with a fixed target consisting of seven stacked segments of beryllium. When protons collide with them, they produce secondary particles, predominantly pions, with kaons constituting a smaller fraction.

Surrounding the target is the horn, which is a pulsed electromagnet made from aluminium that produces a toroidal magnetic field and is illustrated in Figure 4.2. It operates at a current of $\sim$ 174 kA, which flows along the inner surface of the horn and returns along the outside (or vice versa) [97]. The horn can be operated in both forward (neutrino) and reverse (antineutrino) modes by switching the polarity of the applied voltage. In forward horn current mode, it focuses positively charged secondary particles resulting from the proton-beryllium collision while simultaneously defocusing negatively charged particles. In reverse horn current mode, this focusing effect is inverted [98].

After exiting the horn, the focused secondary particles enter a 50 m long air-filled decay pipe illustrated in Figure 4.3. At the start of the pipe, the particles must pass through a collimator that serves to block particles travelling at large angles with respect to the beam direction from entering. Inside the pipe, the particles, mainly charged

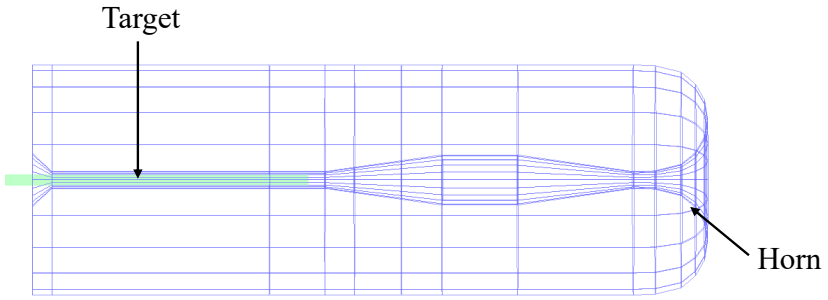

Fig. 4.2 Illustration of the outer and inner conductors of the horn. The target is placed inside the inner conductor. Source: Ref. [99].

pions, decay predominantly to muon (anti-)neutrinos:

$$\pi^+ \to \mu^+ + \nu_\mu \quad \text{or} \quad \pi^- \to \mu^- + \bar{\nu}_\mu. \tag{4.1}$$

The dominant production of muon neutrinos is a consequence of helicity suppression. Pions have zero spin and in their rest frame the momenta of the produced neutrino and antilepton have to be opposite. To conserve angular momentum, their spins must also be opposite. In the limit of zero mass, helicity and chirality are equivalent. Neutrinos are nearly massless and are overwhelmingly in left-handed helicity states, meaning their spin is anti-aligned with their momentum. To conserve angular momentum, the accompanying antilepton must also be in a left-handed helicity state. However, only right-chiral antiparticles couple to the weak interaction. The projection between the antilepton's left-handed helicity state and the interacting right chiral state that couples to the W^+ depends on mass and energy via m/E. This factor suppresses the production of electrons in pion decays due to their small mass. The tau lepton is too heavy to be produced, so among the accessible flavours, muons are favoured [100]:

$$\frac{\Gamma\left(\pi^+ \to e^+\nu_e\right)}{\Gamma\left(\pi^+ \to \mu^+\nu_\mu\right)} \approx 10^{-4}. \tag{4.2}$$

In addition to this primary decay channel, neutrinos can also be produced by the subsequent decay of muons. The main impact of this is the addition of an intrinsic electron (anti-)neutrino component to the beam:

$$\mu^+ \to e^+ + \nu_e + \bar{\nu}_\mu \quad \text{or} \quad \mu^- \to e^- + \bar{\nu}_e + \nu_\mu. \tag{4.3}$$

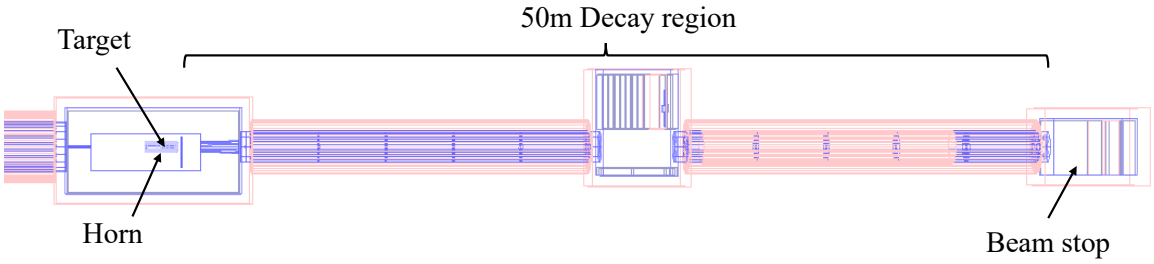

Fig. 4.3 Illustration of the target hall, showing the horn, the decay pipe and the beam stop. At 25 m is an intermediate absorber that can be moved into the decay pipe for testing. Source: Ref. [99].

A beam stop made from steel and concrete is located at the end of the decay pipe to absorb all remaining non-neutrino particles. The overall ratio of ν to $\bar{\nu}$ depends on the horn current mode. For the five runs of data taken by MicroBooNE, the horn operated purely in neutrino mode with an average beam energy of $\sim$ 800 MeV.

4.3 NuMI Target

Similarly to the BNB, the NuMI beam at Fermilab is produced by firing much higher-energy protons from the Main Injector onto a target made of graphite. The resulting mesons are then focused by two magnetic horns. These particles travel through a 675 m long decay pipe filled with helium, where they decay into neutrinos and other secondary particles. An absorber at the end of the decay pipe stops hadrons and is followed by 240 m of rock to stop muons [101]. The NuMI beam achieves much higher neutrino energies with the on-axis ν_μ flux, for instance, peaking at $\sim$ 6 GeV [102]. However, the energies observed by MicroBooNE are lower, as the experiment is positioned off-axis to the beam, as will be described in Chapter 5.

Chapter 5

The MicroBooNE Detector

Fig. 5.1 Liquid-argon short-baseline detectors at Fermilab. The red line at the top illustrates the path of the NuMI beam starting from the target and the line at the bottom illustrates the BNB.

MicroBooNE uses a LArTPC with a total mass of 170 metric tonnes, of which 85 are part of the active volume [103]. It is a single-phase horizontal drift time projection chamber (TPC), meaning an anode and cathode horizontally sandwich a volume of liquid argon. The detector is affiliated with the SBN programme at Fermilab and is located 468.5 metres from the target of the BNB. It also lies 8° off-axis to the NuMI beam. This section summarises the key components of the experiment and is based on the MicroBooNE design and construction report, see Ref. [103].

5.1 Cryostat

A 12.2 m long cylindrical vessel with domed end caps, an inner diameter of 3.81 m, and walls made of 1.1 cm-thick stainless steel serves as the housing for the liquid argon, the TPC, and the light collection system. It has 34 access points for connections to electrical and cryogenic systems on the outside. A nitrogen refrigeration system holds the argon at a temperature of 89.4 K and a pressure of 1.24 bar. To ensure uniformity in the drift velocity, temperature gradients must remain below 0.1 K. To shield the cryostat from outside conditions and fluctuating temperatures, it is coated with 41 cm of sprayed-on polyurethane insulation.

MicroBooNE depends on travelling ionisation electrons reaching a detection mechanism to work and a low rate of attenuation of these charges is important. Argon itself is a noble gas and as such does not attenuate the electrons, but ionisation charges do attach to electronegative impurities, reducing the charges relative to the drift time. An argon purification system is used to minimise this effect. It maintains electronegative impurities at 17 parts per trillion (ppt) O_2 equivalent [104], meeting the < 100 ppt O_2 equivalent target set for observing minimum ionising particles (MIPs) drifting across the full width of the detector. Here, O_2 equivalent includes impurities from other sources, such as H_2O. Additionally, the argon must contain less than 2 parts per million (ppm) N_2, as nitrogen quenches and absorbs scintillation light. However, nitrogen cannot be effectively removed by the filtering system, making this a requirement for the supplied argon. A monitoring system inside the cryostat keeps track of temperature and argon purity.

5.2 Time Projection Chamber

At the heart of the detector lies the liquid argon (LAr), which serves both as the target for neutrino interactions and the detection medium for the resulting final-state particles. A TPC with dimensions 2.56 m (width) $\times$ 2.33 m (height) $\times$ 10.36 m (length) is immersed in the argon and defines the active target volume. The cathode on the left side of the detector, from the perspective of the beam, is constructed from stainless steel sheets and is held at -70 kV. The anode consists of three layers stacked 3 mm apart. Each layer is made up of parallel wires also spaced 3 mm apart, with $\pm 60°$ angular offset between the initial two with the final plane as shown in Figure 5.2. The final layer, whose wire direction is vertical and parallel to the side of the frame, has 3456 wires. The other two have 2400 wires. The wires are kept at ~ 7 N of tension to

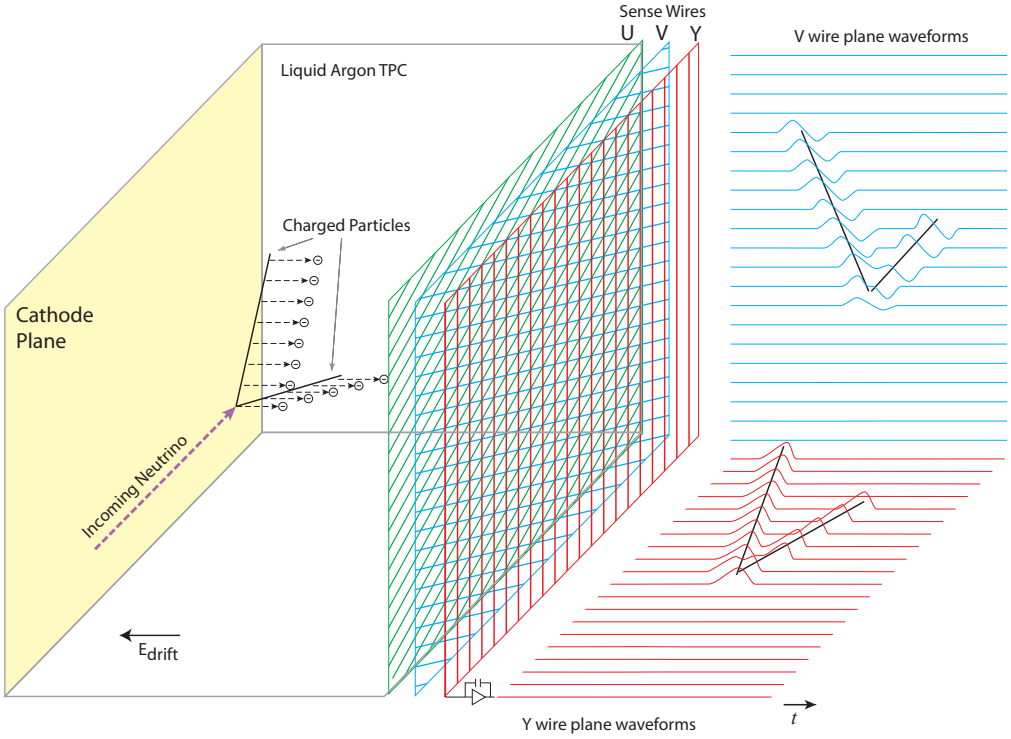

Fig. 5.2 Illustration of a LArTPC with an incoming neutrino creating charged particles that ionise the argon. The ionisation electrons then drift towards the anode under the influence of a strong electric field, where they are recorded on three layers of sense wires. Source: Ref. [103].

keep them from sagging. The sides of the active volume not enclosed by the anode and cathode are surrounded by a field cage consisting of 64 field cage loops, shown in Figure 5.3, that step down the voltage in steps of 2 kV across loops using resistors. This ensures the electric field created between anode and cathode is uniform, with an electric field strength of $E_0 \approx 273\,\mathrm{V/cm}$.

Charged particles produced by neutrino interactions or backgrounds, such as cosmic muons, ionise the argon as they traverse the detector volume. The electric field drifts the free electrons towards the anode at a speed of ~ 1.1 mm/μs [105], kept constant by collisions with the argon atoms. Bias voltages are applied across the wire planes at -110 V, 0 V, and +230 V, starting with the innermost layer, ensuring that the first two planes are transparent to the drift electrons. As electrons pass by these first two wire planes, they induce a bipolar signal, while on the final plane the signal is unipolar as

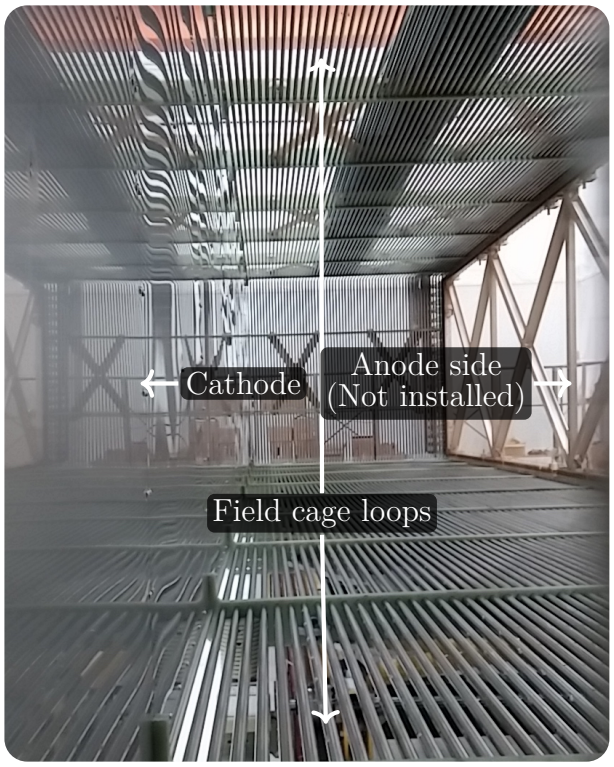

Fig. 5.3 Interior view of the MicroBooNE TPC before anode installation and insertion into the cryostat. Source: Ref. [103].

the electrons are collected directly. The difference between these signals can be seen in Figure 5.4. The figure also shows that the second and third planes are shielded against the effects of more distant charges by the planes in front of them. This is not the case for the first induction plane, which results in it being more susceptible to noise.

The position reconstruction of interactions is achieved along one dimension by measuring the charge distribution across the parallel wires, while the drift time of the electrons provides the orthogonal dimension. This configuration enables the detector to record photograph-like projections of interactions from three different perspectives, allowing for 3D reconstruction of neutrino interactions. An example of a candidate neutrino interaction recorded by the collection plane is shown in Figure 5.5. It shows charged particles produced in an interaction travelling through the argon and producing long tracks or decaying in electromagnetic cascades, producing shower signatures.

5.2.1 Electromagnetic Interactions

Charged particles traversing the detector volume primarily lose energy through ionisation and excitation of the argon. The stopping power, or mean energy loss per unit

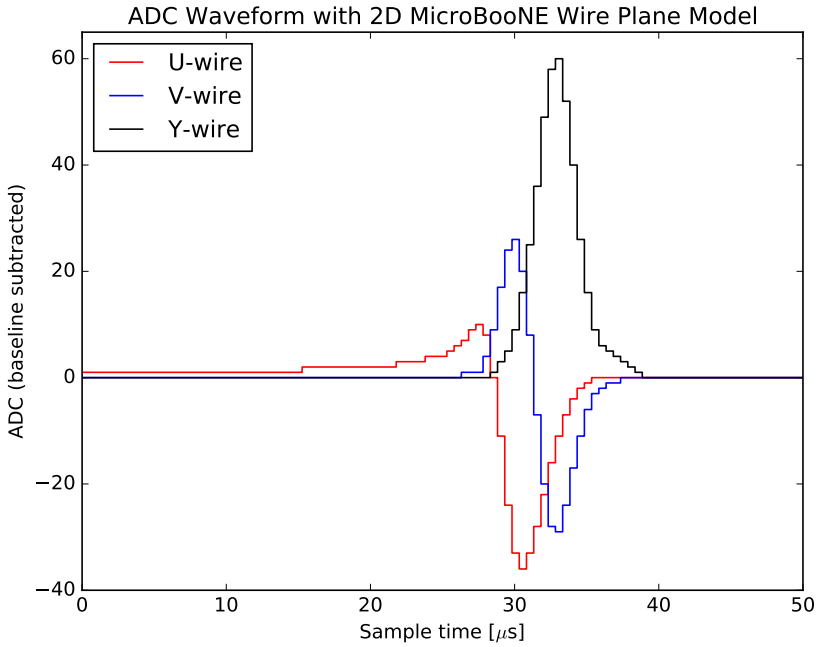

Fig. 5.4 Simulated digitised waveforms for wires from all three planes for an idealised MIP track, illustrating the difference between the bipolar signals for the induction planes in red and blue and the unipolar signal for the collection plane in black. Source: Ref. [106].

path length, can be approximated with the Bethe-Bloch equation for relativistic heavy charged particles [1]:

$$-\left\langle \frac{\mathrm{d}E}{\mathrm{d}x} \right\rangle = Kz^2 \frac{Z}{A} \frac{1}{\beta^2} \left[\frac{1}{2} \ln \left(\frac{2m_e \beta^2 \gamma^2 W_{\max}}{I^2} \right) - \beta^2 - \frac{\delta(\beta\gamma)}{2} \right], \tag{5.1}$$

with the terms being:

- $-\langle \mathrm{d}E/\mathrm{d}x \rangle$: Stopping power (mean energy loss per unit path length).
- K: A constant $K \approx 0.307$ MeV mol^{-1} cm^2 [1].
- z: Charge number of the incident particle.
- Z: Atomic number of the medium.
- A: Atomic mass of the medium (in g/mol).
- $\beta \equiv v/c$: The velocity of the incident particle relative to the speed of light.
- $\gamma \equiv (1 - \beta^2)^{-1/2}$: The Lorentz factor.

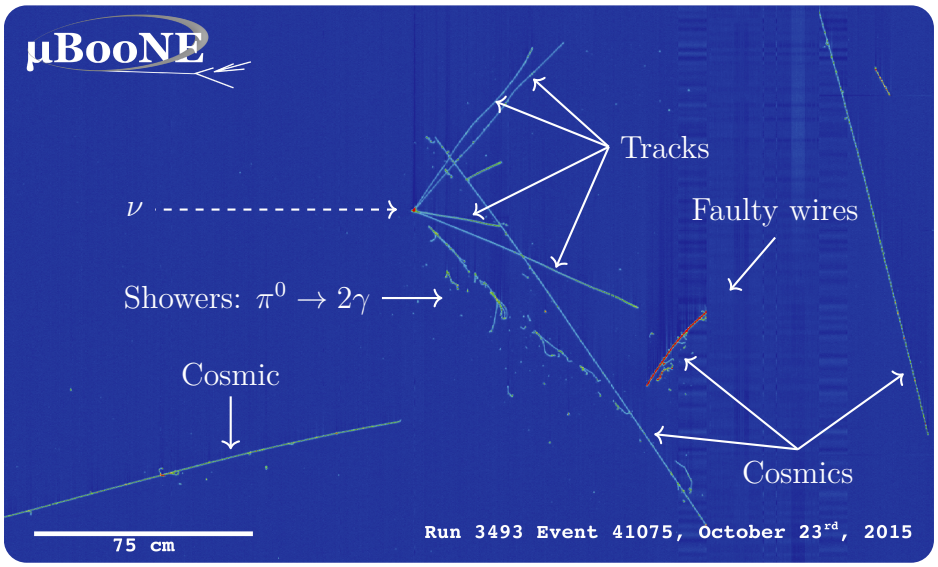

Fig. 5.5 Cropped collection plane recording of candidate neutrino interaction producing tracks and showers. A number of cosmic-ray muon tracks are also visible. Source: MicroBooNE Collaboration.

- $m_e = 0.511$ MeV: Electron rest mass [1].
- W_{max}: Maximum energy transfer to an electron in a single collision,

$$W_{\text{max}} = \frac{2m_e\beta^2\gamma^2}{1 + 2\gamma\frac{m_e}{M} + \left(\frac{m_e}{M}\right)^2}, \tag{5.2}$$

  where M is the mass of the incident particle.
- I: Mean excitation energy of the medium, an empirically determined quantity.
- $\delta(\beta\gamma)$: Density effect correction, which accounts for polarisation of the medium at high energies.

This is only accurate for moderately relativistic particles with $0.1 \lesssim \beta\gamma \lesssim 1000$, beyond this, additional effects such as radiative losses become larger than 1% [1]. The formula also only accurately approximates the energy loss of charged particles heavier than electrons. For electrons and positrons, additional terms need to be added due to their low masses [1]. Figure 5.6 shows the Bethe-Bloch distribution of μ^+ over different energy ranges in a material. The stopping power exhibits a minimum and particles at energies in this range are MIPs.

For electrons and positrons, energy loss occurs through ionisation and bremsstrahlung. The latter is radiation emitted due to acceleration, here from the electric field of

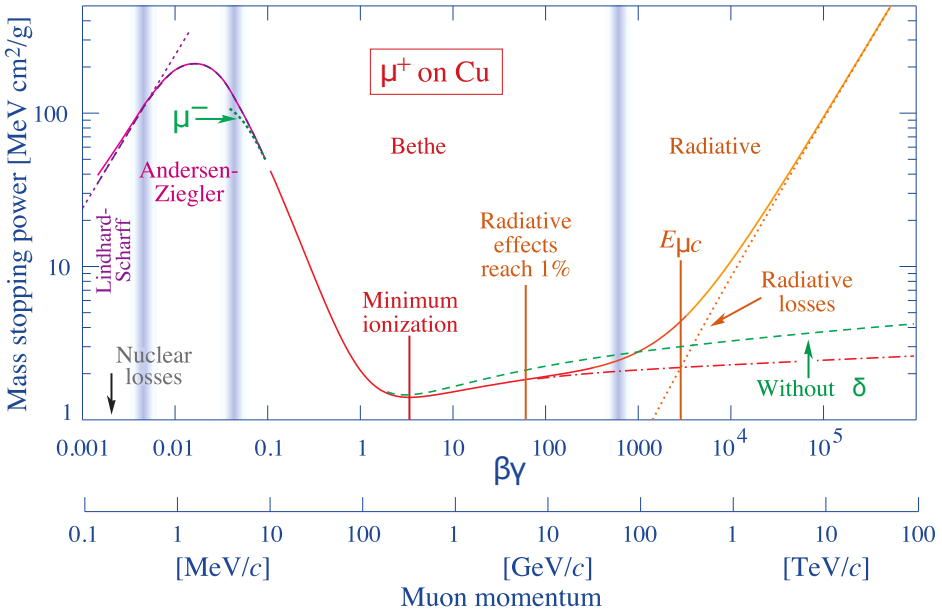

Fig. 5.6 Stopping power for antimuons in copper as a function of $\beta\gamma = p/M$. Source: Ref. [1].

a nucleus. At lower energies, ionisation dominates, similar to heavy charged particles, while at higher energies bremsstrahlung becomes the dominant process.

Low-energy photons transfer their energy to bound electrons via the photoelectric effect, leading to ionisation. Intermediate-energy photons Compton scatter off free or weakly bound electrons. High-energy photons pair-produce electron-positron pairs in the field of a nucleus. Electromagnetic showers are produced in MicroBooNE when an energetic photon, electron or positron interacts with the argon and initiates a cascade of further electrons, positrons, and photons.

5.2.2 Diffusion

Electron diffusion is the spreading of ionisation electrons produced by charged particles relative to the drift time. Under the influence of MicroBooNE's electric field, the diffusion is anisotropic and can be split into two components. The transverse component, denoted D_T, spreads the electron clouds over multiple wires, while the longitudinal component, D_L, which is most strongly affected by the electric field, causes the clouds to spread in the drift dimension and thus broadens the waveform in time, as illustrated in Figure 5.7.

The effects of longitudinal diffusion in argon are not well known, and MicroBooNE has conducted its own study using cosmic muons tagged by a cosmic ray tagger

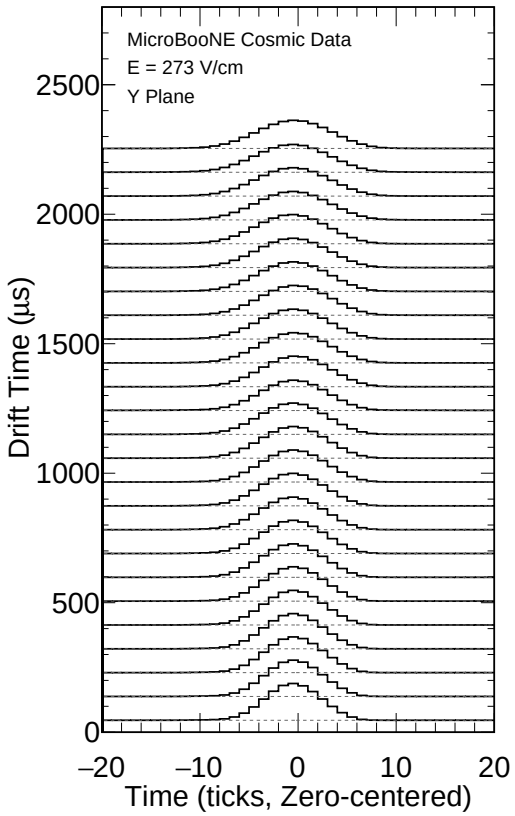

Fig. 5.7 Illustration of waveform broadening due to longitudinal diffusion relative to the drift time. Source: Ref. [107].

(CRT) [107]. The CRT is described in Section 5.6 and, it suffices to mention here, is a scintillator detector surrounding the cryostat that can be used to measure incoming charged particles. The CRT, along with the determination of the start and end points of the track, enables the identification of the muon entry time which is required to precisely establish the electron drift times needed to measure the level of diffusion.

5.2.3 Space Charge Effects

In MicroBooNE, which operates near the Earth's surface, a high flux of cosmic muons leads to significant ionisation, resulting in not only drift electrons but also positive argon ions. The ions drift towards the cathode but are around five orders of magnitude slower than electrons [108], leading to the build-up of a cloud of slow-moving positive charge. This charge results in a non-uniform electric field, with the charge cloud attracting electrons towards the centre of the detector. This is called the space charge effect (SCE).

Along the drift dimension, for instance, the excess charge causes variations in the electric field strength that reach up to 10% near the cathode and 6% near the anode from the nominal strength $E_0 = 273\,\mathrm{V/cm}$ [109]. One major effect of this is spatial displacement, where ionisation electrons deviate from their expected drift paths, leading to reconstructed tracks that appear squeezed in the directions transverse to the drift direction and bent towards the cathode [110]. These effects are illustrated in Figure 5.8. This stretching and squeezing also affects calorimetry and, in particular, the amount of energy transferred to the material per distance, $\mathrm{d}E/\mathrm{d}x$, that is fundamental to particle identification (PID) in MicroBooNE. Variations in the electric field also affect the electron drift velocity and modify the rate of electron-ion recombination. Finally, the SCE exhibits variations over time, with observed fluctuations in the charge distribution of about 4%, potentially influenced by convective flows of liquid argon [105].

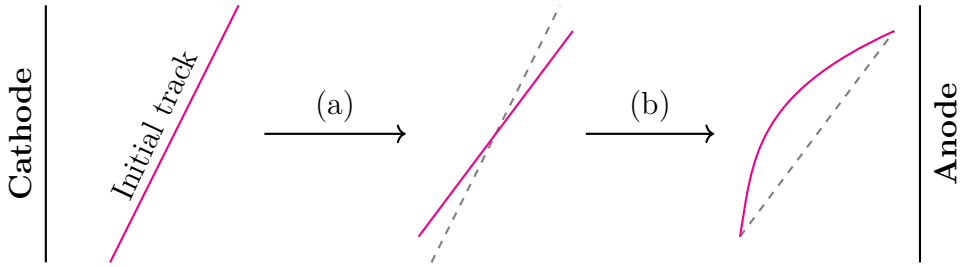

Fig. 5.8 SCE from non-uniform charge build up in the detector, which can be broken down into two transformations with (a) squeezing along the orthogonal directions to the drift axis x, resembling a rotation and (b) bending of tracks towards the cathode. Figure based on Ref. [111].

To mitigate all these effects, MicroBooNE employs two strategies to map the charge buildup. The first is a UV laser system consisting of two units, each with a laser and rotating mirror, that can ionise the argon and produce straight tracks with known positions. These are then recorded by the TPC and can be used to determine the amount of warping. The downside of this system is limited coverage of the detector due to a constrained range of motion for the mirrors [105].

The main method used is to analyse cosmic background samples in which a muon pierces either the cathode or anode of the detector. Tracks that pierce the anode experience no SCE for deposited hits close to the anode due to the negligible distance the ionisation electrons have to travel in the detector. However, this is not true for the other sides pierced by the muons. In the first step, anode-piercing tracks are used to correct the offsets of tracks passing through the other faces of the detector not covered by an anode or cathode, as shown in Figure 5.9. Three-dimensional spatial offsets are determined for the sides of the detector by first directly projecting the track ends onto

the pierced TPC face to determine an orthogonal offset. To determine the offset in the remaining two dimensions, an initial SCE offset map, computed using a Cosmic Ray Simulations for KASCADE (CORSIKA) [112] simulation of muons in the detector, is used. For this, ratios of the measured to the simulated orthogonal offsets across a TPC face are computed. These factors are then used to scale the SCE simulation, setting the strength of the offset in the other two dimensions. The remaining face, the cathode, is calibrated using the scaling factors determined in the first step at the edges of the top and bottom faces near the cathode. The top and bottom values are interpolated to get the scaling map. Using this knowledge about the correct start and end points of tracks passing through the TPC faces, the amount of warping in the whole volume can be determined by examining crossing muon pairs. These pairs do not actually have to occur at the same time but need to come very close to each other (within 1 cm) when combined. The true crossing point, determined by drawing a straight line between the corrected end points of each track, can be compared to the observed crossing point. The detector volume is voxelised, and the median offset in each voxel is used to average out the effects of multiple Coulomb scattering (MCS), which are multiple small-angle deflections due to Coulomb interactions with nuclei. The spatial offset map can then be used to compute the electric field distortions inside the detector [105].

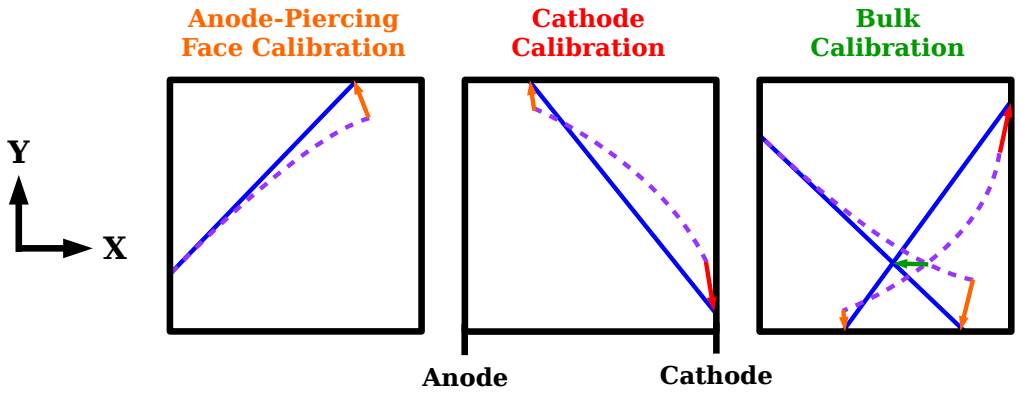

Fig. 5.9 The three SCE calibration steps: first, using anode-piercing cosmic muons to correct the spatial offsets at the detector faces; second, using this information to fine tune a dedicated simulation that determines the offset at the cathode; and finally, comparing the true crossing point of tracks to the observed one to determine the spatial offsets inside the detector. Source: Ref. [105].

A hybrid space charge map is created by combining the UV laser-based measurements with the cosmic muon-based offsets, and this hybrid map is used for all subsequent corrections.

5.2.4 Recombination

Closely connected to SCE is recombination, which is the rate at which ionisation electrons lose their excess energy and recombine with Ar^+ ions. This directly depends on the concentration of positive ions at any point in the detector, which itself depends on the local electric field strength moving the ions. Electrons undergoing recombination attenuate the signal reaching the anode. MicroBooNE measures the charge deposited over distance $\mathrm{d}Q/\mathrm{d}x$ that arrives at the anode. To go from this to the correct deposited energy $\mathrm{d}E/\mathrm{d}x$, recombination has to be taken into account [113].

5.3 Scintillation Light Detection

In addition to producing ionisation electrons, final-state particles can also produce light via Cherenkov radiation or scintillation. The latter is central to MicroBooNE's photomultiplier tube (PMT) light collection system, which provides complementary timing information.

5.3.1 Liquid Argon Scintillation

Charged particles traversing the argon lose energy by ionising and exciting argon atoms, forming bound Ar_2^* excimers (excited dimers) in two relevant electron spin configurations: a singlet state and a triplet state. An illustration of this is shown in Figure 5.10. In both cases, a single electron has been promoted to a higher energy level as illustrated in Figure 5.11. The singlet state is the dominant configuration and has antiparallel electron spins between the excited and the other unpaired electron (total spin zero). This state has a short lifetime of 6 ns [114]. The triplet state, making up about one-quarter of excimers [103], has two parallel spin states (total spin one) and a longer lifetime of 1.6 μs [114], since its decay requires spin flipping. Upon radiative deexcitation, both states decay to two separate ground-state argon atoms while isotropically emitting vacuum ultraviolet (VUV) photons at around 128 nm [115]. Argon is transparent to this wavelength, and these photons are crucial for precise timing and event reconstruction in noble liquid detectors like MicroBooNE.

The light yield depends on $\mathrm{d}E/\mathrm{d}x$ and the electric field strength [117]. Quenching from nitrogen has significant effects on light yield, where N_2 molecules collide with the argon excimers, resulting in a non-radiative collisional reaction. This reduces the light yield and particularly affects the slower decaying triplet state. A $\sim$ 1 ppm N_2 contamination, for instance, results in a $\sim$ 20% reduction in photons [118]. Furthermore,

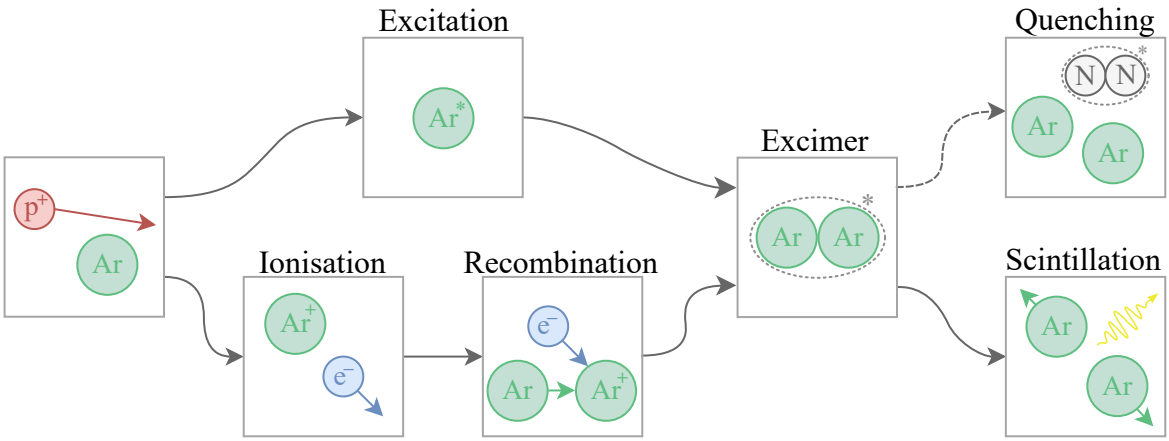

Fig. 5.10 Excimers are produced via two routes. One is called self-trapping and happens via an excited argon atom, the other is the result of ionisation of an argon atom followed by recombination. The excimers can be singlets or triplets, and return to individual ground state atoms via the emission of a photon or by quenching caused by impurities. Figure based on Ref. [116].

photons can also be directly absorbed by impurities. However, this effect is negligible for the irreducible nitrogen contamination given the VUV nature of the scintillation light [119]. In MicroBooNE, the photon yield is O(10,000) per MeV of deposited energy.

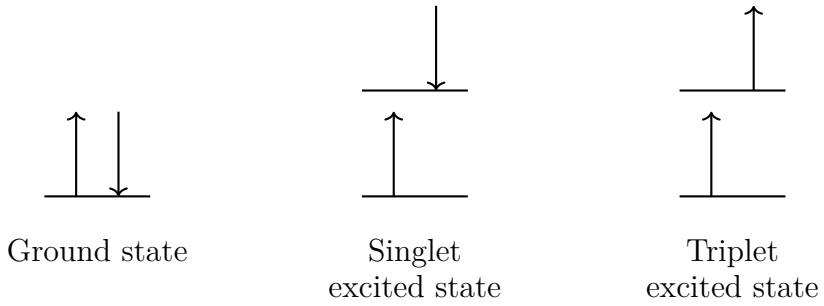

Fig. 5.11 Illustration of spin states for a pair of electrons. The first and second picture show antiparallel spins in the ground and the singlet excited state. The last picture is the triplet excited state.

5.3.2 Light Collection System

There are 32 PMTs mounted on the inside of the cryostat wall behind the anode wires as shown in Figure 5.12. Acrylic plates covered with tetraphenyl butadiene (TPB) are placed in front of the PMTs to wavelength shift incoming VUV photons to the visible spectrum with a peak around 425 nm. This is needed since detecting these small wavelengths is difficult to do with PMTs directly. Figure 5.13 shows that the

installed Hamamatsu cryogenic PMTs have no response to photons below 300 nm [120] and require this wavelength-shifting coating to be effective. Figure 5.13 also shows a secondary light collection system for future detector R&D that makes use of acrylic light guides. However, this is not used for triggering.

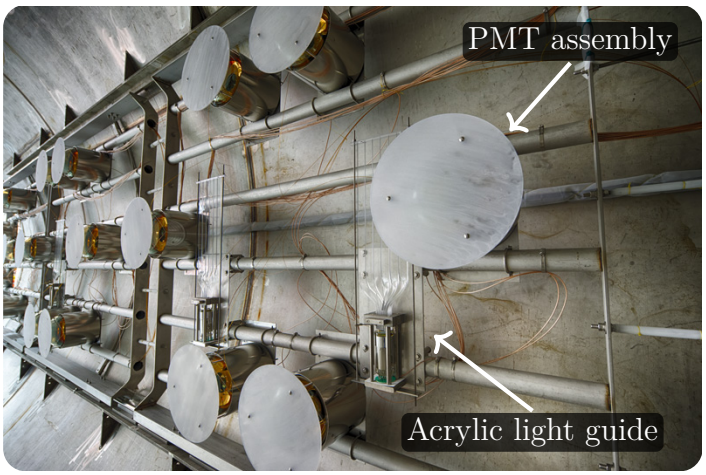

Fig. 5.12 Image of the MicroBooNE light collection system in the cryostat consisting of PMTs with TPB coated plates and a secondary system of acrylic light guides. Source: Ref. [103].

The PMT system is not used to determine the start of a beam interaction, as the 1.6 μs duration of the beam spill is short enough that its time of arrival can be used as the time t_0. However, the relatively long electron drift times on the order of milliseconds, combined with MicroBooNE being a surface detector, results in cosmic rays appearing in almost all recorded interactions. The light distributions across the PMTs give additional information about the z and y positions of interactions without any electron-drift delays. Flash-track matching can thus be used to match observed light to tracks in the detector and can be used to identify the interactions in time with the beam and to reject incidental backgrounds.

5.4 Readout System

The wire readout is shown in the top half of Figure 5.14. It starts with cold electronics that are inside the cryostat. The readout wires are connected to analogue application-specific integrated circuits (ASICs) that first pre-amplify and shape the weak analogue wire signals. The ASICs are placed inside the cryostat to minimise the distance to the wires, reducing noise. After this initial amplification, the signals are less sensitive to noise and can be sent to the warm electronics outside the cryostat via feedthroughs.

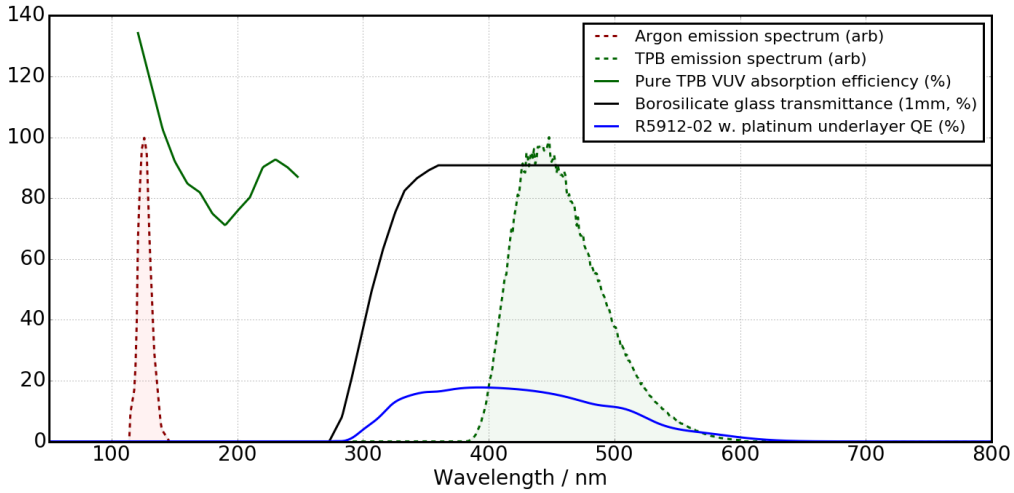

Fig. 5.13 Photon absorption, emission and transmission spectra relevant to the scintillation light detection system. The argon scintillation spectrum is shown in red. The fraction of emitted to absorbed photons for TPB is shown above in green, with it being possible for multiple photons to be emitted for one energetic absorbed photon. The spectrum of the emitted light is the dashed green light. The transmittance of the PMT glass is shown in black and the quantum efficiency of the sensor, which is the ratio of incident to emitted photons, is shown in blue. The emitted scintillation light gets shifted to the detection range of the PMT. Source: Ref. [121].

An intermediate amplifier further boosts the signals to allow them to be sent to the readout electronics several metres away. The readout system consists of analog-to-digital converters (ADCs) and digital data handling modules called front end modules (FEMs) that use field-programmable gate arrays (FPGAs). The ADCs digitise the waveforms in 1.6 ms time windows. These were designed to be large enough to allow electrons to drift the full cathode to anode distance in the planned 500 V/cm electric field. The eventual field strength ended up being roughly half, requiring multiple frames to be read out. There are two data streams that get buffered in the FEMs. These are named SN and NU, with the first continuously sending recorded frames to the data acquisition (DAQ) computers while the NU stream is for triggered recordings. NU uses lossless compression, while SN uses lossy compression to reduce the amount of data that needs to be stored. When a trigger signal is received, the FPGAs crop 4.8 ms out of the recorded frames so that there is 1.6 ms before and 3.2 ms after the received trigger time. The purpose of the SN stream is for use in beam-independent analyses, such as supernova neutrino observations. The DAQ system stores the data on disk and tape and makes it accessible via the Fermilab Serial Access to Metadata (SAM) system.

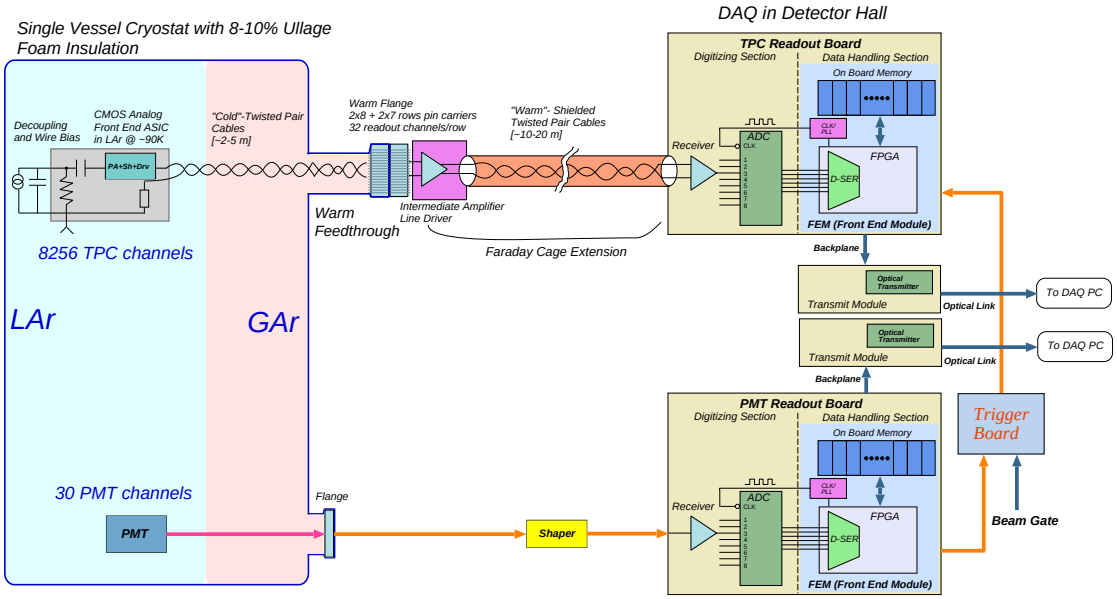

Fig. 5.14 Schematic of the MicroBooNE readout system, illustrating the signal paths from the TPC wires and PMTs to the DAQ system. The layout highlights the separation between cold and warm electronics, the signal digitization and processing stages, and the role of the trigger board in coordinating data collection. Source: Ref. [103].

A single coaxial cable carries the high-voltage into the cryostat for the optical system and the signal out. The PMT readout is shown in the bottom half of Figure 5.14. The signal is split into high- and low-gain channels for a high dynamic range. These are then amplified and receive some analogue processing before being digitised via three readout boards consisting again of ADCs and FPGAs. Two of these boards are dedicated to separately processing high gain signals for in- and out-of-beam-time periods. The third processes the much fewer low gain signals for flashes from all sources. In contrast to the wire readout, the PMT ADCs use a higher sampling rate for digitising the signals. This higher rate enables better determination of the event start time t_0 which is used for non-beam interactions (e.g. cosmic rays). The information is recorded in the NU data stream and sent to the DAQ as four frames, with one preceding, one containing and two following a trigger event. To reduce the amount of data, only sections passing a minimum threshold of recorded photo-electrons are kept. For beam-related triggers, it additionally does 1500 consecutive recordings, equivalent to 23.4 μs, around and during the beam spill. This is called the beam discriminator. The system also records shorter 0.6 μs bursts of PMT data by self-triggering upon

reaching a light threshold inside the remainder of the four frames. This is called the cosmic discriminator.

5.5 Trigger System

To limit the amount of recorded data, a trigger system decides which PMT and TPC recordings are of interest and need to be saved in full. The trigger board accepts several types of inputs. The primary input is a hardware trigger signal, which can be issued by Fermilab's Accelerator Division when a neutrino spill is due to arrive from the BNB or NuMI beams. The trigger board then issues a T1 trigger that is sent to all FEMs, which then record the PMT and TPC data in the NU stream as described in the previous sections.

In periods of no BNB activity, fake beam trigger signals are issued to record realistic cosmic backgrounds, which are referred to as beam-off or EXT data. Some of these are then later combined with simulated neutrino interactions to produce Monte Carlo (MC) simulations with realistic backgrounds. The PMT system also provides inputs to the trigger system. Additionally, there are three types of triggers used for calibration studies from the UV laser system, from the CRT, and from software-based triggers from the DAQ system.

In the DAQ system, a software trigger is also applied before triggered recordings are saved. It filters the hardware-triggered events, retaining only those with a high likelihood of containing neutrino interactions. The selection criteria require events to have a minimum light signal across all PMTs coincident with a beam spill. This filter reduces the amount of data that needs to be stored by two orders of magnitude [122].

5.6 Cosmic Ray Tagger

There is one additional component that was added to the detector later on. The CRT is an external subsystem designed to identify and reject cosmic ray muons that enter the TPC. The CRT consists of scintillation modules placed around the detector, except for the beam entry and exit faces due to space constraints. Each module contains plastic scintillator strips with wavelength-shifting fibres that guide scintillation light to silicon photomultipliers (SiPMs). The strips are arranged in two layers with perpendicular orientations to provide 2D position information. The output electronic signals are then processed by front end boards (FEBs). This system provides precise timing and

position information about tracks piercing the TPC and can be used to reject cosmic muons [123].

The CRT self-triggers but uses the hardware trigger as a reference point in time. To later match the recorded signals with the other data from the detector, the CRT and TPC both store GPS timestamps for any recordings. Data collection occurs via dedicated DAQ machines that process and store event information for later analysis. The CRT has been used for calibration studies, but given that the information is only available for the later Runs 3-5 of the experiment, most physics analyses do not incorporate the information directly.

5.7 Operation

MicroBooNE recorded data for five runs between 2016 and 2020, corresponding to 1.3×10^{21} protons on target (POT) from the BNB. During this time, MicroBooNE had to compensate for non-functioning components and changes in the detector, some of which are described below.

TPCs using wire planes are vulnerable to shorted or otherwise malfunctioning channels due to the large number of densely stacked wires in the anode. Following installation, approximately 10% of the channels in MicroBooNE are non-functional, as shown in Figure 5.15. These observations represent a snapshot in time, as reported in Ref. [106]. The number of faulty wires is largely stable, but there is fluctuation in some wires over time. Among the 516 ASICs, 14 are misconfigured, possibly due to electrostatic discharge during installation, but their channels remain usable with additional noise filtering. Additionally, six ASICs are not connected to wires due to installation errors, and 19 cannot be initialised in the cold argon, likely due to power circuit issues. Approximately 20 channels experience intermittent non-responsiveness due to periodic ASIC saturation. One V wire is in contact with multiple U wires, resulting in 287 non-functioning U channels, 259 without signal and 28 exhibiting high noise. This contact also leads to charge collection on U wires and a reduction in signal amplitude in the subsequent V and Y layers. A total of 126 Y channels are unusable due to shorting with V wires, 116 producing no signal and 10 exhibiting high noise. This causes ionisation electrons that would normally be collected by the Y plane to instead be collected by the V plane, resulting in unipolar signals on this plane. Furthermore, 36 additional high-noise channels are present that are not in proximity to shorted wires. The extent of the faulty channels is manageable, and 97% of the detector volume has coverage by two or more readout planes [106].

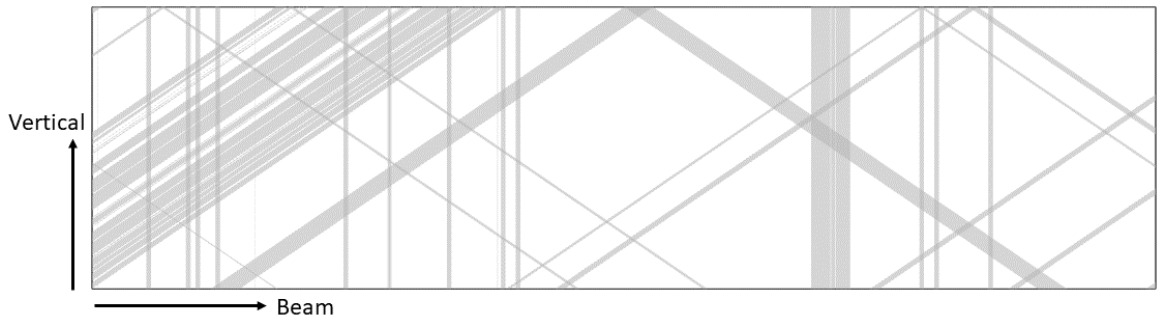

Fig. 5.15 Noisy and unresponsive wires in the anode cover 30% of the area. The regions with more than one faulty wire, e.g. overlapping unresponsive regions between the collection and one of the induction planes, is much smaller at 3%. Source: Ref. [124].

Additionally, one PMT became unresponsive after Run 2 [125]. The light yield in the detector also decreased on average by 25% during the first three runs of the experiment, as shown in Figure 5.16. This required some time-dependent corrections and additional uncertainties to be added, but had no real effect on the experiment's ability to record neutrino interactions. The cause of this has not been definitively determined [126].

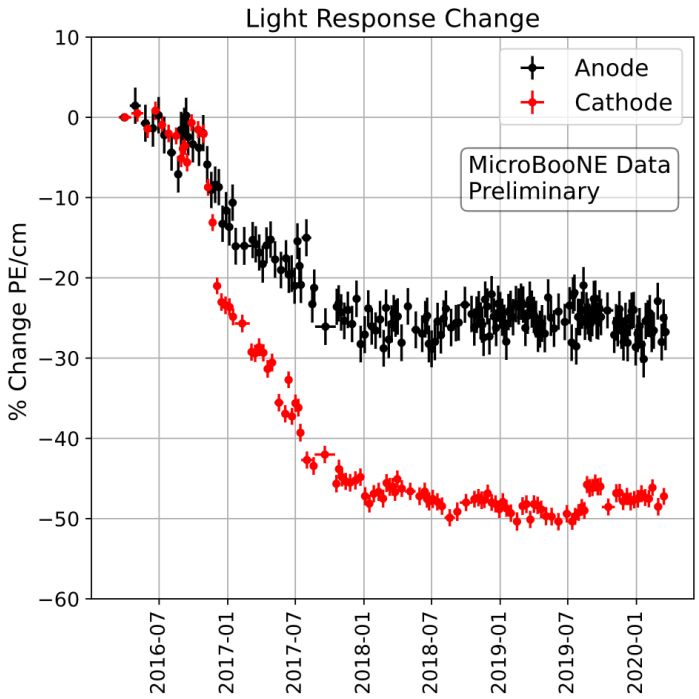

Fig. 5.16 Light yield from tracks at the anode and cathode in MicroBooNE decreasing over time. Source: Ref. [126].

There have also been intentional changes. Electronics upgrades after Run 1 significantly reduced noise for the TPC readout. The PMT threshold for the NuMI beam was adjusted to a lower value during Run 3. The CRT was installed halfway through the experiment.

Chapter 6

Simulation and Reconstruction

MicroBooNE's simulation and reconstruction pipeline is centred around the Liquid Argon Software (LArSoft) framework [127], which is developed across the different LArTPC experiments at Fermilab. The two sections of this chapter provide an overview of the MC simulation used to model events in the detector, followed by a summary of how simulated and data events are then reconstructed.

6.1 Simulation

The simulation of events in MicroBooNE starts with the modelling of the neutrino beam flux, followed by neutrino interactions, the transport of final-state particles, the detector response, and finally, the addition of cosmic-ray backgrounds.

6.1.1 Boosted Neutrino Beam Flux

The BNB flux simulation for MicroBooNE is adapted from the MiniBooNE experiment, situated in the same beam line and documented in Ref. [98], with additional constraints on $\pi^{\pm}$ and K^{+} production [97] from measurements taken by the Hadron Production Experiment (HARP) [128] and the SciBar Booster Neutrino Experiment (SciBooNE) [129]. It begins with the modelling of the incoming protons. Their spatial distribution is determined via a beam simulation using the TRANSPORT package [130], which was validated upstream by comparing its predictions with measurements made by beam profile monitors [131]. The main simulation uses the GEANT4 toolkit [132–134], version `8.1`, which models the final stretch of the BNB beam line, including the target hall and the decay pipe. For this, protons are generated with randomised positions and kinematics according to the determined beam characteristics. GEANT4

then step-by-step simulates the transport of particles, considering the current-induced fields of the magnetic focusing horn, interactions with matter, and decays that do not produce neutrinos.

The rates of hadronic interactions of protons, neutrons, and pions on beryllium and aluminium are governed by custom cross-section tables [98]. Other particle-nucleus interactions are handled by GEANT4 using the standard QGSP BERT configuration [134]. Final state configurations are also determined by GEANT4 with this configuration, except for the main interaction of incoming protons with beryllium, for which a custom set of double differential cross-section tables in longitudinal and transverse particle momentum is used. These tables are computed for meson production using different parameterisations dependent on the available data. A Sanford-Wang parameterisation [135], an empirical formula for modelling meson production from high energy proton-target collisions, is used to smoothly fit data from various incident proton energies for $\pi^{\pm}$ and K^0 production [98]. For K^+ production, data in the BNB proton energy range are sparse, so a different parameterisation is adopted to maintain a consistent cross-section shape across energies. This approach is based on Feynman scaling, which assumes that the inclusive hadron production cross section can be parameterised independent of the incident energy at high energies [136]. K^- and secondary nucleon production cross sections, due to a lack of experimental data in the relevant kinematic regions, are determined from predictions of the hadronic interaction package MARS [137]. Multiplicities and kinematics are randomly sampled from the probability distributions defined by these cross-section tables.

Finally, a custom decay model uses available branching fraction data and accounts for polarisation and kinematics of produced mesons and muons to compute their ultimate decays to neutrinos. The flux of neutrinos is then computed by projecting it onto a planar cross section of the detector volume at the required distance and position.

The predicted BNB neutrino flux at MicroBooNE, with the beam only operating in neutrino mode, is predominantly of muon flavour, with 93.7% being ν_μ and 5.8% being $\bar{\nu}_\mu$. There are smaller electron flavour contributions of 0.5% for ν_e and 0.05% for $\bar{\nu}_e$. The flux prediction is shown in Figure 6.1. Of the muon neutrinos arriving at MiniBooNE and MicroBooNE, $\sim 97\%$ come from the decay of π^+, followed by $\sim 3\%$ produced via K^+, and only negligible contributions from other mesons, led by K^0. $\bar{\nu}_\mu$ is dominated by π^- decay at $\sim 90\%$, followed by $\sim 5\%$ coming from muon decays following a $\pi^+ \to \mu^+$ decay and smaller kaon contributions. Mainly muon and kaon decays contribute to ν_e and $\bar{\nu}_e$ production [98].

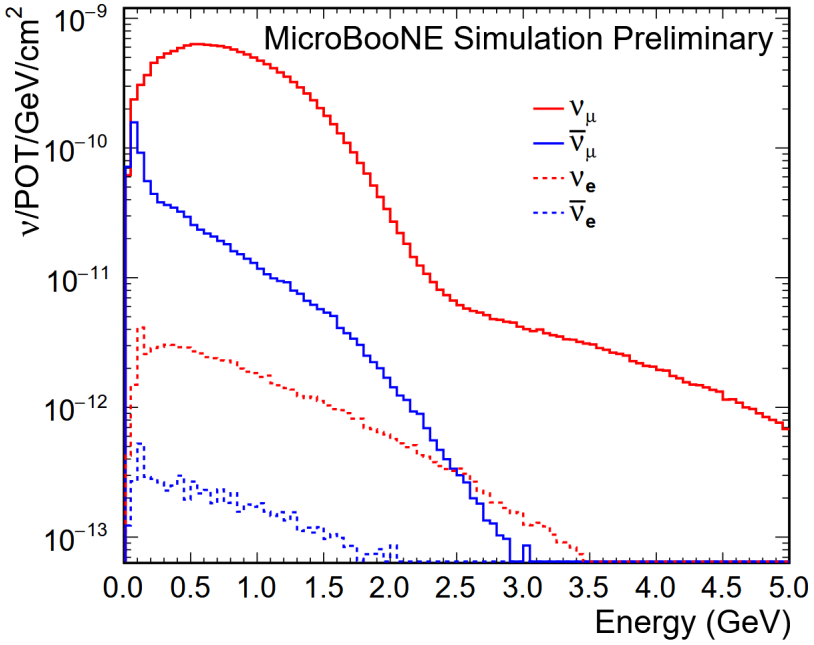

Fig. 6.1 Neutrino flux for muon and electron (anti-)neutrinos arriving at the MicroBooNE detector. Source: Ref. [97].

6.1.2 Event Generation

A tuned configuration of the neutrino MC generator GENIE [138, 139], version `3.0.6`, is used to simulate neutrino interactions across all MicroBooNE analyses, according to the predicted flux. It uses a custom MicroBooNE tune [140] that is based on the model configuration `G18_10a_02_11a`. A summary of the physics model, referred to throughout this thesis as GENIE `G18`, is provided in Table 6.1. The tuned version constrains CC QE and CC MEC interactions with data from T2K. The effect of this tuning is minimal for the signal prediction of the single charged pion analysis, but it does affect predicted backgrounds, which are rich in pionless CC events. This section gives an overview of the internal models used in this GENIE configuration, as well as differences with a newer DUNE/Short-Baseline Near Detector (SBND) model set `AR23_20i_00_000` produced with GENIE version `3.04.02` and referred to as GENIE `AR23` as well as alternative generators: Giessen Boltzmann-Uehling-Uhlenbeck (GiBUU) `2023` (Patch 3) and the new version `2025` (Patch 1) [141], NEUT version `5.4.0.1` [142] and the Wrocław Neutrino Generator (NuWro) version `21.09.2` [143].

	G18_10a Model Set
Nuclear ground state	Local Fermi Gas
Quasi-elastic	València QE [144, 145] with dipole $F_A(Q^2)$
2p2h	València 2p2h [146]
Resonance	Kuzmin-Lyubushkin-Naumov Berger-Sehgal [147–150]
Shallow and deep inelastic	Bodek and Yang [151]
Coherent π	Berger-Sehgal [152]
Hadronisation	Andreopoulos-Gallagher-Kehayias-Yang [153]
FSI	INTRANUKE hA18 [154]

Table 6.1 Comprehensive model configuration for GENIE *G18_10a* as used by MicroBooNE.

6.1.2.1 Nuclear Ground State

The simulation of neutrino-nucleus interactions begins with a model of the target nucleus in its ground state. The properties of this state, particularly the momentum, spatial distribution, and separation energy of the nucleons, play a central role in accurately modelling the kinematics of outgoing particles.

The impulse approximation is an approach used to model neutrino-nucleus scattering by assuming that the neutrino interacts with a single bound nucleon inside the nucleus, while the remaining nucleons act as passive spectators [155]. In this approximation, the outgoing nucleon is described as a free particle, meaning it does not undergo any further interactions with the residual nucleus as it exits. This approach neglects both final state interactions and nucleon-nucleon correlations, thereby simplifying the calculation by factorising the nuclear cross section into an independent lepton-nucleon interaction and a nuclear structure model that describes the momentum and energy distribution of bound nucleons. The underlying assumption is that the nucleus can approximately be treated as a collection of independently scattering bound nucleons, and requires that the four-momentum transfer mediated by the exchanged $W^{\pm}$ or Z boson is sufficiently large for its wavelength $\lambda \sim 1/|q|$ to resolve individual nucleons rather than interact

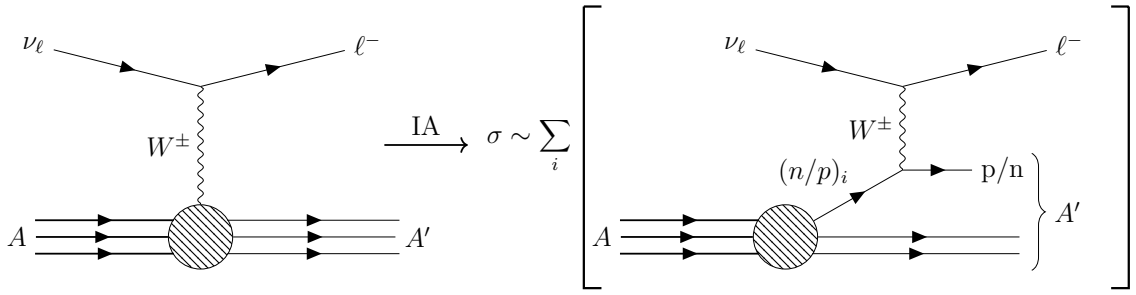

Fig. 6.2 Feynman diagram showing a CCQE neutrino interaction with a nucleus on the left, and the same interactions factorised into the sum of individual nucleon contributions using the impulse approximation on the right.

coherently with the whole nucleus [156]. This factorisation is illustrated in Figure 6.2. The QE cross section on a free nucleon $\sigma_{\nu\mathrm{N}}$ from Equation (3.1) can then be used to estimate the cross section for the interaction with a nucleus as

$$\frac{\mathrm{d}\sigma_{\mathrm{IA}}}{\mathrm{d}\omega\ \mathrm{d}\Omega} = \int \mathrm{d}^3\vec{p}\mathrm{d}E_{\mathrm{sep}}\ P(\vec{p}, E_{\mathrm{sep}})\ \frac{\mathrm{d}\sigma_{\nu\mathrm{N}}}{\mathrm{d}\omega\ \mathrm{d}\Omega}, \tag{6.1}$$

where, rather than a sum over fixed initial nucleon states, the spectral function $P(\vec{p}, E_{\mathrm{sep}})$ gives the continuous probability density of finding a nucleon with momentum $\vec{p}$ and separation energy E_{sep} inside the nucleus [155].

A commonly used approach to model the kinematic distribution of the nucleons described by the spectral function relies on Fermi gas models. GENIE `G18` uses a local Fermi gas (LFG) model described by the València group as part of their QE+MEC model [144–146]. LFG models represent an evolution from the earlier relativistic Fermi gas (RFG) models, which describe the nucleus as a sphere of uniform nucleon density filled with non-interacting nucleons which occupy momentum states up to a fixed global Fermi momentum k_F^N for protons and neutrons $N \in \{n, p\}$, in accordance with the Pauli exclusion principle. LFG models still treat the nucleons as non-interacting particles and avoid modelling the complex intranuclear dynamics, but use a local density approximation to account for the spatial distribution of nucleons within the nucleus. In these models, local nucleon densities for neutrons and protons $\rho_N(r)$ are used to define position-dependent Fermi momenta, which for the argon model in GENIE use two-parameter Fermi distributions [144]:

$$\rho_N(r) = \frac{\rho_N(0)}{1 + \exp\left(\frac{r-R}{a}\right)}, \tag{6.2}$$

where $\rho_N(0)$ is the central density, R is the half-density radius, and a characterises the surface diffuseness. The local Fermi momentum is then given by [144]:

$$k_F^N(r) = [3\pi^2 \rho_N(r)]^{1/3}, \tag{6.3}$$

which in turn determines the maximum momentum available to nucleons at each point within the nucleus. Pauli blocking is applied to prevent outgoing nucleons from occupying already filled states below $k_F^N(r)$.

6.1.2.2 Quasielastic Scattering

Neutrino generators employ several QE scattering models. GENIE `G18` and NEUT have implementations based on the València model. GENIE `AR23` uses a superscaling approach based on SuSAv2 [157]. NuWro relies on the Llewellyn Smith model with random phase approximation (RPA) corrections [158]. GiBUU uses its own model together with its Boltzmann-Uehling-Uhlenbeck (BUU) transport simulation [141].

Accounting for nuclear effects is the main challenge in QE modelling, as it is necessary to accurately predict both the cross section and the kinematic properties of the outgoing particles. These properties are more sensitive to the modelling of the nuclear ground state than in higher-energy interactions such as DIS. The València model employs several corrections:

- **Random Phase Approximation:** The València model enhances the simple picture of non-interacting nucleons in the LFG model by including long-range correlations treated using RPA. When a neutrino interacts with a nucleon inside the nucleus, the interaction is modified by the surrounding strongly interacting nucleons. The dominant impact is a suppression of the axial nuclear response, leading to a reduction in the predicted QE cross section. This effect is most pronounced at low four-momentum transfer [144].

- **Nuclear Binding Energy Corrections:** In the Fermi gas model, infinitesimally small energy transfers suffice to lift a nucleon into an unoccupied state and produce a 1p1h excitation. However, real nuclei have an energy gap due to a minimum required excitation energy. This requirement is imposed in an ad hoc manner using experimental measurements of this minimum energy and is most relevant for low-energy neutrino interactions [144].

- **Coulomb Corrections:** Coulomb distortions of interactions occur due to the charged lepton in CC neutrino interactions propagating in the Coulomb field

of the nucleus. This results in an enhancement of cross sections for neutrino processes and suppression for antineutrino processes and is accounted for by modifying the outgoing lepton energy and momentum [144].

6.1.2.3 Meson Exchange Currents

The neutrino event generators employ different MEC models: GENIE `G18` and NEUT use the MEC treatment described by the València model [144–146], while the GENIE `AR23` configuration uses the SuSAv2 MEC approach [157]. NuWro uses the MEC component of the València model [144–146]. GiBUU has its own implementation of MEC contributions within its BUU transport framework [141].

The València MEC model calculates CC interactions in which a $W^{\pm}$ is absorbed by nucleons coupled via the exchange of a virtual meson. It provides predictions for the cross section as a function of the energy and momentum transferred from the lepton system to the nucleus, incorporating the same corrections described for QE scattering.

6.1.2.4 Resonance Production

Resonance production in the various generators is handled as follows. GENIE and NEUT employ the Kuzmin-Lyubushkin-Naumov Berger-Sehgal (KLM-BS) model [147–150], which is a substantial update to the long-used Rein-Sehgal (RS) model [159]. The RS model predicts the production of 16-18 distinct resonances, depending on the implementation. The KLM-BS model builds upon this by, among other things, more carefully accounting for the impact of the non-zero mass of the final-state lepton. This is important for accurately describing the cross section at low Q^2. NuWro calculates resonance cross sections using the Adler–Rarita–Schwinger formalism [160] for only the $\Delta(1232)$ resonance, which dominates at accelerator neutrino energies. GiBUU models resonance production according to the Mainz Unitary Isobar Model (MAID) [161, 156].

To accurately predict the kinematics of pion production, generators also need to consider non-resonant (also called background) contributions. These are possible tree-level Feynman diagrams without a resonance. An example of these is a nucleon-pole diagram, where an off-shell nucleon propagates before emitting a pion and going on-shell [162]. Contributions from these channels are small, but do have an impact on the kinematics of the pion predictions [163].

6.1.2.5 Shallow and Deep Inelastic Scattering

GENIE, NuWro, and NEUT all employ the Bodek-Yang (BY) model for DIS [151], which is an effective leading order parton model that starts from existing parton distribution functions obtained from global fits to data and introduces modifications to extend their validity to GeV-scale neutrino interactions. The SIS region, where interactions transition from RES to DIS is one of the least constrained parts of neutrino-interaction generators and shows significant variation between generator implementations [164]. In GENIE, after the primary neutrino-quark interaction, hadronisation is handled using the hybrid Andreopoulos-Gallagher-Kehayias-Yang (AGKY) model [165], which, depending on the hadronic invariant mass, uses the empirical Koba-Nielsen-Olesen (KNO) model [166] or relies on the PYTHIA generator [167]. GiBUU simulates inelastic processes with its own custom model [141].

6.1.2.6 Coherent Pion Production

Coherent pion production is treated using the coherent Berger-Sehgal (BS) model [152] in GENIE, NuWro and NEUT. It leverages the PCAC theory, which connects forward neutrino scattering to pion-nucleon cross sections and uses available pion scattering data to constrain uncertainties [152]. GiBUU does not simulate coherent interactions.

6.1.2.7 Final State Interactions

One of the main sources of uncertainty in neutrino-nucleus scattering is that there is not a one-to-one relation between particles produced in the initial scattering and the particles exiting the nucleus. Hadrons can undergo a variety of further final-state interactions (FSI) inside the residual nucleus. For instance, a pion produced in a resonance interaction can undergo (multiple) further interactions such as elastic or inelastic scattering, charge exchange (e.g. $\pi^+ + n \to \pi^0 + p$), pion absorption, or pion production. An illustration of this is shown in Figure 6.3. To correctly reconstruct neutrino energies, experiments need to account for the produced visible final state particles. FSI alter the energy and momentum of outgoing particles. They can also change the number of final-state particles, resulting, for instance, in QE interactions with a final state pion or a resonance interaction without a pion appearing like a QE interaction.

Many generators employ intranuclear cascade (INC) models for handling FSI. These vary greatly but all begin with the hadrons produced at the interaction vertex and then use a mean free path for the hadron's propagation inside the nucleus, determined

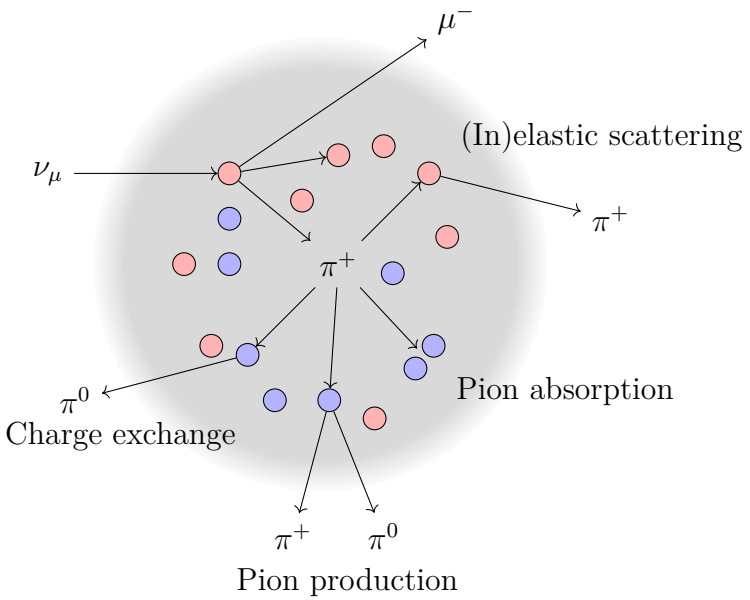

Fig. 6.3 Illustration of several final state interactions on neutrons and protons that a charged pion produced in the nucleus can undergo.

from their total cross section with nucleons. For example, given the total cross section of a pion with nucleons and the nucleon density in the nucleus, the mean free path is [168]

$$\lambda(E, r) = \frac{1}{\sigma^{\text{tot}}_{\pi^+ N}(E)\rho(r)}. \tag{6.4}$$

Using a MC method, the particle can then be propagated in small steps ($\Delta l \ll \lambda$) with an interaction probability at each step given by $\Delta l/\lambda$. If an interaction occurs, the type is randomly chosen based on partial cross sections. This is repeated for the outgoing particles until all are absorbed or have exited the nucleus [1].

The impulse approximation is used to model the neutrino–nucleus interaction. However, further simplifications are employed in neutrino generators to manage the computational complexity of propagating resulting hadrons. These include treating particles as having sharply defined energies and momenta, and neglecting the inherent width of their spectral functions and broadening effects such as short-range correlations. The nuclear density distribution is assumed to remain invariant during the reaction. Interactions are modelled only with stationary nucleons, neglecting interactions among ejected particles. Lastly, the free particle approximation assumes nucleons within the nucleus are not bound by a potential and travel in straight-line trajectories between collisions, with binding energy effects introduced separately. This contrasts with models like GiBUU, which directly simulate binding potentials [156]. In general, GiBUU aims

for a less classical treatment of FSI by relying on a transport model that uses the BUU equations to propagate hadrons through the nuclear medium and incorporates more nuclear properties directly into the simulation, rather than relying on ad hoc corrections.

All GENIE configurations considered in this analysis employ the `hA2018` FSI model, which is a data-driven, effective intranuclear cascade model. Unlike the full cascade simulations in NuWro and NEUT, which explicitly propagate hadrons step by step through the nuclear volume as described above, `hA2018` parameterises the net effect of FSI in what is effectively a single propagation step. For each produced hadron, the mean free path is used to compute a probability for it to undergo one or more interactions before exiting the nucleus. If an interaction is deemed to occur, the specific final state (e.g. elastic scatter, charge exchange, absorption, or pion production) is chosen probabilistically based on measured branching fractions for hadron-nucleus scattering [168].

6.1.3 Particle Transport

After GENIE generates the list of final-state particles emerging from the struck argon nucleus, GEANT4 propagates them through a detailed model of the detector and its surroundings. It handles relevant physical processes that particles undergo as they traverse matter, including continuous energy loss for charged particles via ionisation and excitation, scintillation light production, trajectory deflection via MCS, secondary interactions of hadrons on argon nuclei, the decay of unstable particles, and the modelling of electromagnetic showers.

6.1.4 Detector Response Simulation

GEANT4 is not used to simulate the drifting of the ionised electrons or the propagation of scintillation light in MicroBooNE. Instead, the final stage of the simulation involves converting the produced energy depositions and photons into the raw electronic signals that would be recorded by the LArTPC wires and PMTs.

The Modified Box Model [169] is used to describe electron-ion recombination and determine the fraction of ionisation charge that escapes and drifts towards the detection wires. It is modelled as:

$$R = \frac{1}{\xi}\ln(\alpha + \xi), \quad \text{with } \xi = \beta \left(\frac{\mathrm{d}E}{\mathrm{d}x}\right), \tag{6.5}$$

where $\alpha < 1$ and β are empirical parameters tuned to data. In simulation, this is applied by computing the deposited charge per unit length as a function of the change in energy per unit length:

$$\frac{\mathrm{d}Q}{\mathrm{d}x} = \frac{R}{W_{\mathrm{ion}}} \left(\frac{\mathrm{d}E}{\mathrm{d}x} \right) \tag{6.6}$$

with $W_{\mathrm{ion}} = 23.6\,\mathrm{eV}$ is the average ionisation energy of liquid argon [170]. This allows conversion from energy loss to collected charge, accounting for recombination.

LArSoft uses a dedicated detector simulation to model the electric field response produced by the ionisation electrons. The simulation includes a detailed model of the detector's electric field and electronics response, including amplification, shaping, noise filtering, and deconvolution, to produce realistic digitised waveforms for each wire.

The optical system is simulated using a lookup table to provide the probability of a photon produced by GEANT4 at a given position in the detector reaching a PMT. The table is created using a full GEANT4 simulation of photons in the detector. The lookup table approach is used as a full simulation that keeps track of all scintillation photons for each event is currently computationally unfeasible. Convolutions with real recorded single-photon PMT responses are used to realistically model the effects of the electronics and are combined with additional noise and modelling of the digitisation process [171].

6.1.5 Overlaid Backgrounds

MicroBooNE records interactions for which the neutrino beam timing coincides with the detection of scintillation light. Since the MicroBooNE detector is surface-based, there are significant backgrounds from outside the detector that are included. To generate more realistic MC event samples, MicroBooNE models these background interactions using an overlay technique. In this approach, the simulated neutrino interactions are superimposed onto real data events that were recorded during periods with the beams turned off. This way the simulation inherits an accurate model of not only the cosmic-ray background, but also all ambient detector noise at the time of recording.

6.1.6 Prediction Samples

Neutrino MC samples, as described above, consist of simulated neutrino interactions and overlaid background data. These MC samples are the core of the predicted

interactions. Two additional sample types are included to correctly model beam spills that do not produce a neutrino interaction in the detector. The first is pure beam-off background recordings without simulated interactions, accounting for mistriggering due to cosmic-ray backgrounds. The second is simulated neutrino interactions occurring outside the cryostat in the surrounding structures and rock, whose particles travel into the detector. This also has beam-off backgrounds overlaid, and the sample type is referred to as 'dirt'.

An alternative neutrino MC prediction has also been produced by the collaboration using NuWro instead of GENIE, but otherwise following the same production pipeline, including the overlaying of real backgrounds. This is used for validation and uncertainty estimation.

Finally, to quantify systematic uncertainties due to the modelling of the detector, detector variation samples have been produced by the collaboration. These vary parameters of the detector model and will be described in Section 8.2.4.

6.2 Reconstruction

The event reconstruction pipeline is the bridge between the raw electronic signals produced by the detector and the high-level physics quantities used in analyses. This section provides a summary of the Pandora-based reconstruction workflow, tracing the path from raw detector waveforms to the final data products. The entire process is applied to both MC events and real detector data.

6.2.1 Low-level Reconstruction

The first stage of the reconstruction is the processing of the signals from the TPC readout wires and the PMTs. The raw TPC wire signals are contaminated with various sources of excess noise, which is in addition to the irreducible electronics noise planned for in the detector design. The sources of this have been categorised as low-frequency noise from voltage regulators, harmonic noise from the high-voltage power supply for the cathode, and position-dependent bursts of noise, possibly originating from another power supply [106]. Using the coherence of the low-frequency noise between different channels and the narrow frequency peaks of the harmonic noise, these are corrected for. The burst noise is reduced to acceptable levels without additional filtering by the signal processing pipeline. An example of an event display with and without noise filtering applied is shown in Figure 6.4.

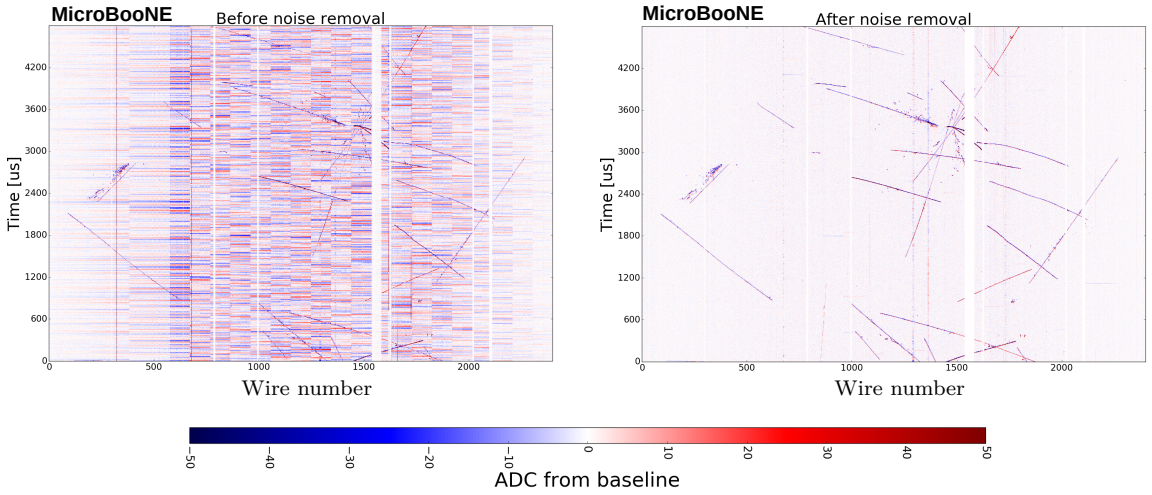

Fig. 6.4 Event display from the second induction plane showing the raw signal as the baseline-subtracted ADC data on the left and the noise-filtered version on the right. Source: Ref. [106].

The signal measured on a TPC wire is the convolution of the true spatial and temporal distribution of drifting ionisation electrons with the wire plane's field response and the readout electronics response. The purpose of deconvolution is to invert this convolution process, recovering a waveform that best represents the original ionisation charge distribution as a function of time. MicroBooNE employs 2D deconvolution techniques that correct for signal induction effects across neighbouring wires over time [172].

Following deconvolution, the next step is to identify discrete charge depositions, or 'hits'. Algorithms scan the processed waveforms to locate region of interest (ROI) likely to contain genuine signals. Within each identified ROI, a hit-finding algorithm searches for local maxima and fits a Gaussian to each peak. The resulting calorimetric hits represent localised charge depositions, characterised by their wire number, peak time, and integrated charge [172].

In addition to the TPC charge readout reconstruction, the light information from the optical system is processed to provide timing information for each event. Light detected by the PMTs is grouped into flashes, which represent bursts of scintillation light from particle interactions. These flashes are used to determine when an interaction occurred, which is essential for reconstructing the position of the event within the detector.

6.2.2 High-level Reconstruction with Pandora

Following low-level signal processing, the collections of calorimetric hits and flashes are passed to one of three high-level reconstruction frameworks: Pandora [173, 174], Wire-Cell [175, 124], or a deep-learning-based approach [176]. Their main role is to group the lists of discrete hits into coherent structures for each wire plane, use that to reconstruct charged particles in 3D, and ultimately produce a hierarchical description of particles in the event. This section focuses only on the Pandora pattern-recognition framework, which is both the most widely used of the three and the one used in the analysis described in this work.

Pandora is a software development kit to built reconstruction pipelines for fine-grained detectors, but is mainly used with LArTPCs. It uses a multi-algorithm approach in which a large number of task-specific algorithms are combined to reconstruct events. At the heart of the Pandora reconstruction is the grouping of hits in each readout plane into clusters associated with individual particles. By comparing the reconstructed clusters between the different planes, the interactions are reconstructed in 3D. The Pandora reconstruction flow in MicroBooNE employs a two-pass strategy to reconstruct and separate cosmic-ray muons and neutrino interactions. The first pass of the reconstruction utilises the `PandoraCosmic` algorithm chain, which is optimised for reconstructing long tracks characteristic of cosmic-ray muons. Following this first reconstruction pass, hits from unambiguous cosmic muon tracks are set aside and not considered in subsequent reconstruction steps.

The remaining collection of hits is then used as input to the second pass, which uses the `PandoraNu` reconstruction chain. It starts by running some of the same 2D and 3D reconstruction algorithms used in `PandoraCosmic`. The 3D hits are then separated into 'slices' that represent topologically distinct collections that could contain a neutrino interaction. Each slice is then reconstructed under both cosmic-ray and neutrino interaction hypotheses. The latter also includes estimating a 3D neutrino interaction vertex. This produces sets of reconstructed particles organised according to which particle originates from which other. A support vector machine (SVM) trained on a range of reconstructed event features, including particle multiplicity, spatial orientations, and the position of the reconstructed interaction vertex within the detector, scores each slice on a scale from 0 for cosmic-like to 1 for neutrino-like. This score, along with information from the optical flashes, is used to identify the most probable neutrino interaction slice. An example of a reconstructed simulated CC muon neutrino event is shown in Figure 6.5.

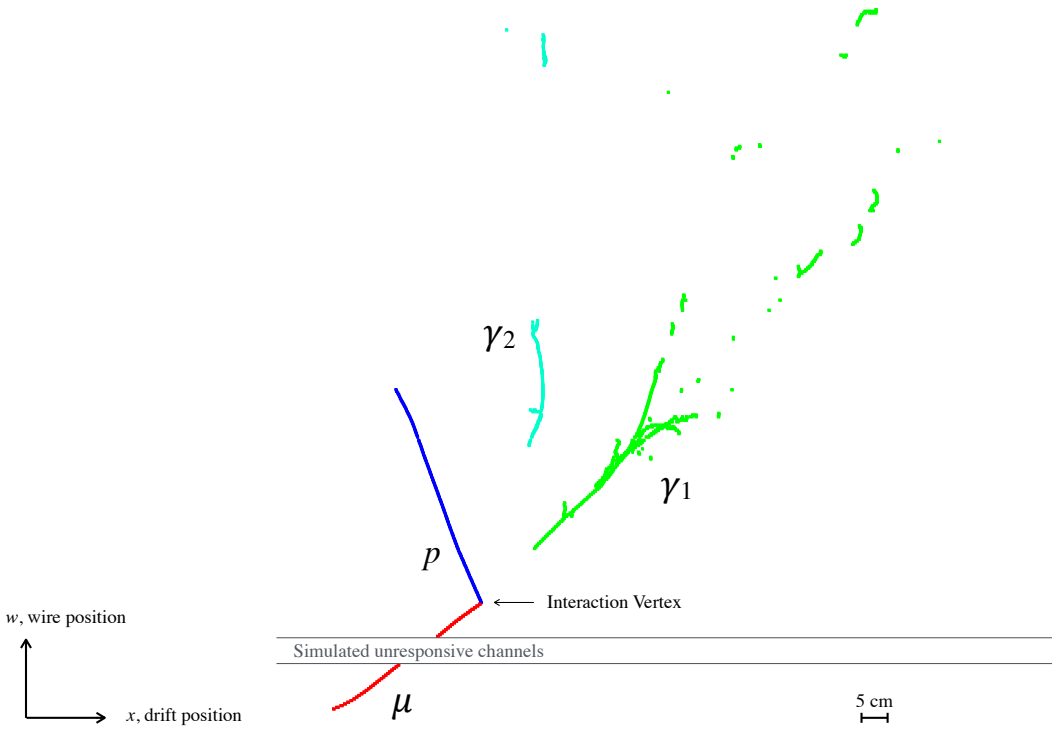

Fig. 6.5 Pandora-reconstructed simulated neutrino event with colour-coded clusters in one readout plane. It shows four correctly reconstructed particles, two tracks and two electromagnetic showers coming from the decay of a π^0. Source: Ref. [174].

6.2.3 Calibration

After pattern recognition, a set of calibrations is applied to the reconstructed particles. Using long anode-cathode-piercing cosmic muon tracks, position-dependent $\mathrm{d}Q/\mathrm{d}x$ corrections are determined for the drift direction x of the detector and separately for the xz plane. This corrects for effects of space charge, cross-connected TPC wires, electron attenuation, and diffusion. Separately, and only for data, changes in charge deposition $\mathrm{d}Q/\mathrm{d}x$ are corrected as a function of time to account for longer-term effects such as variations in argon purity. This is not done for the simulation, which is constant in time [110].

The conversion between ADC readout values to true electron numbers is calibrated using stopping muons from neutrino interactions in MicroBooNE in the framework of the Modified Box Model [169] and separately checked using proton tracks. The resulting measurement of change in deposited charge per unit length $\mathrm{d}Q/\mathrm{d}x$ is used to estimate the energy loss per unit length $\mathrm{d}E/\mathrm{d}x$ of particles.

An inverse of the space charge applied to simulated events can also be applied after reconstruction to both data and MC events to correct the spatial distortions caused by

changes in the electric field of the detector. This is relevant, for instance, for estimating momentum from the length of tracks.

6.2.4 Data Reduction

The final stage of the data processing pipeline is the distillation of the vast information from the reconstruction into a format optimised for physics analysis. For this analysis, this is the 'PeLEE' ntuples, which contain a large set of particle- and event-level variables, many of which were originally created for one of MicroBooNE's low energy excess (LEE) searches [177].

Chapter 7

Signal Definition and Selection

7.1 Motivation

A precise understanding of neutrino-nucleus interactions is essential for the success of current and future neutrino oscillation experiments. Uncertainties in modelling interactions limit the precision with which oscillation parameters can be determined, impacting the search for CP violation in the lepton sector and efforts to test for physics beyond the Standard Model [178, 34, 179]. At the energies relevant to accelerator neutrino oscillation experiments, theoretical models continue to face significant challenges, including the previously described treatment of nuclear structure, multi-nucleon processes, and FSI.

Cross-section measurements play a key role in improving these models and in reducing uncertainties for current and future neutrino experiments [180]. Argon is the target material used in several current and future TPC neutrino oscillation experiments. Specifically, the long-baseline experiment DUNE [181] and the SBN program [182] at Fermilab rely on this detector technology for their precise particle tracking and calorimetry.

MicroBooNE has collected an extensive data set of neutrino interactions on argon. This work leverages this data to measure muon neutrino charged-current single charged-pion production (CC1$\pi^{\pm}$) cross sections. Previously, MicroBooNE has published results for π^0 production in NC and CC neutrino interactions [183–186], as well as CC ν_e and $\bar{\nu}_e$ $\pi^{\pm}$ production [187]. Improving CC pion production models is important, as these interactions dominate at energies relevant to experiments such as NOvA [34] and DUNE [188].

7.2 Signal Definition

A key consideration in any neutrino cross-section measurement is the definition of the signal process. In neutrino-nucleus scattering, the final-state can be significantly modified by nuclear effects as described in Section 6.1.2.7. This means that the observable final state may differ from the one produced at the interaction vertex. As a result, there are two common approaches to defining a signal: interaction-based and topological.

Interaction-based definitions specify the signal in terms of the underlying neutrino interaction mode, such as charged-current pion production. These definitions allow direct association with individual theoretical models (e.g. for resonance production) and make comparisons between measurements and models fairly straightforward for theorists. However, this requires measurements to be corrected for nuclear effects and introduces a large dependence on the FSI model used [188].

By contrast, topological definitions describe the signal in terms of the observable final-state particles, meaning the particles that exit the nucleus which can be detected. The downside of this approach is that comparisons between different measurements and simulations are more challenging, as all possible interaction paths producing the same set of final states must be considered and modelled in comparisons. While this does not avoid the complexities of modelling FSI, it shifts them to the comparisons between measurements and simulation. This reduced model dependence of the measurement makes it more robust to future developments in generator modelling and increases its long-term utility. Figure 7.1 illustrates how different interactions contribute to a topological signal definition for charged-current pion production.

This analysis adopts a topological definition of the CC1$\pi^{\pm}$ signal, requiring one (anti-)muon, one charged pion, and any number of nucleons:

$$\overset{(-)}{\nu}_{\mu} + \mathrm{Ar} \rightarrow 1\mu^{\pm} + 1\pi^{\pm} + \mathrm{X} \tag{7.1}$$

where X represents the residual nucleus and the nucleons.

Without a magnetic field, MicroBooNE cannot distinguish between π^{+} and π^{-}. Moreover, $\bar{\nu}_{\mu}$ interactions are included as part of the signal, although their presence in the BNB is small, as described in Section 6.1.1. To be considered a signal event, the neutrino interaction vertex must additionally be contained within a specified fiducial

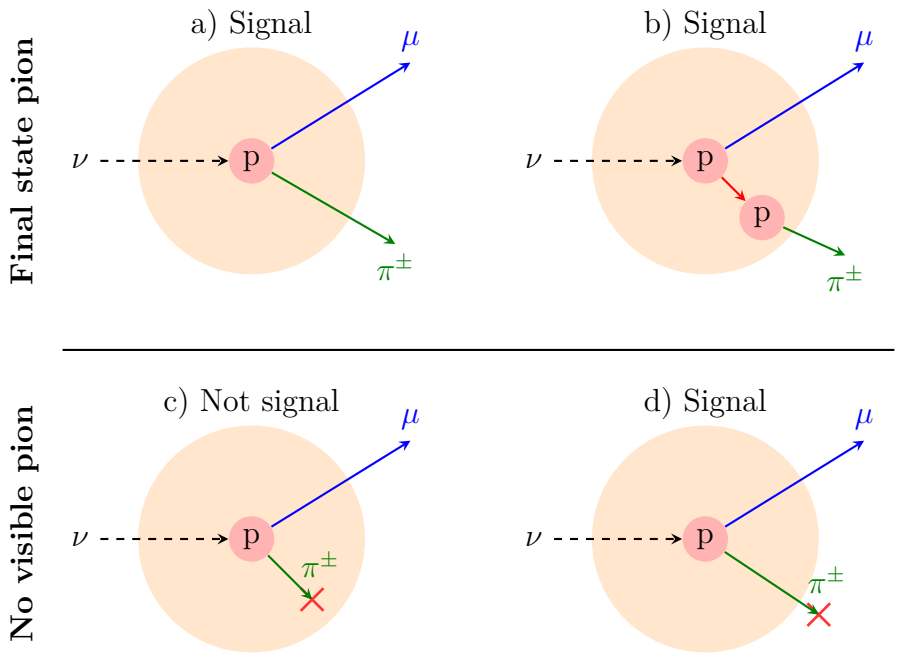

Fig. 7.1 Topological signal definition for CC single charged pion production. The shown processes are: (a) A pion exits the nucleus and is visible in the detector. (b) A pion is produced inside the nucleus via final state interactions and exits. (c) A pion produced at the vertex is absorbed before exiting. (d) A pion exits the nucleus and is quickly absorbed in the detector medium. This illustration ignores phase-space restriction that may result in any of these events not counting as signal.

volume of the detector. This volume is defined as:

$$\begin{aligned} 10\,\text{cm} \leq x \leq 246.35\,\text{cm}, \\ -106.5\,\text{cm} \leq y \leq 106.5\,\text{cm}, \\ 10\,\text{cm} \leq z \leq 986.8\,\text{cm}, \end{aligned} \tag{7.2}$$

providing a 10 cm gap away from the active TPC boundaries on all sides, except for the downstream end, where the distance is extended to 50 cm.

Furthermore, signal events are only those within the defined phase space:

$$\begin{aligned} \text{Muon momentum: } p_\mu > 150\,\text{MeV}, \\ \text{Pion momentum: } p_\pi > 100\,\text{MeV}, \\ \text{Muon-pion opening angle: } \theta_{\mu\pi} < 2.65\,\text{rad}. \end{aligned}$$

The lower limit on the particle momenta comes from minimum length requirements for their selection and momentum estimation. In particular, short reconstructed charged

pion tracks in the few-centimetre range tend to be dominated by incorrectly merged Michel electron tracks. Michel electrons originate from the decay chain $\pi^{\pm} \to \mu^{\pm} \to e^{\pm}$ and can add additional charge at the end of a reconstructed track when not reconstructed properly. The opening-angle phase space restriction excludes back-to-back muon-pion pairs, which are challenging to distinguish from long cosmic muon tracks and result in a phase space region with few signal events but high background contamination. These requirements are justified in Section 7.6.3.

7.3 Kinematic Variables

Reporting cross sections in terms of interaction quantities such as the squared four-momentum transfer Q^2, the energy transfer ω, or the neutrino energy E_ν is beneficial from a phenomenological perspective, as these variables are closely connected to the theoretical description of neutrino-nucleon interactions and offer direct physical insights when comparing data to predictions from interaction generators. However, such quantities cannot be directly measured in neutrino experiments. Their reconstruction depends on knowledge of the incoming neutrino energy, which is not known on an event-by-event basis and must be measured itself. Due to the presence of undetectable particles such as neutrons or charged particles below the detection threshold, this estimation necessarily involves model assumptions, introducing a degree of model dependence [188].

Observables that can be measured directly in the detector, avoiding this model dependence, are preferred. In comparisons between measured differential cross sections and simulations, it is then the responsibility of the generator models to provide accurate predictions for the kinematics of these observables. By focusing on such quantities, the resulting measurements again are more robust to future developments in generator modelling, thereby increasing their long-term utility. This analysis presents five single-differential cross-section measurements, in addition to an integrated total cross section. The kinematic variables are:

Muon angle, θ_μ: the angle between the initial direction of the muon outside the nucleus and the beam axis.

Pion angle, θ_π: the angle between the initial direction of the charged pion outside the nucleus and the beam axis.

Muon-pion opening angle, $\theta_{\mu\pi}$: the angle between the initial muon and pion directions outside the nucleus.

Muon momentum, p_μ: the initial momentum of the muon outside the nucleus.

Pion momentum, p_π: the initial momentum of the pion outside the nucleus.

The angles are taken from the Pandora 3D reconstructed particles and illustrated in Figure 7.2. The momentum of tracks that stop in the detector could be obtained by converting the deposited charge dQ/dx along the track length into an estimate of the energy loss $\mathrm{d}E/\mathrm{d}x$, as described in Section 6.2.3. However, due to detector effects such as the angular dependence between the track direction and the wire orientation, reconstruction errors, and calibration challenges, MicroBooNE relies on fitted functions of the track range, which map the distance a particle travels before coming to rest to its momentum [189]. The range is the direct line distance between the start and end points of a track, ignoring any track curvature. This assumes that particles slow down approximately linearly and requires them to come to rest. This works well for muons but not for hadrons, such as charged pions, which may undergo hadronic inelastic interactions.

Charged particles traversing a medium also undergo MCS, which are multiple small-angle deflections due to Coulomb interactions with nuclei. The deflections depend on a particle's momentum and can be used to estimate the momentum from a track that has been three-dimensionally reconstructed [190, 191]. MicroBooNE uses this to estimate the momentum of long muon tracks that are not fully contained in the detector, where using the range of the track is not an option [189].

This analysis uses a subset of fully contained events for the muon momentum estimation, avoiding the use of MCS, described later in Section 7.6.5. The charged pion momentum is estimated from the travelled range as well and also requires additional steps. Charged pions frequently scatter on the argon and can lose energy in invisible ways such as exciting a nucleus and producing free neutrons. Additionally, they may undergo further interactions such as charge exchange, absorption, or decay before coming to rest. For this reason, a subset enriched in unscattered pions is selected in Section 7.6.4 using a BDT-based approach [192], which aims to select charged pions without visible scattering that come to rest in the detector before decaying.

7.4 Prior Measurements

A previous CC single charged pion production cross-section measurement on argon has been made using the 0.24-ton active-mass Argon Neutrino Teststand (ArgoNeuT) detector at Fermilab [193] using 1.25×10^{20} POT in the higher-mean-energy NuMI

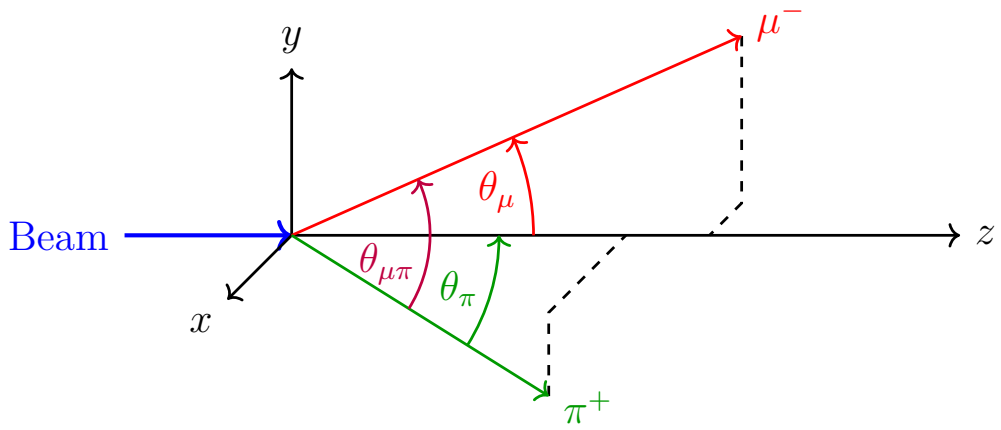

Fig. 7.2 Schematic of a charged-current pion production event, showing the outgoing muon and pion trajectories relative to the incoming neutrino beam. The angles θ_μ, θ_π and $\theta_{\mu\pi}$ are the muon–beam, pion–beam and muon–pion opening angles, respectively.

beam [101]. That experiment measured CC1$\pi^\pm$ interactions for beams in neutrino and antineutrino mode separately, collecting 115 ν_μ and 158 $\bar{\nu}_\mu$ events after background subtraction. The MicroBooNE analysis described here has selected 6816 events after background subtraction, offering a substantial improvement in statistical precision. Additionally, MicroBooNE is reporting a differential cross section with respect to pion momentum.

CC1$\pi^\pm$ cross sections have also been measured for several other target materials, including water, carbon, hydrocarbons, and some metals. A complete overview is shown in Table 7.1, listing (anti-)neutrino CC1$\pi^\pm$ measurements as well as more exclusive measurements focused on coherent pion production. The Main Injector Experiment for ν-A (MINERvA) [194] has measured many of these and has shown challenges for existing models in describing data across different nuclear targets. Cross-section changes that result from varying the size of the target nucleus are referred to as the A-dependence of the cross section. For instance, the measured CC charged pion production cross sections per nucleon for iron and lead are around 80% and 50% of the hydrocarbon value, a scaling relationship that many generators failed to predict accurately [195]. Extrapolation from better-measured nuclei, such as carbon, to the heavier argon nucleus is therefore not reliable, and dedicated measurements on argon are required.

MicroBooNE [187], as well as T2K [196], have also reported first cross-section measurements for electron (anti-)neutrino CC1$\pi^\pm$ events. These measurements benefit

from better lepton-pion separation due to EM shower production, but contain relatively few events because the beams are predominantly composed of muon-flavour neutrinos.

Experiment	Target	$\pi^{\pm}$	π^0
NOMAD	C	-	NC [197]
K2K	C_8H_8	CC [198], CC [199]	CC [200]
	H_2O	-	NC [201]
MiniBooNE	CH_2	CC [202, 203]	CC [204], NC [205], NC [206]
SciBooNE	C_8H_8	CC [207]	NC [208], NC [209]
MINOS	Fe	-	NC [210]
ArgoNeuT	Ar	CC [211], CC [193]	NC [212]
MINERνA	C	CC [213], CC+NC [214, 215], CC [195]	CC [216]
	C_8H_8	CC [217–219, 195], CC+NC [215]	CC [218, 220, 221], NC [222]
	H_2O	CC [195]	-
	Fe	CC+NC [215], CC [195]	-
	Pb	CC+NC [215], CC [195]	-
NOvA	C	-	NC [223], CC [224]
T2K	C_8H_8	CC [225], CC [226, 227], CC ν_e [196]	-
	H_2O	CC [228]	-
MicroBooNE	Ar	CC ν_e [187], CC [229] (this work)	CC [183], NC [184, 186, 230]

Table 7.1 List of all neutrino-induced pion-production cross-section measurements to date. Except where specified, these are muon (anti-)neutrino measurements.

7.5 Data and Simulation Samples

The analysis uses data from all five runs of MicroBooNE, corresponding to 1.11×10^{21} POT. The data and simulation samples used in this analysis were produced through the common MicroBooNE simulation and reconstruction workflows, with contributions from this author in processing the samples. Missing is the first of four epochs of Run 4, whose data-MC agreement was still being validated by the collaboration at the

time of unblinding, as well as some additional data from Run 1 that also only became available later. Table 7.2 shows the POT of the data and simulation samples used in this analysis.

	1	**2**	**3**	**4bcd**	**5**	**Combined**
Beam-on Data	1.67	2.62	2.64	2.74	1.48	11.14
Neutrino MC: Training	6.42	5.08	6.57	10.48	4.86	33.40
Neutrino MC: Testing	6.42	5.08	6.57	10.48	4.86	33.40
Dirt MC	3.16	9.51	3.27	8.32	3.57	27.83

Table 7.2 POT of Run 1-5 samples in units of 10^{20}. The main MC sample is split up into a set used for training BDTs and a test set used for the cross-section extraction.

Cosmic background interactions can produce scintillation light in coincidence with a beam spill. These interactions mimicking neutrinos are modelled using dedicated beam-off samples collected with a dedicated trigger, which are scaled to the beam-on data. For this, the ratio of hardware triggers announcing an incoming beam spill in the beam-on samples to the hardware triggers of the beam-off sample without actual beam activity is used. The number of hardware triggers recorded for the samples in this interaction are shown in Table 7.3.

	1	**2**	**3**	**4bcd**	**5**	**Combined**
Beam-off Data	6.6×10^7	1.5×10^8	2.1×10^8	2.1×10^8	1.1×10^8	7.5×10^8
Beam-on Data	3.7×10^7	6.2×10^7	6.4×10^7	6.4×10^7	3.5×10^7	26.1×10^7

Table 7.3 Number of hardware triggers recorded in the beam-off sample. Each beam-on trigger marks an incoming beam spill registered by the DAQ. In beam-off runs, these triggers occur without any actual beam activity.

7.6 Event Selection

This section describes the signal event selection. First, a short summary of a commonly used preselection in MicroBooNE for CC muon (anti-)neutrino events is provided. This is followed by a description of the BDTs trained for particle identification in the analysis. The main selection criteria, including the use of the BDTs, are described after

that. Finally, the construction of dedicated subsets for the two momentum differential cross sections is described, and the performance of the selection is evaluated.

7.6.1 Preselection

The preselection inclusively selects CC muon (anti-)neutrino interactions in MicroBooNE and distinguishes them from NC and electron (anti-)neutrino interactions. The selection criteria in this analysis follow the selection described in Ref. [116], and this section provides a short summary.

A series of particle-level requirements are applied to identify potential muon candidates. For an event to be considered further, at least one reconstructed particle must satisfy all of the following:

Track score: Pandora provides a score for each reconstructed particle that indicates how shower-like versus track-like it is on a scale from 0 to 1. This uses a set of metrics that include the total length of the reconstructed particle in the detector, the distance from the reconstructed neutrino interaction vertex to the start of the particle, and changes along its length, such as in its transverse extent [174]. Distributions of this metric for different simulated particles in MicroBooNE are shown in Figure 7.3. Muon candidates must be clearly identified as track-like particles via a high track score ≥ 0.85.

Vertex distance: Potential muon tracks must start within 4 cm of the reconstructed neutrino vertex, which helps reduce cosmic rays being misidentified as muons originating from a neutrino interaction.

Generation: Next, only primary tracks in Pandora's reconstruction hierarchy are considered. This is sorting out particles that appear to come from the decay or interaction of primary particles in the argon.

Track length: The muon candidate must also have a track length of at least 20 cm. This corresponds to a momentum above 150 MeV, which aligns with the muon momentum phase space restriction that is enforced in the analysis.

χ^2_p, χ^2_μ and χ^2_p/χ^2_μ: In the last steps, the energy loss curve $\mathrm{d}E/\mathrm{d}x$ for reconstructed calorimetric hits at the end of a track is compared to simulated distributions for muons and protons. The resulting metrics shown in Figure 7.4, which are denoted χ^2, are used to determine how muon- or proton-like a given track is. This is done by requiring a proton score of $\chi^2_p > 60$ and a muon score of $\chi^2_\mu < 30$.

To strongly favour muon agreement, a proton-to-muon χ^2 ratio requirement of $\chi^2_p/\chi^2_\mu > 7$ is also applied. The double-peaked distribution of the muons in these plots is the result of the difference between contained and exiting muons.

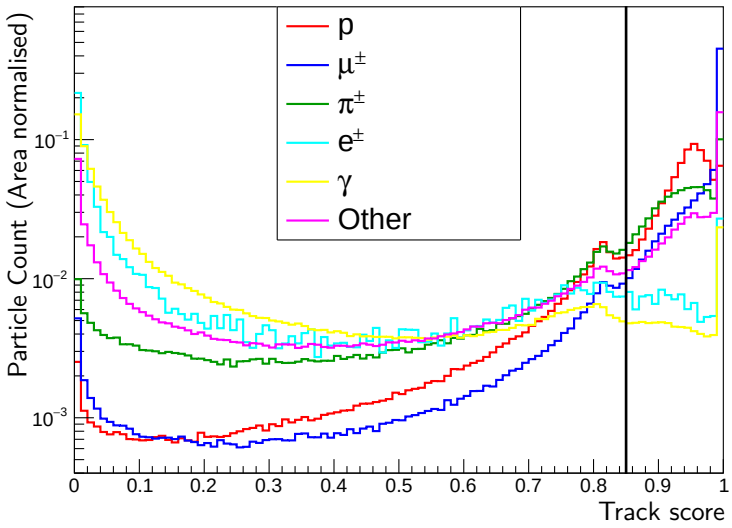

Fig. 7.3 Track scores computed by Pandora of different simulated particles. Of the named particles, protons, muons and charged pions produce tracks. Neutral pions decaying to photons are counted as photons here. Particles left of the vertical line are rejected.

Next, three quality requirements are applied at the event level:

Particle start: All primary particles must start at least 10 cm away from all TPC boundaries.

Fiducial vertex: The reconstructed neutrino interaction vertex is within the fiducial volume defined in Equation (7.2).

Topological score: The topological score calculated by Pandora described in Section 6.2.2 is used to distinguish neutrino events from cosmic-ray backgrounds. Its distribution for simulated neutrino and recorded cosmic events is shown in Figure 7.5. A minimum topological score of 0.25 is required in the preselection, which, while later superseded in the pion selection by a more stringent requirement on this variable, is mentioned here for completeness, as events passing the preselection are used to train BDTs in the next section.

An overview of the applied selection criteria is provided in Table 7.4.

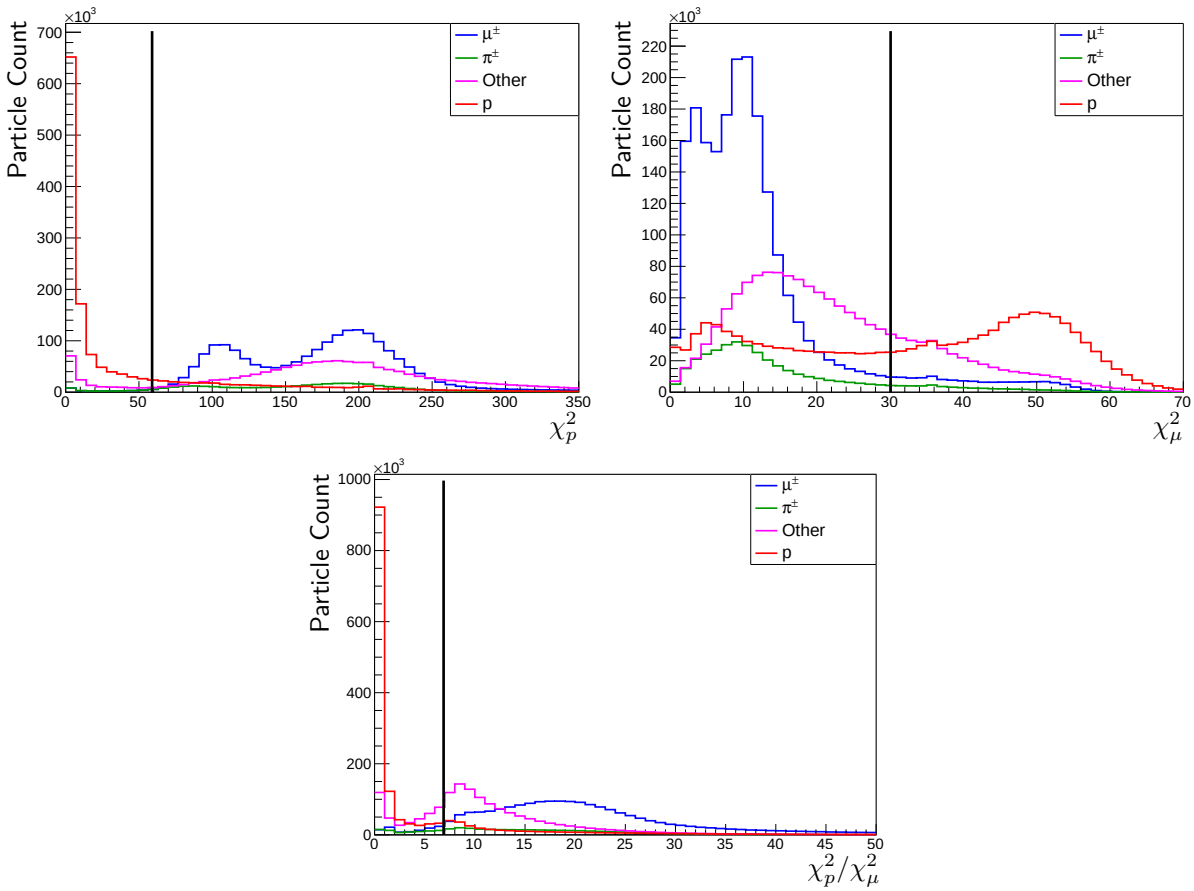

Fig. 7.4 The χ^2 metric shows the agreement of the energy loss curve, $\mathrm{d}E/\mathrm{d}x$, for reconstructed calorimetric hits at the end of a track with templates for muons and protons. The top left plot shows scores for simulated particles under a proton hypothesis χ^2_p, the top right shows scores under a muon hypothesis χ^2_μ, and the bottom plot shows the per-particle ratios χ^2_p/χ^2_μ. Particles right of the vertical line for the χ^2_μ plot are rejected, and particles left of the vertical line are rejected for the other two plots.

7.6.2 Boosted Decision Trees

This analysis uses three BDTs to identify particles: one for muons, one for protons, and one to identify unscattered pions. The set of input variables used by each BDT is derived from an iterative feature selection process [192] that considered several additional variables. As part of this, the BDTs were retrained multiple times, each time removing one feature to assess its impact on performance. Changes in performance were used to gauge the relative importance of each variable. Features found to have little or no impact were excluded, and the process was repeated until all remaining inputs made a significant contribution. The result is the list of six variables for the

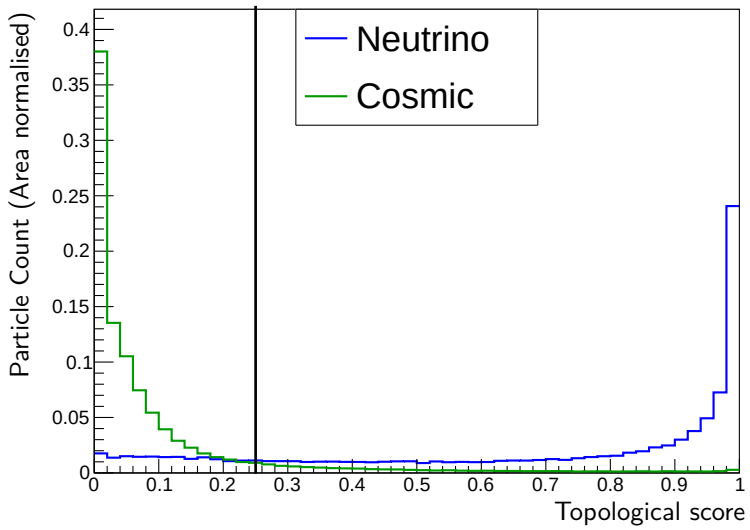

Fig. 7.5 Distribution of topological scores assigned to Pandora-reconstructed events. The cosmic distribution corresponds to pure beam-off detector data, while the neutrino distribution shows simulated neutrino events with beam-off overlay, in which at least 50% of the neutrino interaction was reconstructed as part of the event. This excludes cases where only the overlaid background was reconstructed as the neutrino candidate. Events left of the vertical line are rejected.

Particle-level Preselection	
Track score	Track score > 0.85
Vertex distance	Particle to neutrino vertex distance $< 4\,\text{cm}$
Generation	Pandora generation $= 2$ (primary particles only)
Track length	Track length $> 20\,\text{cm}$
χ^2_p	Proton $\chi^2 > 60$
χ^2_μ	Muon $\chi^2 < 30$
χ^2_p/χ^2_μ	Proton χ^2/ Muon $\chi^2 > 7$
Event-level Preselection	
Particle start	Tracks cannot start closer than 10 cm from a detector boundary
Fiducial vertex	Neutrino vertex inside fiducial volume
Topological score	Topological score ≥ 0.25

Table 7.4 Selection criteria for the CC muon (anti-)neutrino preselection.

muon and unscattered pion BDTs listed below. The proton BDT uses five variables, as it does not rely on the number of descendant particles.

The first three variables rely on multi-plane calorimetric information to ensure robust $\mathrm{d}E/\mathrm{d}x$ reconstruction [231]. When possible, collection plane information is preferred due to its higher resolution and accuracy when measuring the deposited charge dQ/dx [232]. For tracks travelling at small angles relative to the collection plane wires, the information from the induction planes is used, weighted by the number of hits in each. The general definition for a calorimetric input variable L is [192]:

$$L = \begin{cases} L_W & \text{if } \sin^2\theta_W \geq 0.175 \\ \dfrac{L_U N_U + L_V N_V}{N_U + N_V} & \text{if } \sin^2\theta_W < 0.175, \end{cases} \tag{7.3}$$

where $L_{U,V,W}$ are the plane-specific values, $N_{U,V,W}$ are the calorimetric hit counts for each plane, and θ_W is the angle between track direction and the orientation of the collection wires in the XZ plane. The variables are defined below and shown in Figure 7.7:

- **Bragg Log-Likelihood Ratios:** The proton-to-MIP and charged-pion-to-MIP log-likelihood ratios are computed from the last 30 cm of a track, comparing observed $\mathrm{d}E/\mathrm{d}x$ values with templates for protons, pions, and MIPs that are shown in Figure 7.6 [233]. The resulting metrics, LLR(p/MIP) and LLR(π/MIP), reflect the compatibility of a track with a proton or pion hypothesis.

- **Truncated Mean** $\mathrm{d}E/\mathrm{d}x$**:** Computed from the beginning and middle sections of a track, this is the mean $\mathrm{d}E/\mathrm{d}x$ after removing the first three hits, the final 30 cm of the track, and outliers with $\mathrm{d}E/\mathrm{d}x$ beyond one standard deviation from the median.

The energy loss simulation of tracks in the detector has been tuned to data [231], but uncertainties remain, and the calorimetric variables show some differences between data and MC for this selection. In particular, the data peak of the truncated mean $\mathrm{d}E/\mathrm{d}x$ distribution in Figure 7.7c is at slightly lower values than the simulation. This is a result of differences in MicroBooNE's simulation of electron-ion recombination with data. This is accounted for as an uncertainty via the usage of varied detector model simulations, as described in Section 8.2.4.

The remaining three variables describe the particle topology and are shown in Figure 7.8:

- **Descendant Particle Count:** This variable counts the number of reconstructed descendant particles associated with a given primary in the Pandora hierarchy. It provides a measure of decay activity.

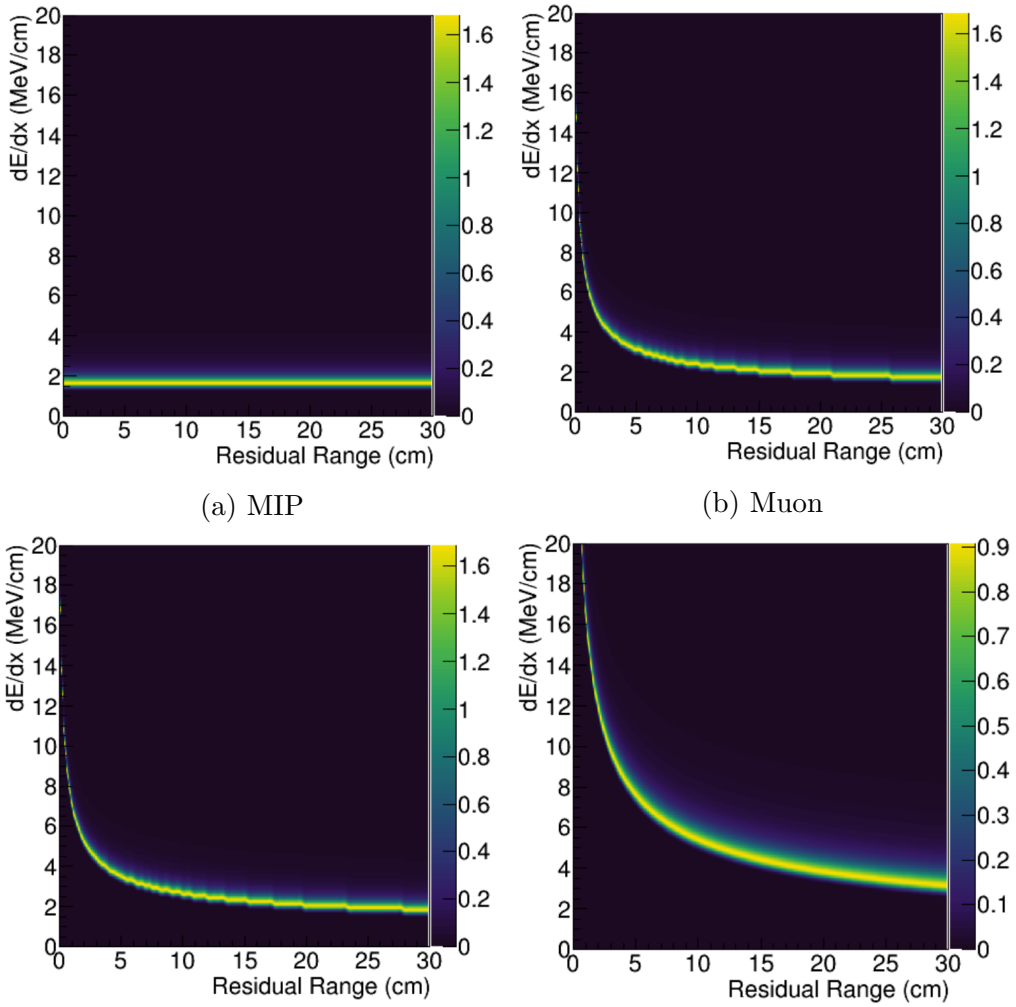

(a) MIP (b) Muon

(c) Charged pion (d) Proton

Fig. 7.6 Computed probability distributions for the energy deposition $\mathrm{d}E/\mathrm{d}x$ of different particle types as a function of the distance to the end of a track for the collection plane of the MicroBooNE detector. Source: Ref. [233].

- **Track Wiggliness:** The standard deviation of the angular differences between the directions at adjacent points along the trajectory of a fitted track. More colloquially, this is a metric for the wiggliness of the track and provides information about scattering and decays. The two-peaked appearance of the distribution in Figure 7.8b is a feature of the logarithmic scaling of the x-axis.
- **Track-Shower Score:** The SVM-based score from Pandora that quantifies how track-like or shower-like a particle topology is.

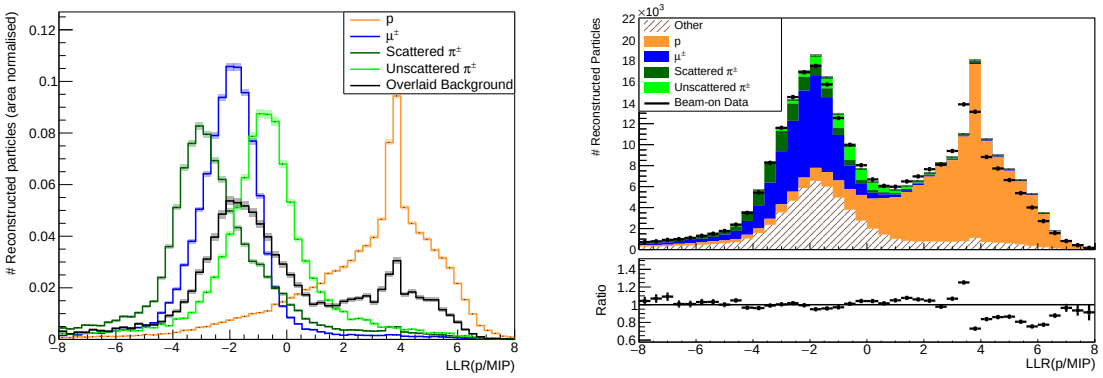

(a) Proton-to-MIP Bragg log-likelihood ratio

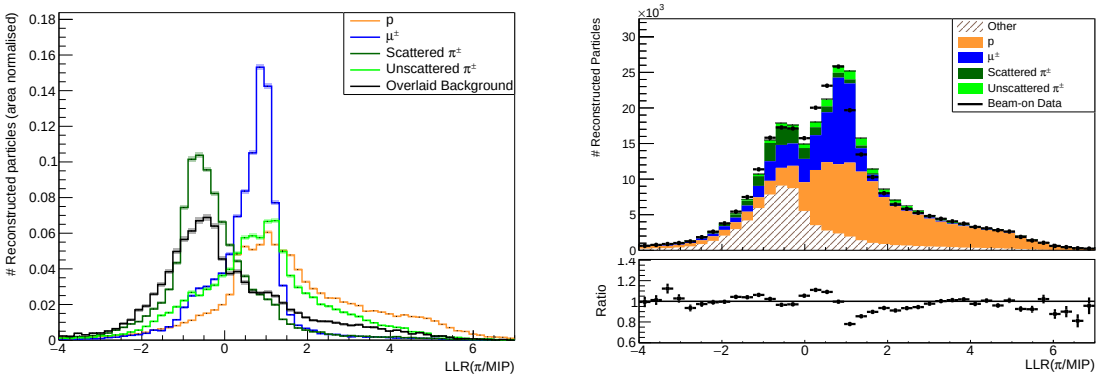

(b) Charged-pion-to-MIP Bragg log-likelihood ratio

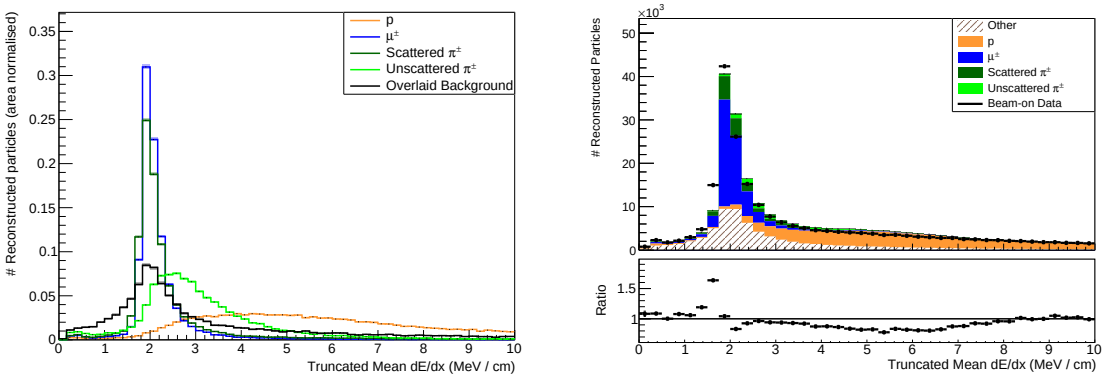

(c) Truncated mean dE/dx

Fig. 7.7 Distributions of calorimetric input variables for simulated CC1$\pi^{\pm}$ events and data. Each variable is shown as an area-normalised distribution of particle types for simulated signal events (left) and the stacked simulation compared to data (right). The ratio plots shown are between the data and MC. The *Overlaid Background* category for the simulated signal events on the left contains cosmic muons that were reconstructed as part of a signal event. The *Other* category for the comparison with real data contains all particles, including those not belonging to signal events, such as π^0 or photons. Only statistical uncertainties are shown.

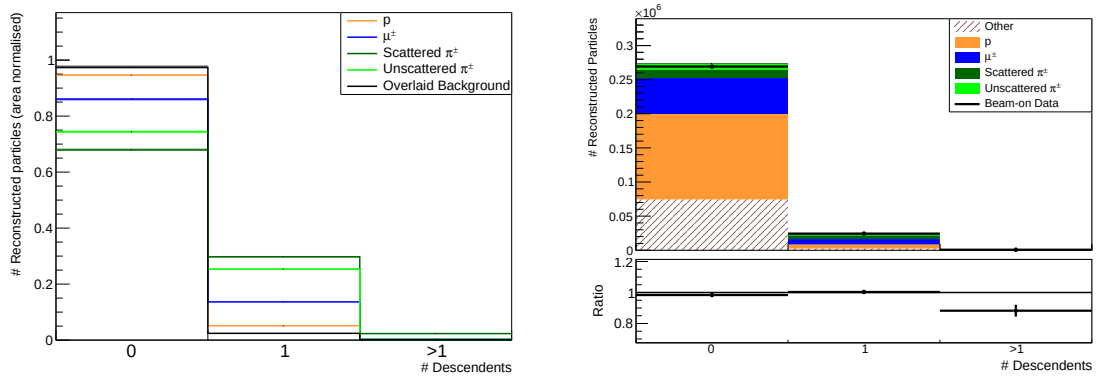

(a) Descendant particle count

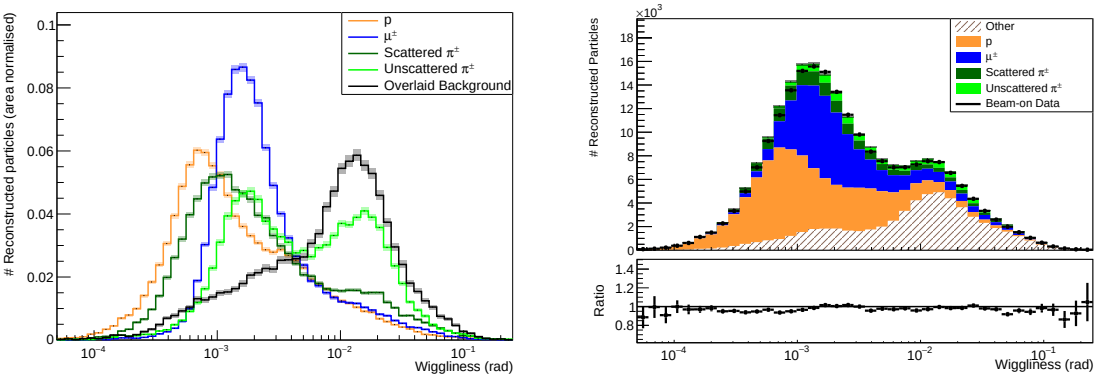

(b) Track wiggliness

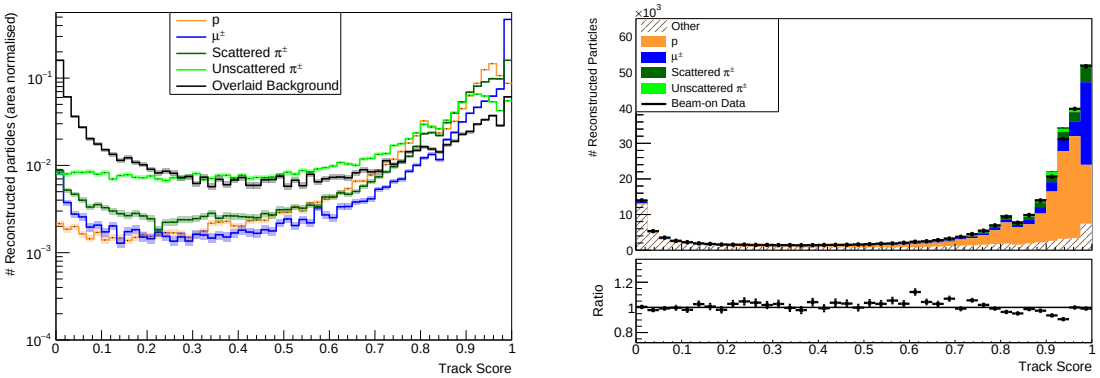

(c) Track–shower score

Fig. 7.8 Distributions of topological input variables for simulated CC1$\pi^{\pm}$ events and data in the same format as Figure 7.7. The double-peaked appearance of the area normalised wiggliness distributions is a result of the log-scaled x-axis.

This analysis relies on the same set of calorimetric and topological features above. Those not common to MicroBooNE have been reimplemented as part of MicroBooNE's shared PeLEE sample production pipeline.

Each BDT is trained using the Toolkit for Multivariate Data Analysis (TMVA) framework [234] to recognise its target and reject other particle types. Training uses contained reconstructed particles from GENIE MC signal events that pass the preselection. Each reconstructed particle needs to have a label of the true particle type, which comes from a truth matching process that identifies the simulated particle that contributed most to a reconstructed track. The simulated particle categories are $\mu^{\pm}$, p, *Scattered* $\pi^{\pm}$ and *Unscattered* $\pi^{\pm}$. For the latter two, additional scattering information is used from the GEANT4 transport simulation to distinguish between pions that undergo elastic or inelastic hadronic interactions in the simulation and those that do not. *Overlaid Background* is the label assigned to all reconstructed particles that cannot be matched to a simulated particle, such as cosmic muons in the real beam-off data that is overlaid on all simulated interactions. This category also includes reconstructed tracks in which the contributions to the individual calorimetric hits are a mix of simulated and overlay backgrounds, with the latter dominating.

The GENIE sample is split into two equally sized subsets: one for training and one for testing, with the training set corresponding to approximately 63,000 particles. The testing set is also later used for the cross-section extraction. To reduce the influence of poorly reconstructed tracks, particles are weighted by their completeness, which is defined as the fraction of calorimetric hits from the matched simulated particle that are assigned to the reconstructed particle. Matching between simulated and reconstructed particles is done on the basis of which simulated particle contributes the largest number of hits to a given reconstructed particle. Overlaid cosmic-ray tracks are assigned uniform weights.

The particle separation power of the BDTs for the training and the unseen test events is shown in Figure 7.9 with no signs of overfitting. Comparisons with data are shown in the next section, where the BDT scores are used as part of the event selection.

7.6.3 General CC1$\pi^{\pm}$ Selection

The general charged pion selection builds upon the preselection described earlier and applies a series of criteria designed to isolate events with a topology consistent with the signal definition: one muon, one charged pion, and any number of protons. This selection forms the basis for all cross-section measurements presented in this analysis, with additional subset requirements applied later for specific differential measurements.

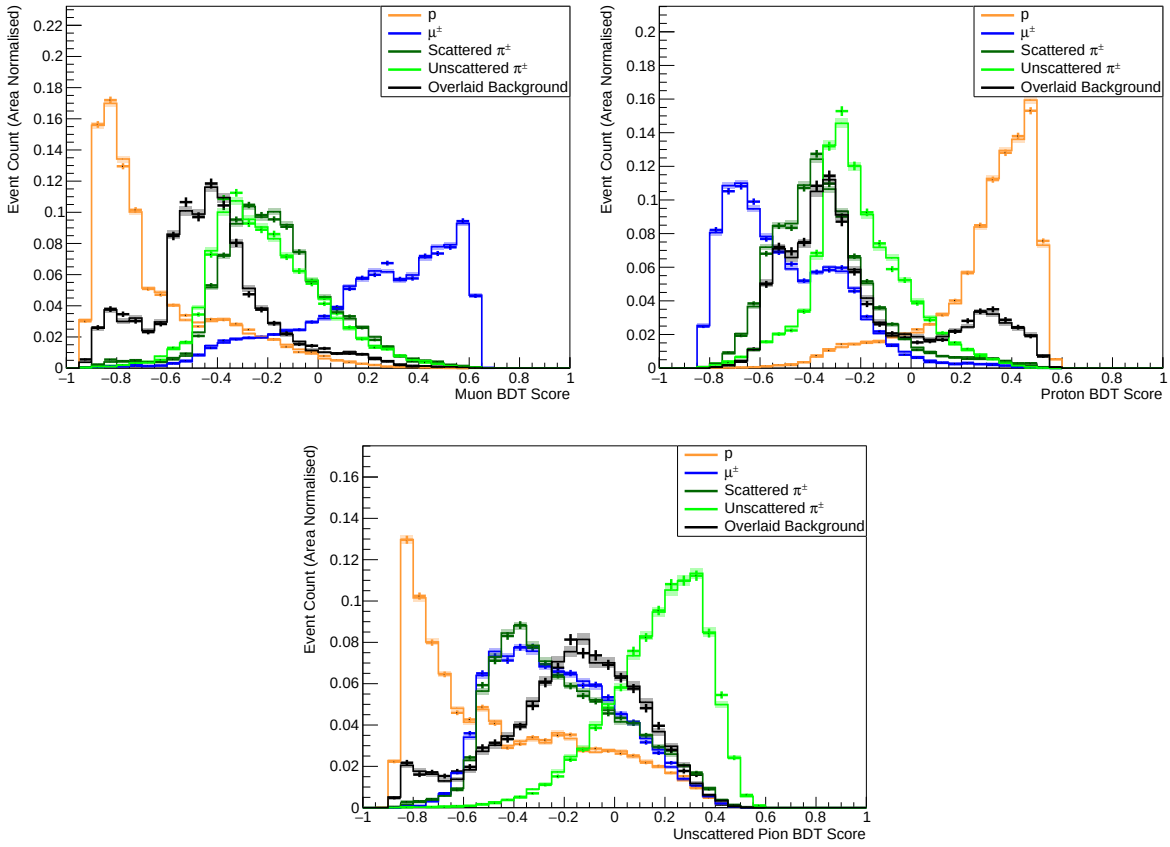

Fig. 7.9 Area normalised BDT-score distributions of contained reconstructed particles from GENIE simulated signal events passing the preselection. The points denote the training sample and the solid line the unseen testing sample, with statistical uncertainties shown. *Overlaid Background* particles are reconstructed tracks dominated by overlaid beam off contributions.

The general selection process follows this sequence: events with the correct particle multiplicity are selected, and muon, proton, and pion candidates are identified. This is followed by a series of quality requirements, and finally, phase space restrictions are applied in accordance with the signal definition. Each step is described below, with data–simulation comparisons provided for each requirement.

Number of Reconstructed Tracks: To enforce the signal topology consisting of a muon, a charged pion, and any number of protons, a minimum of two tracks is required to be present in the event. As Figure 7.10 shows, this removes mainly pionless events without protons. These events include mainly interactions producing a muon and any number of non-visible neutrons.

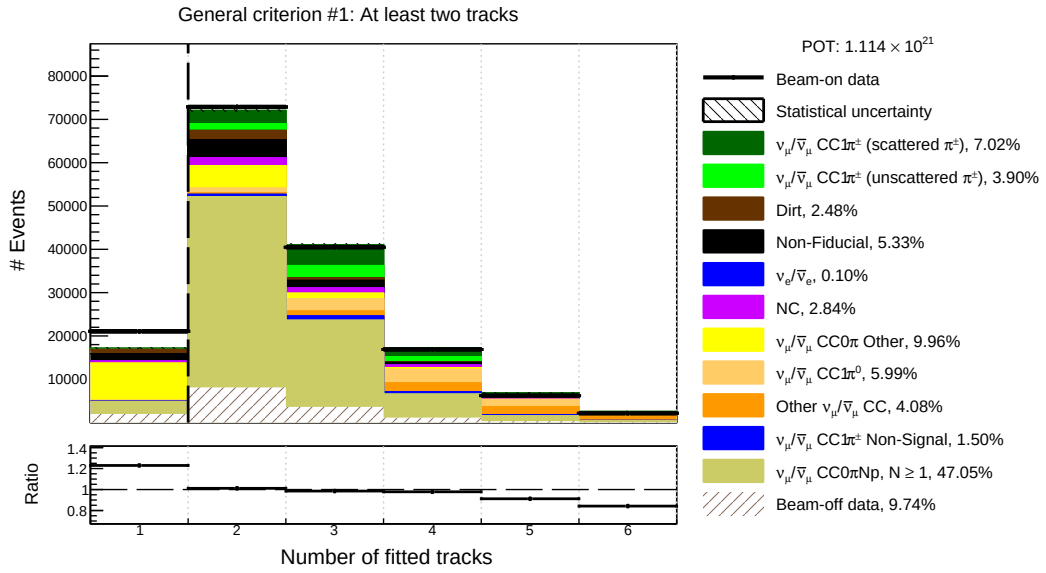

Fig. 7.10 The number of reconstructed tracks is shown for data as black points and simulation as a stacked histogram of event categories. The ratio of these is shown on the bottom. Events to the left of the line are rejected. This is mainly removing muon (anti-)neutrino events without pions and protons in bright yellow. The main background of this analysis CC0πNp, N$\geq$ 1, which is pionless events with protons, is shown separately in dark yellow.

Number of Uncontained Tracks: Muons produced in CC interactions tend to receive a significant fraction of the neutrino energy. Protons have a higher average ionisation loss $\langle \mathrm{d}E/\mathrm{d}x \rangle$ compared to muons and charged pions. Hadrons also frequently scatter inelastically on argon. As a result, muons typically have longer tracks and are much more likely to exit the detector. If there is one escaping track, defined as a track that ends within 5 cm of a TPC boundary, it is always identified as the muon candidate. As Figure 7.11 shows, events with more than one escaping particle are removed. This is mainly a quality requirement, removing events close to a TPC boundary that have a significant fraction of the event outside the detector.

Muon Identification for Fully Contained Events: For fully contained events, the particle with the highest muon BDT score, as shown in Figure 7.12, is selected as the muon candidate. No events are rejected at this step. The overall data–simulation agreement yields a p-value of 0.05, with some shape and normalisation differences observable for the least muon-like (most proton-like) particles. These deviations likely stem from differences in the modelling of calorimetric variables, mainly arising from the treatment of recombination effects [113], and are visible in the input variables

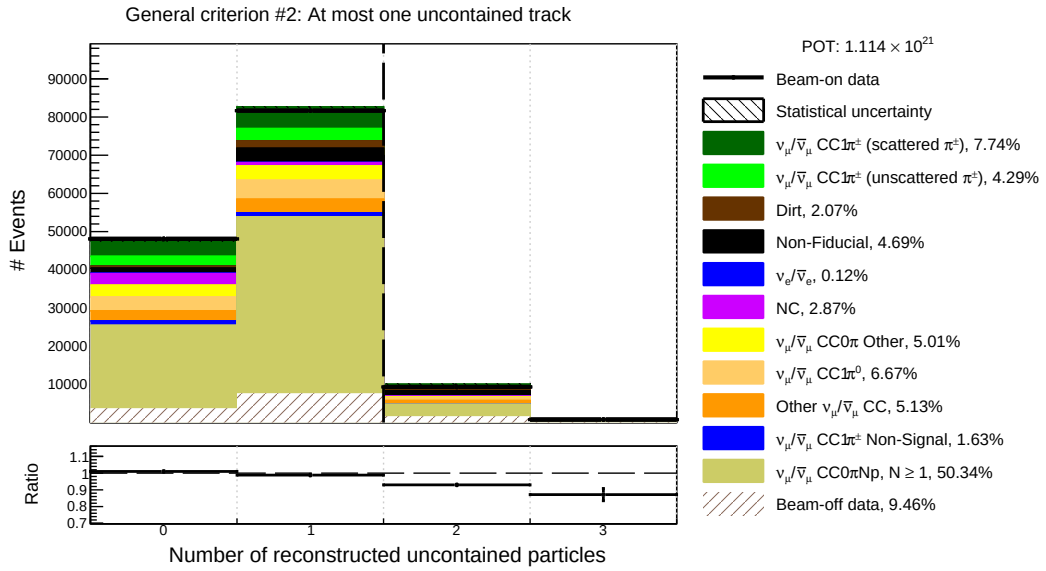

Fig. 7.11 The number of reconstructed tracks ending within 5 cm of the detector boundaries. Most events are either fully contained inside the detector or have one exiting particle, which is almost always a muon. Events to the right of the line with more than one exciting particle are rejected.

Figure 7.7. These modelling differences are addressed via the systematic uncertainties described in Chapter 8, which are included in the shaded bands of Figure 7.12. Despite these discrepancies at low scores, the selection of the muon candidate is quantitatively robust. The muon candidate is defined as the track with the highest score, which typically resides in the well-modelled region above -0.7. Consequently, while these shape differences in Figure 7.12 may affect the assigned BDT scores at the extremes of the distributions, their impact on particle selection is minimal because the selection is determined solely by the highest-scoring particle, making it insensitive to small local shifts.

Proton and Pion Identification: After a muon candidate has been determined, the remaining particles are evaluated on how proton-like they are using their proton BDT score shown in Figure 7.13. Particles to the right of the -0.06 threshold are considered protons. If exactly one particle remains after this selection step that is not identified as either the muon or a proton, it is classified as the charged pion. Otherwise, the event is rejected as shown in Figure 7.14. As with the muon BDT score distribution, there is a divergence in the number of protons. This variation at high BDT values, however, does not influence the identification of pion candidates, which are selected from tracks left of the threshold value.

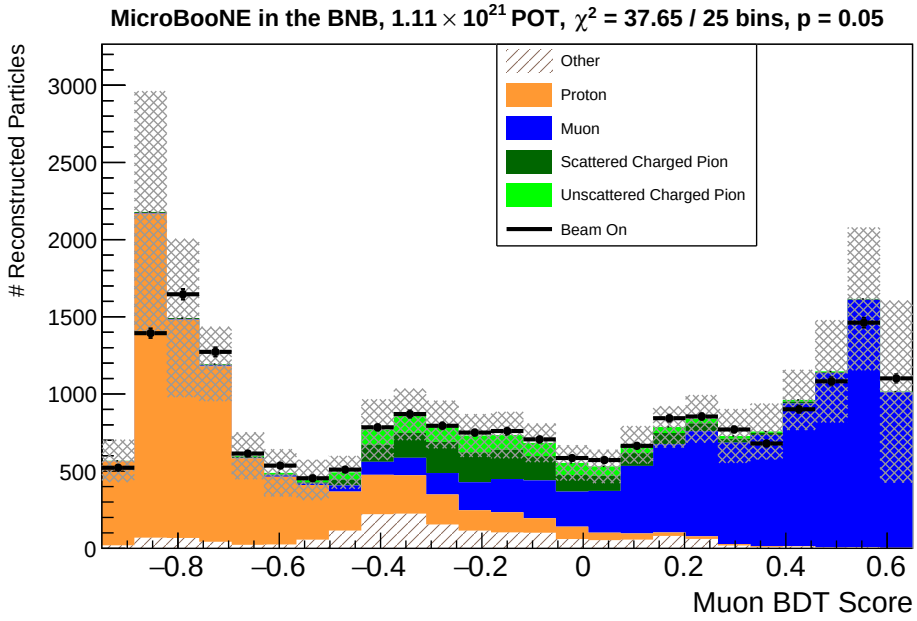

Fig. 7.12 Muon BDT scores for reconstructed particles, showing the predicted distribution as a stacked histogram and the data distribution as black dots. The distribution shows particles in events that pass all prior requirements and where the event is fully contained. Statistical and systematic uncertainties on the stacked histogram prediction, as described in Chapter 8, are shown as grey shaded bands. The highest-scoring track is selected as the muon candidate in fully contained events.

Valid Pion $\mathrm{d}E/\mathrm{d}x$**:** This requirement removes events where the energy loss of the pion candidate is unphysical and characteristic of misidentified protons using the same truncated mean $\mathrm{d}E/\mathrm{d}x$ variable used for the BDT defined in Section 7.6.2. Calorimetry is poor for tracks travelling directly towards the wire planes, as the charge is continuously deposited on few wires. This is one cause for protons to be misidentified as pions. The requirement $\langle \mathrm{d}E/\mathrm{d}x \rangle > 1\,\mathrm{MeV/cm}$ is enforced for the pion candidate as shown in Figure 7.15, rejecting those with very small energy loss.

Three Pion & Muon Perspectives: The three-dimensional reconstruction of events in Pandora relies on the matching of reconstructed particles across the different wire planes. This can be more challenging for shorter tracks, especially when data is not available from all three planes due to the particle lying in an unresponsive region of one of the wire planes, as described in Section 5.7. The limited information can lead to reconstruction failures, including incorrect angle reconstruction in three dimensions. A visible failure mode is tracks being reconstructed as isochronous with no extent in the drift dimension x, corresponding to peaks at $\phi = \pm\pi/2$ in Figure 7.16. To address

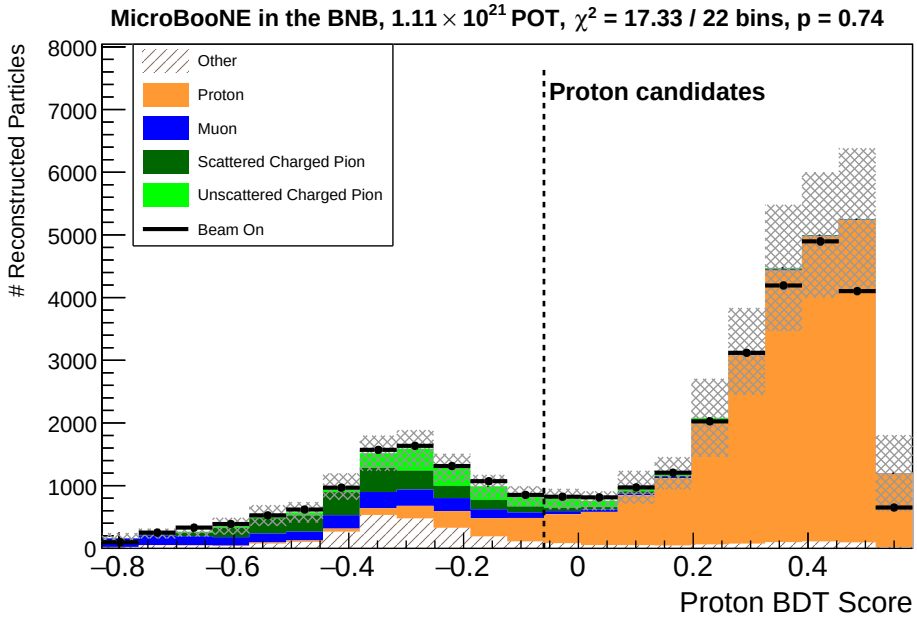

Fig. 7.13 Proton BDT scores for reconstructed particles, showing the predicted distribution as a stacked histogram and the data distribution as black dots. The distribution shows particles that passed all prior criteria and are not the identified muon candidate. Statistical and systematic uncertainties on the stacked histogram prediction, as described in Chapter 8, are shown as grey shaded bands. Particles right of the line are considered protons.

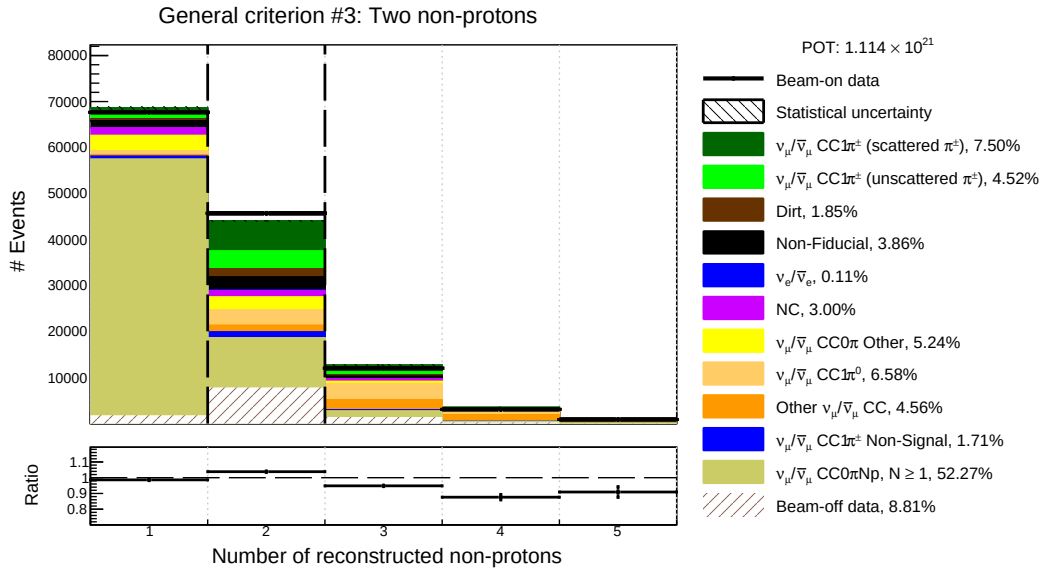

Fig. 7.14 The number of reconstructed particles classified as neither muon nor pion. Events between the two dashed lines are selected.

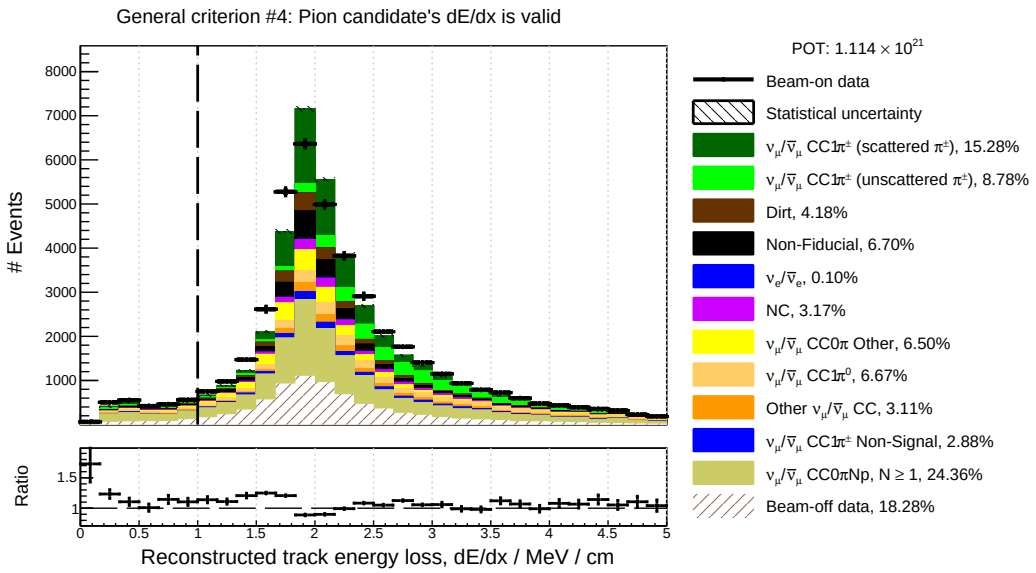

Fig. 7.15 The truncated $\mathrm{d}E/\mathrm{d}x$ of the pion candidate. Events to the left of the line are rejected.

this, a quality requirement is enforced that pions have to have hits on all three wire planes. The same requirement is also enforced for the muon candidate, but due to their on average much longer track lengths, it is much rarer for them to completely lie in an unresponsive detector region, and the impact of this requirement is very small.

Topological Score 2: Events with a topological score below 0.25 are already removed by the CC inclusive muon (anti-)neutrino preselection. In addition to this preselection criterion, a second more stringent threshold requiring a score > 0.67 is applied in the pion selection to further reduce cosmic and dirt backgrounds by removing events that are ambiguous in origin, as shown in Figure 7.17.

Tracks Near Vertex: The largest distance allowed between the reconstructed neutrino vertex and the start point of all primary particles is 9.5 cm as shown in Figure 7.18, ensuring that all particles originate close to the vertex. This removes events with photons, particularly from π^0 decays, and other backgrounds not directly attached to the neutrino vertex.

Muon–Pion Opening Angle Phase Space Restriction: The event reconstruction occasionally splits a single long track, such as a stopping muon, into two back-to-back tracks, mimicking a muon–pion topology and substantially increasing the background. To suppress this, events must satisfy $\theta_{\mu\pi} < 2.65$, which excludes

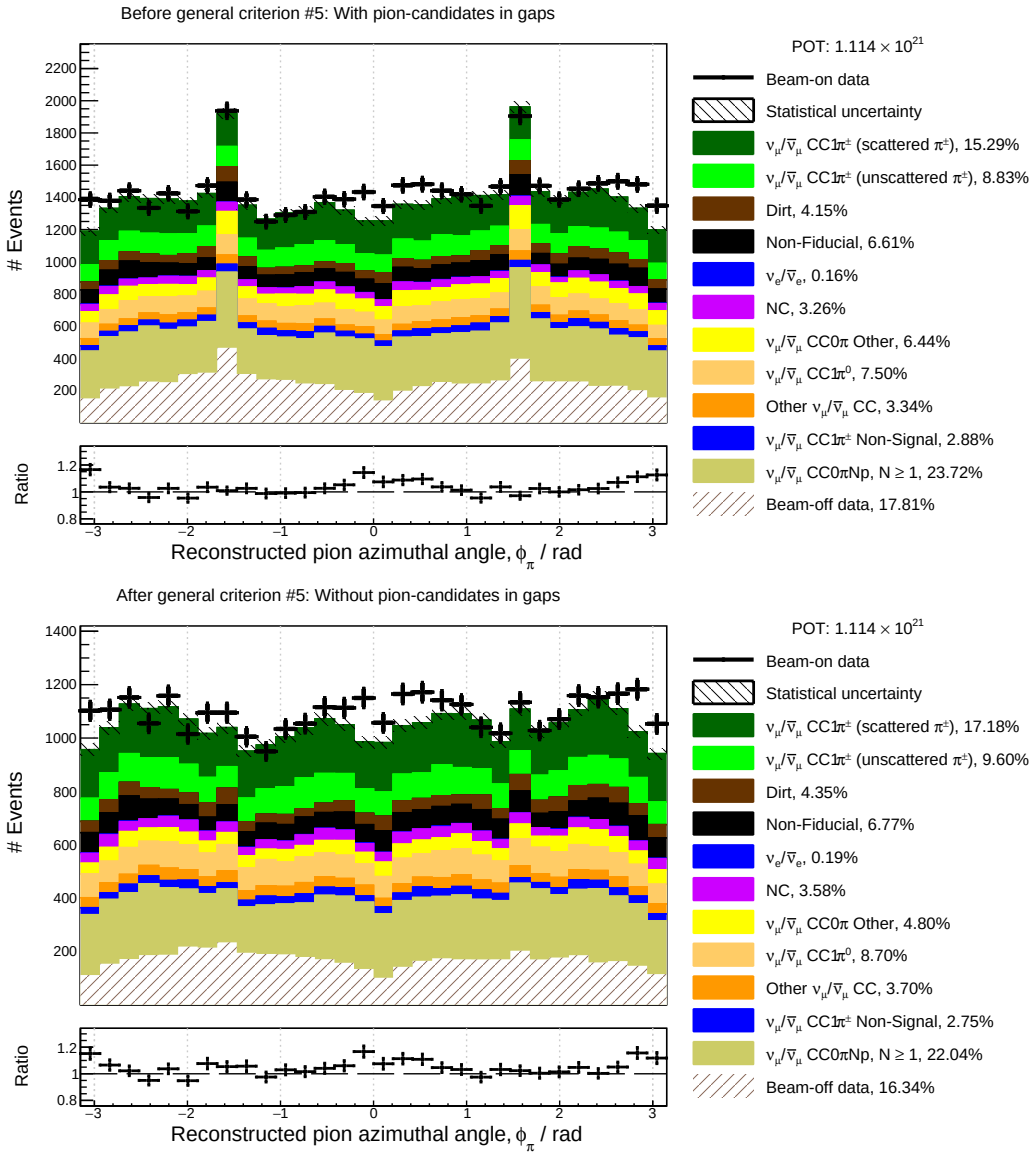

Fig. 7.16 Azimuthal angle of the reconstructed pion candidate before (left) and after (right) removing events in which the pion candidate does not have hits on all three planes.

this region of the phase space with a high background contamination, as shown in Figure 7.19.

Muon Momentum Phase Space Restriction: The muon momentum is required to be greater than $p_\mu > 150\,\text{MeV}$ to maintain consistency with the minimum track length requirement used in the preselection. Figure 7.20 shows the requirement on reconstructed muon momentum. The data-simulation difference results from issues

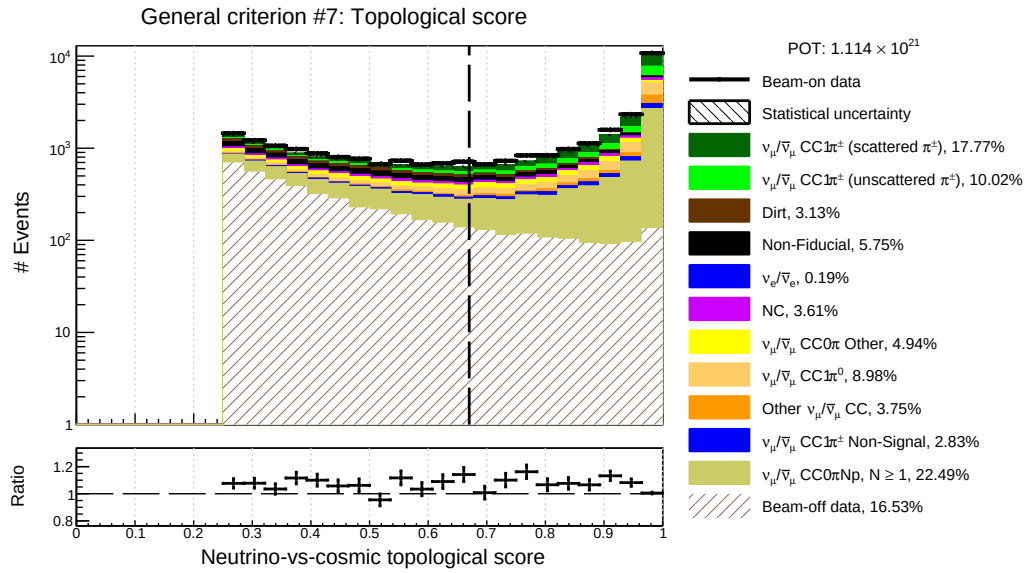

Fig. 7.17 The topological score of the events as determined by Pandora. To show the distribution of beam off overlaid background, the y-axis uses a log-scale due to the concentration of events in the furthest right bin. Events to the left of the line are rejected.

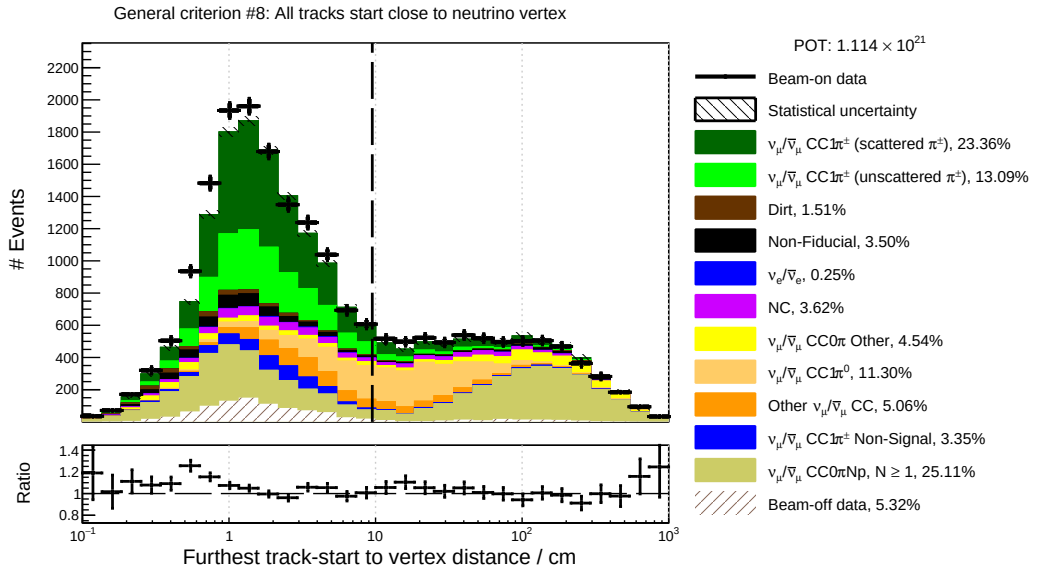

Fig. 7.18 The largest distance between the reconstructed neutrino vertex and the start point of all tracks. Events to the right of the line are rejected.

with the momentum estimation method used for uncontained muon tracks, which appears to be biased towards lower momenta. This is the motivation behind the

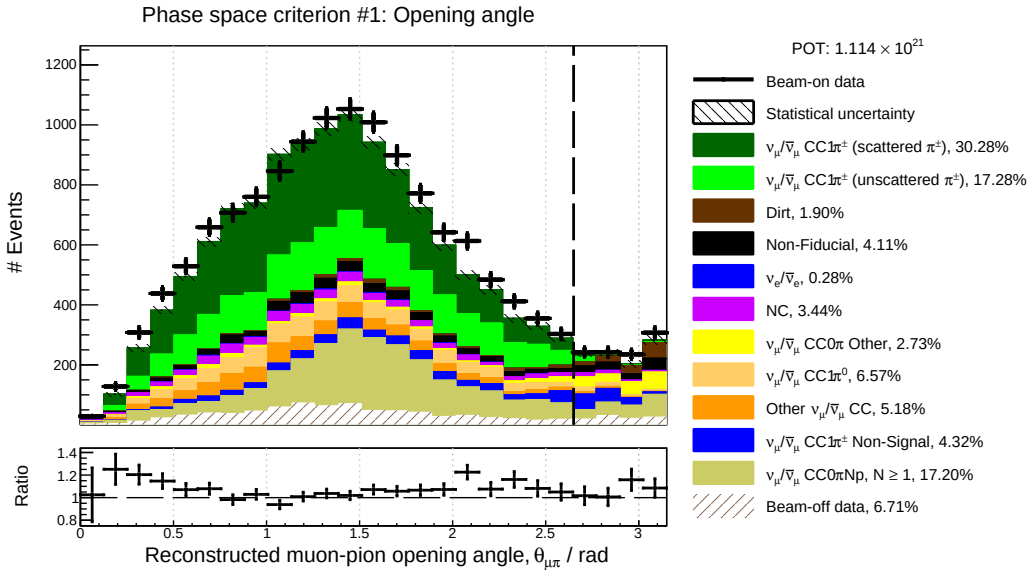

Fig. 7.19 The opening angle between the reconstructed muon and pion candidates for MC events only. Events to the right of the line are rejected.

separate subset of events for the muon momentum differential cross section discussed in Section 7.6.5.

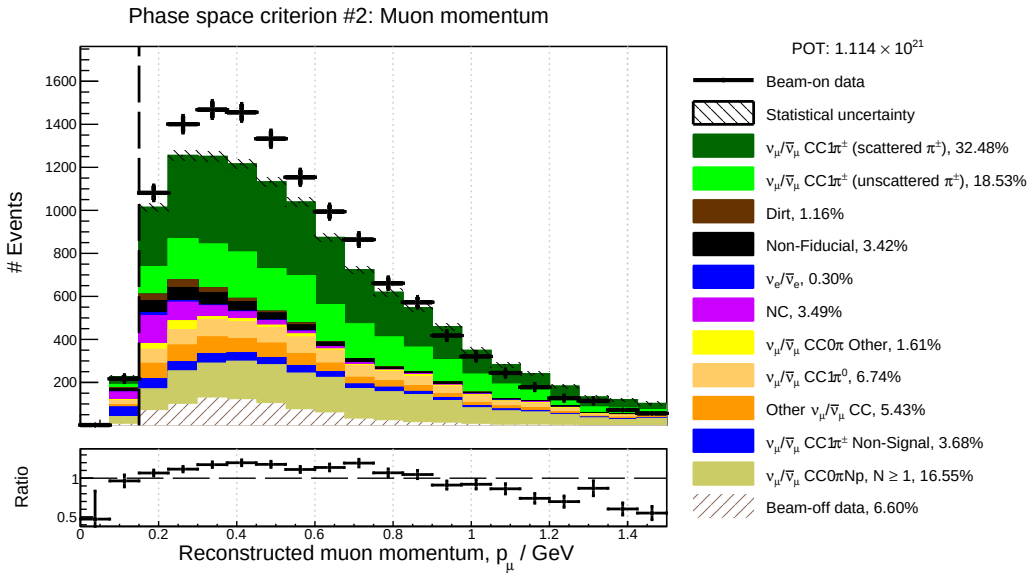

Fig. 7.20 The momentum of the reconstructed muon candidates. Events to the left of the line are rejected.

Pion Momentum Phase Space Restriction: A requirement of $p_\pi > 100\,\text{MeV}$ is imposed on the reconstructed pion momentum, as shown in Figure 7.21. In practice, this threshold is already effectively applied for well-reconstructed events, as shown in Figure 7.22, where reconstructed momenta rarely fall below 100 MeV. These events with low true pion momentum are effectively excluded from the selection due to their short track lengths, which prevent the calculation of key BDT variables. Consequently, true low pion momentum events that do get selected typically involve either the wrong particle being identified as the pion candidate or reconstruction failures, such as merged pion and Michel electron tracks. The smearing effect arising from such reconstruction failures is illustrated in Figure 7.23, which shows the distribution of reconstructed versus true pion azimuthal angle ϕ_π across bins of true pion momentum. Since ϕ_π is uncorrelated with pion kinematics, deviations from a diagonal structure indicate misreconstruction. This is evident below 100 MeV, where the distribution becomes distinctly non-diagonal.

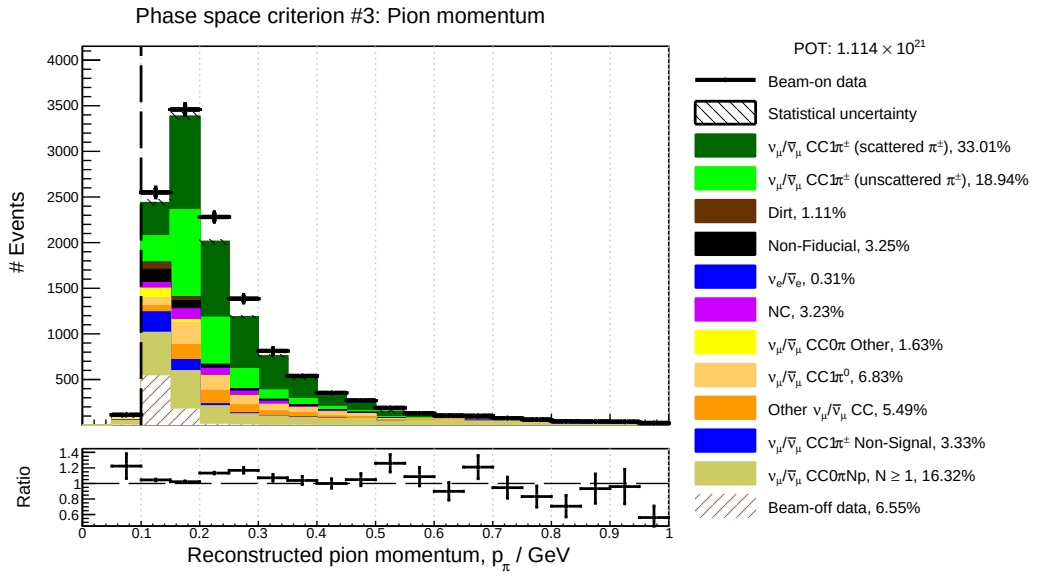

Fig. 7.21 Momentum distribution of reconstructed pion candidates. Events to the left of the line are rejected.

Excluding events with below-threshold true pion momentum introduces additional model dependence, as these events now contribute to the MC background that is subtracted from data. For a total cross-section measurement, not enforcing a lower momentum bound would be preferable, as it avoids this dependence. However, as seen in Figure 7.23, for differential cross-section measurements there is no reliable kinematic information in this region, and including such events would lead to additional smearing.

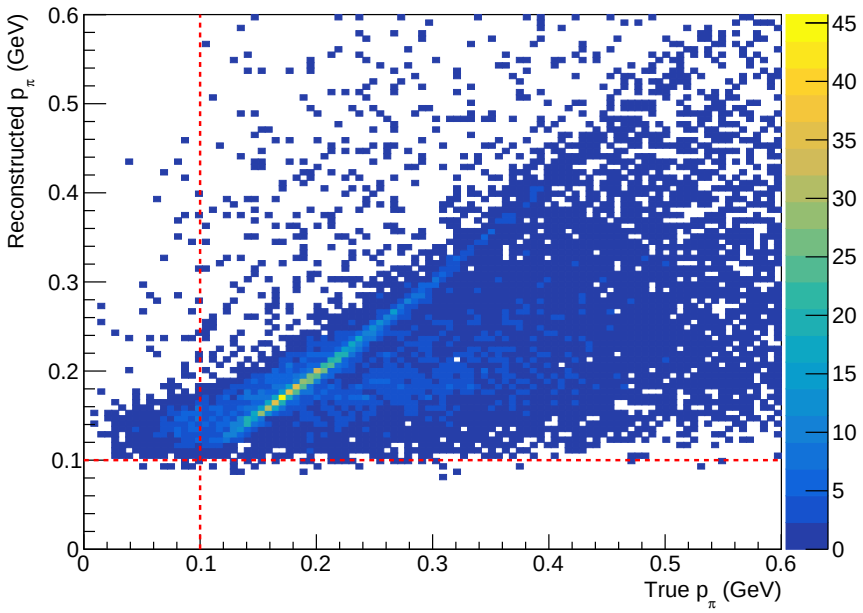

Fig. 7.22 True versus reconstructed charged pion momentum for selected signal events. The red lines show the 100 MeV phase space restriction, applied consistently to both true and reconstructed pion momentum.

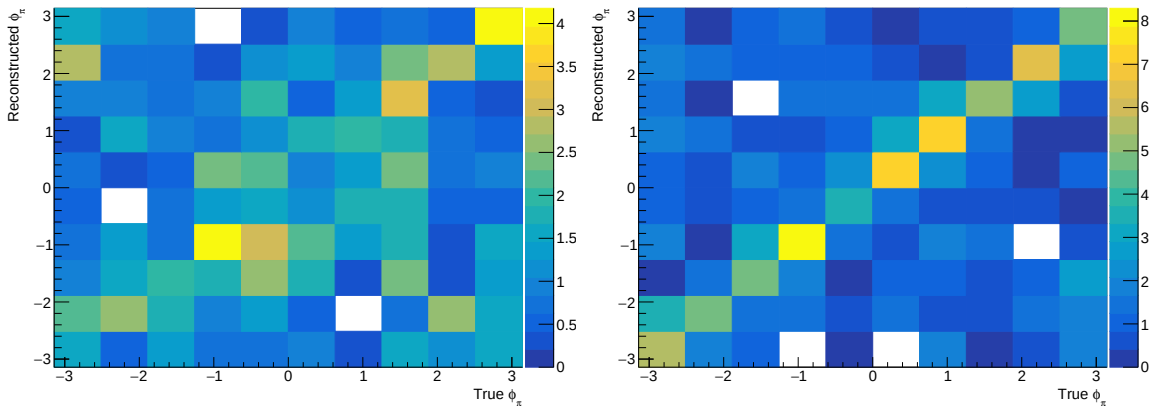

(a) $80 \leq p_\pi < 100$ MeV (b) $100 \leq p_\pi < 120$ MeV

Fig. 7.23 True versus reconstructed pion azimuthal angle ϕ_π in different regions of true pion momentum.

This requirement marks the end of the general selection used for the total and angular differential cross sections. One additional criterion each is enforced for the selections used to calculate the muon and pion momentum differential cross sections.

7.6.4 Pion Momentum Subset

The momentum of pions is measured using a subset of events rich in unscattered pions that have come to rest. This subset is created by applying a -0.03 minimum threshold on the unscattered pion BDT score, shown in Figure 7.24. As with previous distributions, this is presented with full statistical and systematic uncertainties. While the data points generally fall within the shaded uncertainty bands, some systematic shape differences are observable. Most notably, the simulation under-predicts the data to the right of the selection threshold. These discrepancies indicate that pion scattering and secondary interactions, to which the BDT is sensitive, are not perfectly modelled by the central value simulation. However, the fact that the data remains within the grey bands suggests that the systematic uncertainty treatment, described in Chapter 8, provides a sufficiently conservative estimate to account for these modelling limitations. Relevant here, beyond general uncertainties on flux, detector, and interaction modelling, are uncertainties on the pion–argon interaction cross section. The event-level impact of the BDT threshold is illustrated in Figure 7.25, which demonstrates that this selection step creates an unscattered-enhanced sample by excluding a significant fraction of events that show signs of pion scattering, such as visible kinks in the track topology, secondary vertex activity, or the absence of a clear Bragg peak.

The pion momentum for this subset is estimated from the track range. The accuracy of this estimator is characterised by the resolution, defined as the standard deviation of the relative difference δ_p between reconstructed and true momentum for correctly identified pion tracks:

$$\delta_p = (p^{\text{reco}} - p^{\text{truth}})/p^{\text{truth}}. \tag{7.4}$$

This yields a resolution of $\sigma = 0.20$ for the δ_p distribution of the simulated subset. Figure 7.26 shows the differences between the reconstructed and true charged pion momentum for simulated events that pass or fail the unscattered pion BDT requirement. The same range-based momentum estimation is applied to all events, with the latter group exhibiting a biased and down-smeared distribution, which arises from momentum being underestimated for scattered charged pions. Excluding scattered pions is therefore necessary to accurately estimate the momentum from the track length.

The signal definition remains the same for the cross-section measurement performed as a function of pion momentum, but the selected unscattered pions are generally of lower energy. Figure 7.27 presents the true momentum distributions for scattered and unscattered $\pi^{\pm}$ in simulated signal events. The extractable pion momentum differential cross section using unscattered pions is thus limited to lower energies.

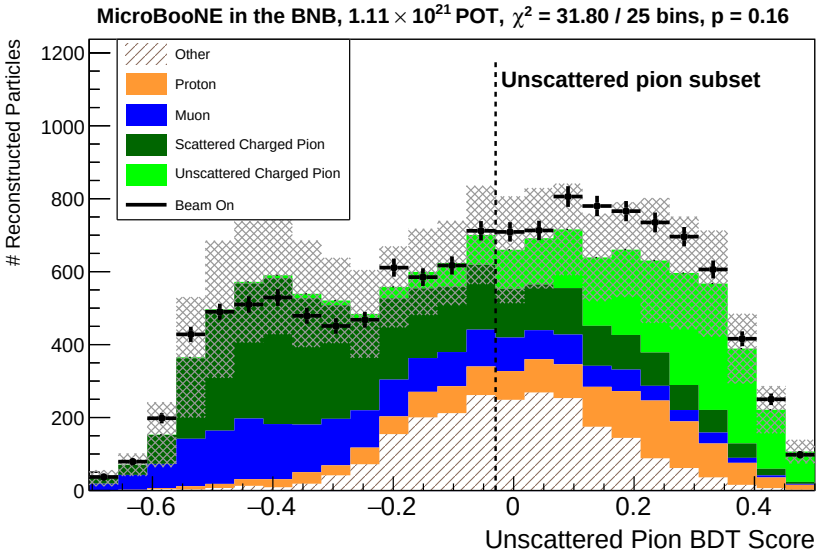

Fig. 7.24 Unscattered pion BDT scores for reconstructed particles, showing the predicted distribution as a stacked histogram and the data distribution as black dots. Only particles that passed the general selection are shown. Statistical and systematic uncertainties on the stacked histogram prediction, as described in Chapter 8, are shown as grey shaded bands. Events to the left of the line are rejected.

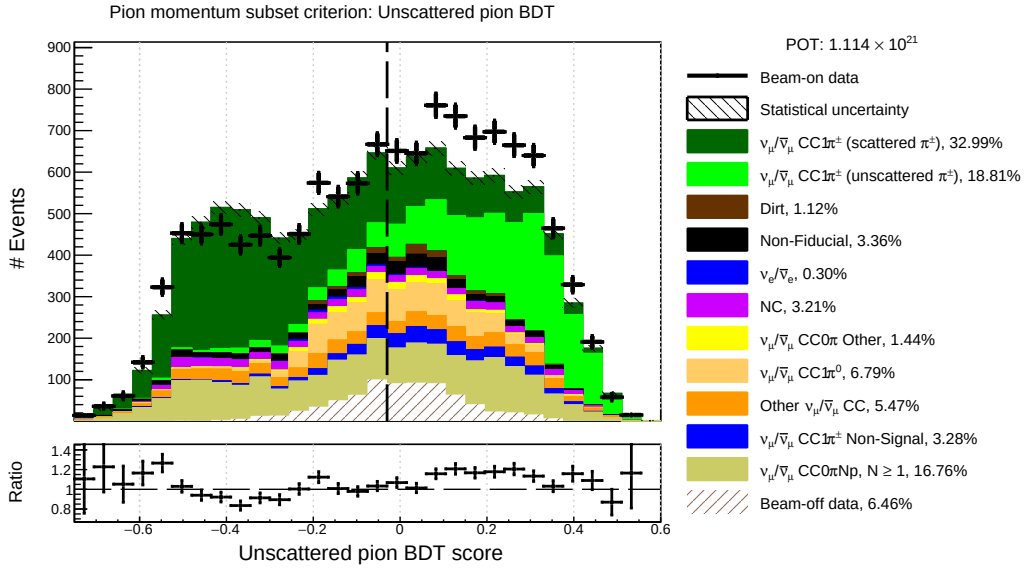

Fig. 7.25 Unscattered pion BDT response. Events to the left of the line are rejected.

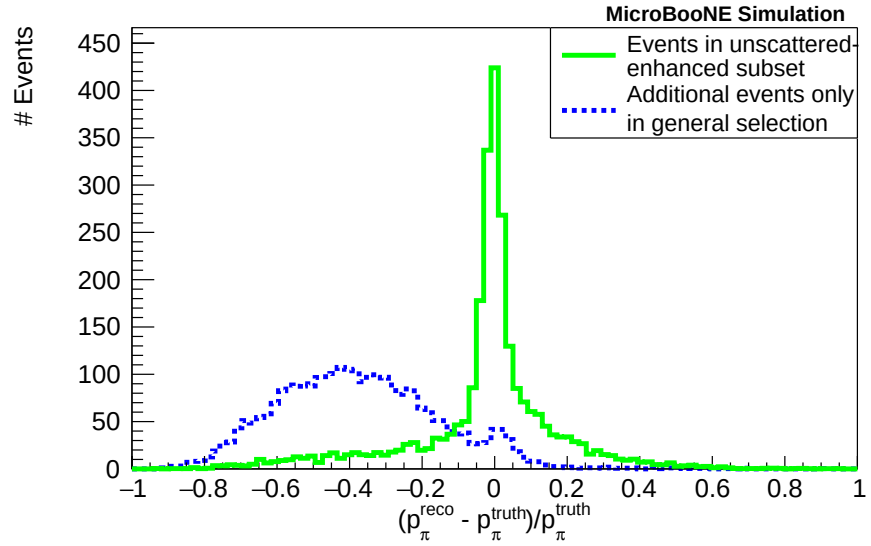

Fig. 7.26 The relative difference between true and reconstructed pion momentum deviations as defined in Equation (7.4) for correctly identified pion candidates in selected signal events, with green representing events passing the unscattered pion BDT threshold and blue representing all other events in the general selection. Together they show all events in the general selection.

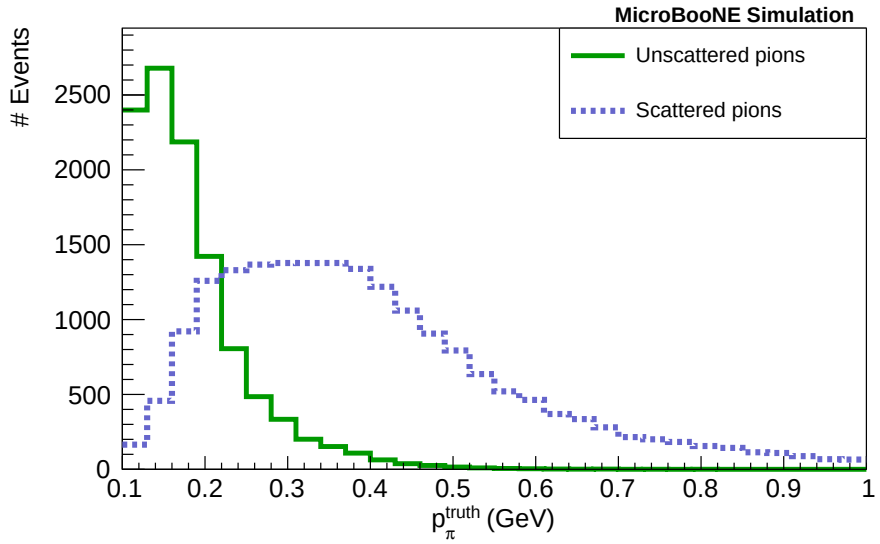

Fig. 7.27 True pion momentum distribution of all signal events, showing contributions from scattered and unscattered charged true pions as predicted by GENIE + GEANT4.

7.6.5 Muon Momentum Subset

Some previous MicroBooNE analyses have employed both range-based and MCS muon momentum estimation techniques [235–237, 186]. Recent results, such as the single

differential muon momentum cross section for CC π^0 events reported in Ref. [186], have highlighted significant shape discrepancies between data and simulation. These discrepancies are found for uncontained muons, for which MCS is used to estimate momentum, and are not observed in fully contained muons. Although uncontained muons are typically of higher energy, which introduces some physical differences between the sets of muons, it is likely that the discrepancies arise from shortcomings of the MCS implementation itself.

Figure 7.28 compares the relative momentum resolution, defined in Equation (7.4), between contained muons estimated from range and uncontained muons estimated using MCS. The range-based estimation achieves a much better resolution of $\sigma = 0.08$, compared to $\sigma = 0.29$ for the MCS method. Consequently, the cross section as a function of muon momentum reported in this analysis uses only the more accurate range-based technique. The additional requirement is enforced in Figure 7.30 and shows significant improvement in data-MC agreement. The trade-off for this is a reduction in the number of considered events for this differential cross section. As for the pion momentum subset, the signal definition remains unchanged, but the muon momentum distribution is lower for fully contained events, as shown in Figure 7.29.

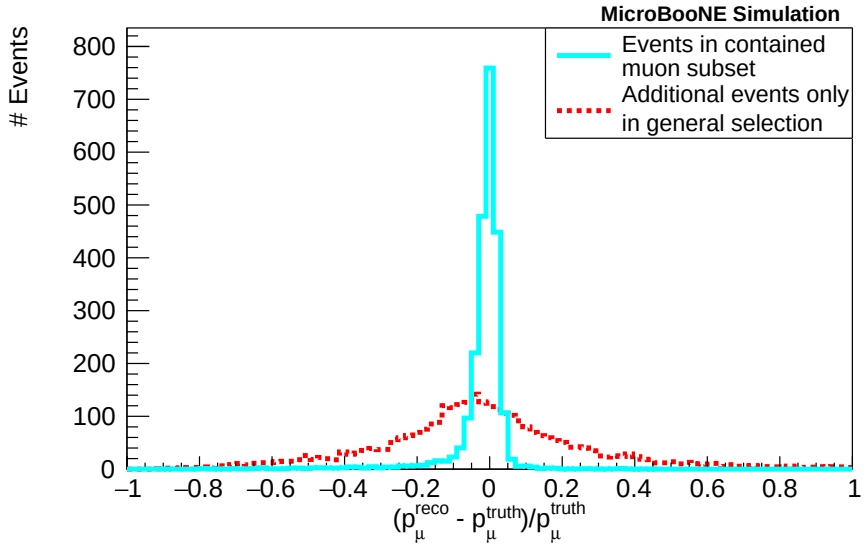

Fig. 7.28 The relative difference between true and reconstructed muon momentum for correctly identified muon candidates in selected signal events, with cyan being contained and red being uncontained muons. Together they show all events in the general selection.

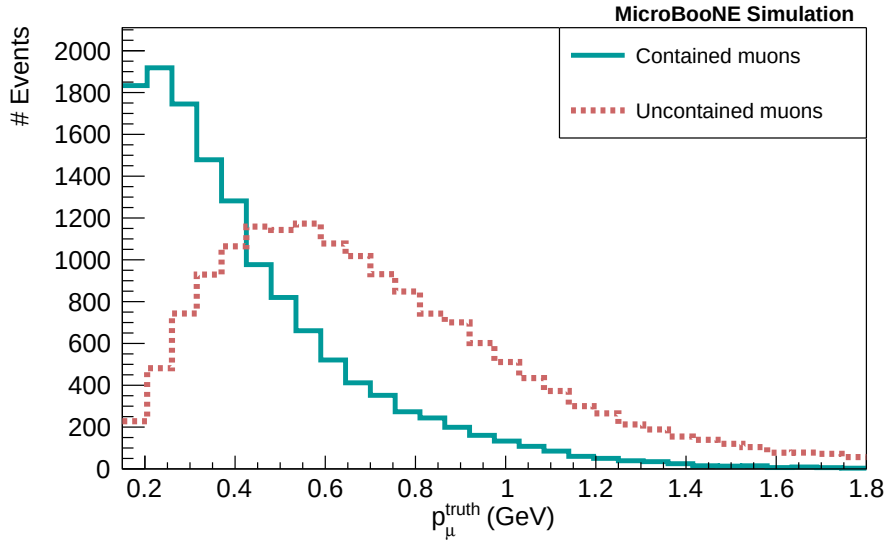

Fig. 7.29 True muon momentum distribution of all signal events, distinguishing between contained and uncontained true muons as predicted by GENIE + GEANT4.

7.6.6 Selection Performance

The selection performance is assessed in terms of efficiency, purity, and the ability to correctly select unscattered pions. Efficiency is defined as the fraction of signal events that are selected. Purity is the fraction of selected events that are signal events. The unscattered charged pion fraction is the fraction of selected signal events that have a charged pion that does not interact beyond ionisation with the argon and comes to rest in the detector. Figure 7.31 shows the impact of each selection criterion on these metrics with the additional momentum subsets shown as the last two points.

Figure 7.32 shows that the kinematic variables of the simulated GENIE events are well reconstructed along the diagonal of the confusion matrices, which compare the reconstructed quantities to their corresponding true values.

In addition to selecting events with the correct set of final-state particles, the analysis must accurately identify which track corresponds to the muon and which to the pion. Table 7.5 highlights the strong dependence of this identification on the relative track lengths of the two particles. The typically lower momentum of pions compared to muons, combined with their higher rate of nuclear interactions, makes selecting the exiting track as the muon a powerful strategy for particle identification. Similarly, even for the muon BDT-based selection, which does not use particle length as an input, the relative track lengths are important. As the table shows, when the pion track is longer than the muon track, the ability to distinguish between them is

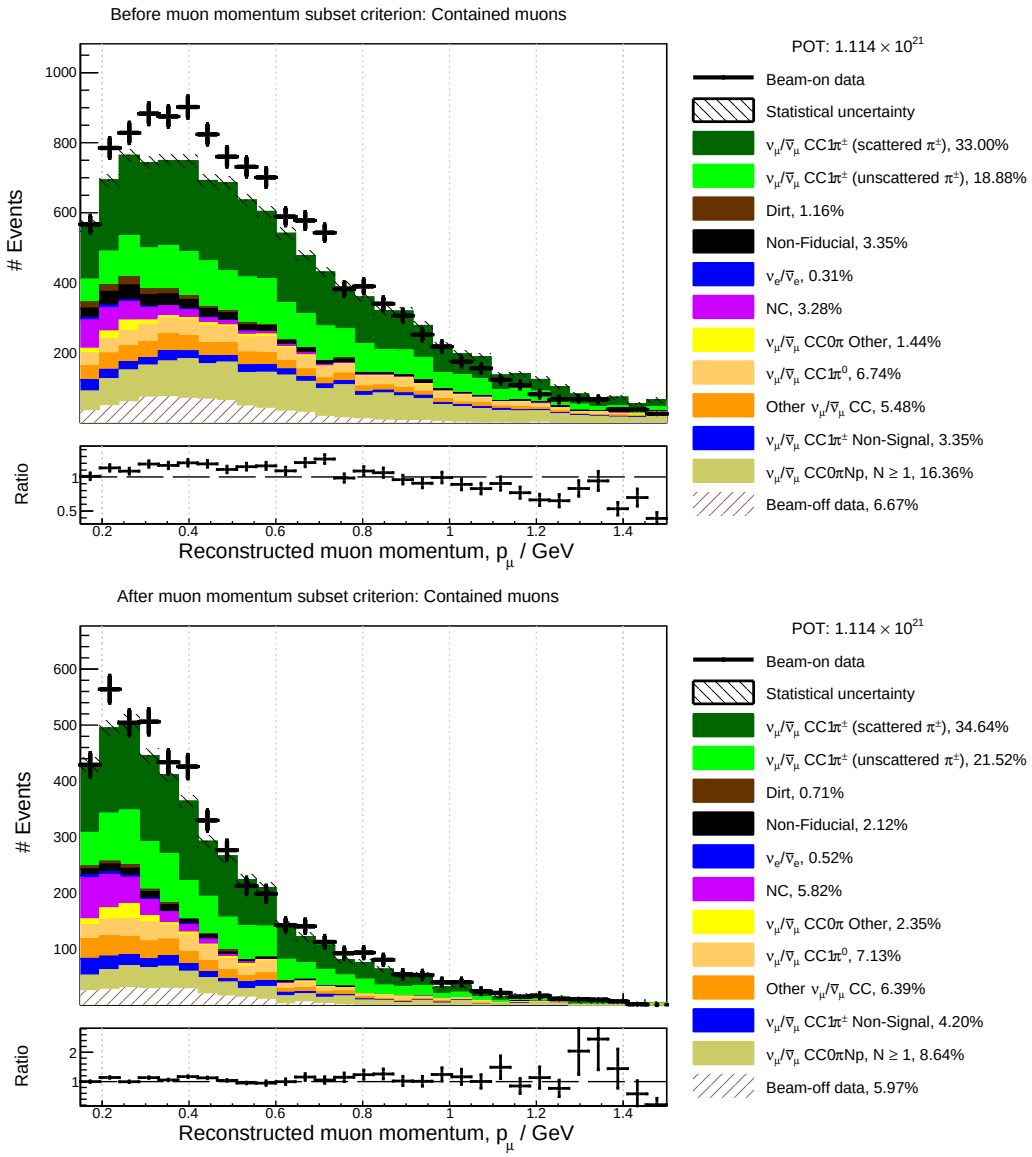

Fig. 7.30 Muon momentum of all reconstructed muon candidates (left) and of contained muon candidates only (right).

reduced. However, such events represent only a small fraction of the overall signal, and this selection provides robust separation in the phase space regions where most events lie.

A step-by-step summary of the data and predicted event counts, together with their data–simulation ratios, is shown in Table 7.6. This highlights once more the trade-off in efficiency for the dedicated subsets, as well as their higher data–simulation ratios, particularly for the pion momentum subset.

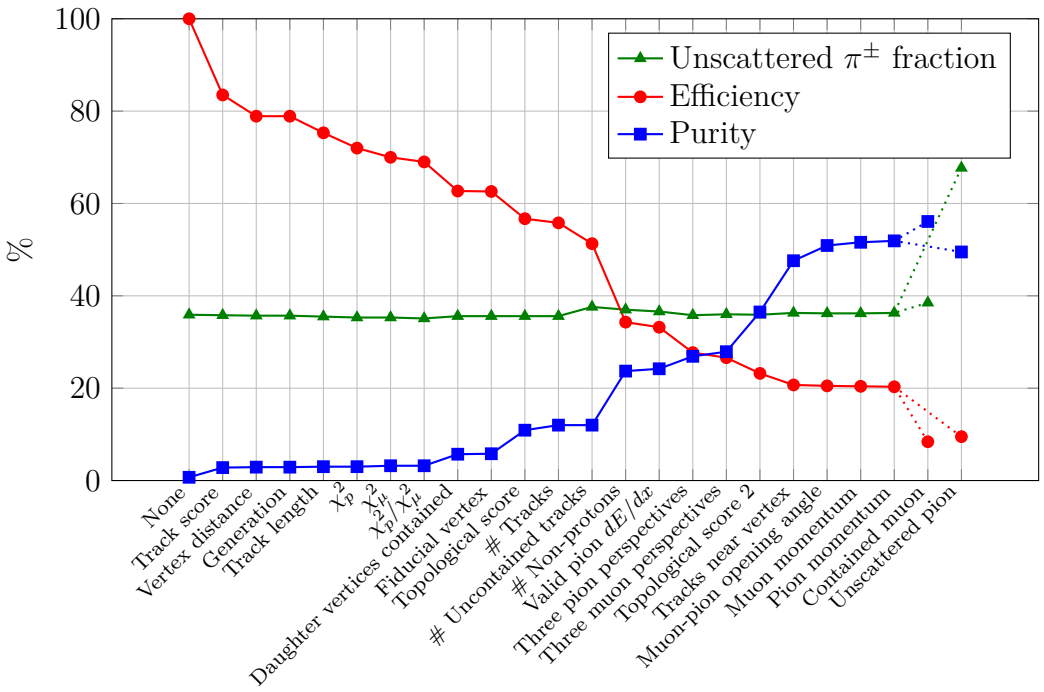

Fig. 7.31 Efficiency, purity, and the unscattered $\pi^{\pm}$ fraction at each selection criterion. The final two points are the momentum subsets deriving from the general selection, which ends with the 'Pion momentum' phase-space requirement.

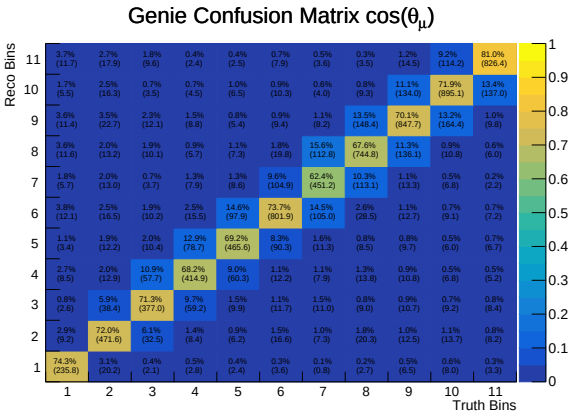

(a) Cosine of the muon angle

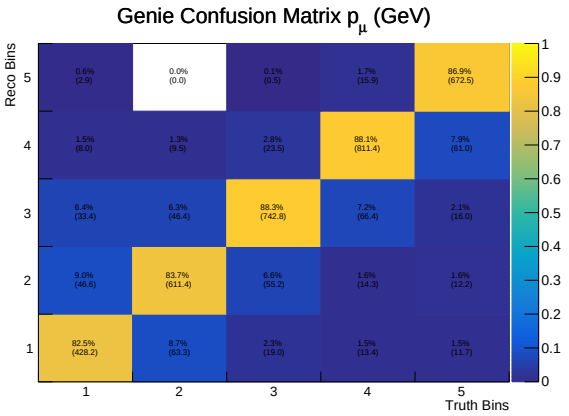

(b) Muon momentum

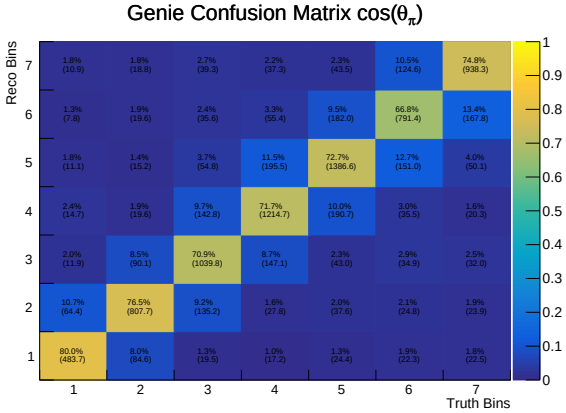

(c) Cosine of the pion angle

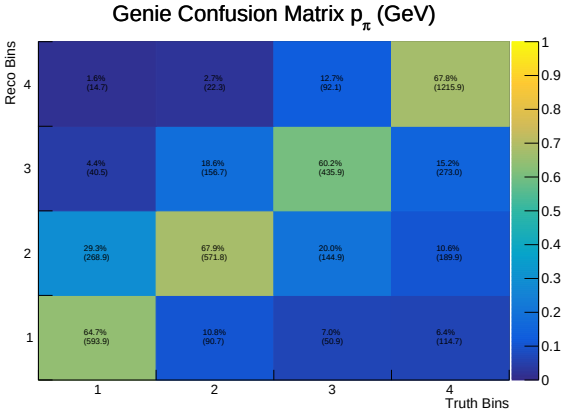

(d) Pion momentum

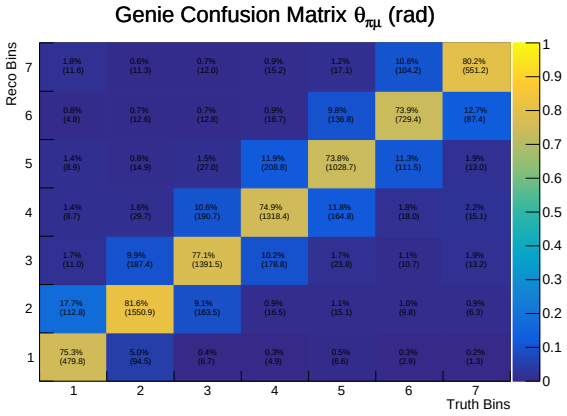

(e) Muon-pion opening angle

Fig. 7.32 Confusion matrices of GENIE CV signal events for the five kinematic variables.

	$R_\mu > R_\pi$	
	No	**Yes**
Fraction of Correct Muon Candidates		
Contained Muons	53% of 408	86% of 2396
Uncontained Muons	95% of 76	99% of 3319
Fraction of Correct Pion Candidates		
Unscattered Pions	59% of 398	88% of 3554
Scattered Pions	65% of 86	95% of 2162

Table 7.5 Fractions of correctly identified muon and pion candidates from selected GENIE signal events, categorized by whether the true track length R of the muon exceeds that of the pion. Results are shown for contained and uncontained muons as well as scattered and unscattered charged pions as simulated by GEANT4. The number of simulated events in each category is also shown.

Finally, a breakdown of the topologies making up the selected simulated events is shown in Table 7.7, which shows that the single largest contribution to the backgrounds comes from muon (anti-)neutrino CC events with zero pions and at least one proton, arising primarily from the misidentification of proton tracks as charged pions.

The next chapter will discuss the uncertainties in this analysis and show that they are especially large in the low-pion-momentum range, which makes up a significant portion of the pion momentum subset.

General Selection	**Prediction** [$\times 10^3$]			
Criteria for Runs 1-5	**Signal**	**Background**	**Data** [$\times 10^3$]	**Ratio**
Particle-level Preselection				
None	30.5 (100%)	4552.3 (100%)	4108.5 (100%)	0.9
Track score	25.5 (83.5%)	885.1 (19.44%)	881.5 (21.45%)	0.97
Vertex distance	24.0 (78.9%)	817.1 (17.95%)	815.7 (19.85%)	0.97
Generation	24.0 (78.9%)	817.0 (17.95%)	815.6 (19.85%)	0.97
Track length	23.0 (75.3%)	752.3 (16.53%)	752.6 (18.32%)	0.97
χ^2_p	22.0 (72.0%)	711.1 (15.62%)	711.4 (17.32%)	0.97
χ^2_μ	21.4 (70.0%)	646.9 (14.21%)	646.3 (15.73%)	0.97
χ^2_p/χ^2_μ	21.0 (69.0%)	627.2 (13.78%)	625.4 (15.22%)	0.96
Event-level Preselection				
Particle start	19.1 (62.7%)	317 (6.96%)	339.0 (8.25%)	1.01
Fiducial vertex	19.1 (62.6%)	309.7 (6.80%)	331.9 (8.08%)	1.01
Topological score	17.3 (56.7%)	141.5 (3.11%)	161.0 (3.92%)	1.01
Charged Pion Selection				
# Tracks ≥ 2	17.0 (55.8%)	124.6 (2.74%)	140.0 (3.41%)	0.99
# Uncontained tracks ≤ 1	15.7 (51.3%)	114.9 (2.52%)	129.8 (3.16%)	0.99
# Non-protons $= 2$	10.5 (34.3%)	33.6 (0.74%)	45.7 (1.11%)	1.04
Valid pion dE/dx	10.1 (33.2%)	31.7 (0.70%)	43.2 (1.05%)	1.03
Pion not in gap	8.5 (27.7%)	23.0 (0.51%)	32.9 (0.80%)	1.04
Muon not in gap	8.1 (26.6%)	21.0 (0.46%)	30.5 (0.74%)	1.05
Topological score 2	7.1 (23.2%)	12.3 (0.27%)	20.0 (0.49%)	1.04
Tracks near vertex	6.3 (20.7%)	7.0 (0.15%)	13.9 (0.34%)	1.05
Phase Space Requirements				
Muon-pion opening angle	6.3 (20.5%)	6.0 (0.13%)	12.9 (0.31%)	1.05
Muon momentum	6.2 (20.4%)	5.8 (0.13%)	12.7 (0.31%)	1.05
Pion momentum	6.2 (20.3%)	5.8 (0.13%)	12.6 (0.31%)	1.05
Subset 1: Muon Momentum Criterion applied to general selection				
Contained muon	2.6 (8.4%)	2.0 (0.04%)	4.9 (0.12%)	1.07
Subset 2: Pion Momentum Criterion applied to general selection				
Unscattered pion	2.9 (9.5%)	2.9 (0.06%)	6.5 (0.16%)	1.12

Table 7.6 GENIE predicted signal and background event counts, data event count and the data-MC ratio after every criterion for the general and the two subset selections. Percentages indicate the fraction of events remaining after each criterion is applied, normalised to the pre-selection total. The results for each selection are coloured green.

Category			**Fraction**
Signal			
CC	$\nu_\mu/\bar{\nu}_\mu$	$1\pi^\pm$ (unscattered)	33.1%
		$1\pi^\pm$ (scattered)	18.8%
Background			
CC	$\nu_\mu/\bar{\nu}_\mu$	0πNp, N ≥ 1	16.8%
		0π other	1.4%
		$1\pi^0$	6.7%
		$1\pi^\pm$ (non-signal)	3.3%
		Other	5.5%
	$\nu_e/\bar{\nu}_e$		0.3%
NC			3.2%
Non-Fiducial			3.4%
External			6.4%
Dirt			1.1%

Table 7.7 Breakdown by category of selected simulated events. External are cosmic background events from the beam-off data.

Chapter 8

Binning and Uncertainties

This chapter describes the bin structure of the differential cross sections of the analysis, the treatment of uncertainties, and a sideband check.

8.1 Bin Structure

The predicted distribution histogram ρ^i is constructed for the reconstructed kinematic variable x^i. Here, $i \in \{1, \ldots, N_{\text{var}}\}$ labels the five variables considered in this analysis: muon angle, muon momentum, pion angle, pion momentum, and the muon-pion opening angle. Each variable x^i has N^i_{bins} discrete bins indexed by $a \in \{1, \ldots, N^i_{\text{bins}}\}$. Each bin covers a phase space

$$\Delta x^i_a = x^i_{a+1} - x^i_a, \tag{8.1}$$

where $x^i_1, \ldots, x^i_{N^i_{\text{bins}}+1}$ are the bin edges, listed in Table 8.1. Bin edges were chosen with the aim of maintaining a sufficient number of events in each bin and considering the resolutions of the kinematic variables. The momentum variables, for instance, have fewer bins, concentrated in the lower momentum regions where most events lie. The last bins of the momentum variables are open-ended, but a finite upper limit is used when normalising the cross-section measurements by bin width.

The content of bin a in histogram ρ^i is then given by

$$\rho^i_a = d^{\text{off},i}_a + s^{\nu,i}_a + s^{\text{dirt},i}_a, \tag{8.2}$$

where $d^{\text{off},i}_a$ is the event count from recorded beam-off background data, $s^{\nu,i}_a$ is the GENIE-predicted central value (CV) neutrino interaction contribution, and $s^{\text{dirt},i}_a$ is

Bin	Total	$\cos(\theta_\mu)$	p_μ / GeV	$\cos(\theta_\pi)$	p_π / GeV	$\theta_{\mu\pi}$ / rad
1	All	$[-1, -0.27)$	$[0.15, 0.23)$	$[-1, -0.47)$	$[0.10, 0.16)$	$[0, 0.49)$
2	-	$[-0.27, 0.29)$	$[0.23, 0.32)$	$[-0.47, 0)$	$[0.16, 0.19)$	$[0.49, 0.93)$
3	-	$[0.29, 0.46)$	$[0.32, 0.45)$	$[0, 0.39)$	$[0.19, 0.22)$	$[0.93, 1.26)$
4	-	$[0.46, 0.58)$	$[0.45, 0.66)$	$[0.39, 0.65)$	$[0.22, 0.6/\infty)$	$[1.26, 1.57)$
5	-	$[0.58, 0.67)$	$[0.66, 1.5/\infty)$	$[0.65, 0.84)$	-	$[1.57, 1.88)$
6	-	$[0.67, 0.77)$	-	$[0.84, 0.93)$	-	$[1.88, 2.21)$
7	-	$[0.77, 0.82)$	-	$[0.93, 1]$	-	$[2.21, 2.65]$
8	-	$[0.82, 0.88)$	-	-	-	-
9	-	$[0.88, 0.93)$	-	-	-	-
10	-	$[0.93, 0.97)$	-	-	-	-
11	-	$[0.97, 1]$	-	-	-	-

Table 8.1 Bin-range definitions for each observable. The last bins of the momentum variables are open-ended but use a finite bin limit for cross-section calculations.

the contribution from simulated out-of-detector neutrino interactions with surrounding material.

Uncertainties are handled using the MicroBooNE-internal tool *xsec_analyzer*, developed by Steven Gardiner and described in part in Ref. [238]. It uses a block-matrix approach to presenting results, allowing covariances to be reported not only within each differential cross section but also between them. To facilitate this, the individual histograms ρ^i for each reconstructed variable are concatenated into a single stacked vector:

$$\mathbf{p} = \begin{pmatrix} \rho^1 \\ \rho^2 \\ \vdots \\ \rho^{N_{\text{var}}} \end{pmatrix}, \tag{8.3}$$

as illustrated on the right side of Figure 8.1. The associated covariance matrix $\mathbf{V}_{ab}$ is constructed by evaluating bin-to-bin variations across a set of systematically varied universes $u = 1, \ldots, N_{\text{univ}}$, each representing a modified version $\mathbf{p}^u$ of the CV prediction $\mathbf{p}^{\text{CV}}$. A covariance matrix is then computed across these variations:

$$\mathbf{V}_{ab} = \frac{1}{N_{\text{univ}}} \sum_{u=1}^{N_{\text{univ}}} \left[\mathbf{p}_a^u - \mathbf{p}_a^{CV}\right] \left[\mathbf{p}_b^u - \mathbf{p}_b^{CV}\right]. \tag{8.4}$$

The blockwise structure of the covariance matrix is illustrated on the left side of Figure 8.1.

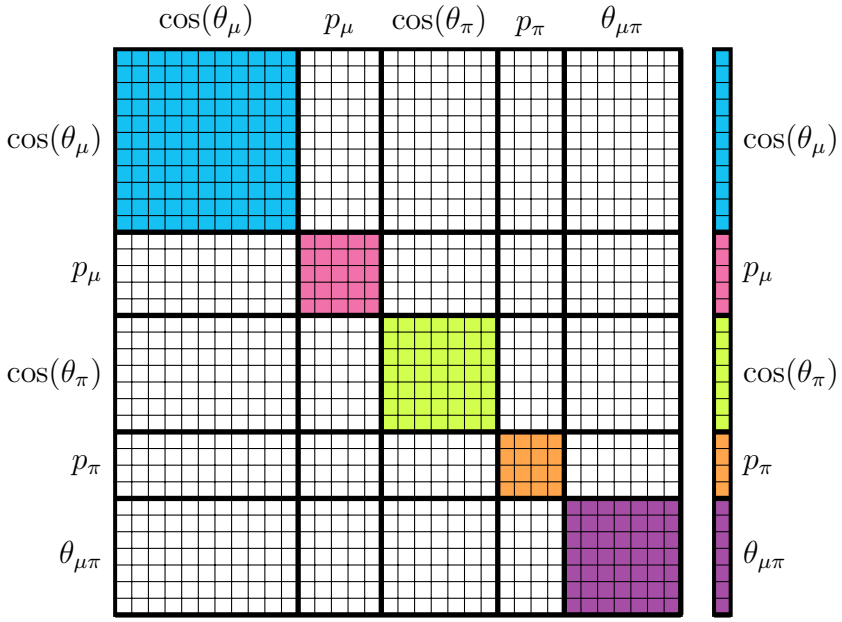

Fig. 8.1 Illustration of a concatenated one-dimensional histogram (right), which combines the bins of all kinematic variables. An example would be a histogram of data or predicted event counts. On the left is a block matrix constructed from this vector, such as a covariance matrix. The coloured blocks indicate covariances within each differential cross section, while the white regions show covariances between bins of different kinematic variables.

8.2 Uncertainties

The following sections briefly lay out the uncertainties considered in this analysis, starting with those using Equation (8.4), which are categorised as either *unisims* or *multisims*. Here, *unisims* refer to single-parameter variations, where a single change, for example a variation of a parameter in the detector simulation or the use of an alternative model, is compared across one or two universes. *Multisims* correspond to ensembles of MC universes in which several parameters are varied simultaneously according to their uncertainties, allowing for efficient estimation of the combined change caused by possibly correlated sources of uncertainty. Following this, the treatment of fully correlated uncertainties arising from two normalisation parameters is described. Finally, the handling of statistical uncertainties is explained.

8.2.1 Flux

As described in Section 6.1.1, the MicroBooNE flux simulation is an updated version of the one developed by MiniBooNE. It uses the same set of systematic uncertainties, of which this section provides a brief overview [98, 97, 239].

8.2.1.1 Beam Unisims

The non-hadron-production contributions encompass simulation uncertainties not arising from proton collisions with the beryllium target. This includes uncertainties on the pulsed currents applied to the focusing horn and the skin effect, which is the tendency of alternating currents to be strongest close to the surface of a conductor and to fall off exponentially with depth. This skin depth is a source of uncertainty that affects the magnetic field produced. Finally, uncertainties for the pion and nucleon cross sections on beryllium and aluminium are considered. The unisims are produced by varying each parameter by $\pm 1\sigma$, or by switching between models for the skin depth, producing sets of two alternative universes per parameter (one for skin depth).

Event weights are calculated per neutrino flavour ($\nu_\mu, \nu_e, \bar{\nu}_\mu, \bar{\nu}_e$) and in bins of true neutrino energy. For each unisim with two variations, the weight assigned to an event is given by the ratio of the shifted flux prediction to the CV prediction in that bin:

$$w^u = \begin{cases} 1 + r^u \left(\dfrac{\Phi_{+1\sigma}}{\Phi_{\mathrm{CV}}} - 1 \right), & r^u \geq 0, \\ 1 + |r^u| \left(\dfrac{\Phi_{-1\sigma}}{\Phi_{\mathrm{CV}}} - 1 \right), & r^u < 0. \end{cases} \tag{8.5}$$

For unisims with only a single variation, such as the skin depth, the missing opposite shift is constructed by reflecting the available variation about the CV. Random values r^u, drawn from a standard normal distribution across $u \in \{1, 2, \ldots, 1000\}$ universes, then vary the strength of the alternative prediction. The final weight in each universe is the product of the contributions from all individual unisims, creating a combined estimate of the uncertainty.

8.2.1.2 Hadron Production

As described in Section 6.1.1, the neutrino flux is produced mainly via the production and decay of pions, with smaller contributions coming from kaons. Uncertainties in the production of these hadrons constitute the largest source of flux uncertainty. To estimate charged pion production uncertainties, the double-differential cross sections

reported by the HARP experiment [128] are varied by sampling from a multivariate Gaussian distribution using the provided covariance matrix, which encodes correlated fluctuations in pion momentum and angle bins. A spline interpolation is then applied to the varied cross sections, enabling smooth comparisons with the CV Sanford–Wang parameterisation described in Section 6.1.1. The ratio of the varied cross section to the central value yields the event weight for each universe [239].

A more direct approach is used for K^+ and K^0 production. Their cross sections are randomly varied according to the covariance matrices of the fitted parameters of their respective Feynman and Sanford–Wang parameterisations. Weights are again calculated by comparing the central cross section to the randomly varied ones. For K^-, a simpler 100% normalisation uncertainty is applied due to their small impact, which is propagated by generating weights from a Gaussian distribution. The final weights are combined with the beam unisim weights to produce a single set of 1000 alternative universes for the MC.

8.2.2 Interaction Model

Uncertainties on the CV interaction generator, the MicroBooNE-tune of GENIE using T2K data as described in Section 6.1.2, are assessed through multisim variations of GENIE parameters and unisim variations with alternative GENIE configurations or other generators.

8.2.2.1 GENIE Multisims

A multisim approach is used for the majority of interaction model uncertainties by simultaneously varying a set of 44 GENIE model parameters, listed in Ref. [240], across $u \in \{1, 2, \ldots, 600\}$ universes. Each universe represents a set of varied parameters:

$$\boldsymbol{\theta}^{(u)} = \left(\theta_1^{(u)}, \ldots, \theta_{44}^{(u)}\right), \tag{8.6}$$

where each $\theta_j^{(u)}$ was drawn independently from a Gaussian around the parameter central value:

$$\theta_j^{(u)} \sim \mathcal{N}\left(\theta_j^{\mathrm{CV}}, \sigma_j^2\right), \tag{8.7}$$

with σ_j being the standard deviation. For parameters tuned by MicroBooNE, σ_j comes from the fit to the T2K data, while for untuned parameters, the default uncertainties determined by the GENIE collaboration from fits to data are used. Event weights are calculated for the alternative parameter universes using the GENIE Reweight package.

8.2.2.2 GENIE Unisims

A smaller set of uncertainties is assessed with unisims, where a single parameter is replaced by an alternative model prediction. These unisims cover changes to the angular distributions of final-state nucleons in 2p2h interactions (isotropic changed to $\cos^2\theta$ distribution), photons from radiative Δ decays (isotropic to $\cos^2\theta$), and pions from Δ resonance decays (RS prediction to isotropic). The total cross sections for CC and NC coherent pion production are individually scaled up by 100%. The strength of the CCQE RPA correction is shifted up and down by one standard deviation. Shape-only variations of the CCQE form factors are considered for both the axial and vector terms (axial: dipole to z-expansion, vector: BBA07 [80] to dipole). Finally, the lepton kinematics in CC 2p2h events are compared between the MicroBooNE-tuned and untuned València model [240].

8.2.2.3 Second-Class Current Unisim

F_V^3 and F_A^3 are hypothetical second-class current form factors. Upper limits constrain them to be small, but they could still have a few-percent effect on the total CCQE cross section [241]. The NEUT [242] generator is used to evaluate the CCQE cross section with these form factors. By comparing it with GENIE cross sections without the second-class current contributions, alternative event weights are calculated [140].

8.2.2.4 NuWro Unisim

Cross-section extraction tests using simulated events produced with the NuWro interaction generator, described in Section 9.3.2, show that the uncertainties on the GENIE CV prediction, as described above, are not sufficient to consistently extract cross sections close to the true underlying kinematic distributions of the NuWro mock data. Similar issues with uncertainty coverage have been reported in Refs. [237, 243], and, following their example, an additional unisim variation representing the difference between the GENIE CV and the NuWro prediction is included.

8.2.3 Hadronic Reinteractions

Hadrons produced in neutrino interactions can undergo secondary interactions with the liquid argon, altering the observed energy and topology of the event. For example, the absorption or inelastic scattering of charged pions, often accompanied by the production of undetected nucleons, can bias momentum estimation if not properly modelled.

Similarly, charge exchange to neutral pions may prevent signal events from being correctly identified. These effects, collectively referred to as hadronic reinteractions, are an important source of systematic uncertainty, particularly for pion kinematics which are highly sensitive to such processes. In MicroBooNE, particle transport is simulated using GEANT4, and uncertainties on hadronic pion and nucleon cross sections are assessed using the Geant4Reweight framework [244]. Instead of regenerating simulated samples under different hadronic interaction models, Geant4Reweight applies a reweighting procedure: events are first generated under the CV model, and then weights are computed to approximate their phase-space distributions under varied interaction models. Elastic and inelastic cross sections are varied across momentum ranges, with the GEANT4 predictions fitted to external data. Best-fit parameters and associated uncertainties are derived from the resulting covariance matrix. These are propagated through 1000 reweighted universes, with MicroBooNE reweighting the transport of charged pions and protons in argon for the channels listed in Table 8.2 [245].

Reweighted Channels	**Definition**
Elastic Channels	
p: Elastic	$p + A \to p + A$
$\pi^{\pm}$: Elastic	$\pi^{\pm} + A \to \pi^{\pm} + A$
Inclusive Inelastic Channels	
p: Total Inelastic	$p + A \to A' + X$
Exclusive Inelastic Channels	
$\pi^{\pm}$: Quasielastic	$\pi^{\pm} + A \to \pi^{\pm} + A' + kN$
$\pi^{\pm}$: Absorption	$\pi^{\pm} + A \to A' + kN$
$\pi^{\pm}$: Single Charge Exchange	$\pi^{\pm} + A \to \pi^{0} + A' + kN$
$\pi^{\pm}$: Double Charge Exchange	$\pi^{\pm} + A \to \pi^{\mp} + A' + kN$
$\pi^{\pm}$: Pion Production	$\pi^{\pm} + A \to m\pi + A' + kN$

Table 8.2 Reweighted GEANT4 channels. A is the initial nucleus and A' is the resulting nucleus after the interaction. X is the set of possible inelastic products. m is the number of outgoing pions and k is any number of knocked-out nucleons N.

8.2.4 Detector Variations

Separate MC samples are used to account for detector simulation uncertainties. This section provides an overview of the uncertainty estimation approaches for the wire response simulation, photon production and detection simulation, and the modelling of ion build-up in the detector [246].

8.2.4.1 Wire Response

Uncertainties in the wire response are assessed with a data-driven waveform modification method that operates directly on the Gaussian hits fitted to the real and simulated waveforms, defined by their total charge Q and their width σ. Changes in these two quantities are evaluated for four dedicated wire-modification variations [247]:

- **Drift-position dependence** x: This captures effects that vary primarily with drift distance, for example longitudinal diffusion, electron attenuation, and any residual drift-dependent response.
- **Transverse-position dependence** (y, z): This two-dimensional variation maps dependencies in the wire-plane dimensions.
- **Angular dependence in the XZ plane**: The angle of a track with respect to the transverse wire-plane direction (z here refers to the axis perpendicular to the drift direction x and the wire direction y in each plane).
- **Angular dependence in the YZ plane**: The angle of a track with respect to the wire direction in each plane.

The above variables are treated as uncorrelated because non-uniformities in the electric field due to the space-charge effect have been corrected to first order, as described in Section 5.2.3. The y- and z-dependences are considered together since they strongly depend on properties of individual wires, and effects such as non-responsive wires affect both dimensions in a correlated way.

Q and σ are measured using anode- and cathode-piercing cosmic muons throughout the detector volume. The detector simulation uses the CORSIKA [112] framework to generate cosmic muon events. For each variable, starting with the drift direction x, ratios of binned data and simulated calorimetric hit properties are computed:

$$R_i^Q = \left\langle Q^{\text{data}}(x) \right\rangle_i \,/\, \left\langle Q^{\text{sim}}(x) \right\rangle_i , \tag{8.8}$$

$$R_i^\sigma = \left\langle \sigma^{\text{data}}(x) \right\rangle_i \,/\, \left\langle \sigma^{\text{sim}}(x) \right\rangle_i , \tag{8.9}$$

where the value within each bin is the mean computed after iteratively truncating the distribution tails until the mean converges, thereby reducing the impact of asymmetric smearing. The ratio histograms are smoothed using spline fits. The same approach is used for the remaining three variables, except the hits are first corrected for effects along the drift dimension using the above-computed ratios. The variations along the

transverse dimensions y and z are treated together as the ratio of two-dimensional histograms.

A single alternative universe is computed for each of the four variables by modifying Q and σ of the Gaussians fitted to the simulated hits according to the computed ratios. The altered hits then undergo the remaining reconstruction chain in the same way as the unmodified CV sample. These alternative universes are used as unisims to assess the detector systematic variations.

8.2.4.2 Optical Response

As described in Section 6.1.4, a position-based photon visibility map is used to efficiently compute the probability of a photon being detected by a PMT at any point in the detector. Three detector variations of the optical response are produced by modifying the photon visibility maps [126]:

- **Light yield**: Comparisons with data indicate that the light yield, defined as the ratio of PMT-observed photons to reconstructed track length, is overestimated in the nominal simulation [126]. A downscaling of the scintillation light yield by 25% is applied as an alternative universe by uniformly rescaling the lookup map.
- **Rayleigh scattering**: The Rayleigh scattering length of VUV photons in LAr is varied by a position-dependent rescaling. The GEANT4 photon simulation is run once with the nominal Rayleigh scattering length of 60 cm and once with 120 cm. The ratio of these results is then used to rescale each voxel in the visibility map.
- **Photon attenuation**: This variation models position-dependent quenching and absorption responsible for the reduction in collected light near the anode and cathode. Starting with Run 3 and persisting in subsequent runs, declines in light yield are observed at both the anode and cathode. This effect is modelled by modifying the quenching and absorption lengths of photons in the simulation near these regions to reproduce the observed behaviour, producing an alternative photon visibility map.

All three optical variations are propagated through the full reconstruction chain, in the same way as the nominal simulation, and used as unisim uncertainties.

8.2.4.3 Ion Build-up

Two additional detector variations are used to account for uncertainties in the modelling of positive ion build-up in the detector:

- **Recombination**: Uncertainties in how energy loss dE/dx relates to the measured deposited charge dQ/dx are treated by altering the empirical parameter β of the Modified Box Model for electron-ion recombination described in Section 6.1.4. The variation was chosen to be conservative and to cover measured distortions of the electric field [247].

- **Space Charge Effect**: The MicroBooNE UV laser system is used to estimate the residual bias that remains after the space-charge correction described in Section 5.2.3 and Section 6.2.3 is applied [105]. This position-dependent bias is then used to calculate an alternative space-charge map.

8.2.5 Fully Correlated Uncertainties

Uncertainties on the overall normalisation factors are added as fractional deviations κ from the CV. This only uses the simulated components of s^{CV}, excluding the beam-off component [248]:

$$V_{ab} = \kappa^2 (s_a^{\nu} + s_a^{\mathrm{dirt}})(s_b^{\nu} + s_b^{\mathrm{dirt}}). \tag{8.10}$$

The following fully correlated uncertainties are considered:

- **Target:** A $\kappa = 1\%$ normalisation uncertainty is assumed on the number of argon nuclei in the fiducial volume of the detector.

- **Protons-On-Target:** A $\kappa = 2\%$ normalisation uncertainty is used to account for the uncertainty on the protons delivered to the target to produce the BNB. This uncertainty stems from the agreement observed between the two toroids monitoring the beam [98].

8.2.6 Statistical Uncertainties

Two-dimensional reconstructed event rate histograms are used to calculate the statistical uncertainties. Events that are in both bin a and b of the same one-dimensional data, beam-off, neutrino MC, or dirt MC histogram $x \in \{d, d^{\mathrm{off}}, s^{\nu}, s^{\mathrm{dirt}}\}$ fall into bin x_{ab} of the corresponding two-dimensional histogram. The two-dimensional histograms are needed to account for the fact that the same events are found in the different kinematic histograms and the statistical fluctuations in each bin are not independent Poisson distributions. Since the histograms are concatenated into one in the blockwise approach, statistical uncertainties must be computed using these 2D counts x_{ab} to accurately include inter-bin correlations [238].

The beam-off and MC samples have different weights for each run as they are scaled to the data. The beam-on data events always have unit weight. The MC samples also contain per-event weights resulting from the MicroBooNE GENIE tune. The 2D histogram entries are the sum over all event weights w^i for the set of events X_{ab}:

$$x_{ab} = \sum_{i \in X_{ab}} w^i, \tag{8.11}$$

and using Poisson statistics, the statistical uncertainties are obtained by summing the squared weights in each bin:

$$V_{ab}^{x\ \text{Stat.}} = \sum_{i \in X_{ab}} (w^i)^2. \tag{8.12}$$

This gives covariance matrices for the data statistical uncertainties $V^{\text{Data Stat.}}$ and the statistical uncertainties on the prediction:

$$V^{\text{Pred. Stat.}} = V^{\text{Neutrino MC Stat.}} + V^{\text{Dirt MC Stat.}} + V^{\text{Beam-off Stat.}}. \tag{8.13}$$

8.2.7 Total Uncertainties

Uncertainties are further combined by summing the individual covariance matrices. For the total uncertainty, this gives

$$V^{\text{total}} = \sum_{\alpha} V^{\alpha}, \tag{8.14}$$

where α runs over all individual data and simulation uncertainty sources described in the previous sections.

Uncertainties throughout this analysis are shown in one of two ways:

- **Data-simulation comparisons of selected event rates**: Beam-on statistical uncertainties are shown on the data, the remaining uncertainties are shown as a band on the prediction. Both signal and background predictions are varied.
- **Extracted cross sections**: The total uncertainty is shown on the extracted cross section. Only the background prediction is varied.

Figure 8.2 shows a breakdown of the fractional uncertainties for the MC prediction. This includes uncertainties on the signal events and shows cross-section uncertainties dominate. Uncertainties on the extracted cross sections will be shown in Chapter 10.

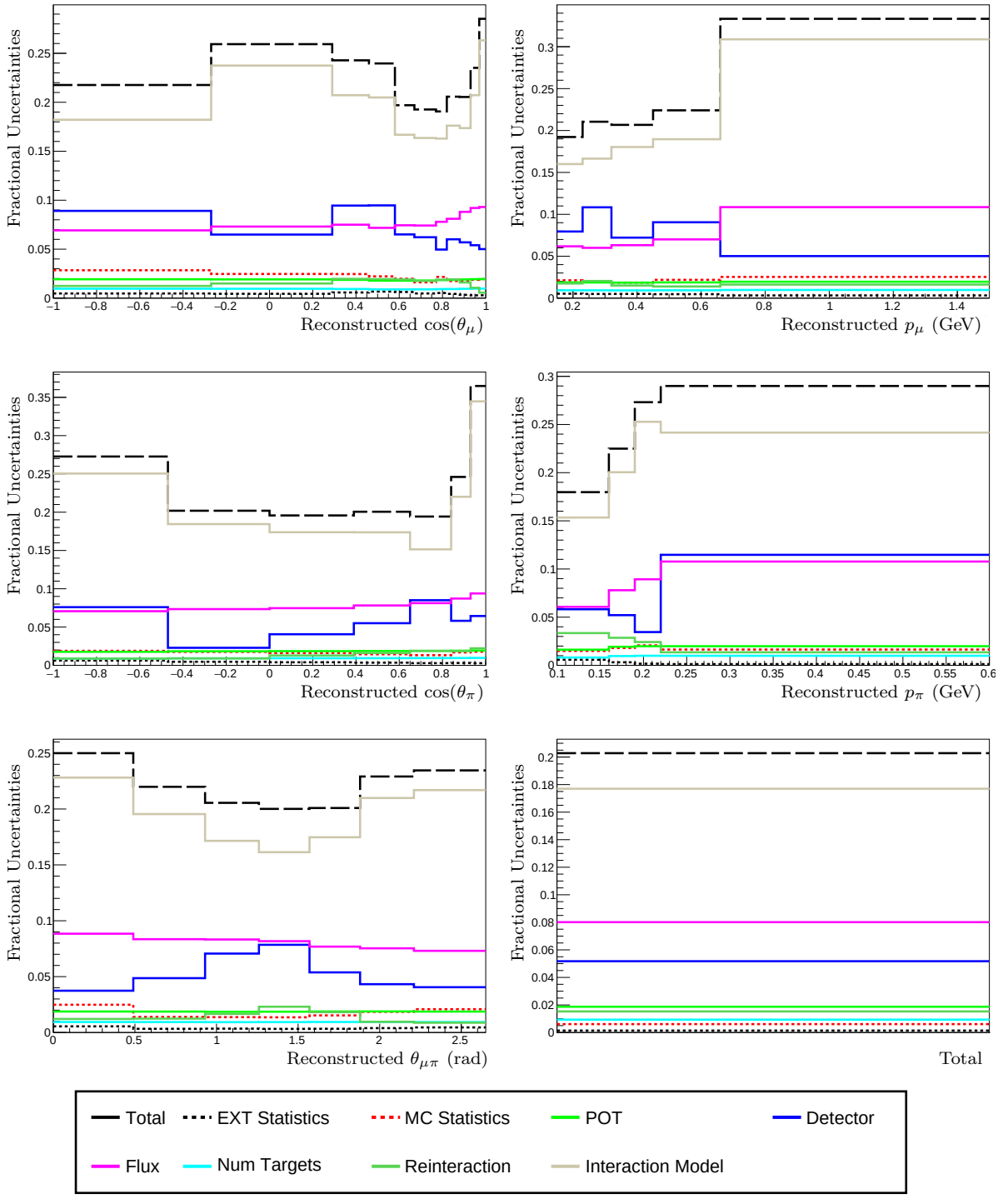

Fig. 8.2 Fractional uncertainties of the signal + background cross-section predictions. The plots include uncertainties on the signal events, showing very high interaction model uncertainties.

8.3 Sideband Study

The previous chapter has shown that the dominant background of the analysis is topologies consisting of muon and proton tracks without pions. To verify that the background modelling is well-behaved, an orthogonal sideband selection is employed by modifying the criteria used in the main selection. Instead of requiring one muon, any number of identified protons, and one other particle (the charged pion candidate), the sideband selection targets events with one muon, one or more protons, and no other particles. This is done by changing the requirement of two non-protons (a muon and a charged pion candidate) to one non-proton (only the muon candidate), which is shown in Figure 8.3.

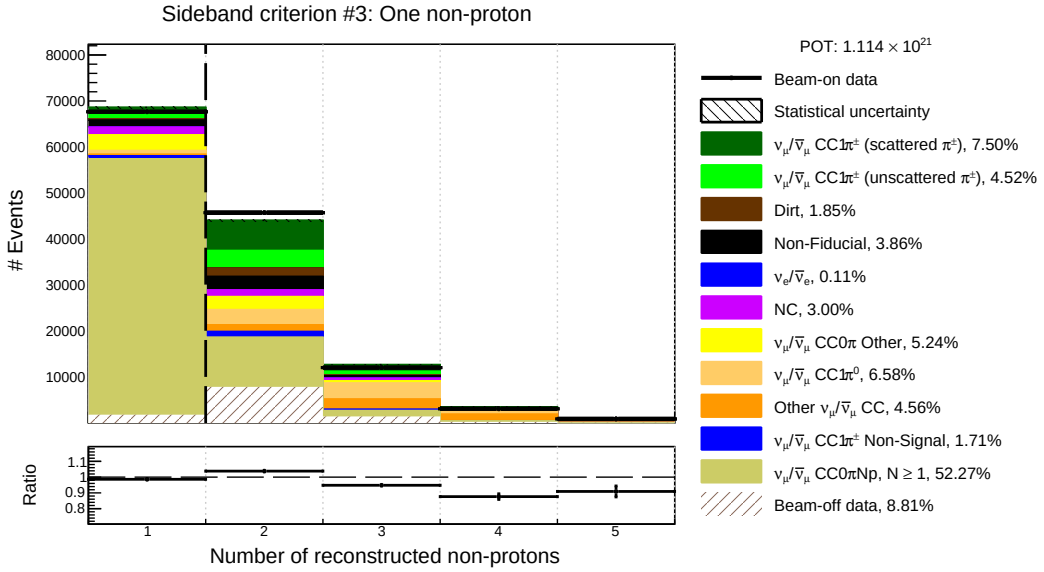

Fig. 8.3 The number of reconstructed particles classified as neither muon nor pion. Events to the right of the line are rejected.

The remaining criteria are kept the same, but those applying to the pion candidate are instead applied to the proton candidate for the sideband selection. In the case of multiple protons, the leading proton, determined by track length, is chosen as the pion-equivalent.

To better match the kinematics of protons misidentified as pions in selected background events, additional criteria are applied to select events with more MIP-like tracks. The leading proton is required to have a minimum muon BDT score > -0.4 and a low proton BDT score of < 0.1, close to the selection threshold of > -0.06, above which particles are considered protons. Together, these criteria exclude the most clearly identifiable protons, leaving only more pion-like protons in the sideband selection.

Figure 8.4 shows how these criteria improve the kinematic agreement between true CC0πXp events in the main and sideband selections.

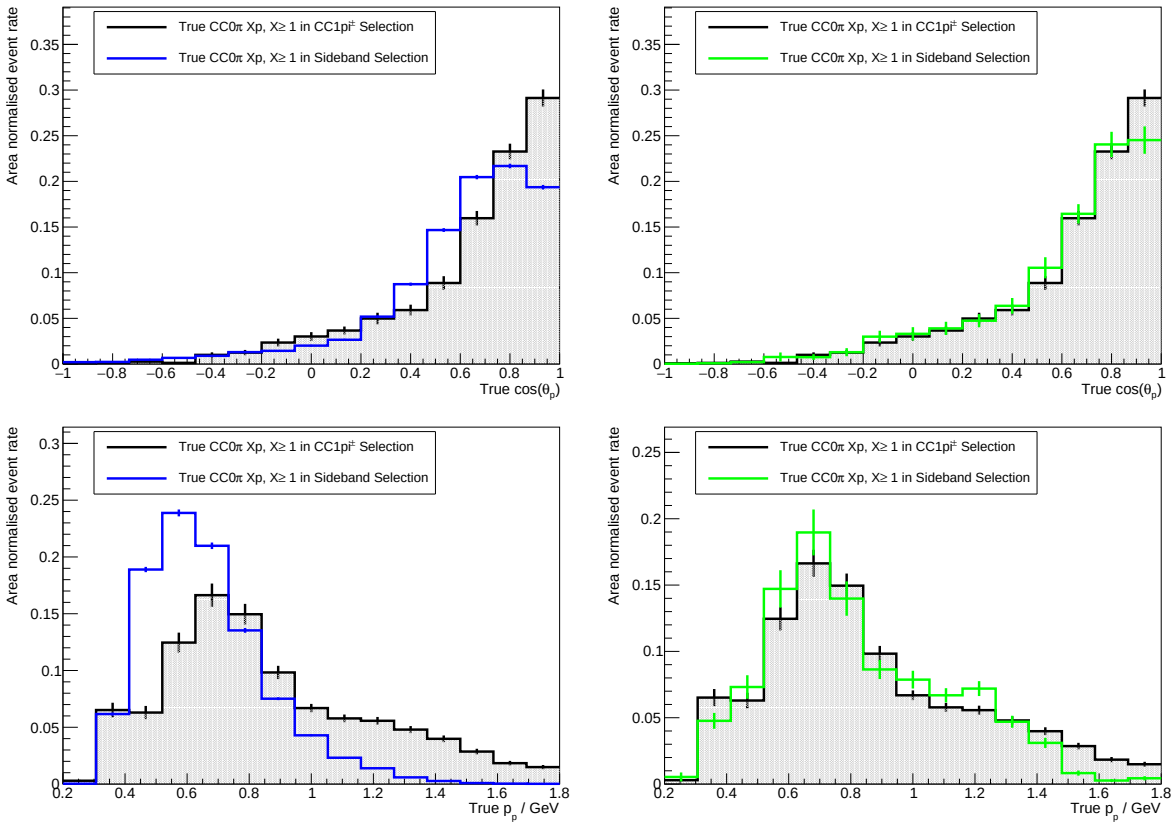

Fig. 8.4 The black lines show the true CC0π events with at least one proton in the neutrino MC sample selected by the main analysis. The coloured lines show events from the orthogonal sideband: blue for the selection without the additional criteria, and green for the selection with extra criteria applied to better match the kinematics of the main selection.

The sideband comparison with data uses the same binning as the main selection. It also relies on the same full uncertainty treatment used for the main selection. The muon kinematic variables are computed identically to the main selection, and the pion kinematic variables once again use the leading proton. The momentum of the leading proton is determined using the pion momentum estimator used for the CC1$\pi^{\pm}$ selection to match how misidentified CC0π Xp, X$\geq$ 1 events are treated in the main selection. The mapping is shown in Table 8.3.

The sideband comparison between data and simulation across the kinematic variables is shown in Figure 8.5. It highlights known GENIE modelling differences with MicroBooNE data, such as a dip at low Q^2 with very forward muon angles in Figure 8.5b

CC $1\pi^{\pm} \geq$ 0p		Sideband CC $0\pi^{\pm} \geq$ 1p
Muon momentum	$\leftrightarrow$	Muon momentum
Muon zenith angle	$\leftrightarrow$	Muon zenith angle
Pion momentum	$\leftrightarrow$	Leading proton momentum (via pion momentum estimator)
Pion zenith angle	$\leftrightarrow$	Leading proton zenith angle
Muon-pion opening angle	$\leftrightarrow$	Muon-leading proton opening angle

Table 8.3 Correspondence between kinematic variables in the main and the sideband selection.

for CC events with protons and no pions as reported in Ref. [249]. An attempt was made to incorporate the sideband information as an additional constraint using the method outlined in Ref. [238], as implemented within MicroBooNE's shared analysis tools. In practice, this approach did not yield reduced uncertainties, and its behaviour was found to be sensitive to implementation details. Given the lack of improvement and the additional time that would have been required to make this procedure work, it was ultimately abandoned. Nevertheless, the sideband data-simulation comparison shows agreement within uncertainties across all kinematic variables, indicating that differences are well covered by the included uncertainties. This validation provides some confidence in the modelling of the dominant background in this analysis. The next chapter covers the cross-section extraction and includes further robustness checks using simulated data.

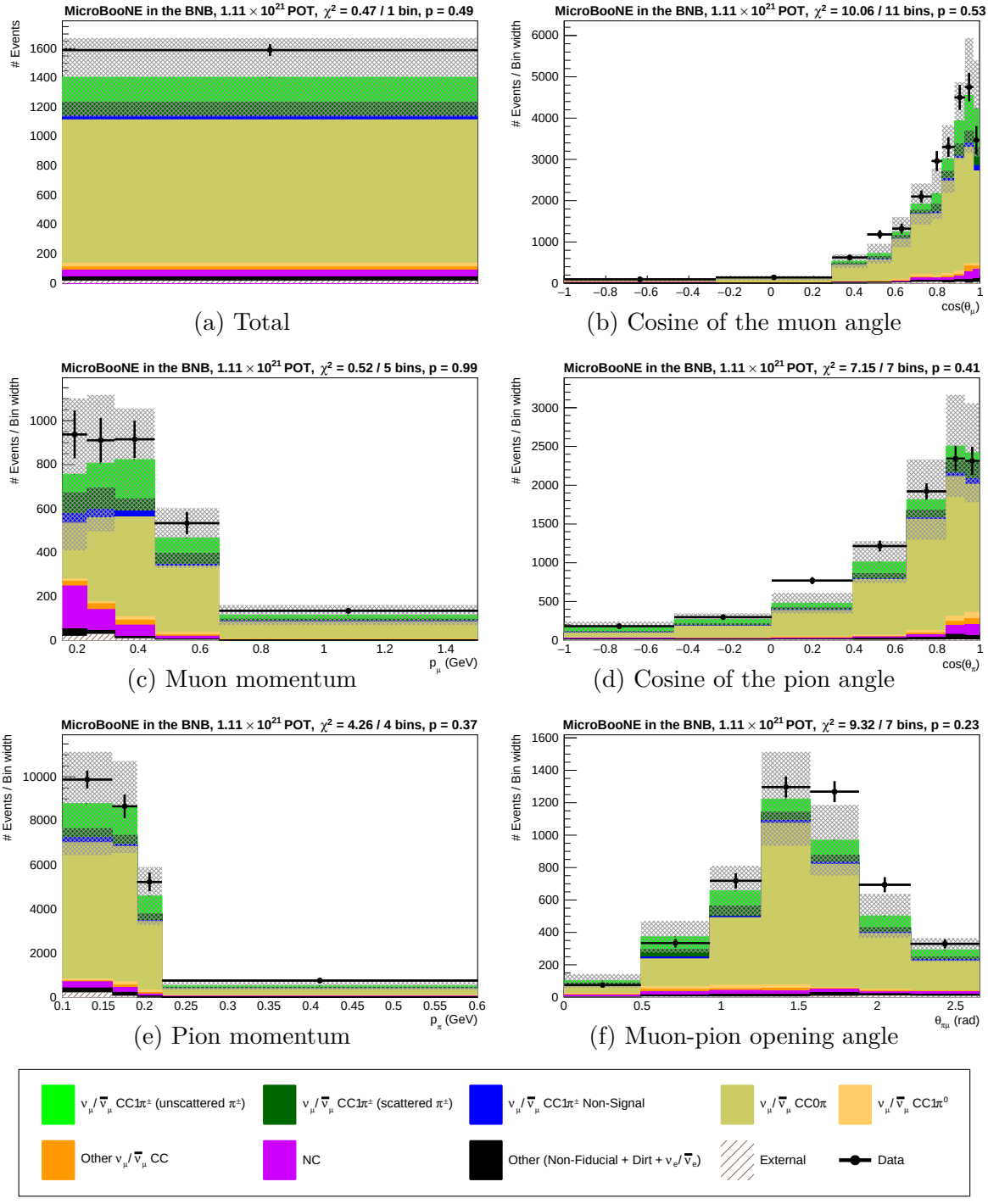

(a) Total

(b) Cosine of the muon angle

(c) Muon momentum

(d) Cosine of the pion angle

(e) Pion momentum

(f) Muon-pion opening angle

Fig. 8.5 The sideband selection using the binning used for the main analysis and treating the leading proton like the pion in the main selection. The plots include full statistical and systematic uncertainties. Overall data-simulation agreement is good.

Chapter 9

Cross-Section Extraction

The fundamental observable in a neutrino experiment is the count of interactions in the detector. A target containing N_T nuclei is exposed to a neutrino-energy-dependent flux $\Phi_\kappa(E_\nu)$ of flavour $\kappa \in \{e, \mu, \tau\}$. The total number of interactions of neutrinos of flavour κ is given by

$$R_\kappa = N_T N_{\mathrm{POT}} \int \Phi_\kappa(E_\nu)\, \sigma_\kappa(E_\nu)\, \mathrm{d}E_\nu, \tag{9.1}$$

where N_{POT} is the total number of protons on target, and $\sigma_\kappa(E_\nu)$ is the total neutrino-nucleus cross section describing the probability that a neutrino of energy E_ν interacts with a target nucleus. The flux of neutrinos of flavour κ arriving at the detector is the sum of initially produced neutrinos maintaining or oscillating to this flavour, which is given by

$$\Phi_\kappa(E_\nu) = \sum_{\lambda}^{\text{flavours}} P_{\nu_\lambda \to \nu_\kappa}\left(L/E_\nu\right)\ \Phi_\lambda^{\text{Init.}}\left(E_\nu\right), \tag{9.2}$$

where $P_{\nu_\lambda \to \nu_\kappa}(L/E_\nu)$ is the oscillation probability from Equation (2.36) and $\Phi_\lambda^{\text{Init.}}(E_\nu)$ is the initial flux directed towards the neutrino target. Understanding the change in the neutrino flux, and thus the oscillation properties of the neutrinos, is the ultimate goal of many neutrino experiments. However, the flux is folded with the cross section. Additional complexity arises from the electrically neutral nature and extremely low interaction rate of neutrinos, which is not only a challenge for their detection but also for their production. Neutrinos from accelerator beams are produced via the decays of mesons, which themselves originate from proton beam collisions with a fixed target. This process results in a broad energy spectrum which, once produced, cannot be controlled or monochromatised, unlike beams of electrically charged particles. However, since the oscillation probability depends on the neutrino energy E_ν, knowledge of this

energy is crucial for extracting oscillation parameters. As the neutrino energy cannot be measured directly, it must be inferred from the observed kinematics of the particles produced in interactions at the detector. This is done either via the kinematics of the outgoing lepton for QE-like interactions or by reconstructing and summing the energies of all visible final-state particles. Both methods are sensitive to nuclear effects, such as FSI, and detector limitations, such as an inability to detect neutrons or sub-threshold charged particles. Because the neutrino interaction rate scales with the target mass, heavy nuclei are typically employed to increase the number of interactions. However, this comes at the cost of introducing more complex nuclear effects. Uncertainties in the cross sections propagate to the reconstructed energy spectrum, which has the potential to bias oscillation measurements [250]. The study of neutrino oscillation thus requires a good understanding of neutrino–nucleus interactions.

Cross-section measurements are typically reported as flux-integrated quantities, which avoids the need to determine neutrino energies:

$$\sigma = \frac{1}{\mathbf{\Phi}} \int \Phi(E_\nu)\, \sigma(E_\nu)\, \mathrm{d}E_\nu, \tag{9.3}$$

with $\mathbf{\Phi}$ being the integrated flux:

$$\mathbf{\Phi} = \int \mathrm{d}E_\nu \Phi(E_\nu). \tag{9.4}$$

This approach reduces the dependence on an individual cross-section model that would otherwise be needed to estimate neutrino energies. As previously described, cross sections can be reported with respect to directly observable kinematic quantities, such as the momentum and angles of final-state particles. The simplest case is a differential cross section with respect to a single kinematic variable x. The average of the single-differential cross section can then be measured for a set of discrete bins:

$$\left\langle \frac{\mathrm{d}\sigma}{\mathrm{d}x} \right\rangle_a = \frac{1}{\Delta x_a} \int_{x_a}^{x_{a+1}} \frac{\mathrm{d}\sigma}{\mathrm{d}x} \mathrm{d}x, \tag{9.5}$$

where x_a and x_{a+1} are the edges of the a^{th} bin of width Δx_a.

The experimentally accessible quantity is the number of reconstructed events in the detector, not all of which are guaranteed to be signal events. To correct for this, an estimate of the background must be subtracted from the recorded events:

$$\left\langle \frac{\mathrm{d}\sigma}{\mathrm{d}x} \right\rangle_a = \frac{d_a - \rho_a^{\text{CV Backg.}}}{\mathbf{\Phi} N_T N_{\text{POT}} \Delta x_a}, \tag{9.6}$$

with d_a being the selected data events and $\rho_a^{\text{CV Backg.}}$ being the selected non-signal events that are part of the CV prediction defined in Equation (8.2).

The measured event rate is affected by detector effects, which can be described as the combined impact of smearing and efficiency. Smearing refers to bin migration, where events originating in a given true kinematic bin end up in a different measured bin. Selection efficiency in this context is the probability that an event produced in a true kinematic bin is successfully reconstructed and selected.

To compare a truth-level prediction to the measured reconstructed distribution, one must account for both selection efficiency and bin migration. These detector, reconstruction, and selection effects are taken from the fully simulated and reconstructed CV prediction. Let n_α^{CV} be the number of CV signal events generated in true bin α, and let $n_{a\alpha}^{\text{CV}}$ be the subset of those that pass the analysis selection and are also in reconstructed bin a. The selection efficiency in true bin α is then [238]

$$\epsilon_\alpha = \frac{\sum_a n_{a\alpha}^{\text{CV}}}{n_\alpha^{\text{CV}}}. \tag{9.7}$$

The conditional probability to reconstruct a selected event from true bin α into reconstructed bin a, which describes the smearing effects, is [238]

$$S_{a\alpha} = \frac{n_{a\alpha}^{\text{CV}}}{\sum_a n_{a\alpha}^{\text{CV}}}, \tag{9.8}$$

and the response matrix mapping true counts to reconstructed selected counts is then

$$\mathcal{R}_{a\alpha} = \frac{n_{a\alpha}^{\text{CV}}}{n_\alpha^{\text{CV}}} = S_{a\alpha}\,\epsilon_\alpha. \tag{9.9}$$

Given a theoretical prediction for the true signal distribution $n_\alpha^{\text{pred.}}$, a value for the selected events in reconstructed bin a is obtained by forward-folding with the response matrix $\mathcal{R}$:

$$\rho_a^{\text{pred.}} = \sum_\alpha \mathcal{R}_{a\alpha}\, n_\alpha^{\text{pred.}}. \tag{9.10}$$

The folded truth distribution can then be used to calculate the cross section for the prediction in terms of reconstructed quantities:

$$\left\langle \frac{\mathrm{d}\sigma}{\mathrm{d}x} \right\rangle_a^{\text{pred.}} = \frac{\rho_a^{\text{pred.}}}{\boldsymbol{\Phi} N_T N_{\text{POT}} \Delta x_a}, \tag{9.11}$$

which can be compared to the measured distribution from Equation (9.6).

More commonly, one inverts the detector effects to obtain the unfolded, or 'true', differential cross section. This allows for direct comparisons between different experiments and facilitates easier interpretation in the context of theoretical models. An unfolding matrix $U_{\alpha a}$ is used to convert the measured event counts with reconstructed kinematic values into truth-level distributions, with the aim of removing efficiency and smearing effects. The differential cross-section distribution in true kinematic bins α is then

$$\left\langle \frac{\mathrm{d}\sigma}{\mathrm{d}x} \right\rangle_{\alpha} = \frac{\sum_a U_{\alpha a} \left(d_a - \rho_a^{\text{CV Backg.}} \right)}{\mathbf{\Phi} N_T N_{\text{POT}} \Delta x_\alpha}. \tag{9.12}$$

The challenging part of unfolding is deriving an unfolding matrix U from the response matrix $\mathcal{R}$:

$$\mathcal{R} \xrightarrow{\text{Inversion}} U.$$

Creating an exact inverse matrix for which

$$U\mathcal{R} = \mathbb{I} \tag{9.13}$$

holds, with $\mathbb{I}$ being the identity matrix, is trivially done via

$$U^{\text{direct}} = (\mathcal{R}^T\mathcal{R})^{-1}\mathcal{R}^T, \tag{9.14}$$

which is a left inverse of the response matrix, as the matrix need not be square and the number of true and reconstructed bins can differ [251].

However, this is not a good approach to unfolding, as the problem is ill-posed and small differences, such as statistical noise in the data, can result in highly oscillatory solutions [252]. To address the large fluctuations, regularisation is used. This incorporates a priori knowledge about the expected form of the true distribution. Many regularisation methods exist. A commonly used method is Tikhonov regularisation [253], also known as ridge regression when simply penalising large values.

Any regularised unfolding matrix U can be decomposed as

$$U = A_C U^{\text{direct}}, \tag{9.15}$$

where A_C is a matrix that describes the effects of the regularisation [251] and can be any type of matrix. It is up to the regularisation method to find one with a good trade-off between adding bias and reducing the variance (i.e., oscillations) of the unfolded results.

To achieve this, unfolding methods typically have a free parameter to set the strength of the regularisation that is applied. An illustration of this is shown in

Figure 9.1. A different approach, and the one utilised in this analysis, is the Wiener-filtered singular value decomposition (SVD) method [251]. It constructs a filter that optimises the unfolded measurement based on the predicted true signal distribution. This suppresses unphysical oscillations in the unfolded result while avoiding tuning parameters.

A detailed description of the unfolding methods and the relation between the Wiener-SVD method and Tikhonov regularisation is provided in Appendix A.

9.1 Total Cross-Section Extraction

The extraction of the total cross section represents the simplest case of the unfolding problem. As there is only one true bin and one corresponding reconstructed bin, bin migration effects are, by definition, impossible, and the unfolding process reduces to a straightforward efficiency correction:

$$\sigma^{\text{true}} = \frac{d - \rho^{\text{bkgd}}}{\epsilon \mathbf{\Phi} N_T N_{\text{POT}}}. \tag{9.16}$$

9.2 Analysis Extraction Details

All cross-section extractions in this analysis are performed with the half of the GENIE CV neutrino events not used to train the BDTs. The product of integrated flux and POT for the MicroBooNE samples used in this analysis is shown in Table 9.1. The number of scattering targets is $N_T = 1.03 \times 10^{30}$ argon nuclei inside the analysis volume.

Integrated Flux Predictions

$\mathbf{\Phi}_{\nu_\mu} N_{\text{POT}}$	$\mathbf{\Phi}_{\bar{\nu}_\mu} N_{\text{POT}}$	Total $\mathbf{\Phi} N_{\text{POT}}$
8.22×10^{11} cm^{-2}	0.51×10^{11} cm^{-2}	8.73×10^{11} cm^{-2}

Table 9.1 Product of integrated muon (anti-)neutrino flux predictions and 1.11×10^{21} POT for the data used in this analysis. The flux value is approximated using the flux in the entire active volume, instead of the slightly smaller analysis volume imposed by the additional limitations on the neutrino vertex.

This analysis employs the Wiener-SVD technique, with the GENIE CV simulation serving as the true signal input. As described in the first section, a choice must be

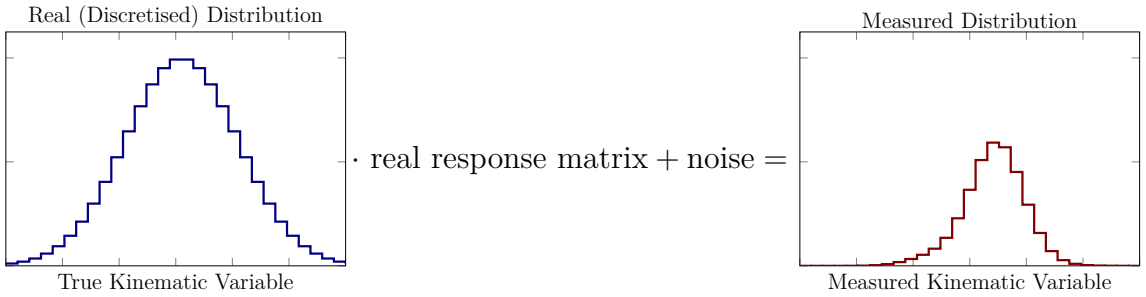

(a) The real distribution of a variable of interest is transformed to reconstructed space via the real response matrix, which encapsulates the actual (unknown) detector and reconstruction effects that yield the measured distribution. Part of this transformation is noise due to the finite statistics of the measurement.

$$\begin{pmatrix} \text{response matrix} \\ \text{from simulation} \end{pmatrix}^{-1} \cdot \text{measured distribution} =$$

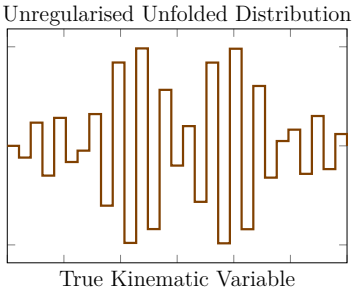

(b) The most direct method for obtaining an estimate of a true distribution from a measured distribution involves using a response matrix and performing a direct matrix inversion. In particle physics, the response matrix typically comes from simulation, in which case all uncertainties, including systematic ones, contribute to the noise of the transformation. As a result of the noise, the inversion is an ill-posed problem, and the unfolded distribution exhibits strong unphysical oscillations.

$$\begin{pmatrix} \text{regularised} \\ \text{unfolding matrix} \end{pmatrix} \cdot \text{measured distribution} =$$

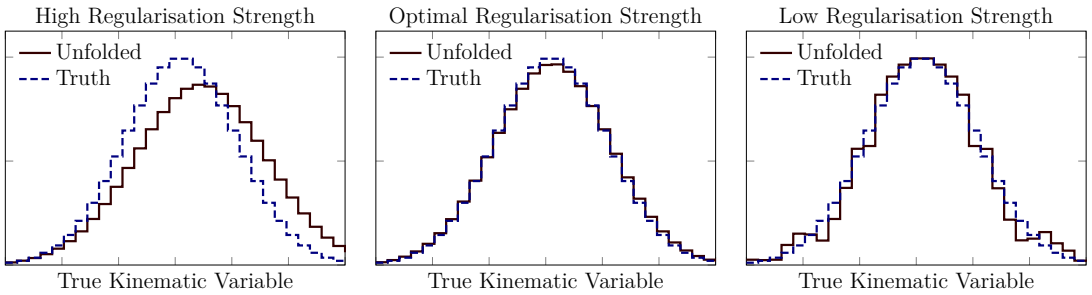

(c) Applying regularisation uses additional information to guide the unfolding towards a physical distribution. Methods such as Tikhonov regularisation require adjusting a regularisation strength parameter. The plot on the left here illustrates the effect of over-regularisation, where the unfolded distribution is strongly biased. At the other extreme, under-regularisation leads to high-variance solutions and oscillations, which in the limit approach the unregularised solution. The challenge is finding the right balance between bias and variance.

Fig. 9.1 Illustrations of the transformation from truth to measured space and unfolding with different regularisation strengths.

made for the C matrix, i.e., whether to regularise the absolute values or the first- or second-order derivatives of the unfolded truth. A common choice for unfolding in particle physics is to regularise based on the second derivative of the solution. This tends to smooth oscillations in the unfolded result by damping curvature, which biases the solution towards smoothness. First-derivative regularisation biases towards a flat solution. Biasing towards zero by regularising the absolute values is less commonly used in these cases.

The choice, however, is less important for this analysis. Like all unfolded measurements, the results are reported in a regularised vector space of the truth, but by publishing the regularisation matrix A_C along with them, any theoretical prediction can be transformed into the same space. Effects from the choice of regularisation therefore have no impact, at least for these comparisons, as applying A_C to a theoretical prediction preserves the data-prediction agreement through the unfolding process.

The regularisation matrices for first- and second-derivative Wiener-SVD unfolding are compared in Figure 9.2 for one kinematic variable. It shows that more smearing is observed when using the second derivative, meaning a larger transformation separates the regularised and actual truth spaces. For this reason, this analysis regularises the first derivative.

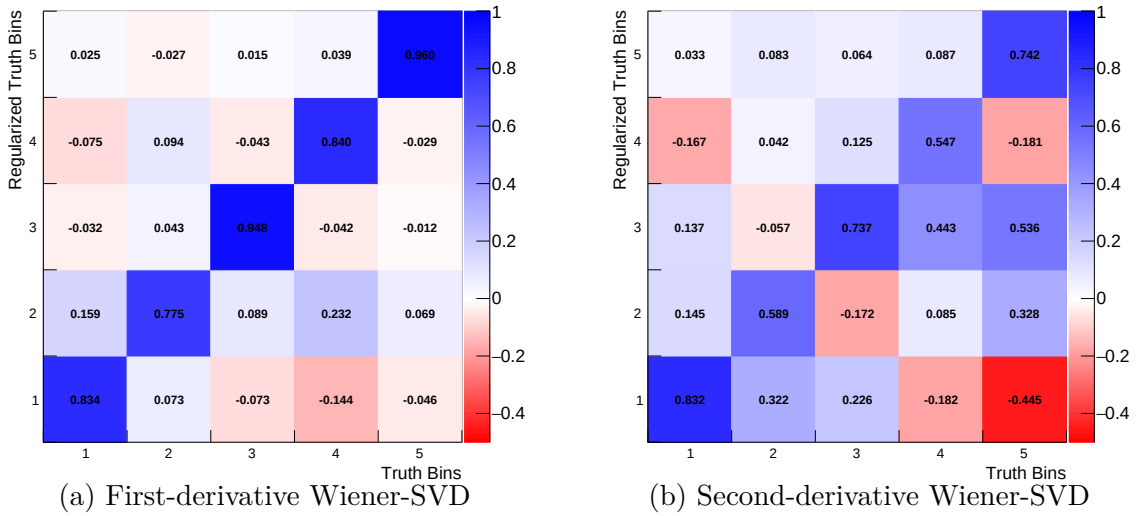

(a) First-derivative Wiener-SVD (b) Second-derivative Wiener-SVD

Fig. 9.2 Regularisation matrices A_C for first- and second-derivative Wiener-SVD unfolding of the muon momentum distribution using the GENIE CV prediction. The first derivative shows less smearing.

9.3 Validation Studies

Before unblinding and unfolding the real data, a number of mock-data studies are performed by treating simulated event samples as data.

9.3.1 Closure Test

To test the unfolding procedure, a closure test is performed by treating the Run 1–5 MicroBooNE Tune GENIE CV prediction as data. The mock data is then unfolded via the Wiener-SVD method. The unfolded results are compared to the true distributions of the GENIE CV signal events. Since the prediction, which is also used to compute the response matrix, is the same as the data, the unfolded distributions must reproduce the prediction exactly, which they do within floating-point accuracy, as Figure 9.3 shows.

9.3.2 NuWro Mock-Data Study

The closure test is primarily used to check the unfolding machinery for implementation errors. This mock-data test with an alternative generator evaluates whether the unfolding procedure can accurately recover the true kinematic distributions when the input model differs from the CV GENIE prediction, as is the case with real data. For this, simulated data produced with the alternative neutrino event generator NuWro version `19.02.1` is used. Like the GENIE samples, these events have undergone the entire detector simulation and reconstruction pipeline. With a POT of 1.7×10^{21}, the sample provides an exposure of similar magnitude to the real Run 1–5 BNB POT of 1.1×10^{21}. As the differences between the GENIE MC and the NuWro mock-data samples are confined to the generator model, only statistical and model uncertainties are considered.

The level of agreement between the unfolded and true distributions is evaluated using a χ^2 test statistic,

$$\chi^2 = \left(\hat{n} - n^{\text{pred.}}\right)^T V_{\text{unf}}^{-1} \left(\hat{n} - n^{\text{pred.}}\right), \tag{9.17}$$

where $n^{\text{pred.}}$ is the truth distribution of the simulated sample, $\hat{n}$ is the unfolded distribution of the reconstructed quantities of the same sample with covariances V_{unf}. From this, p-values are obtained via

$$p = 1 - F_{\chi^2}\left(\chi^2,\, N_{\text{bins}}\right), \tag{9.18}$$

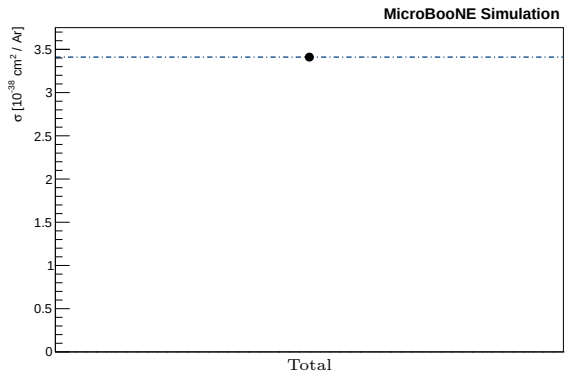

(a) Total

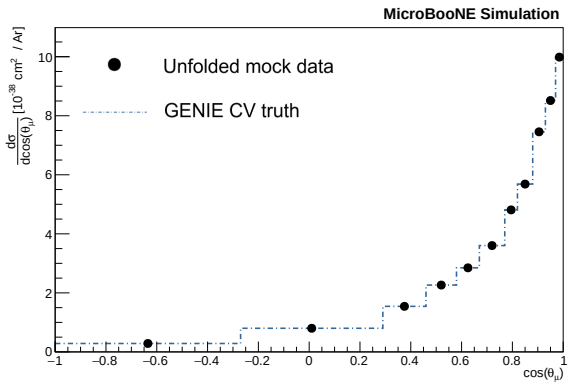

(b) Cosine of the muon angle

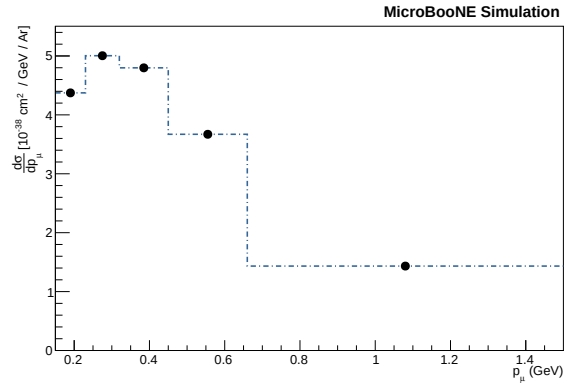

(c) Muon momentum

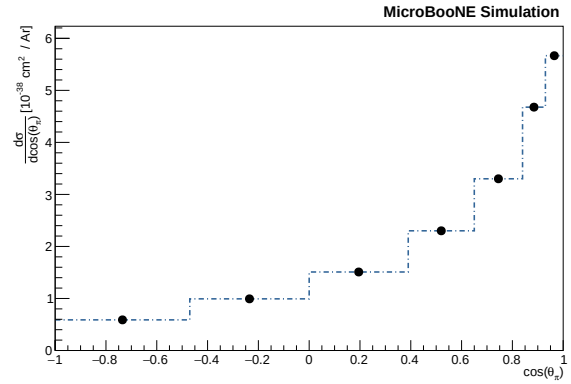

(d) Cosine of the pion angle

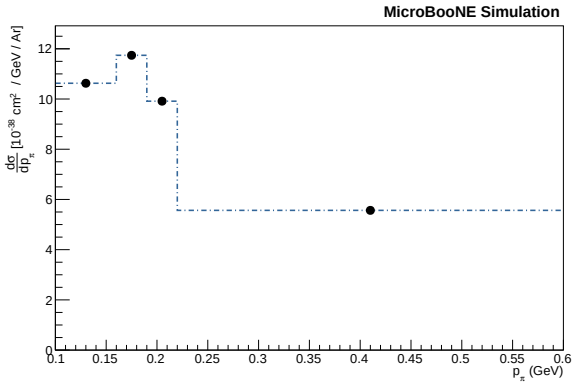

(e) Pion momentum

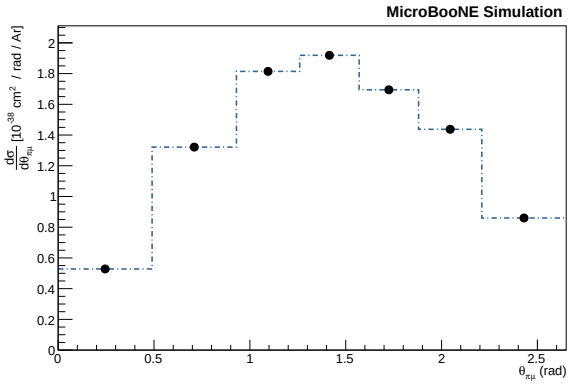

(f) Muon-pion opening angle

Fig. 9.3 Closure tests using the Runs 1–5 GENIE MC samples as data. The blue line shows the true signal distributions for the GENIE CV simulation. The black dots are the reconstructed kinematic distributions of the same unfolded GENIE samples. They close perfectly to reproduce the true distributions.

where F_{χ^2} is the cumulative distribution function of the χ^2 distribution with N_{bins} degrees of freedom.

Since this is comparing unfolded and true distributions from the same generator model, p-values that deviate significantly from unity can be a sign of underestimated interaction model uncertainties, and similar issues with uncertainty coverage have been reported in prior MicroBooNE analyses [237, 243]. Following their approach, an additional unisim uncertainty for the difference between the GENIE CV and NuWro predictions is included as previously described in Section 8.2.2.4. The effect of this is listed in Table 9.2.

	***p*-values**		
	NuWro Unisim		
Kinematic variable	**Without**		**With**
Cosine of muon angle	0.92	→	1.00
Muon momentum	0.58	→	0.95
Cosine of pion angle	0.42	→	0.99
Pion momentum	0.18	→	0.90
Muon–pion opening angle	0.97	→	1.00

Table 9.2 Comparison of p-values when comparing unfolded NuWro mock data with the underlying true distributions for the different kinematic variables, without and with an additional NuWro-based uncertainty.

Figure 9.4 shows the distribution of the selected NuWro events and the unfolded cross-section distributions obtained from them. The unfolded plots also show the true distributions of the GENIE CV prediction and the true distribution of the NuWro sample. The unfolded distributions closely match the true NuWro distributions.

9.3.3 Charge-Exchange Mismodelling Study

The GENIE configuration for the prediction in this analysis uses the hA2018 intranuclear cascade model for FSI [154]. A shortcoming that has been discovered for this model is an unphysical overprediction of the pion-nucleon charge-exchange cross section below $\sim$ 400 MeV and an underprediction above this, as shown in Figure 9.5. This issue stems from an over-reliance on an older simulation to fill gaps where experimental data is unavailable [254]. This is relevant to this analysis as it affects the conversion of charged pions to neutral pions in the FSI simulation.

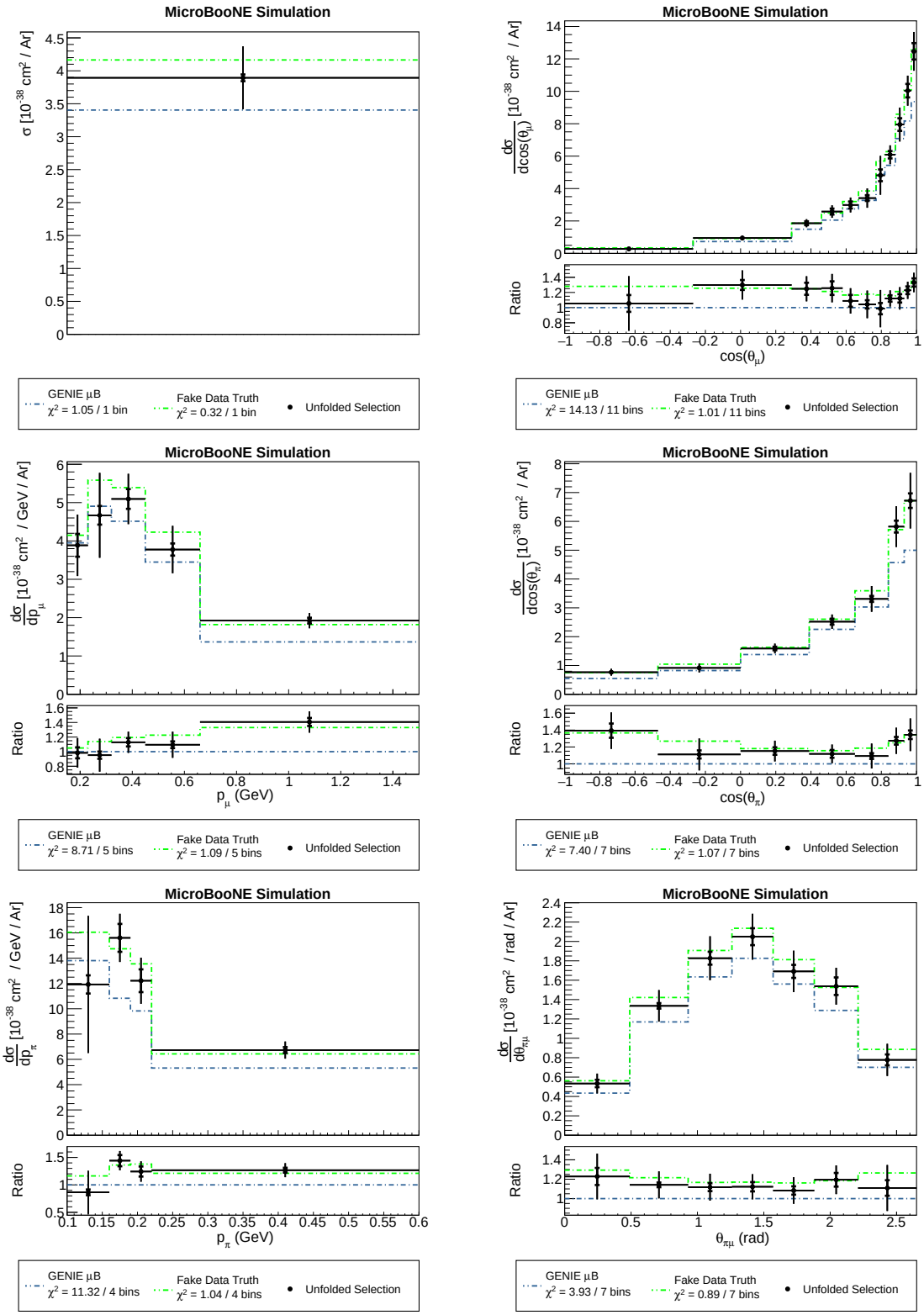

Fig. 9.4 Unfolded NuWro mock-data cross sections. The black dots are the unfolded NuWro selection with uncertainties. The green line is the true NuWro distribution with the additional smearing matrix A_C applied. The dashed blue line is the true GENIE CV prediction with A_C applied.

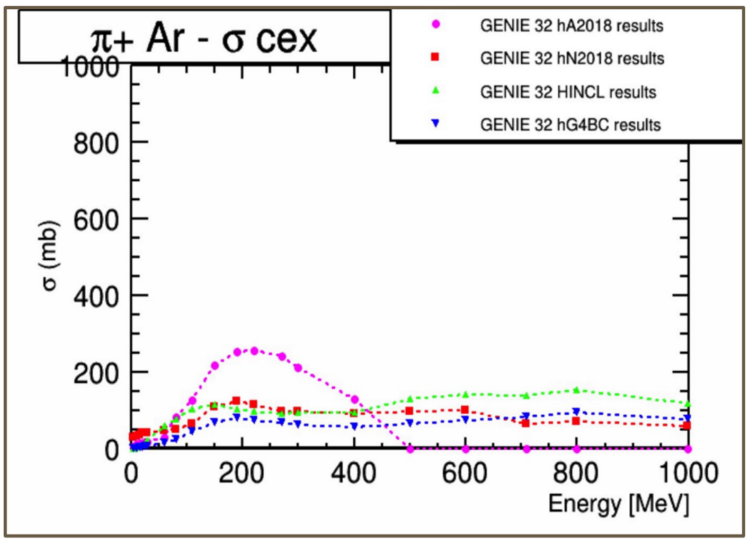

Fig. 9.5 Comparison of the π^+ on Argon charge-exchange cross section for different GENIE FSI models, with the hA2018 model showing an unphysical distribution. Source: Ref. [254].

The mock-data test with NuWro, which uses its own cascade model not affected by this issue, has shown that, within the included uncertainties, it is possible to successfully unfold differential cross-section measurements despite this FSI mismodelling in the prediction.

To further verify that this mismodelling does not significantly affect the selection process and that the number of selected signal events does not deviate substantially, a modified simulation sample produced for MicroBooNE was used [254]. This sample reweights the GENIE Run 1 events based on the fixed charge-exchange cross sections from an updated hA2025 model. The comparison of the selection efficiencies between the original and reweighted samples in Figure 9.6 shows no large differences across the kinematic bins.

Together with the other mock-data studies, this gives confidence in the selection and the robustness of the unfolding technique. The results of unblinding and unfolding the real data are presented in the next chapter.

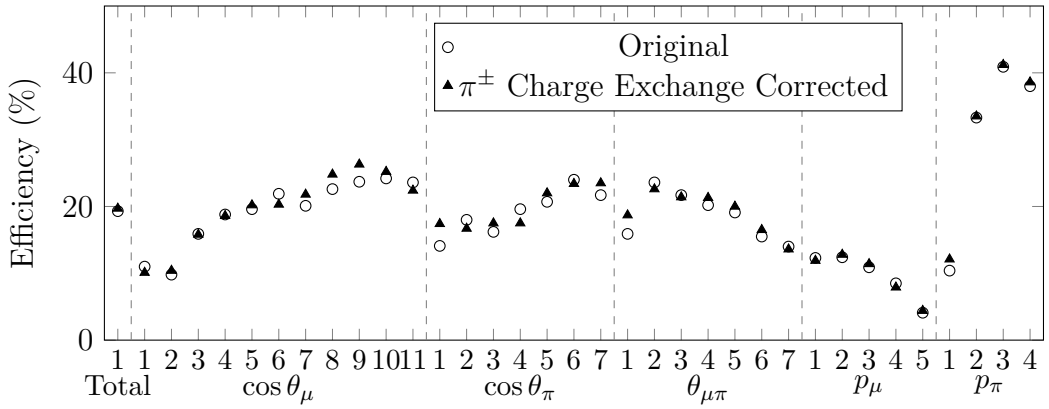

Fig. 9.6 The selection efficiency for the nominal Run 1 neutrino interaction MC is compared to a reweighted version that corrects for charge-exchange mismodelling. The muon and pion momentum sections have different overall efficiencies, as they use the additional criteria for the momentum subsets. No uncertainties are available for the reweighted sample as this is essentially a bug fix in the model. This comparison, thus, serves as an additional sanity check together with the mock data studies. No significant differences are observed for this selection.

Chapter 10

Results

The analysis was approved for unblinding by a MicroBooNE-internal editorial board and subsequently received experiment approval to be made public [229]. This chapter first presents the unblinded reconstructed data, followed by the unfolded cross-section measurements, and finally compares the results to state-of-the-art interaction generator predictions.

10.1 Unblinded Data

A summary of the selected event counts for the CC1$\pi^{\pm}$ analysis and its two momentum subsets is shown in Table 10.1 with uncertainties. The general selection represents a 25-fold increase in the number of background-subtracted data events compared to the only prior measurement on argon made by ArgoNeuT [193], but at a much lower beam energy that makes direct comparisons not viable. The results of this analysis should therefore be considered complementary to the prior measurements, rather than superseding them. Figure 10.1 shows in detail the predicted and observed event rates across the five differential kinematic variables as well as for the total event rate. The pion and muon momentum distributions are displayed using their respective dedicated subsets. Data–simulation agreement is good, with distributions captured within the total uncertainty band of the prediction across all of the phase space. However, the comparison here includes uncertainties on the predicted signal events, which is not the case for the extracted cross-section measurements in the next section.

Event displays of recorded interactions passing the selection are shown in Figure 10.2. The first example clearly shows a long muon-like track, a shorter proton-like track, and a pion candidate track that appears to decay to a Michel electron via a muon.

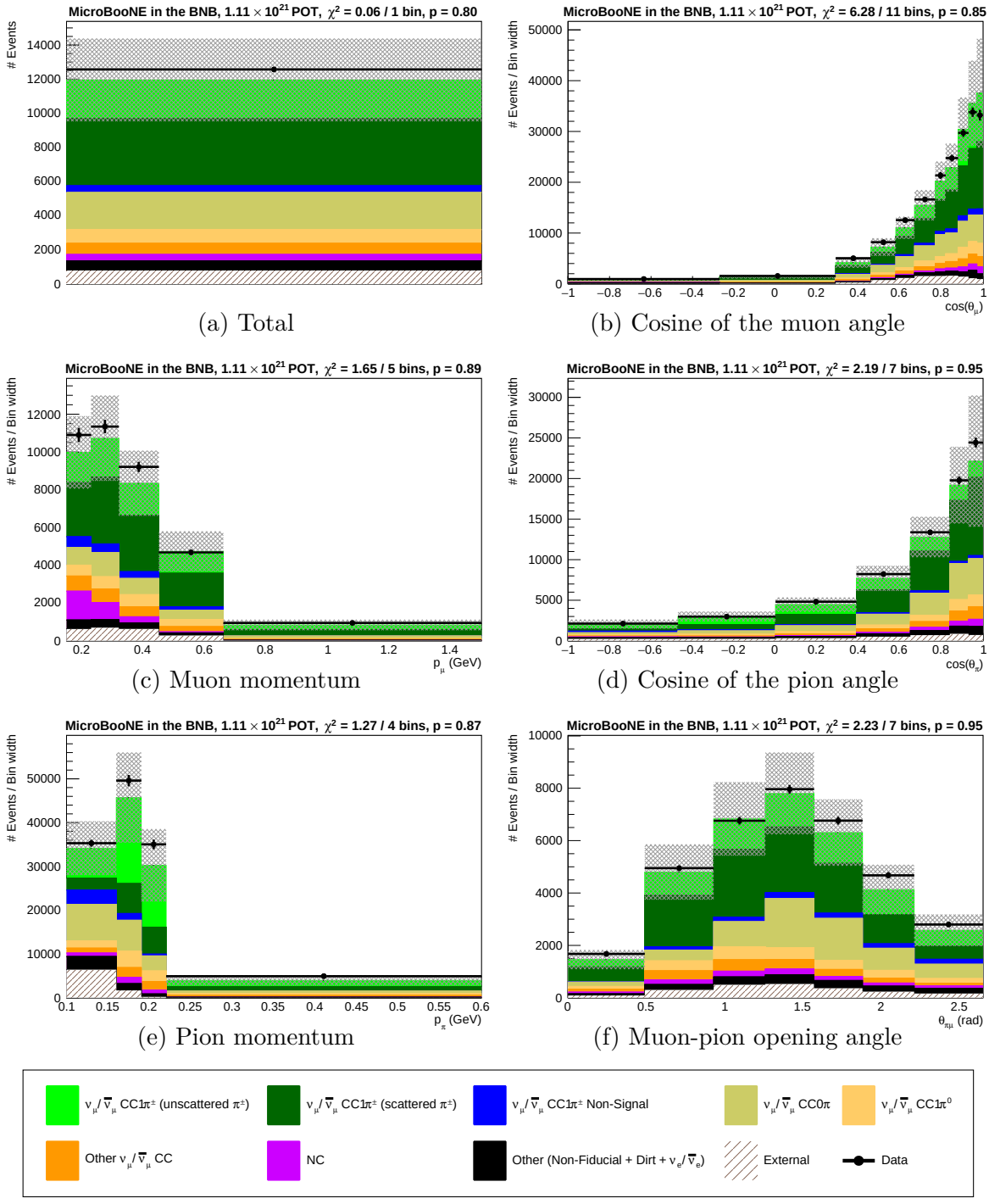

(a) Total (b) Cosine of the muon angle

(c) Muon momentum (d) Cosine of the pion angle

(e) Pion momentum (f) Muon-pion opening angle

Fig. 10.1 The stacked histogram shows the predicted rate of events passing the selection. The grey grid is the total uncertainty on the signal + background prediction. Black dots are measured event rates with statistical uncertainties. The plots shown are (a) the total event rate, (b) the scattering angle between the muon and the neutrino beam, (c) the muon momentum using the contained muon subset, (d) the scattering angle between the pion and the neutrino beam, (e) the pion momentum using the unscattered pion subset, and (f) the opening angle between the muon and the pion. The last bins of the muon and pion momentum selections serve as overflow bins. The dark and light green stacks are scattered and unscattered charged pion signal events. The ν_μ *CC1*$\pi^\pm$ *Non-Signal* events are selected events with the right topology but outside the defined phase space. *External* are cosmic background events from the beam-off data.

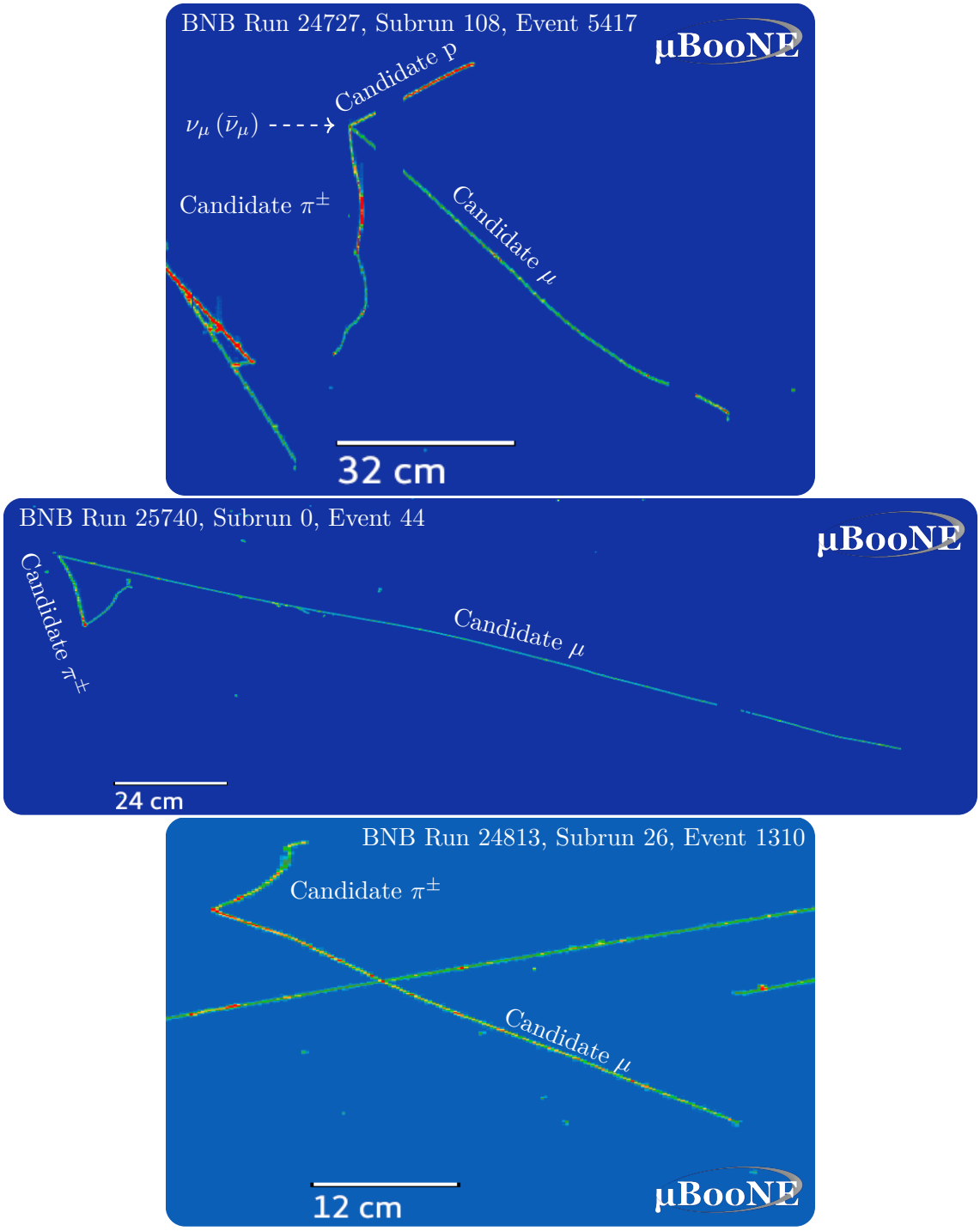

Fig. 10.2 Two event display from the collection plane and one from the first induction plane of different selected events in the detector consisting of a long muon candidate and a charged pion candidate. The first event also shows a shorter proton track candidate. The pions appear to decay to a Michel electron via a muon. Cosmic rays are visible in the bottom left corner of the first event display and across the third one. Sections of tracks are missing due to unresponsive detector wires.

Selections	**Selected Events**		**Efficiency**	**Purity**	**Unscattered $\pi^{\pm}$ fraction**
	Data	**Prediction**			
General	12566	11949 ± 2426	20.3%	52%	36%
Unscattered pion	6535	5843 ± 1120	9.5%	50%	68%
Contained muon	4867	4547 ± 931	8.4%	56%	39%

Table 10.1 The number of data and predicted events selected by the general and the two subset selections. The prediction includes all statistical and systematic uncertainties. Also shown are the efficiency, purity, and the fraction of unscattered pion events for the prediction.

10.2 Unfolded Measurements

The total flux-integrated cross section is extracted from the efficiency-corrected and background-subtracted event count, as described in Equation (9.16) using the flux and target size values given in Section 9.2. It is measured to be

$$\boxed{\sigma = (3.75 \ \pm \ 0.07 \ (\text{stat.}) \ \pm \ 0.80 \ (\text{syst.})) \times 10^{-38} \, \text{cm}^2/\text{Ar}} \tag{10.1}$$

at a mean neutrino beam energy of approximately 0.8 GeV. A breakdown of the uncertainties for the extracted total cross section is provided in Table 10.2, which shows flux, interaction model and detector modelling uncertainties dominate.

The differential cross sections have been unfolded using the first-derivative Wiener-SVD approach. The raw extracted cross-section values are shown in Figure 10.4. These values are not bin-width normalised and are combined into one histogram (vector) here as described in Equation (8.3). Each distribution was unfolded independently of the others using the blockwise unfolding approach, but the results are reported together with the covariance matrix between all unfolded bin values $\boldsymbol{\mathcal{V}}_{\text{unf}}$, as defined in Appendix A [229]. The main benefit of providing covariances not just between bins of the same kinematic variable but also between different differential cross sections is to enable more rigorous model development and tuning by allowing models to be evaluated against multiple distributions simultaneously, and to accurately quantify the goodness-of-fit [238]. For better visualisation, Figure 10.5 shows the correlation matrix instead, which is a normalised measure of the linear relationship between the bins:

$$\boldsymbol{\Gamma}_{\alpha\beta} = \frac{\left(\boldsymbol{\mathcal{V}}_{\text{unf}}\right)_{\alpha\beta}}{\sqrt{\left(\boldsymbol{\mathcal{V}}_{\text{unf}}\right)_{\alpha\alpha} \left(\boldsymbol{\mathcal{V}}_{\text{unf}}\right)_{\beta\beta}}}. \tag{10.2}$$

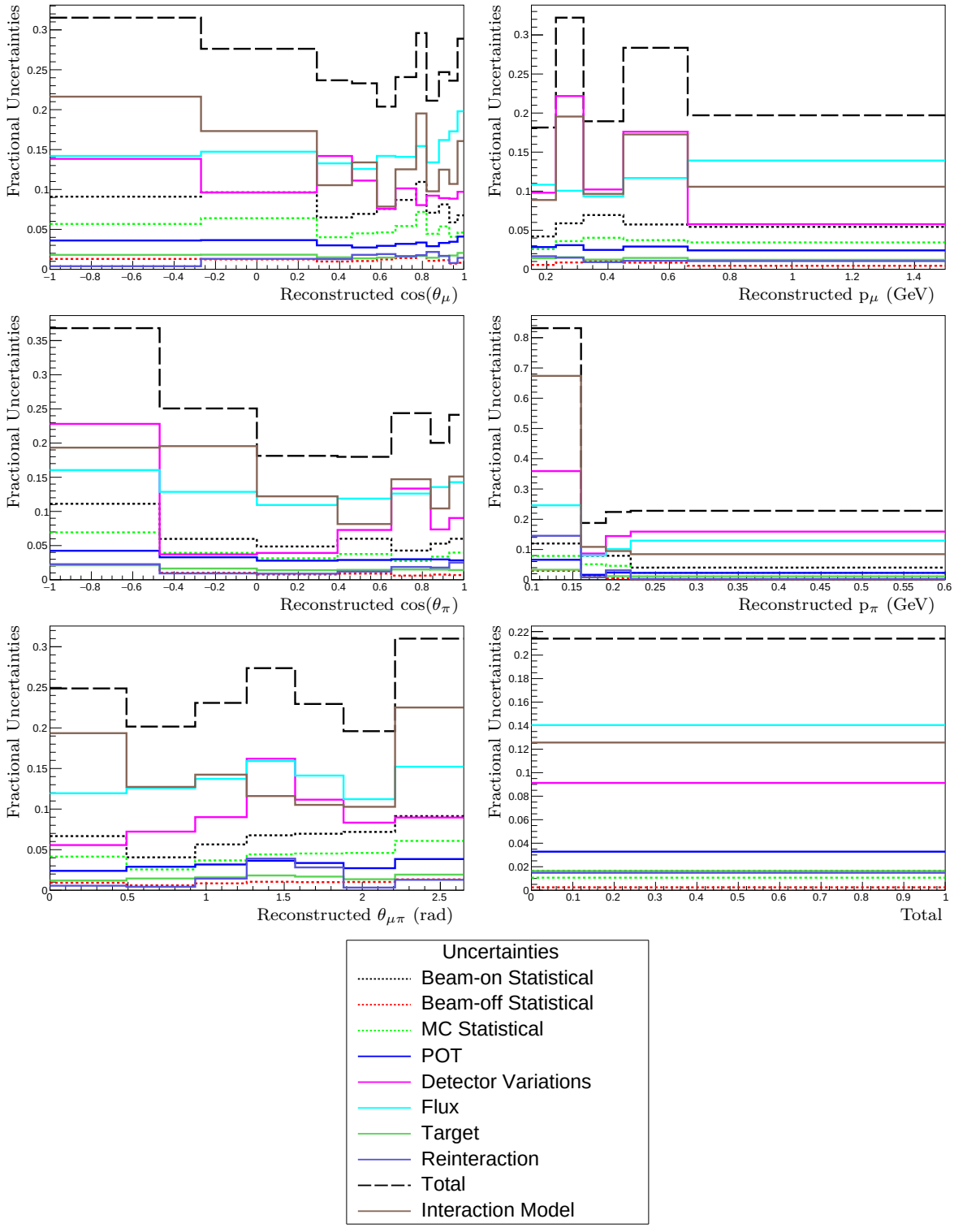

Fig. 10.3 Fractional uncertainties for the unfolded differential and total cross-section bins, showing the dominance of flux, interaction model and detector simulation uncertainties.

Category	**Uncertainty (%)**
Total	21.4
Systematic	21.3
Flux	14.1
Interaction model	12.6
Detector	9.1
POT	3.3
Target	1.6
Reinteraction	1.5
Statistical	2.0
Data	1.6
Background	1.1

Table 10.2 Fractional uncertainties for the extracted total cross section. The background statistical uncertainty contains the simulated neutrino prediction and the beam-off sample.

A breakdown of the uncertainties, specifically the diagonal elements of the covariance matrix, for each bin is shown in Figure 10.3. It highlights how MicroBooNE's flux modelling, the neutrino interaction model, and the detector simulation are the main systematic uncertainties limiting this measurement.

Theoretical predictions for the true cross-section distributions need to be smeared with the regularisation matrix shown in Figure 10.6 to apply the effects of regularisation and to preserve the data-generator χ^2 agreement through unfolding when comparing the prediction to the unfolded results in Figure 10.4. Some stronger smearing, for instance, can be seen for one of the muon-pion opening angle bins. However, by choosing the first derivative Wiener-SVD method for this analysis, the smearing is overall kept low, as previously described in Section 9.2.

10.3 Generator Comparisons

The unfolded cross sections are compared with predictions from several event generators, listed in Table 10.4, using the NUISANCE framework [255]. Among these is the recently updated GiBUU 2025 (Patch 1). Publications on π^0 cross sections from MicroBooNE [256] or using MicroBooNE data [186] have demonstrated a strong sensitivity of GiBUU 2023 (Patch 3) to changes to in-medium effects, which are effects on particles while inside the nucleus. In particular, these studies suggest a better

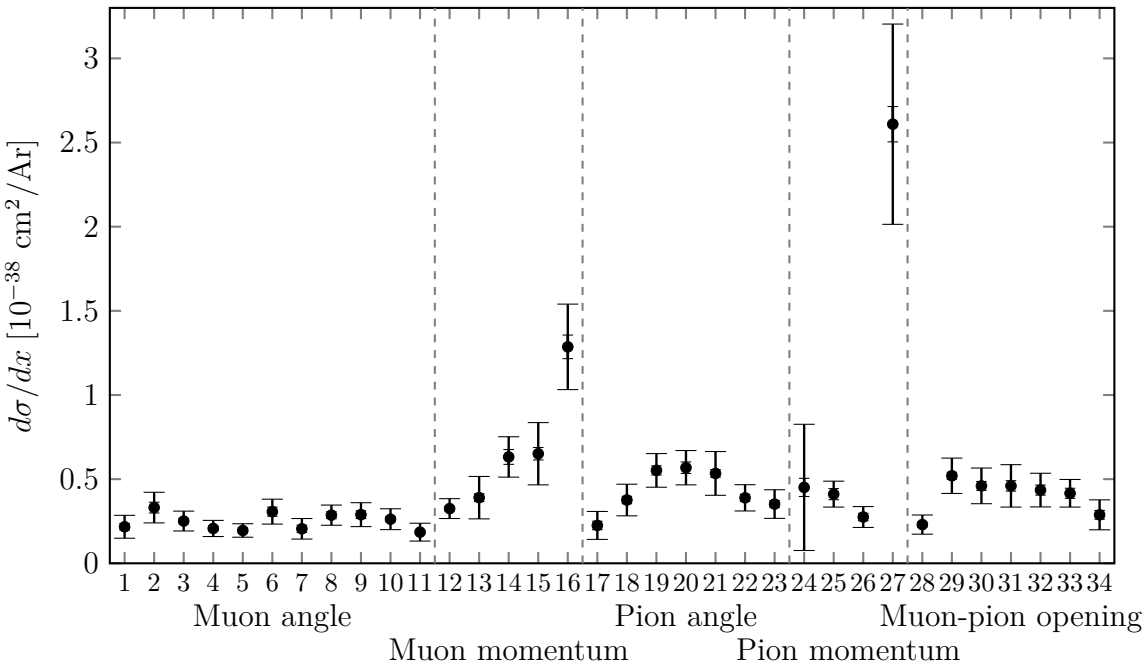

Fig. 10.4 Extracted differential cross-section values with inner error bars showing statistical uncertainties on the data and outer error bars showing the total uncertainties. The measurements are not normalised by bin width.

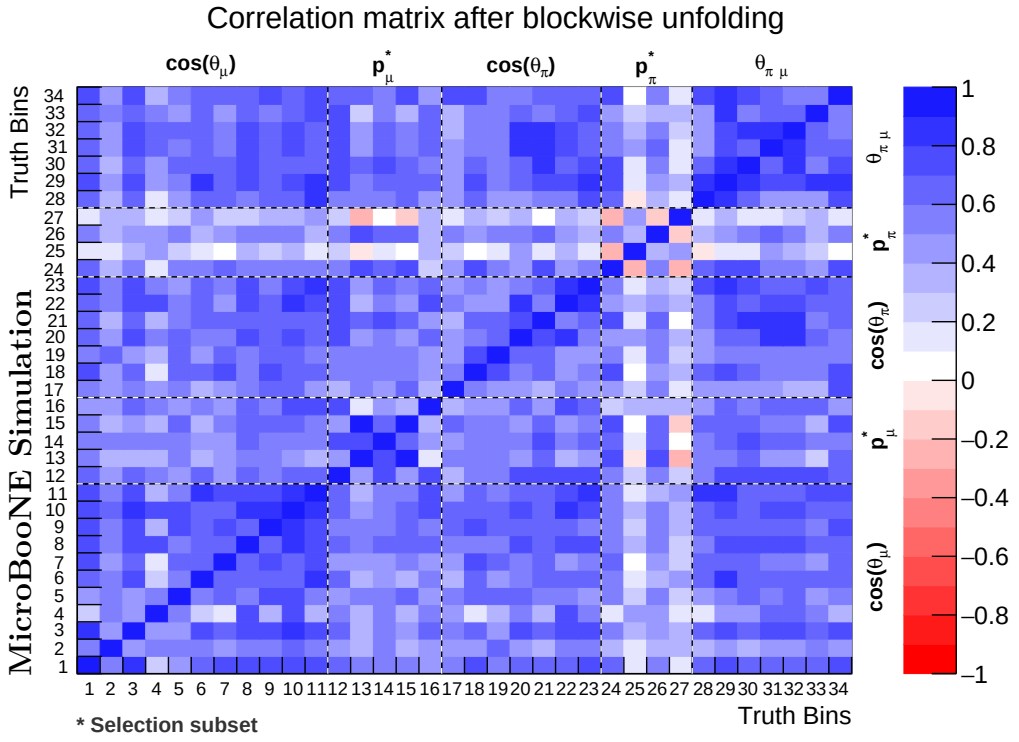

Fig. 10.5 Blockwise correlation matrix of each unfolded bin with each other unfolded bin. The dashed lines separate bins from different differential cross sections.

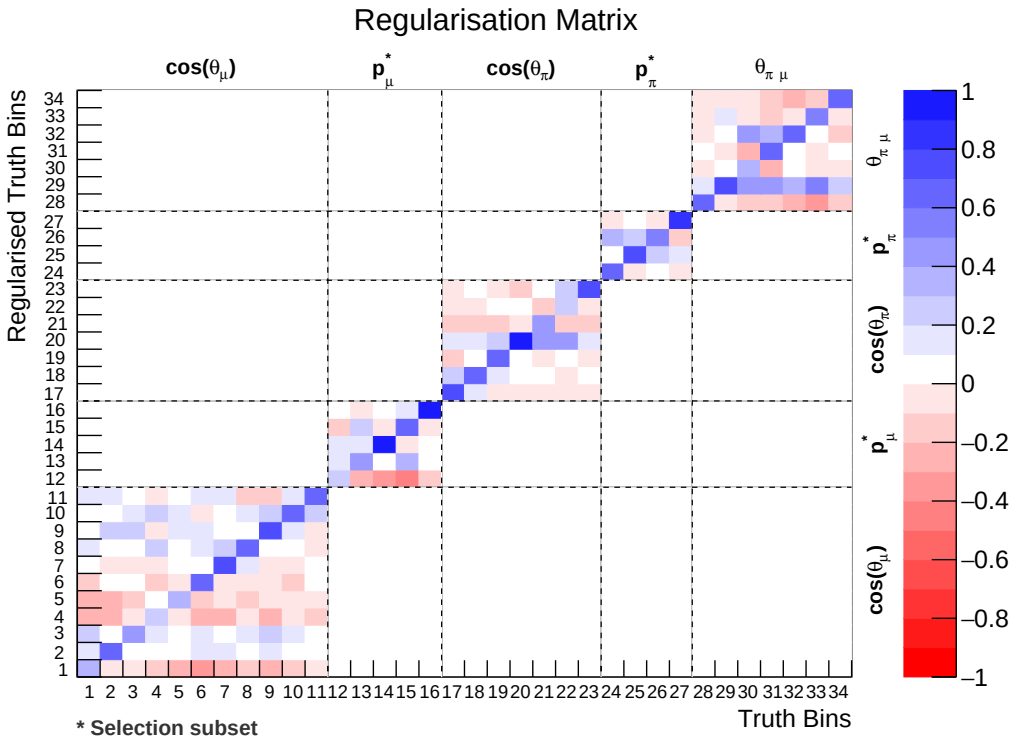

Fig. 10.6 Block-diagonal regularisation matrix A_C that needs to be applied to predictions (before applying any bin width normalisation) to compare them to the unfolded data results in Figure 10.4. This matrix applies scaling and smearing.

agreement with data when collisional broadening of the Δ resonance is absent, a change now implemented by default in the 2025 GiBUU configuration [257].

The regularisation matrix A_C is applied to the differential cross-section predictions. No regularisation is applied to the single bin measurement of the total cross section. Table 10.3 summarises the p-values quantifying data-generator agreement for the individual cross-section measurements described below.

Generators	**Total**	$\cos(\theta_\mu)$	p_μ	$\cos(\theta_\pi)$	p_π	$\theta_{\pi\mu}$
GENIE μB	0.85	0.26	0.78	0.84	0.67	0.68
GENIE G18	0.91	0.25	0.82	**0.85**	**0.72**	0.67
GENIE AR23	0.67	0.20	0.71	0.77	0.54	0.58
NuWro	0.44	0.00	0.82	0.79	0.62	**0.78**
GiBUU 2023	0.08	0.33	0.12	0.13	0.01	0.15
GiBUU 2025	**0.99**	**0.72**	**0.90**	0.24	0.19	0.54
NEUT	0.24	0.00	0.69	0.30	0.29	0.54

Table 10.3 P-values of the different generator-data comparisons. Highlighted is the best fit for each cross section.

Name	Version	Configuration	Tune
GENIE μB	3.0.6	`G18_10a_02_11a`	MicroBooNE Tune
GENIE G18	3.04.02	`G18_10a_02_11a`	–
GENIE AR23	3.04.02	`AR23_20i_00_000`	–
NuWro	21.09.2	Default	–
GiBUU 2023	2023 (patch 3)	Default	–
GiBUU 2025	2025 (patch 1)	Default	–
NEUT	5.4.0.1	Default	–

Table 10.4 Summary of the generators used in the comparisons with the unfolded data results.

10.3.1 Total Cross Section

The total flux-integrated cross section using all selected CC1$\pi^\pm$ events is shown in Figure 10.7. This result is unregularised, meaning the generator predictions have no additional scaling or smearing applied, unlike the differential cross sections. The result closely matches the GiBUU 2025 prediction and also shows very good agreement with all other generators apart from GiBUU 2023. NuWro and NEUT predict higher, while GENIE predicts lower cross sections than the unfolded data. GiBUU 2023 tends

to systematically underpredict pion production cross sections for MicroBooNE, as previously reported on π^0 production in Ref. [186]. These earlier MicroBooNE results are also likely to have contributed to the significant improvement in agreement now seen with the newer GiBUU version [256].

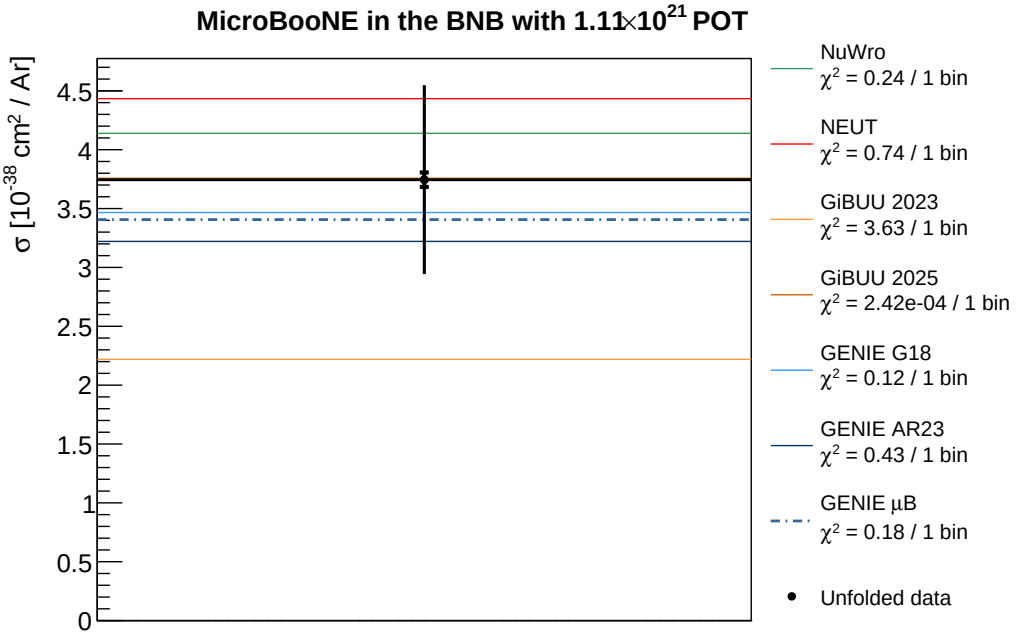

Fig. 10.7 The total extracted cross section. The black dot represents the efficiency-corrected selection with the associated total uncertainty. The thicker inner error bar is the statistical uncertainty only. The dashed blue line is the GENIE CV truth prediction. The other lines are predictions from alternative generators and tunes. The line of the GiBUU 2025 prediction is under the data point.

10.3.2 Differential Cross Sections

The differential cross section with respect to the cosine of the muon angle, shown in Figure 10.8, reveals significant divergence among generator predictions at very forward angles, where momentum transfer to the nucleus is minimal. GiBUU 2025 performs best, followed by the GENIE predictions. NuWro and NEUT overpredict in this region and do not agree well with data, as the p-values in Table 10.3 show. Models overpredicting at low momentum transfer, Q^2, for single pion final states has been well documented by several experiments, including MINOS [258], MiniBooNE [202], and MINERvA [217]. It also again matches MicroBooNE's result for the CC ν_μ π^0 cross section [186]. MINOS and MINERvA have improved their data-simulation agreement by introducing ad hoc Q^2-dependent suppression functions for resonance production simulations [217, 259].

The muon momentum differential cross section shown in Figure 10.9, using the subset

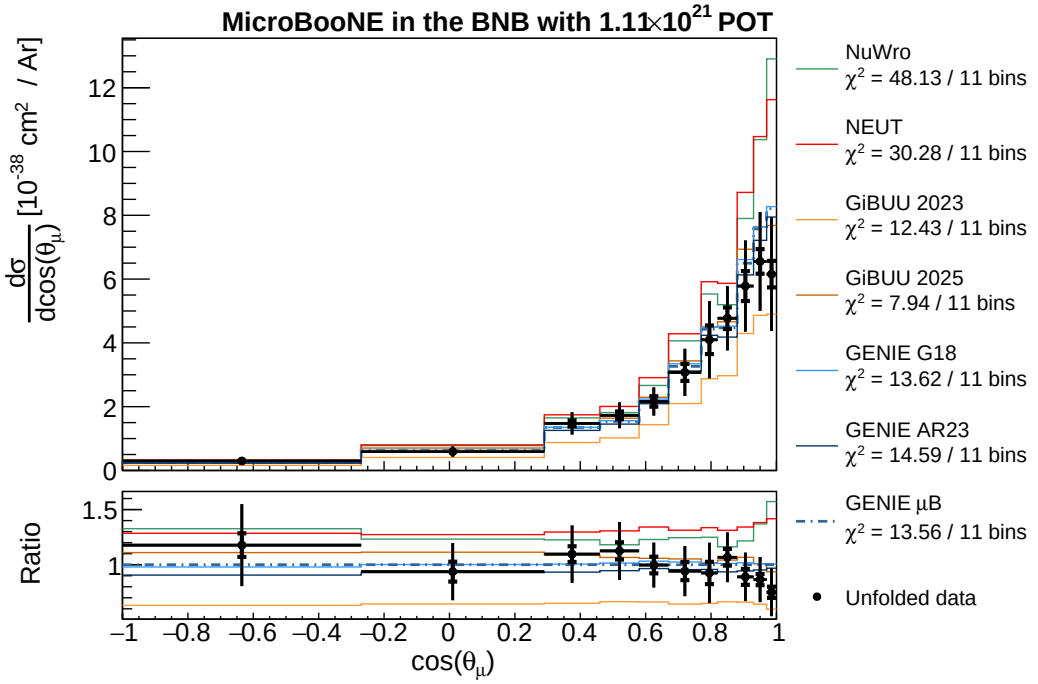

Fig. 10.8 Unfolded differential cross section with respect to the cosine of the muon angle with the beam axis.

of completely contained events described in Section 7.6.5, demonstrates good agreement with all models except GiBUU 2023 due to it systematically underpredicting. The pion angle differential cross section in Figure 10.10 shows strong agreement with GENIE models in the backward direction, while NuWro, NEUT, and GiBUU 2025 overpredict there. In the forward direction, measured cross sections consistently exceed GENIE and GiBUU 2025 predictions, aligning better with NuWro and NEUT due to their higher total cross-section predictions. Overall, data-simulation agreement is best for the GENIE configurations and NuWro, with NEUT and GiBUU performing worse. Figure 10.11 shows the differential cross section with respect to pion momentum, using the unscattered-enhanced subset of events described in Section 7.6.4. The large uncertainties in the first bin are driven by uncertainties on the background prediction arising from the neutrino interaction model. GENIE and NuWro predictions sit around 7×10^{-38} cm^2/GeV/Ar, but NEUT and GiBUU 2025 significantly deviate, predicting much higher cross sections at low pion momentum. Comparison with Figure 10.12, which has FSI disabled for the generators, shows that these higher values are driven by their final-state simulations. At higher energies, FSI simulation suppresses the predictions, contributing to the underprediction in the last bin. Overall, data-simulation

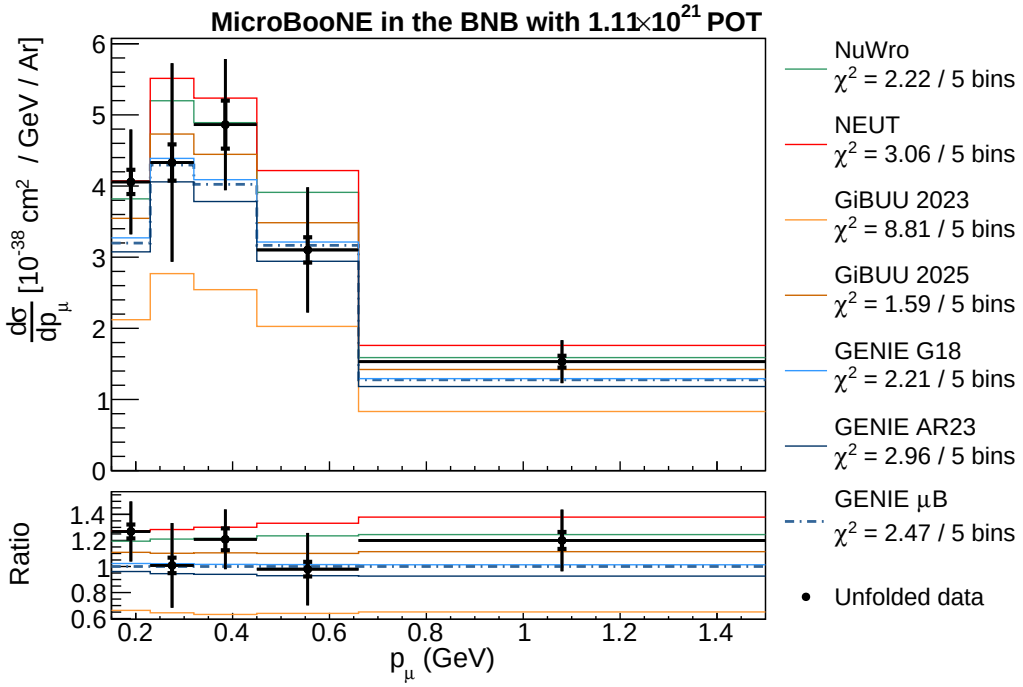

Fig. 10.9 Unfolded differential cross section with respect to muon momentum using the dedicated selection subset defined in the text.

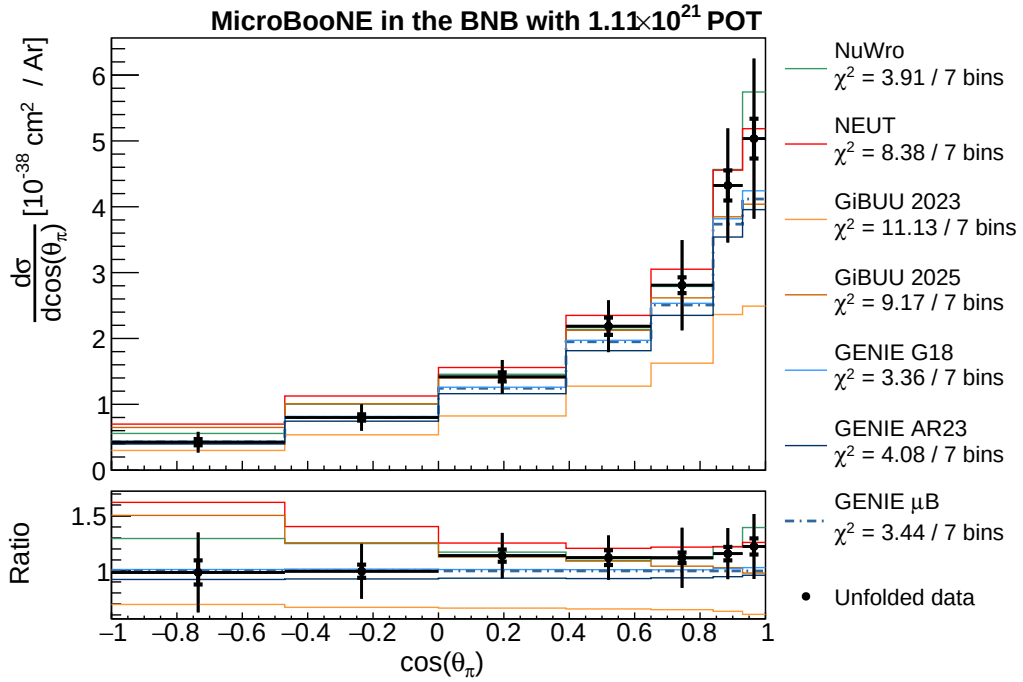

Fig. 10.10 Unfolded differential cross section with respect to the cosine of the pion angle with the beam axis.

agreement is best with GENIE and NuWro, followed by NEUT and GiBUU 2025. GiBUU 2023 shows poor agreement with the data.

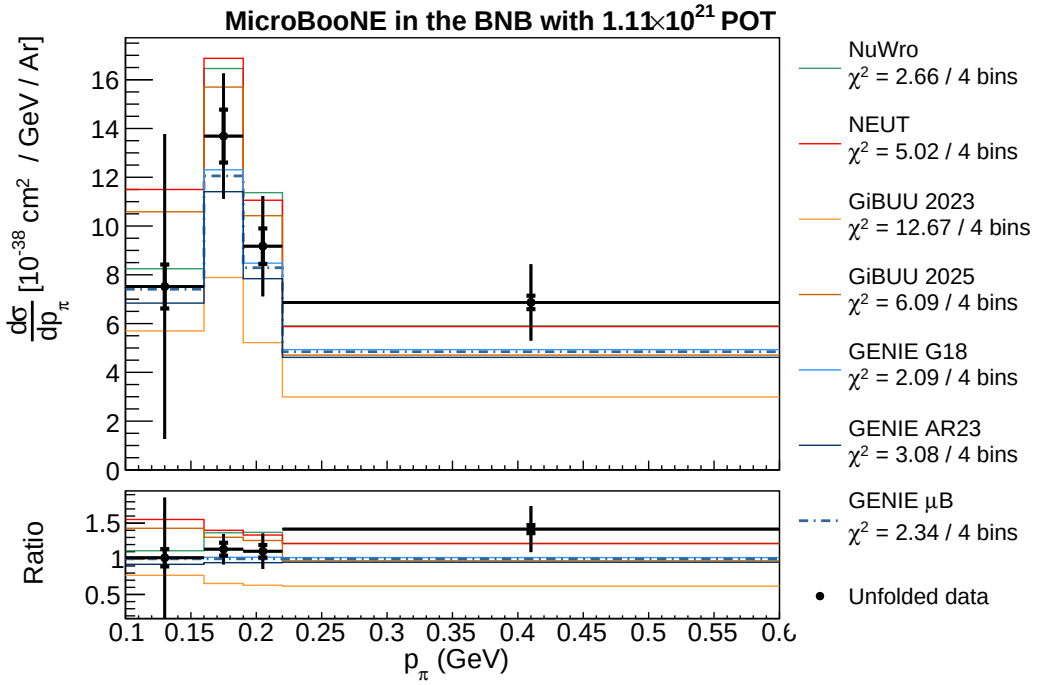

Fig. 10.11 Unfolded differential cross section with respect to pion momentum using the dedicated selection subset defined in the text.

Finally, Figure 10.13 shows the differential cross section with respect to the opening angle between muon and pion using all selected events. Data-simulation agreement is generally good apart from GiBUU 2023, with NuWro performing best, followed by GENIE, GiBUU 2025, and NEUT.

10.4 Summary

This analysis has successfully leveraged MicroBooNE's large collection of recorded neutrino-argon interactions to report unfolded muon neutrino single charged pion cross-section measurements. The generator comparisons show no one generator captures the data features perfectly across all kinematic variables. Overall, GiBUU 2025 performs best for the total and muon kinematic variables, but, apart from GiBUU 2023, has the worst agreement with data for the pion variables. GENIE and NuWro give the closest predictions for those differential cross sections. Predictions of the most forward muon angle cross section are generally higher than the data, especially for NuWro and NEUT,

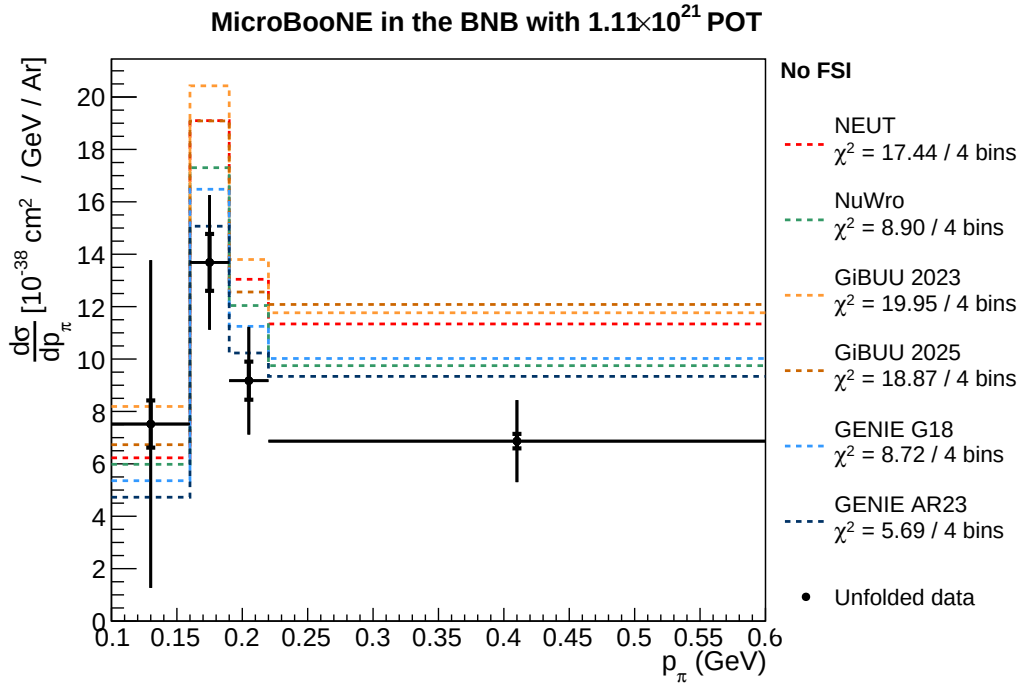

Fig. 10.12 Comparison between the unfolded pion momentum cross section and generator predictions with FSI disabled.

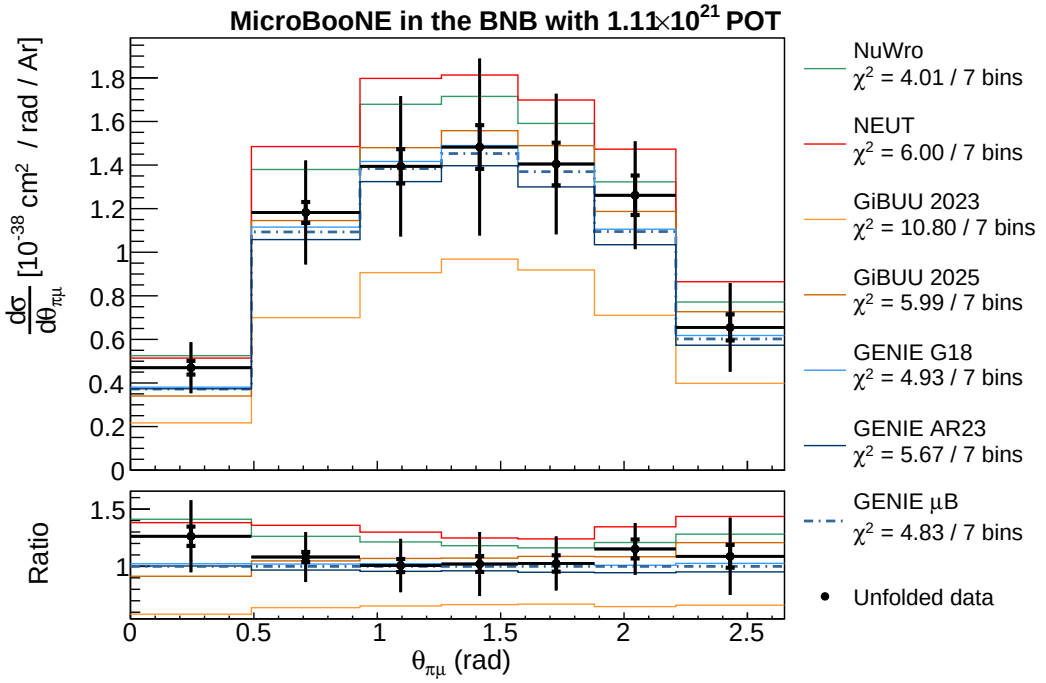

Fig. 10.13 Unfolded differential cross section with respect to the muon-pion opening angle.

signalling deficiencies in low-Q^2 modelling. At backward pion angles, NEUT, GiBUU 2025, and, to a lesser extent, NuWro have higher predictions than both GENIE and the data. Finally, uncertainties and differences between generators are both large at low pion momentum. The measurements here are limited by systematic uncertainties in the detector simulation, the background estimation, and the neutrino flux modelling as highlighted previously in Figure 8.2. Future work to reduce these uncertainties, especially at low pion momentum, is needed.

Chapter 11

Conclusion and Outlook

This thesis presents new flux-integrated measurements of CC muon (anti-)neutrino cross sections on argon for events with a charged pion and any number of nucleons in the final state. Measurements are reported for the total cross section and for five kinematic variables: muon momentum, pion momentum, muon angle with respect to the beam, pion angle with respect to the beam, and the muon–pion opening angle. The analysis employs a BDT-based selection and defines subsets of events for muon and pion momentum estimation. The pion momentum differential cross section represents the first such measurement on argon. The total cross section is measured to be $\sigma = (3.75 \pm 0.07\ (\text{stat.}) \pm 0.80\ (\text{syst.})) \times 10^{-38}\,\text{cm}^2/\text{Ar}$ at a mean neutrino beam energy of ~ 0.8 GeV. Data from all five experimental runs of the MicroBooNE detector in the BNB were utilised, resulting in up to a factor 25 increase in the background-subtracted event count compared with a prior measurement of this process on argon by ArgoNeuT. Compared with ArgoNeuT, which used the NuMI beam, these cross-section measurements provide new data at lower beam energies and are therefore complementary to the existing data. This work has been published in Ref. [229]. The measurements are limited by systematic uncertainties, the dominant sources of which are the neutrino flux, the neutrino interaction model, and the detector simulation.

The cross-section measurements presented in this work have been compared to a suite of modern neutrino-nucleus interaction generators, providing insights into current modelling strengths and areas for refinement. While the total cross section is well described by all generators within the uncertainties, notable tensions emerge in specific kinematic regions. The latest version of GiBUU performs best for the total and muon kinematic variables, but shows lower agreement with data for the pion variables than other generators. GENIE and NuWro give the closest predictions for those differential cross sections. A notable pattern in the modelling of the hadronic final

state is that several generators overpredict at backward pion angles and underpredict at high pion momentum. Predictions for the forward muon angle shape generally exceed the data, and are especially high for NuWro and NEUT, signalling deficiencies in low-Q^2 modelling. Finally, uncertainties and variations among generators are both high at low pion momentum, with the latter driven by differences in FSI modelling.

The significance of these measurements for the field comes from the crucial role resonance-producing neutrino–nucleus interactions will play in the future DUNE experiment, where, due to higher beam energies compared to MicroBooNE, these interactions will dominate. The wide energy spectrum with which neutrino beams are produced necessitates the reconstruction of the energy of each interacting neutrino for oscillation measurements. This requires accurate neutrino interaction generators, and thus precise cross-section measurements are crucial for reducing the systematic uncertainties that limit neutrino oscillation experiments. This is of particular importance for the search for CP violation in the lepton sector.

Direct measurements on argon are important to tune empirical generator models. Beyond that, this analysis also contributes to the collective set of cross-section measurements made on a variety of different nuclear targets. It therefore provides a valuable source of data to better understand the A-dependence, i.e. the change of the cross section with nuclear target size, for resonance production.

MicroBooNE is pursuing multiple further charged pion analyses focused on exploring proton multiplicity, transverse kinematic imbalance variables (which are variables particularly sensitive to nuclear effects [227]), measurements of charged pion channels using the NuMI beam data, and coherent pion production. Several of these ongoing analyses make use of knowledge, samples, and tools produced during this analysis.

The SBND experiment at Fermilab [260], which started continuously taking beam data in December 2024 and is expected to run until 2027, will be another major step forward for neutrino–argon interaction statistics, with an expected order-of-magnitude increase in flux compared to MicroBooNE [261]. However, to fully leverage this, improvements in systematic uncertainties are essential. SBND benefits from reduced interaction model uncertainties resulting from the suite of cross-section measurements from MicroBooNE and other prior experiments. For instance, SBND's charged pion measurements will benefit from the improved constraints on pionless cross sections produced by MicroBooNE that form the major background of this analysis. In the same way, this analysis will reduce uncertainties on QE-like cross-section measurements. SBND will also make use of new techniques and flux models, as well as benefit

from improvements in LArTPC reconstruction and simulation software resulting from MicroBooNE and the DUNE development effort.

Beyond existing analysis methodologies, new approaches to charged pion and muon measurements also have the potential to improve selection purity and extend cross-section measurements to new energy regions. The Liquid Argon In A Testbeam (LArIAT) experiment has shown that muons and charged pions stopping in liquid argon can undergo nuclear capture on argon nuclei, producing very short MeV-scale energy deposits or 'blips' upon the subsequent de-excitation of the nucleus [262]. These blips provide a handle for distinguishing between muons and pions, with pions found to generate more of them due to their higher rest mass. This offers a promising new method for improving muon–pion separation in liquid argon detectors, though its practical use will require improved modelling of nuclear de-excitation processes and reconstruction of the blips. Additionally, an algorithm that fits the measured energy loss along the section of a charged pion track before it visibly scatters to a theoretical model, effectively calculating the total length the particle would have travelled had it not interacted inelastically, provides a way to estimate the momentum from charged pions scattering on the argon [263]. This approach would allow measurements to be extended to higher pion momenta.

References

[1] S. Navas *et al.* (Particle Data Group), *Review of particle physics*, Phys. Rev. D **110**, 030001 (2024).

[2] E. Noether, *Invariant Variation Problems*, Gott. Nachr. **1918**, 235–257 (1918), arXiv:physics/0503066.

[3] R. Purdy, *Particle Physics: An Introduction*, Essentials of Physics Series (Mercury Learning And Information, 2023).

[4] Y.-R. Liu, H.-X. Chen, W. Chen, X. Liu, and S.-L. Zhu, *Pentaquark and Tetraquark states*, Prog. Part. Nucl. Phys. **107**, 237–320 (2019), arXiv:1903.11976 [hep-ph].

[5] S. S. Agaev, K. Azizi, and H. Sundu, *Newly observed exotic doubly charmed meson Tcc+*, Nucl. Phys. B **975**, 115650 (2022), arXiv:2108.00188 [hep-ph].

[6] T. Nakano and K. Nishijima, *Charge Independence for V-particles*, Prog. Theor. Phys. **10**, 581–582 (1953).

[7] M. Gell-Mann, *The interpretation of the new particles as displaced charge multiplets*, Nuovo Cim. **4**, 848–866 (1956).

[8] M. Atzori Corona, M. Cadeddu, N. Cargioli, F. Dordei, and C. Giunti, *Refined determination of the weak mixing angle at low energy*, Phys. Rev. D **110**, 033005 (2024), arXiv:2405.09416 [hep-ph].

[9] J. Goldstone, *Field Theories with Superconductor Solutions*, Nuovo Cim. **19**, 154–164 (1961).

[10] O. W. Greenberg, *Why is CPT fundamental?*, Found. Phys. **36**, 1535–1553 (2006), arXiv:hep-ph/0309309.

[11] C. S. Wu, E. Ambler, R. W. Hayward, D. D. Hoppes, and R. P. Hudson, *Experimental Test of Parity Conservation in β Decay*, Phys. Rev. **105**, 1413–1414 (1957).

[12] J. H. Christenson, J. W. Cronin, V. L. Fitch, and R. Turlay, *Evidence for the 2π Decay of the K_2^0 Meson*, Phys. Rev. Lett. **13**, 138–140 (1964).

[13] J. Chadwick, *The intensity distribution in the magnetic spectrum of β particles from radium (B + C)*, Verh. Phys. Gesell. **16**, 383–391 (1914).

[14] C. Jensen, *Controversy and consensus : nuclear beta decay 1911-1934*, Science networks. Historical studies ; v. 24 (Birkhäuser, Basel, 2000).

[15] C. L. Cowan, F. Reines, F. B. Harrison, H. W. Kruse, and A. D. McGuire, *Detection of the free neutrino: A Confirmation*, Science **124**, 103–104 (1956).

[16] G. Danby, J. M. Gaillard, K. A. Goulianos, L. M. Lederman, N. B. Mistry, M. Schwartz, and J. Steinberger, *Observation of High-Energy Neutrino Reactions and the Existence of Two Kinds of Neutrinos*, Phys. Rev. Lett. **9**, 36–44 (1962).

[17] K. Kodama *et al.* (DONUT), *Observation of tau neutrino interactions*, Phys. Lett. B **504**, 218–224 (2001), arXiv:hep-ex/0012035.

[18] R. Davis Jr., D. S. Harmer, and K. C. Hoffman, *Search for neutrinos from the sun*, Phys. Rev. Lett. **20**, 1205–1209 (1968).

[19] Y. Fukuda *et al.* (Super-Kamiokande), *Evidence for oscillation of atmospheric neutrinos*, Phys. Rev. Lett. **81**, 1562–1567 (1998), arXiv:hep-ex/9807003.

[20] B. Pontecorvo, *Neutrino Experiments and the Problem of Conservation of Leptonic Charge*, Sov. Phys. JETP **26**, 984–988 (1968).

[21] Q. R. Ahmad *et al.* (SNO Collaboration), *Direct evidence for neutrino flavor transformation from neutral-current interactions in the sudbury neutrino observatory*, Phys. Rev. Lett. **89**, 011301 (2002).

[22] Q. R. Ahmad *et al.* (SNO Collaboration), *Measurement of the Rate of* $\nu_e + d \rightarrow p + p + e^-$ *Interactions Produced by* ^8B *Solar Neutrinos at the Sudbury Neutrino Observatory*, Phys. Rev. Lett. **87**, 071301 (2001).

[23] L. Wolfenstein, *Neutrino Oscillations in Matter*, Phys. Rev. D **17**, 2369–2374 (1978).

[24] S. P. Mikheyev and A. Y. Smirnov, *Resonance Amplification of Oscillations in Matter and Spectroscopy of Solar Neutrinos*, Sov. J. Nucl. Phys. **42**, 913–917 (1985).

[25] A. Y. Smirnov, in *10th International Workshop on Neutrino Telescopes* (2003) pp. 23–43, arXiv:hep-ph/0305106.

[26] I. Esteban, M. C. Gonzalez-Garcia, M. Maltoni, I. Martinez-Soler, J. a. P. Pinheiro, and T. Schwetz, *NuFit-6.0: updated global analysis of three-flavor neutrino oscillations*, JHEP **12**, 216, arXiv:2410.05380 [hep-ph].

[27] C. Giunti, *Neutrino Flavor States and the Quantum Theory of Neutrino Oscillations*, AIP Conf. Proc. **1026**, 3–19 (2008), arXiv:0801.0653 [hep-ph].

[28] A. G. Cohen, S. L. Glashow, and Z. Ligeti, *Disentangling Neutrino Oscillations*, Phys. Lett. B **678**, 191–196 (2009), arXiv:0810.4602 [hep-ph].

[29] A. D. Sakharov, *Violation of CP Invariance, C asymmetry, and baryon asymmetry of the universe*, Pisma Zh. Eksp. Teor. Fiz. **5**, 32–35 (1967).

[30] W. Bernreuther, *CP violation and baryogenesis*, Lect. Notes Phys. **591**, 237–293 (2002), arXiv:hep-ph/0205279.

[31] C. Jarlskog, *Commutator of the Quark Mass Matrices in the Standard Electroweak Model and a Measure of Maximal CP Nonconservation*, Phys. Rev. Lett. **55**, 1039 (1985).

[32] K. Abe *et al.* (T2K), *The T2K Experiment*, Nucl. Instrum. Meth. A **659**, 106–135 (2011), arXiv:1106.1238 [physics.ins-det].

[33] D. S. Ayres, G. R. Drake, M. C. Goodman, J. J. Grudzinski, V. J. Guarino, R. L. Talaga, A. Zhao, P. Stamoulis, E. Stiliaris, G. Tzanakos, *et al.* (NOvA), The nova technical design report (2007).

[34] M. A. Acero *et al.* (NOvA), *Improved measurement of neutrino oscillation parameters by the NOvA experiment*, Phys. Rev. D **106**, 032004 (2022), arXiv:2108.08219 [hep-ex].

[35] K. Abe *et al.* (T2K), *Measurements of neutrino oscillation parameters from the T2K experiment using* 3.6×10^{21} *protons on target*, Eur. Phys. J. C **83**, 782 (2023), arXiv:2303.03222 [hep-ex].

[36] M. Aker *et al.* (Katrin), Direct neutrino-mass measurement based on 259 days of KATRIN data (2024), arXiv:2406.13516 [nucl-ex].

[37] A. G. Adame *et al.* (DESI), DESI 2024 VI: Cosmological Constraints from the Measurements of Baryon Acoustic Oscillations (2024), arXiv:2404.03002 [astro-ph.CO].

[38] D. Naredo-Tuero, M. Escudero, E. Fernández-Martínez, X. Marcano, and V. Poulin, *Critical look at the cosmological neutrino mass bound*, Phys. Rev. D **110**, 123537 (2024), arXiv:2407.13831 [astro-ph.CO].

[39] E. K. Akhmedov, in *ICTP Summer School in Particle Physics* (1999) pp. 103–164, arXiv:hep-ph/0001264.

[40] S. Weinberg, *Baryon and Lepton Nonconserving Processes*, Phys. Rev. Lett. **43**, 1566–1570 (1979).

[41] M. J. Dolinski, A. W. P. Poon, and W. Rodejohann, *Neutrinoless Double-Beta Decay: Status and Prospects*, Ann. Rev. Nucl. Part. Sci. **69**, 219–251 (2019), arXiv:1902.04097 [nucl-ex].

[42] J. J. Gómez-Cadenas, J. Martín-Albo, J. Menéndez, M. Mezzetto, F. Monrabal, and M. Sorel, *The search for neutrinoless double-beta decay*, Riv. Nuovo Cim. **46**, 619–692 (2023).

[43] M. Agostini *et al.* (GERDA), *Final Results of GERDA on the Search for Neutrinoless Double-β Decay*, Phys. Rev. Lett. **125**, 252502 (2020), arXiv:2009.06079 [nucl-ex].

[44] S. Bilenky, *Introduction to the physics of massive and mixed neutrinos*, Lecture Notes in Physics, Vol. 817 (Springer-Verlag, 2010).

[45] S. Böser, C. Buck, C. Giunti, J. Lesgourgues, L. Ludhova, S. Mertens, A. Schukraft, and M. Wurm, *Status of Light Sterile Neutrino Searches*, Prog. Part. Nucl. Phys. **111**, 103736 (2020), arXiv:1906.01739 [hep-ex].

[46] A. Aguilar *et al.* (LSND), *Evidence for neutrino oscillations from the observation of $\bar{\nu}_e$ appearance in a $\bar{\nu}_\mu$ beam*, Phys. Rev. D **64**, 112007 (2001), arXiv:hep-ex/0104049.

[47] A. A. Aguilar-Arevalo *et al.* (MiniBooNE), *Significant Excess of ElectronLike Events in the MiniBooNE Short-Baseline Neutrino Experiment*, Phys. Rev. Lett. **121**, 221801 (2018), arXiv:1805.12028 [hep-ex].

[48] F. Dydak *et al.*, *A Search for Muon-neutrino Oscillations in the Δm^2 Range 0.3-eV^2 to 90-eV^2*, Phys. Lett. B **134**, 281 (1984).

[49] P. Adamson *et al.* (MINOS+), *Search for sterile neutrinos in MINOS and MINOS+ using a two-detector fit*, Phys. Rev. Lett. **122**, 091803 (2019), arXiv:1710.06488 [hep-ex].

[50] M. G. Aartsen *et al.* (IceCube), *Searching for eV-scale sterile neutrinos with eight years of atmospheric neutrinos at the IceCube Neutrino Telescope*, Phys. Rev. D **102**, 052009 (2020), arXiv:2005.12943 [hep-ex].

[51] P. Abratenko *et al.* (MicroBooNE), *Search for an Excess of Electron Neutrino Interactions in MicroBooNE Using Multiple Final-State Topologies*, Phys. Rev. Lett. **128**, 241801 (2022), arXiv:2110.14054 [hep-ex].

[52] P. Abratenko *et al.* (MicroBooNE), Enhanced Search for Neutral Current Δ Radiative Single-Photon Production in MicroBooNE (2025), arXiv:2502.05750 [hep-ex].

[53] P. Abratenko *et al.* (MicroBooNE), Inclusive Search for Anomalous Single-Photon Production in MicroBooNE (2025), arXiv:2502.06064 [hep-ex].

[54] A. M. Abdullahi *et al.* (MicroBooNE), First Search for Dark Sector e^+e^- Explanations of the MiniBooNE Anomaly at MicroBooNE (2025), arXiv:2502.10900 [hep-ex].

[55] G. Mention, M. Fechner, T. Lasserre, T. A. Mueller, D. Lhuillier, M. Cribier, and A. Letourneau, *The Reactor Antineutrino Anomaly*, Phys. Rev. D **83**, 073006 (2011), arXiv:1101.2755 [hep-ex].

[56] H. Almazán *et al.* (STEREO), *STEREO neutrino spectrum of ^{235}U fission rejects sterile neutrino hypothesis*, Nature **613**, 257–261 (2023), arXiv:2210.07664 [hep-ex].

[57] H. de Kerret *et al.* (Double Chooz), *Double Chooz θ_{13} measurement via total neutron capture detection*, Nature Phys. **16**, 558–564 (2020), arXiv:1901.09445 [hep-ex].

[58] F. Kaether, W. Hampel, G. Heusser, J. Kiko, and T. Kirsten, *Reanalysis of the GALLEX solar neutrino flux and source experiments*, Phys. Lett. B **685**, 47–54 (2010), arXiv:1001.2731 [hep-ex].

[59] J. N. Abdurashitov *et al.* (SAGE), *Measurement of the solar neutrino capture rate with gallium metal. III: Results for the 2002–2007 data-taking period*, Phys. Rev. C **80**, 015807 (2009), arXiv:0901.2200 [nucl-ex].

[60] V. V. Barinov *et al.*, *Results from the Baksan Experiment on Sterile Transitions (BEST)*, Phys. Rev. Lett. **128**, 232501 (2022), arXiv:2109.11482 [nucl-ex].

[61] J. H. Choi *et al.* (RENO), *Observation of Energy and Baseline Dependent Reactor Antineutrino Disappearance in the RENO Experiment*, Phys. Rev. Lett. **116**, 211801 (2016), arXiv:1511.05849 [hep-ex].

[62] F. P. An *et al.* (Daya Bay), *Measurement of the Reactor Antineutrino Flux and Spectrum at Daya Bay*, Phys. Rev. Lett. **116**, 061801 (2016), [Erratum: Phys.Rev.Lett. 118, 099902 (2017)], arXiv:1508.04233 [hep-ex].

[63] Y. Abe *et al.* (Double Chooz), *Improved measurements of the neutrino mixing angle θ_{13} with the Double Chooz detector*, JHEP **10**, 086, [Erratum: JHEP 02, 074 (2015)], arXiv:1406.7763 [hep-ex].

[64] Y. J. Ko *et al.* (NEOS), *Sterile Neutrino Search at the NEOS Experiment*, Phys. Rev. Lett. **118**, 121802 (2017), arXiv:1610.05134 [hep-ex].

[65] A. P. Serebrov *et al.*, *Search for sterile neutrinos with the Neutrino-4 experiment and measurement results*, Phys. Rev. D **104**, 032003 (2021), arXiv:2005.05301 [hep-ex].

[66] H. Almazán *et al.* (STEREO), *First antineutrino energy spectrum from ^{235}U fissions with the STEREO detector at ILL*, J. Phys. G **48**, 075107 (2021), arXiv:2010.01876 [hep-ex].

[67] M. Andriamirado *et al.* (PROSPECT), *Final Measurement of the U235 Antineutrino Energy Spectrum with the PROSPECT-I Detector at HFIR*, Phys. Rev. Lett. **131**, 021802 (2023), arXiv:2212.10669 [nucl-ex].

[68] P. Bakhti, M.-G. Park, M. Rajaee, C. S. Shin, and S. Shin, Revisiting Reactor Anti-Neutrino 5 MeV Bump with ^{13}C Neutral-Current Interaction (2024), arXiv:2405.08724 [hep-ph].

[69] A. Diaz, C. A. Argüelles, G. H. Collin, J. M. Conrad, and M. H. Shaevitz, *Where Are We With Light Sterile Neutrinos?*, Phys. Rept. **884**, 1–59 (2020), arXiv:1906.00045 [hep-ex].

[70] M. Aker *et al.* (KATRIN), *KATRIN: status and prospects for the neutrino mass and beyond*, J. Phys. G **49**, 100501 (2022), arXiv:2203.08059 [nucl-ex].

[71] D. Racco, P. Zhang, and H. Zheng, Neutrino masses from large-scale structures: future sensitivity and theory dependence (2024), arXiv:2412.04959 [astro-ph.CO].

[72] A. Cabrera *et al.*, *Synergies and prospects for early resolution of the neutrino mass ordering*, Sci. Rep. **12**, 5393 (2022), arXiv:2008.11280 [hep-ph].

[73] P. B. Denton, M. Friend, M. D. Messier, H. A. Tanaka, S. Böser, J. a. A. B. Coelho, M. Perrin-Terrin, and T. Stuttard, Snowmass Neutrino Frontier: NF01 Topical Group Report on Three-Flavor Neutrino Oscillations (2022), arXiv:2212.00809 [hep-ph].

[74] M. A. Acero *et al.*, *White paper on light sterile neutrino searches and related phenomenology*, J. Phys. G **51**, 120501 (2024), arXiv:2203.07323 [hep-ex].

[75] M. Thomson, *Modern particle physics* (Cambridge University Press, New York, 2013).

[76] T. Leitner, O. Buss, L. Alvarez-Ruso, and U. Mosel, *Electron- and neutrino-nucleus scattering from the quasielastic to the resonance region*, Phys. Rev. C **79**, 034601 (2009), arXiv:0812.0587 [nucl-th].

[77] L. Alvarez-Ruso *et al.* (NuSTEC), *NuSTEC White Paper: Status and challenges of neutrino–nucleus scattering*, Prog. Part. Nucl. Phys. **100**, 1–68 (2018), arXiv:1706.03621 [hep-ph].

[78] F. J. Ernst, R. G. Sachs, and K. C. Wali, *Electromagnetic form factors of the nucleon*, Phys. Rev. **119**, 1105–1114 (1960).

[79] R. Bradford, A. Bodek, H. S. Budd, and J. Arrington, *A New parameterization of the nucleon elastic form-factors*, Nucl. Phys. B Proc. Suppl. **159**, 127–132 (2006), arXiv:hep-ex/0602017.

[80] A. Bodek, S. Avvakumov, R. Bradford, and H. S. Budd, *Vector and Axial Nucleon Form Factors:A Duality Constrained Parameterization*, Eur. Phys. J. C **53**, 349–354 (2008), arXiv:0708.1946 [hep-ex].

[81] A. W. Thomas, in *International Symposium on Non-Nucleonic Degrees of Freedom Detected in Nucleus (NNDF 96)* (1996) pp. 142–149, arXiv:nucl-th/9609052.

[82] C. Alexandrou, S. Bacchio, M. Constantinou, J. Finkenrath, K. Hadjiyiannakou, K. Jansen, and G. Koutsou, *Nucleon strange electromagnetic form factors*, Phys. Rev. D **101**, 031501 (2020), arXiv:1909.10744 [hep-lat].

[83] B. Märkisch *et al.*, *Measurement of the Weak Axial-Vector Coupling Constant in the Decay of Free Neutrons Using a Pulsed Cold Neutron Beam*, Phys. Rev. Lett. **122**, 242501 (2019), arXiv:1812.04666 [nucl-ex].

[84] H. S. Budd, A. Bodek, and J. Arrington, in *2nd International Workshop on Neutrino-Nucleus Interactions in the Few GeV Region* (2003) arXiv:hep-ex/0308005.

[85] M. L. Goldberger and S. B. Treiman, *Form-factors in Beta decay and muon capture*, Phys. Rev. **111**, 354–361 (1958).

[86] M. Gell-Mann and M. Levy, *The axial vector current in beta decay*, Nuovo Cim. **16**, 705 (1960).

[87] D. Casper, *The Nuance neutrino physics simulation, and the future*, Nucl. Phys. B Proc. Suppl. **112**, 161–170 (2002), arXiv:hep-ph/0208030.

[88] J. Formaggio and G. Zeller, *From eV to EeV: Neutrino Cross Sections Across Energy Scales*, Rev. Mod. Phys. **84**, 1307–1341 (2012), arXiv:1305.7513 [hep-ex].

[89] G. Breit and E. Wigner, *Capture of Slow Neutrons*, Phys. Rev. **49**, 519–531 (1936).

[90] E. A. Paschos, J.-Y. Yu, and M. Sakuda, *Neutrino production of resonances*, Phys. Rev. D **69**, 014013 (2004), arXiv:hep-ph/0308130.

[91] W. Rarita and J. Schwinger, *On a theory of particles with half integral spin*, Phys. Rev. **60**, 61 (1941).

[92] K. Xie, J. Gao, T. J. Hobbs, D. R. Stump, and C. P. Yuan (CTEQ-TEA), *High-energy neutrino deep inelastic scattering cross sections*, Phys. Rev. D **109**, 113001 (2024), arXiv:2303.13607 [hep-ph].

[93] Y. S. Jeong and M. H. Reno, *Neutrino cross sections: Interface of shallow- and deep-inelastic scattering for collider neutrinos*, Phys. Rev. D **108**, 113010 (2023), arXiv:2307.09241 [hep-ph].

[94] E. A. Paschos and D. Schalla, *Coherent Pion Production by Neutrinos*, Phys. Rev. D **80**, 033005 (2009), arXiv:0903.0451 [hep-ph].

[95] I. Ruiz Simo, J. E. Amaro, M. B. Barbaro, A. De Pace, J. A. Caballero, and T. W. Donnelly, *Relativistic model of 2p-2h meson exchange currents in (anti)neutrino scattering*, J. Phys. G **44**, 065105 (2017), arXiv:1604.08423 [nucl-th].

[96] Accelerator Division, Operations Department, *Concepts Rookie Book*, Fermilab (2020).

[97] MicroBooNE Collaboration, *Booster Neutrino Flux Prediction at MicroBooNE*, MicroBooNE Public Note 1031-PUB (Fermi National Accelerator Laboratory, Batavia, IL, USA, 2018).

[98] A. A. Aguilar-Arevalo *et al.* (MiniBooNE), *The Neutrino Flux Prediction at MiniBooNE*, Phys. Rev. D **79**, 072002 (2009), arXiv:0806.1449 [hep-ex].

[99] J. L. Paton, in *25th International Workshop on Neutrinos from Accelerators* (2025) arXiv:2501.06323 [hep-ex].

[100] A. Aguilar-Arevalo *et al.* (PiENu), *Improved Measurement of the $\pi \to e\nu$ Branching Ratio*, Phys. Rev. Lett. **115**, 071801 (2015), arXiv:1506.05845 [hep-ex].

[101] P. Adamson *et al.*, *The NuMI Neutrino Beam*, Nucl. Instrum. Meth. A **806**, 279–306 (2016), arXiv:1507.06690 [physics.acc-ph].

[102] MicroBooNE Collaboration, *Updates to the NuMI Flux Simulation at MicroBooNE*, MicroBooNE Public Note 1129-PUB; FERMILAB-FN-1253-PPD (Fermi National Accelerator Laboratory, Batavia, IL, USA, 2024).

[103] R. Acciarri *et al.* (MicroBooNE), *Design and Construction of the MicroBooNE Detector*, JINST **12** (02), P02017, arXiv:1612.05824 [physics.ins-det].

[104] MicroBooNE Collaboration, *A Measurement of the Attenuation of Drifting Electrons in the MicroBooNE LArTPC*, MicroBooNE Public Note 1026-PUB (Fermi National Accelerator Laboratory, Batavia, IL, USA, 2017).

[105] P. Abratenko *et al.* (MicroBooNE), Measurement of Space Charge Effects in the MicroBooNE LArTPC Using Cosmic Muons (2020), arXiv:2008.09765 [physics.ins-det].

[106] R. Acciarri *et al.* (MicroBooNE), *Noise Characterization and Filtering in the MicroBooNE Liquid Argon TPC*, JINST **12** (08), P08003, arXiv:1705.07341 [physics.ins-det].

[107] P. Abratenko *et al.* (MicroBooNE), *Measurement of the longitudinal diffusion of ionization electrons in the MicroBooNE detector*, JINST **16** (09), P09025, arXiv:2104.06551 [physics.ins-det].

[108] T. Yang, *Calibration of calorimetric measurement in a liquid argon time projection chamber*, Instruments **5**, 2 (2020), arXiv:2012.01319 [physics.ins-det].

[109] C. Adams *et al.* (MicroBooNE), *A method to determine the electric field of liquid argon time projection chambers using a UV laser system and its application in MicroBooNE*, JINST **15** (07), P07010, arXiv:1910.01430 [physics.ins-det].

[110] C. Adams *et al.* (MicroBooNE), *Calibration of the charge and energy loss per unit length of the MicroBooNE liquid argon time projection chamber using muons and protons*, JINST **15** (03), P03022, arXiv:1907.11736 [physics.ins-det].

[111] M. Mooney, in *Meeting of the APS Division of Particles and Fields* (2015) arXiv:1511.01563 [physics.ins-det].

[112] D. Heck, J. Knapp, J. N. Capdevielle, G. Schatz, and T. Thouw, CORSIKA: A Monte Carlo code to simulate extensive air showers (1998).

[113] C. Adams *et al.* (MicroBooNE), *Calibration of the charge and energy loss per unit length of the MicroBooNE liquid argon time projection chamber using muons and protons*, JINST **15** (03), P03022, arXiv:1907.11736 [physics.ins-det].

[114] A. Hitachi, T. Takahashi, N. Funayama, K. Masuda, J. Kikuchi, and T. Doke, *Effect of ionization density on the time dependence of luminescence from liquid argon and xenon*, Phys. Rev. B **27**, 5279–5285 (1983).

[115] M. Suzuki and S. Kubota, *Mechanism of proportional scintillation in argon, krypton and xenon*, Nucl. Instrum. Meth. **164**, 197–199 (1979).

[116] W. Van De Pontseele, *Search for Electron Neutrino Anomalies with the MicroBooNE Detector*, Ph.D. thesis, Oxford U. (2020).

[117] T. Doke, A. Hitachi, J. Kikuchi, K. Masuda, H. Okada, and E. Shibamura, *Absolute Scintillation Yields in Liquid Argon and Xenon for Various Particles*, Jap. J. Appl. Phys. **41**, 1538–1545 (2002).

[118] R. Acciarri *et al.* (WArP), *Effects of Nitrogen contamination in liquid Argon*, JINST **5**, P06003, arXiv:0804.1217 [nucl-ex].

[119] B. J. P. Jones, C. S. Chiu, J. M. Conrad, C. M. Ignarra, T. Katori, and M. Toups, *A Measurement of the Absorption of Liquid Argon Scintillation Light by Dissolved Nitrogen at the Part-Per-Million Level*, JINST **8**, P07011, [Erratum: JINST 8, E09001 (2013)], arXiv:1306.4605 [physics.ins-det].

[120] H. Photonics, R1408 photomultiplier tube datasheet (2023), accessed: 13-Feb-2025.

[121] B. J. P. Jones, *Sterile Neutrinos in Cold Climates*, Ph.D. thesis, MIT (2015).

[122] D. Kaleko, *PMT Triggering and Readout for the MicroBooNE Experiment*, JINST **8**, C09009, arXiv:1308.3446 [physics.ins-det].

[123] C. Adams *et al.* (MicroBooNE), *Design and construction of the MicroBooNE Cosmic Ray Tagger system*, JINST **14** (04), P04004, arXiv:1901.02862 [physics.ins-det].

[124] P. Abratenko *et al.* (MicroBooNE), *Neutrino Event Selection in the MicroBooNE Liquid Argon Time Projection Chamber using Wire-Cell 3-D Imaging, Clustering and Charge-Light Matching*, JINST **16** (06), P06043, arXiv:2011.01375 [physics.ins-det].

[125] P. Abratenko *et al.* (MicroBooNE), *First demonstration of O(1 ns) timing resolution in the MicroBooNE liquid argon time projection chamber*, Phys. Rev. D **108**, 052010 (2023), arXiv:2304.02076 [hep-ex].

[126] MicroBooNE Collaboration, *Light Yield Calibration in MicroBooNE*, Technical MicroBooNE Note 1120-TECH (Fermi National Accelerator Laboratory, Batavia, IL, USA, 2022).

[127] E. L. Snider and G. Petrillo, *LArSoft: Toolkit for Simulation, Reconstruction and Analysis of Liquid Argon TPC Neutrino Detectors*, J. Phys. Conf. Ser. **898**, 042057 (2017).

[128] M. G. Catanesi *et al.* (HARP), *The HARP detector at the CERN PS*, Nucl. Instrum. Meth. A **571**, 527–561 (2007).

[129] A. A. Aguilar-Arevalo *et al.* (SciBooNE), Bringing the SciBar Detector to the Booster Neutrino Beam (2006), arXiv:hep-ex/0601022.

[130] D. C. Carey, K. L. Brown, and F. Rothacker, Third Order TRANSPORT with MAD Input: A Computer Program for Designing Charged Particle Beam Transport Systems (1998).

[131] J. Chew, ed., *Particle accelerator. Proceedings, Conference, PAC 2003, Portland, USA, May 12-16, 2003* (2003).

[132] S. Agostinelli *et al.* (GEANT4), *GEANT4–a simulation toolkit*, Nucl. Instrum. Meth. A **506**, 250–303 (2003).

[133] J. Allison *et al.*, *Geant4 developments and applications*, IEEE Trans. Nucl. Sci. **53**, 270 (2006).

[134] J. Allison *et al.*, *Recent developments in Geant4*, Nucl. Instrum. Meth. A **835**, 186–225 (2016).

[135] J. R. Sanford and C. L. Wang, Empirical formulas for particle production in P - Be collision between 10-GeV/c and 35-GeV/c (1967).

[136] C. Mariani, G. Cheng, J. M. Conrad, and M. H. Shaevitz, *Improved Parameterization of K^+ Production in p-Be Collisions at Low Energy Using Feynman Scaling*, Phys. Rev. D **84**, 114021 (2011), arXiv:1110.0417 [hep-ex].

[137] N. V. Mokhov, S. I. Striganov, A. Van Ginneken, S. G. Mashnik, A. J. Sierk, and J. Ranft, in *4th Workshop on Simulating Accelerator Radiation Environments (SARE4) (A Satellite Meeting of ACCAPP 98)* (1998) arXiv:nucl-th/9812038.

[138] C. Andreopoulos *et al.*, *The GENIE Neutrino Monte Carlo Generator*, Nucl. Instrum. Meth. A **614**, 87–104 (2010), arXiv:0905.2517 [hep-ph].

[139] L. Alvarez-Ruso *et al.* (GENIE), *Recent highlights from GENIE v3*, Eur. Phys. J. ST **230**, 4449–4467 (2021), arXiv:2106.09381 [hep-ph].

[140] P. Abratenko *et al.* (MicroBooNE), *New $CC0\pi$ GENIE model tune for MicroBooNE*, Phys. Rev. D **105**, 072001 (2022), arXiv:2110.14028 [hep-ex].

[141] O. Buss, T. Gaitanos, K. Gallmeister, H. van Hees, M. Kaskulov, O. Lalakulich, A. B. Larionov, T. Leitner, J. Weil, and U. Mosel, *Transport-theoretical Description of Nuclear Reactions*, Phys. Rept. **512**, 1–124 (2012), arXiv:1106.1344 [hep-ph].

[142] Y. Hayato, *NEUT*, Nucl. Phys. B Proc. Suppl. **112**, 171–176 (2002).

[143] T. Golan, J. T. Sobczyk, and J. Zmuda, *NuWro: the Wroclaw Monte Carlo Generator of Neutrino Interactions*, Nucl. Phys. B Proc. Suppl. **229-232**, 499–499 (2012).

[144] J. Nieves, J. E. Amaro, and M. Valverde, *Inclusive quasi-elastic neutrino reactions*, Phys. Rev. C **70**, 055503 (2004), [Erratum: Phys.Rev.C 72, 019902 (2005)], arXiv:nucl-th/0408005.

[145] J. Nieves, I. Ruiz Simo, and M. J. Vicente Vacas, *The nucleon axial mass and the MiniBooNE Quasielastic Neutrino-Nucleus Scattering problem*, Phys. Lett. B **707**, 72–75 (2012), arXiv:1106.5374 [hep-ph].

[146] R. Gran, J. Nieves, F. Sanchez, and M. Vicente Vacas, *Neutrino-nucleus quasi-elastic and 2p2h interactions up to 10 GeV*, Phys. Rev. D **88**, 113007 (2013), arXiv:1307.8105 [hep-ph].

[147] K. S. Kuzmin, V. V. Lyubushkin, and V. A. Naumov, *Lepton polarization in neutrino nucleon interactions*, Mod. Phys. Lett. A **19**, 2815–2829 (2004), arXiv:hep-ph/0312107.

[148] K. M. Graczyk and J. T. Sobczyk, *Form Factors in the Quark Resonance Model*, Phys. Rev. D **77**, 053001 (2008), [Erratum: Phys.Rev.D 79, 079903 (2009)], arXiv:0707.3561 [hep-ph].

[149] C. Berger and L. Sehgal, *Lepton mass effects in single pion production by neutrinos*, Phys. Rev. D **76**, 113004 (2007), arXiv:0709.4378 [hep-ph].

[150] J. A. Nowak (MiniBooNE), *Four Momentum Transfer Discrepancy in the Charged Current π^+ Production in the MiniBooNE: Data vs. Theory*, AIP Conf. Proc. **1189**, 243–248 (2009), arXiv:0909.3659 [hep-ph].

[151] A. Bodek and U. K. Yang, *Higher twist, xi(omega) scaling, and effective LO PDFs for lepton scattering in the few GeV region*, J. Phys. G **29**, 1899–1906 (2003), arXiv:hep-ex/0210024.

[152] C. Berger and L. Sehgal, *PCAC and coherent pion production by low energy neutrinos*, Phys. Rev. D **79**, 053003 (2009), arXiv:0812.2653 [hep-ph].

[153] T. Yang, C. Andreopoulos, H. Gallagher, K. Hoffmann, and P. Kehayias, *A Hadronization Model for Few-GeV Neutrino Interactions*, Eur. Phys. J. C **63**, 1–10 (2009), arXiv:0904.4043 [hep-ph].

[154] S. Dytman, *GENIE final state interactions*, AIP Conf. Proc. **1680**, 020005 (2015).

[155] O. Benhar, N. Farina, H. Nakamura, M. Sakuda, and R. Seki, *Electron- and neutrino-nucleus scattering in the impulse approximation regime*, Phys. Rev. D **72**, 053005 (2005), arXiv:hep-ph/0506116.

[156] U. Mosel, *Neutrino event generators: foundation, status and future*, J. Phys. G **46**, 113001 (2019), arXiv:1904.11506 [hep-ex].

[157] J. E. Amaro, M. B. Barbaro, J. A. Caballero, R. González-Jiménez, G. D. Megias, and I. Ruiz Simo, *Electron- versus neutrino-nucleus scattering*, J. Phys. G **47**, 124001 (2020), arXiv:1912.10612 [nucl-th].

[158] C. H. Llewellyn Smith, *Neutrino Reactions at Accelerator Energies*, Phys. Rept. **3**, 261–379 (1972).

[159] D. Rein and L. M. Sehgal, *PCAC and the Deficit of Forward Muons in π^+ Production by Neutrinos*, Phys. Lett. B **657**, 207–209 (2007), arXiv:hep-ph/0606185.

[160] K. M. Graczyk, D. Kielczewska, P. Przewlocki, and J. T. Sobczyk, *C(5)**A axial form factor from bubble chamber experiments*, Phys. Rev. D **80**, 093001 (2009), arXiv:0908.2175 [hep-ph].

[161] D. Drechsel, S. S. Kamalov, and L. Tiator, *Unitary Isobar Model - MAID2007*, Eur. Phys. J. A **34**, 69–97 (2007), arXiv:0710.0306 [nucl-th].

[162] M. Kabirnezhad, *Single pion production in neutrino-nucleon Interactions*, Phys. Rev. D **97**, 013002 (2018), arXiv:1711.02403 [hep-ph].

[163] O. Lalakulich, T. Leitner, O. Buss, and U. Mosel, *One pion production in neutrino reactions: including non-resonant background*, Phys. Rev. D **82**, 093001 (2010), arXiv:1007.0925 [hep-ph].

[164] M. Betancourt *et al.*, *Comparisons and Challenges of Modern Neutrino Scattering Experiments (TENSIONS2016 Report)*, Phys. Rept. **773-774**, 1–28 (2018), arXiv:1805.07378 [hep-ex].

[165] T. Yang, C. Andreopoulos, H. Gallagher, and P. Kehayias, *A hadronization model for the MINOS experiment*, AIP Conf. Proc. **967**, 269–275 (2007).

[166] Z. Koba, H. B. Nielsen, and P. Olesen, *Scaling of multiplicity distributions in high-energy hadron collisions*, Nucl. Phys. B **40**, 317–334 (1972).

[167] T. Sjostrand, S. Mrenna, and P. Z. Skands, *PYTHIA 6.4 Physics and Manual*, JHEP **05**, 026, arXiv:hep-ph/0603175.

[168] S. Dytman, *Final state interactions in neutrino-nucleus experiments*, Acta Phys. Polon. B **40**, 2445–2460 (2009).

[169] R. Acciarri *et al.* (ArgoNeuT), *A Study of Electron Recombination Using Highly Ionizing Particles in the ArgoNeuT Liquid Argon TPC*, JINST **8**, P08005, arXiv:1306.1712 [physics.ins-det].

[170] M. Miyajima, T. Takahashi, S. Konno, T. Hamada, S. Kubota, H. Shibamura, and T. Doke, *Average energy expended per ion pair in liquid argon*, Phys. Rev. A **9**, 1438–1443 (1974).

[171] B. Jones, *Optical Simulations in LArSoft - Technical Manual*, Tech. Rep. (Massachusetts Institute of Technology, 2012) prepared for the MicroBooNE, LBNE and other LArSoft framework experiments.

[172] C. Adams *et al.* (MicroBooNE), *Ionization electron signal processing in single phase LArTPCs. Part I. Algorithm Description and quantitative evaluation with MicroBooNE simulation*, JINST **13** (07), P07006, arXiv:1802.08709 [physics.ins-det].

[173] J. S. Marshall and M. A. Thomson, *The Pandora Software Development Kit for Pattern Recognition*, Eur. Phys. J. C **75**, 439 (2015), arXiv:1506.05348 [physics.data-an].

[174] R. Acciarri *et al.* (MicroBooNE), *The Pandora multi-algorithm approach to automated pattern recognition of cosmic-ray muon and neutrino events in the MicroBooNE detector*, Eur. Phys. J. C **78**, 82 (2018), arXiv:1708.03135 [hep-ex].

[175] X. Qian, C. Zhang, B. Viren, and M. Diwan, *Three-dimensional Imaging for Large LArTPCs*, JINST **13** (05), P05032, arXiv:1803.04850 [physics.ins-det].

[176] MicroBooNE Collaboration, *Reconstruction and Selection of Neutrino Interactions in MicroBooNE using Deep Convolutional Neural Networks*, MicroBooNE Public Note 1123-PUB (Fermi National Accelerator Laboratory, Batavia, IL, USA, 2024).

[177] MicroBooNE, searchingfornues, https://github.com/ubneutrinos/searchingfornues (2024), package to produce the MicroBooNE 'PeLEE' ntuples; originally developed for electron neutrino searches in MicroBooNE.

[178] K. Abe *et al.* (T2K), *Constraint on the matter–antimatter symmetry-violating phase in neutrino oscillations*, Nature **580**, 339–344 (2020), [Erratum: Nature 583, E16 (2020)], arXiv:1910.03887 [hep-ex].

[179] B. Abi *et al.* (DUNE), *Prospects for beyond the Standard Model physics searches at the Deep Underground Neutrino Experiment*, Eur. Phys. J. C **81**, 322 (2021), arXiv:2008.12769 [hep-ex].

[180] A. M. Ankowski and C. Mariani, *Systematic uncertainties in long-baseline neutrino-oscillation experiments*, J. Phys. G **44**, 054001 (2017), arXiv:1609.00258 [hep-ph].

[181] B. Abi *et al.* (DUNE), *Deep Underground Neutrino Experiment (DUNE), Far Detector Technical Design Report, Volume I Introduction to DUNE*, JINST **15** (08), T08008, arXiv:2002.02967 [physics.ins-det].

[182] P. A. Machado, O. Palamara, and D. W. Schmitz, *The Short-Baseline Neutrino Program at Fermilab*, Ann. Rev. Nucl. Part. Sci. **69**, 363–387 (2019), arXiv:1903.04608 [hep-ex].

[183] C. Adams *et al.* (MicroBooNE), *First measurement of ν_μ charged-current π^0 production on argon with the MicroBooNE detector*, Phys. Rev. D **99**, 091102 (2019), arXiv:1811.02700 [hep-ex].

[184] P. Abratenko *et al.* (MicroBooNE), *Measurement of neutral current single $\pi 0$ production on argon with the MicroBooNE detector*, Phys. Rev. D **107**, 012004 (2023), arXiv:2205.07943 [hep-ex].

[185] P. Abratenko *et al.* (MicroBooNE), First double-differential cross section measurement of neutral-current π^0 production in neutrino-argon scattering in the MicroBooNE detector (2024), arXiv:2404.10948 [hep-ex].

[186] P. Abratenko *et al.* (MicroBooNE), *Measurement of the differential cross section for neutral pion production in charged-current muon neutrino interactions on argon with the MicroBooNE detector*, Phys. Rev. D **110**, 092014 (2024), arXiv:2404.09949 [hep-ex].

[187] P. Abratenko *et al.* (MicroBooNE), *First Measurement of ν_e and $\bar{\nu}_e$ Charged-Current Single Charged-Pion Production Differential Cross Sections on Argon Using the MicroBooNE Detector*, Phys. Rev. Lett. **135**, 061802 (2025), arXiv:2503.23384 [hep-ex].

[188] T. Katori and M. Martini, *Neutrino–nucleus cross sections for oscillation experiments*, J. Phys. G **45**, 013001 (2018), arXiv:1611.07770 [hep-ph].

[189] P. Abratenko *et al.* (MicroBooNE), *Determination of muon momentum in the MicroBooNE LArTPC using an improved model of multiple Coulomb scattering*, JINST **12** (10), P10010, arXiv:1703.06187 [physics.ins-det].

[190] V. L. Highland, *Some Practical Remarks on Multiple Scattering*, Nucl. Instrum. Meth. **129**, 497 (1975).

[191] G. R. Lynch and O. I. Dahl, *Approximations to multiple Coulomb scattering*, Nucl. Instrum. Meth. B **58**, 6–10 (1991).

[192] A. Smith, *Measurement of the muon-neutrino charged-current single charged-pion cross-section on argon with the MicroBooNE detector*, Ph.D. thesis, Apollo - University of Cambridge Repository (2021).

[193] R. Acciarri *et al.* (ArgoNeuT), *First measurement of the cross section for ν_μ and $\bar{\nu}_\mu$ induced single charged pion production on argon using ArgoNeuT*, Phys. Rev. D **98**, 052002 (2018), arXiv:1804.10294 [hep-ex].

[194] L. Aliaga *et al.* (MINERvA), *Design, Calibration, and Performance of the MINERvA Detector*, Nucl. Instrum. Meth. A **743**, 130–159 (2014), arXiv:1305.5199 [physics.ins-det].

[195] A. Bercellie *et al.* (MINERvA), *Simultaneous Measurement of Muon Neutrino ν_μ Charged-Current Single π^+ Production in CH, C, H2O, Fe, and Pb Targets in MINERvA*, Phys. Rev. Lett. **131**, 011801 (2023), arXiv:2209.07852 [hep-ex].

[196] K. Abe *et al.* (T2K), First Measurement of the Electron Neutrino Charged-Current Pion Production Cross Section on Carbon with the T2K Near Detector (2025), arXiv:2505.00516 [hep-ex].

[197] C. T. Kullenberg *et al.* (NOMAD), *A Measurement of Coherent Neutral Pion Production in Neutrino Neutral Current Interactions in NOMAD*, Phys. Lett. B **682**, 177–184 (2009), arXiv:0910.0062 [hep-ex].

[198] A. Rodriguez *et al.* (K2K), *Measurement of single charged pion production in the charged-current interactions of neutrinos in a 1.3-GeV wide band beam*, Phys. Rev. D **78**, 032003 (2008), arXiv:0805.0186 [hep-ex].

[199] M. Hasegawa *et al.* (K2K), *Search for coherent charged pion production in neutrino-carbon interactions*, Phys. Rev. Lett. **95**, 252301 (2005), arXiv:hep-ex/0506008.

[200] C. Mariani *et al.* (K2K), *Measurement of inclusive π^0 production in the Charged-Current Interactions of Neutrinos in a 1.3-GeV wide band beam*, Phys. Rev. D **83**, 054023 (2011), arXiv:1012.1794 [hep-ex].

[201] S. Nakayama *et al.* (K2K), *Measurement of single pi0 production in neutral current neutrino interactions with water by a 1.3-GeV wide band muon neutrino beam*, Phys. Lett. B **619**, 255–262 (2005), arXiv:hep-ex/0408134.

[202] A. A. Aguilar-Arevalo *et al.* (MiniBooNE), *Measurement of Neutrino-Induced Charged-Current Charged Pion Production Cross Sections on Mineral Oil at $E_\nu \sim 1$ GeV*, Phys. Rev. D **83**, 052007 (2011), arXiv:1011.3572 [hep-ex].

[203] A. A. Aguilar-Arevalo *et al.* (MiniBooNE), *Measurement of the ν_μ charged current π^+ to quasi-elastic cross section ratio on mineral oil in a 0.8-GeV neutrino beam*, Phys. Rev. Lett. **103**, 081801 (2009), arXiv:0904.3159 [hep-ex].

[204] A. A. Aguilar-Arevalo *et al.* (MiniBooNE), *Measurement of ν_μ-induced charged-current neutral pion production cross sections on mineral oil at $E_\nu \in 0.5 - 2.0$ GeV*, Phys. Rev. D **83**, 052009 (2011), arXiv:1010.3264 [hep-ex].

[205] A. A. Aguilar-Arevalo *et al.* (MiniBooNE), *Measurement of ν_μ and $\bar{\nu}_\mu$ induced neutral current single π^0 production cross sections on mineral oil at $E_\nu \sim \mathcal{O}(1\text{GeV})$*, Phys. Rev. D **81**, 013005 (2010), arXiv:0911.2063 [hep-ex].

[206] A. A. Aguilar-Arevalo *et al.* (MiniBooNE), *First Observation of Coherent π^0 Production in Neutrino Nucleus Interactions with $E_\nu < 2$ GeV*, Phys. Lett. B **664**, 41–46 (2008), arXiv:0803.3423 [hep-ex].

[207] K. Hiraide *et al.* (SciBooNE), *Search for Charged Current Coherent Pion Production on Carbon in a Few-GeV Neutrino Beam*, Phys. Rev. D **78**, 112004 (2008), arXiv:0811.0369 [hep-ex].

[208] Y. Kurimoto *et al.* (SciBooNE), *Measurement of Inclusive Neutral Current Neutral π^0 Production on Carbon in a Few-GeV Neutrino Beam*, Phys. Rev. D **81**, 033004 (2010), arXiv:0910.5768 [hep-ex].

[209] Y. Kurimoto *et al.* (SciBooNE), *Improved Measurement of Neutral Current Coherent π^0 Production on Carbon in a Few-GeV Neutrino Beam*, Phys. Rev. D **81**, 111102 (2010), arXiv:1005.0059 [hep-ex].

[210] P. Adamson *et al.* (MINOS), *Measurement of single π^0 production by coherent neutral-current ν Fe interactions in the MINOS Near Detector*, Phys. Rev. D **94**, 072006 (2016), arXiv:1608.05702 [hep-ex].

[211] R. Acciarri *et al.* (ArgoNeuT), *First Measurement of Neutrino and Antineutrino Coherent Charged Pion Production on Argon*, Phys. Rev. Lett. **113**, 261801 (2014), [Erratum: Phys.Rev.Lett. 114, 039901 (2015)], arXiv:1408.0598 [hep-ex].

[212] R. Acciarri *et al.* (ArgoNeuT), *Measurement of ν_μ and $\bar{\nu}_\mu$ neutral current $\pi^0 \to \gamma\gamma$ production in the ArgoNeuT detector*, Phys. Rev. D **96**, 012006 (2017), arXiv:1511.00941 [hep-ex].

[213] A. Higuera *et al.* (MINERvA), *Measurement of Coherent Production of $\pi^{\pm}$ in Neutrino and Antineutrino Beams on Carbon from E_{ν} of* 1.5 *to* 20 *GeV*, Phys. Rev. Lett. **113**, 261802 (2014), arXiv:1409.3835 [hep-ex].

[214] A. Mislivec *et al.* (MINERvA), *Measurement of total and differential cross sections of neutrino and antineutrino coherent $\pi^{\pm}$ production on carbon*, Phys. Rev. D **97**, 032014 (2018), arXiv:1711.01178 [hep-ex].

[215] M. A. Ramírez *et al.* (MINERvA), *Neutrino-Induced Coherent π^{+} Production in C, CH, Fe, and Pb at $\langle E_{\nu} \rangle \sim 6$* GeV, Phys. Rev. Lett. **131**, 051801 (2023), arXiv:2210.01285 [hep-ex].

[216] D. Coplowe *et al.* (MINERvA), *Probing nuclear effects with neutrino-induced charged-current neutral pion production*, Phys. Rev. D **102**, 072007 (2020), [Erratum: Phys.Rev.D 110, 059903 (2024)], arXiv:2002.05812 [hep-ex].

[217] B. Eberly *et al.* (MINERvA), *Charged Pion Production in ν_{μ} Interactions on Hydrocarbon at $\langle E_{\nu} \rangle = 4.0$ GeV*, Phys. Rev. D **92**, 092008 (2015), arXiv:1406.6415 [hep-ex].

[218] C. L. McGivern *et al.* (MINERvA), *Cross sections for ν_{μ} and $\bar{\nu}_{\mu}$ induced pion production on hydrocarbon in the few-GeV region using MINERvA*, Phys. Rev. D **94**, 052005 (2016), arXiv:1606.07127 [hep-ex].

[219] T. Le *et al.* (MINERvA), *Measurement of $\bar{\nu}_{\mu}$ Charged-Current Single π^{-} Production on Hydrocarbon in the Few-GeV Region using MINERvA*, Phys. Rev. D **100**, 052008 (2019), arXiv:1906.08300 [hep-ex].

[220] T. Le *et al.* (MINERvA), *Single Neutral Pion Production by Charged-Current $\bar{\nu}_{\mu}$ Interactions on Hydrocarbon at $\langle E_{\nu} \rangle = 3.6$ GeV*, Phys. Lett. B **749**, 130–136 (2015), arXiv:1503.02107 [hep-ex].

[221] O. Altinok *et al.* (MINERvA), *Measurement of ν_{μ} charged-current single π^{0} production on hydrocarbon in the few-GeV region using MINERvA*, Phys. Rev. D **96**, 072003 (2017), arXiv:1708.03723 [hep-ex].

[222] J. Wolcott *et al.* (MINERvA), *Evidence for Neutral-Current Diffractive π^{0} Production from Hydrogen in Neutrino Interactions on Hydrocarbon*, Phys. Rev. Lett. **117**, 111801 (2016), arXiv:1604.01728 [hep-ex].

[223] M. A. Acero *et al.* (NOvA), *Measurement of neutrino-induced neutral-current coherent π^{0} production in the NOvA near detector*, Phys. Rev. D **102**, 012004 (2020), arXiv:1902.00558 [hep-ex].

[224] M. A. Acero *et al.* (NOvA), *Measurement of ν_{μ} charged-current inclusive π^{0} production in the NOvA near detector*, Phys. Rev. D **107**, 112008 (2023), arXiv:2306.04028 [hep-ex].

[225] K. Abe *et al.* (T2K), *Measurement of Coherent π^{+} Production in Low Energy Neutrino-Carbon Scattering*, Phys. Rev. Lett. **117**, 192501 (2016), arXiv:1604.04406 [hep-ex].

[226] K. Abe *et al.* (T2K), *Measurement of the muon neutrino charged-current single π^+ production on hydrocarbon using the T2K off-axis near detector ND280*, Phys. Rev. D **101**, 012007 (2020), arXiv:1909.03936 [hep-ex].

[227] K. Abe *et al.* (T2K), *First T2K measurement of transverse kinematic imbalance in the muon-neutrino charged-current single-π^+ production channel containing at least one proton*, Phys. Rev. D **103**, 112009 (2021), arXiv:2102.03346 [hep-ex].

[228] K. Abe *et al.* (T2K), *First measurement of the muon neutrino charged current single pion production cross section on water with the T2K near detector*, Phys. Rev. D **95**, 012010 (2017), arXiv:1605.07964 [hep-ex].

[229] P. Abratenko *et al.* (MicroBooNE), Measurement of single charged pion production in charged-current ν_μ-Ar interactions with the MicroBooNE detector (2025), arXiv:2509.03628 [hep-ex].

[230] P. Abratenko *et al.* (MicroBooNE), *First Double-Differential Cross Section Measurement of Neutral-Current π^0 Production in Neutrino-Argon Scattering in the MicroBooNE Detector*, Phys. Rev. Lett. **134**, 161802 (2025), arXiv:2404.10948 [hep-ex].

[231] P. Abratenko *et al.* (MicroBooNE), *Calorimetric classification of track-like signatures in liquid argon TPCs using MicroBooNE data*, JHEP **12**, 153, arXiv:2109.02460 [physics.ins-det].

[232] C. Adams *et al.* (MicroBooNE), *Ionization electron signal processing in single phase LArTPCs. Part II. Data/simulation comparison and performance in MicroBooNE*, JINST **13** (07), P07007, arXiv:1804.02583 [physics.ins-det].

[233] A. Lister, *Constraint of Systematic Uncertainties in an Electron Neutrino Search Using Muon Neutrinos at MicroBooNE*, Ph.D. thesis, Lancaster U. (2019).

[234] A. Hocker *et al.* (TMVA), TMVA - Toolkit for Multivariate Data Analysis (2007), arXiv:physics/0703039.

[235] P. Abratenko *et al.* (MicroBooNE), *First Measurement of Inclusive Muon Neutrino Charged Current Differential Cross Sections on Argon at $E_\nu \sim 0.8$ GeV with the MicroBooNE Detector*, Phys. Rev. Lett. **123**, 131801 (2019), arXiv:1905.09694 [hep-ex].

[236] P. Abratenko *et al.* (MicroBooNE), *First Measurement of Differential Charged Current Quasielastic-like ν_μ-Argon Scattering Cross Sections with the MicroBooNE Detector*, Phys. Rev. Lett. **125**, 201803 (2020), arXiv:2006.00108 [hep-ex].

[237] P. Abratenko *et al.* (MicroBooNE), *Multidifferential cross section measurements of $\nu\mu$-argon quasielasticlike reactions with the MicroBooNE detector*, Phys. Rev. D **108**, 053002 (2023), arXiv:2301.03700 [hep-ex].

[238] S. Gardiner, Mathematical methods for neutrino cross-section extraction (2024), arXiv:2401.04065 [hep-ex].

[239] J. Zennamo, Ž. Pavlović, A. Wickremasinghe, and R. Castillo Fernandez, *MicroBooNE Flux and Flux Uncertainties*, Tech. Rep. MicroBooNE DocDB-8622-v2 (MicroBooNE Collaboration, 2017) https://microboone-docdb.fnal.gov/cgi-bin/sso/ShowDocument?docid=8622[MicroBooNE internal].

[240] MicroBooNE Collaboration, *Neutrino Interaction Model and Uncertainties for MicroBooNE Analyses*, Tech. Rep. MICROBOONE-NOTE-1074-PUB (Fermi National Accelerator Laboratory, 2020).

[241] F. Akbar, M. Rafi Alam, M. Sajjad Athar, S. Chauhan, S. K. Singh, and F. Zaidi, *Electron and Muon production cross-sections in quasielastic ν ($\bar{\nu}$) - Nucleus scattering for $E_\nu < 1$ GeV*, Int. J. Mod. Phys. E **24**, 1550079 (2015), arXiv:1506.02355 [nucl-th].

[242] Y. Hayato, *A neutrino interaction simulation program library NEUT*, Acta Phys. Polon. B **40**, 2477–2489 (2009).

[243] P. Abratenko *et al.* (MicroBooNE), Measurement of double-differential cross sections for mesonless charged-current muon neutrino interactions on argon with final-state protons using the MicroBooNE detector (2024), arXiv:2403.19574 [hep-ex].

[244] J. Calcutt, C. Thorpe, K. Mahn, and L. Fields, *Geant4Reweight: a framework for evaluating and propagating hadronic interaction uncertainties in Geant4*, JINST **16** (08), P08042, arXiv:2105.01744 [physics.data-an].

[245] J. Calcutt, L. Fields, and K. Mahn, Geantreweight: A framework for pion scattering reweighting (2020), https://microboone-docdb.fnal.gov/cgi-bin/private/ShowDocument?docid=28376[MicroBooNE internal].

[246] P. Abratenko *et al.* (MicroBooNE), *Novel approach for evaluating detector-related uncertainties in a LArTPC using MicroBooNE data*, Eur. Phys. J. C **82**, 454 (2022), arXiv:2111.03556 [hep-ex].

[247] A. Ashkenazi, R. Diurba, A. Fiorentini, A. Furmanski, S. Gardiner, W. Ketchum, D. Martinez, L. Yates, and J. Zennamo, Mcc9 detector systematic uncertainties (2020), https://microboone-docdb.fnal.gov/cgi-bin/private/ShowDocument?docid=27009[MicroBooNE internal].

[248] S. Gardiner, *Double-differential Measurements of Mesonless Charged-current Muon Neutrino Interactions on Argon with Final-State Protons using the MicroBooNE Detector*, Tech. Rep. MICROBOONE-NOTE-1099-INT7-v0.7 (Fermilab, 2023) https://microboone-docdb.fnal.gov/cgi-bin/private/ShowDocument?docid=35518[MicroBooNE internal].

[249] P. Abratenko *et al.* (MicroBooNE), *Measurement of differential cross sections for ν_μ -Ar charged-current interactions with protons and no pions in the final state with the MicroBooNE detector*, Phys. Rev. D **102**, 112013 (2020), arXiv:2010.02390 [hep-ex].

[250] N. M. Coyle, S. W. Li, and P. A. N. Machado, Neutrino-Nucleus Cross Section Impacts on Neutrino Oscillation Measurements (2025), arXiv:2502.19467 [hep-ph].

[251] W. Tang, X. Li, X. Qian, H. Wei, and C. Zhang, *Data Unfolding with Wiener-SVD Method*, JINST **12** (10), P10002, arXiv:1705.03568 [physics.data-an].

[252] V. Blobel, in *PHYSTAT 2011* (CERN, Geneva, 2011) pp. 240–251.

[253] T. A. N., *Solution of incorrectly formulated problems and the regularization method.*, Sov Dok **4**, 1035–1038 (1963).

[254] S. Dytman (2025), nIUWG Meeting, CERN. With plots by Mohamed Ismail.

[255] P. Stowell *et al.*, *NUISANCE: a neutrino cross-section generator tuning and comparison framework*, JINST **12** (01), P01016, arXiv:1612.07393 [hep-ex].

[256] B. Bogart, K. Gallmeister, and U. Mosel, *In-medium changes of nucleon cross sections tested in neutrino-induced reactions*, Phys. Rev. C **110**, 044001 (2024), arXiv:2405.05921 [hep-ex].

[257] Q. Yan, K. Wen, K. Gallmeister, X. Lu, U. Mosel, and Y. Zheng, Understanding neutrino pion production with the GiBUU model (2025), arXiv:2507.20539 [hep-ex].

[258] P. Adamson *et al.* (MINOS), *Study of Quasielastic Scattering using Charged-Current $\nu\mu$ -Iron Interactions in the MINOS Near Detector*, Phys. Rev. D **91**, 012005 (2015), arXiv:1410.8613 [hep-ex].

[259] P. Stowell *et al.* (MINERvA), *Tuning the GENIE Pion Production Model with MINERνA Data*, Phys. Rev. D **100**, 072005 (2019), arXiv:1903.01558 [hep-ex].

[260] M. Nebot-Guinot (SBND), *Status of the Short-Baseline Near Detector at Fermilab*, Phys. Sci. Forum **8**, 22 (2023).

[261] R. Acciarri *et al.* (SBND), The Short-Baseline Near Detector at Fermilab: Input to the European Strategy for Particle Physics 2026 Update (2025), arXiv:2504.00245 [hep-ex].

[262] M. A. Hernandez-Morquecho *et al.* (LArIAT), *Measurements of Pion and Muon Nuclear Capture at Rest on Argon in the LArIAT Experiment*, Phys. Rev. Lett. **134**, 131801 (2025), arXiv:2408.05133 [hep-ex].

[263] A. Abed Abud *et al.* (DUNE), The hypothetical track-length fitting algorithm for energy measurement in liquid argon TPCs (2024), arXiv:2409.18288 [physics.ins-det].

[264] N. Wiener, *Extrapolation, interpolation, and smoothing of stationary time series, with engineering applications/*, first m.i.t. press paperback edition. ed., M.I.T. paperback series ; 9 (Technology Press of the Massachusetts Institute of Technology, Cambridge, Massachusetts, 1949).

Appendix A

Unfolding Method

A.1 Tikhonov Regularisation

A method to obtain a true distribution from a reconstructed one is through a χ^2 minimisation of the difference between the measured data, m, and forward-folded guesses of the true signal distribution, $\hat{n}$. The minimisation approach also incorporates the uncertainties on the measurement in the form of the covariance matrix V:

$$\chi^2(\hat{n}) = (m - \mathcal{R}\hat{n})^T V^{-1} (m - \mathcal{R}\hat{n}), \tag{A.1}$$

and $\mathcal{R}$ is the response matrix as defined in Equation (9.9). This can be rewritten as

$$\chi^2(\hat{n}) = \left(\bar{m} - \bar{\mathcal{R}}\hat{n}\right)^T \left(\bar{m} - \bar{\mathcal{R}}\hat{n}\right), \tag{A.2}$$

by decomposing the inverse covariance matrix as $V^{-1} = Q^T Q$, as described in Ref. [251]. The covariance matrix can then be absorbed into the measured spectrum and detector response as

$$\bar{m} = Qm \quad \text{and} \quad \bar{\mathcal{R}} = Q\mathcal{R}. \tag{A.3}$$

The minimum of this χ^2 function is at

$$\bar{m} = \bar{\mathcal{R}}\hat{n}, \tag{A.4}$$

which is the case when the prediction matches the result of the direct inverse, analogous to Equation (9.14):

$$\hat{n} = (\bar{\mathcal{R}}^T\bar{\mathcal{R}})^{-1}\bar{\mathcal{R}}^T\bar{m}. \tag{A.5}$$

The only difference in this minimisation approach so far is the inclusion of the covariance matrix. However, this does not address the large oscillations. The idea behind Tikhonov regularisation [253] is the addition of a penalty term to the minimisation:

$$\chi^2(\hat{n}) = \left(\bar{m} - \bar{\mathcal{R}}\hat{n}\right)^T \left(\bar{m} - \bar{\mathcal{R}}\hat{n}\right) + \tau(C\hat{n})^T(C\hat{n}), \tag{A.6}$$

where C is a chosen matrix. Common choices include the identity matrix, which penalises large values such as those arising from strong oscillations in the unfolded spectrum, or first- and second-derivative matrices, which penalise bin-to-bin differences and curvature, respectively. The strength of the regularisation is controlled by the free parameter τ, and a suitable value needs to be chosen to balance bias and variance for the unfolded solution.

The minimum of Equation (A.6), found by setting $\frac{d\chi^2(\hat{n})}{d\hat{n}} = 0$, is at:

$$\hat{n} = \left(\bar{\mathcal{R}}^T\bar{\mathcal{R}} + \tau C^T C\right)^{-1}\bar{\mathcal{R}}^T\bar{m} \tag{A.7}$$

$$= C^{-1}\left((\bar{\mathcal{R}}C^{-1})^T(\bar{\mathcal{R}}C^{-1}) + \tau I\right)^{-1}(\bar{\mathcal{R}}C^{-1})^T\bar{m} \tag{A.8}$$

$$= C^{-1}\left(\bar{\mathcal{R}}_C^T\bar{\mathcal{R}}_C + \tau I\right)^{-1}\bar{\mathcal{R}}_C^T\bar{m}, \tag{A.9}$$

which was rewritten in anticipation of the following steps and where on the last line the change of variable $\bar{\mathcal{R}}_C \equiv \bar{\mathcal{R}}C^{-1}$ is made.

To better understand how Tikhonov regularisation addresses the oscillations, it is helpful to re-examine the problem using SVD, as done in Ref. [251]. The redefined response matrix, $\bar{\mathcal{R}}_C$, can be decomposed as

$$\bar{\mathcal{R}}_C = O\Sigma G^T, \tag{A.10}$$

where G is an orthogonal matrix transforming a true signal distribution into an 'effective frequency' basis, where the detector response $\Sigma = \mathrm{diag}(\varsigma_1, \varsigma_2, \dots)$ is a rectangular diagonal matrix containing the singular values ς_i. O is another orthogonal matrix transforming the result into the basis of the measured reconstructed quantity. Substituting Equation (A.10) into Equation (A.9) gives

$$\hat{n} = C^{-1}G(\Sigma^2 + \tau I)^{-1}\Sigma^T O^T\bar{m}. \tag{A.11}$$

This can be rewritten as

$$\hat{n} = C^{-1}G\mathcal{F}\Sigma^{-1}O^T\bar{m}, \tag{A.12}$$

where $\Sigma^{-1} = \text{diag}\left(\frac{1}{\varsigma_1}, \frac{1}{\varsigma_2}, \dots\right)$. The small singular values now correspond to high-frequency components. In the direct inverse, dividing by these small ς_i values dramatically amplifies any noise in the measurement, causing the oscillations. The filter $\mathcal{F} = \text{diag}\left(\frac{\varsigma_1^2}{\varsigma_1^2+\tau}, \frac{\varsigma_2^2}{\varsigma_2^2+\tau}, \dots\right)$ is also a diagonal matrix that reduces the impact of small values of ς_i, with the degree of suppression controlled by the parameter τ.

A.2 The Wiener-SVD Approach

The Wiener-SVD approach to regularisation provides an alternative method for constructing the filter based on principles from signal processing [251]. While the Tikhonov filter uses a single parameter τ to suppress small singular values ς_i, the Wiener-SVD method builds an optimal filter for each component by maximising the signal-to-noise ratio. The method makes use of the Wiener filter [264], which in its classical form for time-series data is defined in the frequency domain as

$$W^{\text{ideal}}(\omega) = \frac{E\left[\left(R(\omega)S(\omega)\right)^2\right]}{E\left[\left(R(\omega)S(\omega)\right)^2\right] + E[N(\omega)^2]}, \tag{A.13}$$

where $S(\omega)$ is the true signal in frequency space, $R(\omega)$ is the response function, and $N(\omega)$ is the noise. Here $E[\cdot]$ denotes the statistical expectation. When the true statistics are unknown, one can replace expectation values with predictions (for instance from simulation):

$$W(\omega) = \frac{\left(\tilde{R}(\omega)\,\tilde{S}(\omega)\right)^2}{\left(\tilde{R}(\omega)\,\tilde{S}(\omega)\right)^2 + \tilde{N}(\omega)^2}. \tag{A.14}$$

The effect of the filter is that it most strongly suppresses the frequencies for which noise dominates over signal contributions. To apply this idea to unfolding, one treats the SVD effective-frequency basis as analogous to the frequency domain. Let n_β^{CV} be the event rate prediction in true-bin space. Transforming this prediction into the effective-frequency basis and applying the response Σ gives the effective amplitude in component i:

$$n_i^{\text{eff.}} = \left(\Sigma G^T C n^{\text{CV}}\right)_i. \tag{A.15}$$

The noise here arises from the uncertainties on the measured data. After the transformation in Equation (A.3), the covariance matrix of $\bar{m}$ is the identity matrix,

and the measurement uncertainties are thus uncorrelated with unit variance. Hence, the expected noise power in each component is one. The Wiener-SVD filter can then be constructed as a diagonal matrix with entries analogous to Equation (A.14):

$$\mathcal{W}_{ii} \;=\; \frac{\left(n_i^{\text{eff.}}\right)^2}{\left(n_i^{\text{eff.}}\right)^2 + 1}. \tag{A.16}$$

This filter $\mathcal{W}$ replaces the Tikhonov filter $\mathcal{F}$ in Equation (A.12), giving the unfolded estimate:

$$\hat{n} = \underbrace{C^{-1} G \mathcal{W} \Sigma^{-1} O^T Q}_{\text{Unfolding matrix } U} m. \tag{A.17}$$

This method does not rely on a tuning parameter, but the dependence on the prediction n^{CV} means it requires the prediction to be a reasonable approximation of the truth.

The unfolded and scaled differential cross sections can then be computed using that unfolding matrix as shown in Equation (9.12). The covariance matrix for the Wiener-SVD unfolded differential cross-section measurements can be computed from the covariance matrix for the background-subtracted event counts before unfolding V together with the unfolding matrix [238]:

$$\left(\mathcal{V}_{\text{unf}}\right)_{\alpha\beta} \;=\; \frac{\sum_{a,b} U_{\alpha a} V_{ab} \left(U^T\right)_{b\beta}}{\left(\boldsymbol{\Phi} N_T N_{\text{POT}}\right)^2 \Delta x_\alpha \Delta x_\beta}. \tag{A.18}$$

For reporting the covariances between bins of all differential cross-section measurements, the block-wise covariance matrix $\mathbf{V}$, as defined in Equation (8.4) but for the background-subtracted event counts, can be unfolded using a block-diagonal unfolding matrix constructed from the individual cross-section unfolding matrices [238]:

$$\mathbf{U} = \text{diag}_{\text{block}}\left(U^{\cos(\theta_\mu)}, U^{p_\mu}, U^{\cos(\theta_\pi)}, U^{p_\pi}, U^{\theta_{\mu\pi}}\right), \tag{A.19}$$

which is then used as in Equation (A.18):

$$\left(\boldsymbol{\mathcal{V}}_{\text{unf}}\right)_{\alpha\beta} \;=\; \frac{\sum_{a,b} \mathbf{U}_{\alpha a} \mathbf{V}_{ab} \left(\mathbf{U}^T\right)_{b\beta}}{\left(\boldsymbol{\Phi} N_T N_{\text{POT}}\right)^2}, \tag{A.20}$$

to get the covariances between bins of all five unfolded differential cross sections. The bin width normalisation is omitted here to have consistent units across all matrix entries.